A Parameterization of the Nucleon-Nucleus Optical Model Potential

by

Robert Lindsay Varner, Jr.

A Dissertation submitted to the faculty of The University of North Carolina at Chapel Hill in partial fulfillment of the requirements for the degree of Doctor of Philosophy in the Department of Physics and Astronomy.

Chapel Hill

1986

Approved by:

Thomas B. Clegg

Adviser

W. J. Thompson

Reader

E. J. Ludwig

Reader

ROBERT LINDSAY VARNER, JR. A Parameterization of the Nucleon-Nucleus Optical Model Potential (Under the direction of Thomas B. Clegg.)

In recent years there have been three major improvements in the tools and techniques of theoretical and experimental nuclear physics which permit an extensive reparameterization of the nucleon-nucleus optical model potential. These include: (1) the development of high intensity beams of polarized protons, and more recently, neutrons, enabling the routine measurement of both cross section and analyzing power data, (2) the development of sophisticated models of the nucleon-nucleus optical model potential, in which the potential may be calculated from a knowledge of the nucleon-nucleon interaction, and (3) the development of powerful computational tools, both hardware and software, allowing simultaneous optimization of the many parameters of a global optical model to fit elastic scattering in hundreds of datasets. We have utilized these developments to aid us in a new parameterization of the optical model potential. We have measured a new set of ($\vec{p}$,p) elastic scattering data at 16 MeV and augmented this data with ($\vec{p}$,p) data from 17 to 65 MeV. We have also included neutron elastic scattering data, both (n,n) and ($\vec{n}$,n), from 10 to 26 MeV. The resulting dataset contains approximately 8800 data points. We have selected our parameterization of the optical potential using guidance from folding-model calculations, then tested the parameters, discarding those to which the analysis appeared insensitive. To estimate the optimum parameter values, we have constructed a program, MINOPT, combining a small, fast optical model program and a modern minimization program. Using these, we have found the best values of the parameters of an optical model potential describing our large database, estimated relative uncertainties in these values, and compared our result with earlier phenomenological analyses and current microscopic predictions.

Acknowledgements

When a graduate student has been measuring and analyzing data as long as I have, he accumulates a great debt to very many people, some of whom may not even be around to receive the thanks heaped upon them in this Acknowledgement. Everyone with whom I have interacted at UNC and TUNL have contributed to my learning and I thank them all. I hope I have contributed to their learning in some fashion. Below, I thank those who have contributed especially to this work.

I must first acknowledge the assistance of those who helped measure and analyze the 16 MeV proton scattering data. These include all members of the UNC Nuclear Group: the faculty Tom Clegg, Ed Ludwig, and Rick Anderson; fellow members of my "generation" of the nuclear group Barry Burks and John Wilkerson; members of the next "generation" of students Jimmy Bowsher, Roy Fauber, Tim Mooney, Ken Nash, and Tom Spencer, who got started by helping in these experiments. I wish to especially thank Tom McAbee and Bill Thompson who are still educating me about the role of effective interactions in the semi-empirical analysis of elastic scattering.

I must also thank the faculty and staff at TUNL for their continual work in keeping the accelerator and data acquisition facilities in operation, particularly Drs. N.R. Roberson and C.R. Gould for their development of the XSYS data acquisition system; S.E. Edwards for his tireless work keeping the VAX and the electronics functioning. Special thanks go to Mike Bailey for her patience in drawing the 8800 data points in figures 4-1 to 5-20.

I wish to also thank the patience of Oak Ridge National Laboratories for permitting me to continue working on the completion of this document and particularly for the use of the Physics Division FPS-164 to complete the uncertainty calculations with MINOPT.

Finally, I must thank my wife Marian, who has generously contributed to this dissertation both materially (with the compuscript preparation) and spiritually (through her constant moral support).

Table of Contents

I. Introduction

The nuclear optical model has long been a fundamental tool of nuclear physics. It is used to describe elastic scattering of particles from nuclei. An optical model which successfully describes elastic scattering is used to calculate distorted waves for use in the Distorted Wave Born Approximation (DWBA), or as a potential to be modified for use in coupled-channels calculations. The optical potential can also be viewed as the one-body approximation of the fundamental many-body problem of nuclear scattering, and thus as a testing ground for microscopic models of nuclear scattering.

This work describes a new parameterization of the nucleon-nucleus optical model at non-relativistic energies. We are motivated to do this for several reasons:

(1) Because of improvements in polarized ion-source technology, we and others have been able to measure accurate elastic scattering of nucleons from nuclei, including analyzing powers as well as cross sections. This provides extra sensitivity to the spin-orbit potential, as well as other components of the optical model;

(2) In recent years, it has become possible to calculate the nucleon-nucleus optical potential starting from knowledge of the nucleon-nucleon interaction. These calculations range from a mostly empirical folding model (Gree68), to fully microscopic approaches of Jeukenne, et al. (Jeuk77). These models can suggest to us what the parameters of the optical model should be, as opposed to the "cut and try" techniques of parameterization characteristic of earlier analyses (Becc69);

(3) Powerful search algorithms capable of searching stably on many parameters have become available, as well as the fast computers

required to implement these searches on large datasets of more than 100 angular distributions (Jame78).

To obtain the potential parameterization, we examined the properties of folding-model calculations, especially for the geometric properties of the real central potential and the spin-orbit potential (Chap. 2). For those parts of the potential not described by folding models or microscopic calculations (the imaginary part of the potential), we examined the phenomenological properties of these potentials in the literature and made a parameterization which is likely to satisfy this phenomenology.

To obtain the required dataset, we first measured at the Triangle Universities Nuclear Laboratory (TUNL) 16-MeV ($\vec{p}$,p) elastic scattering (Chap. 3,4). [The notation $\vec{p}$ and $\vec{n}$ denoted polarized incident beams of protons and deuterons.] The measurement is often regarded as simple, but requires high accuracy and the measurement of many angular distributions with different targets and experimental conditions. We augmented these TUNL data with results from selected laboratories specializing in the measurement of elastic scattering of nucleons (Chap. 5). The proton scattering data are largely simultaneous measurements of cross sections and analyzing powers. The neutron data are mostly cross sections only, except for measurements of ($\vec{n}$,n) analyzing powers available from TUNL.

To construct the search program for such a global optical model search, we combined OPTICS, a fast optical-model program, with MINUIT, a powerful parameter optimization program. The resulting program, MINOPT (Chap. 6), runs on both a DEC VAX 11/780 and an FPS-164 attached processor. The latter computer was fast enough to complete searches on 16 parameters, using 140 datasets, in only 2 to 4 hours, compared with the 20 to 40 hours required on the VAX for each search. The program MINOPT is efficient and is able to estimate an uncertainty for each parameter in a model-free way. The only difficulty arises in understanding the significance of a change in the least squares function, with which we hope to estimate the uncertainty of our parameters (Chap. 6.2, 6.4, 7.2).

This dissertation describes in detail the process outlined above. For the final potential parameter values, we compare the calculations with the data. We also compare the volume integrals of various parts of the potential with 1) previous parameterizations, 2) microscopic calculations, and 3) with phenomenological results. We find that our potential is consistent with previous phenomenological results, and, that the microscopic calculation of Jeukenne, et. al (Jeuk77) agrees closely with our result at energies in the middle of our parameterization of the real potential. We also observe that previous empirical analyses disagree in detail with our results, especially in the isovector behavior of the real potential.

II. Motivation for a New Global Parameterization

2.1 Introduction

The optical model of nucleon scattering has a long history of theoretical and phenomenological study (Hodg71,Satc83). In this chapter, the components of the optical model and our global parameterization of these components are shown, as well as our motivations for performing a new global parameterization. These motivations are of two kinds: first, the improvements possible over previous global analyses in data-set completeness and analysis techniques; and, second, the existence of significant microscopic calculations to guide our parameterization and against which to compare our resulting potential.

2.2 Nuclear Optical Model

The nucleon-nucleus optical model is the reduction of the complicated many-body problem of the scattering of a nucleon from a nucleus to the scattering of a single particle from a complex one-body potential. This potential is complex to model the loss of flux from the incident channel into the inelastic and reaction channels available when a nucleon is incident on a nucleus (Eck77). The values of the model parameters can be derived empirically (by fitting elastic scattering data), or calculated from microscopic models (Brie77, Jeuk77). The resulting potentials serve as a basis for the non-central potentials used in coupled-channels calculations or to generate distorted waves for use in DWBA calculations. We are employing a semi-empirical approach to the optical-model potential, using it as a means of parameterizing a large amount of elastic scattering data. Our results may be used for comparison with potentials derived from microscopic models.

We use the optical potential in a non-relativistic Schrödinger equation. The non-relativistic wave equation is chosen for three reasons. First, the data we analyze are at an energy where

relativistic effects, at least in the kinematics, are small. At the maximum incident energy of E_p=65 MeV considered here, $(v/c)^2$=0.14, which leads to a 7% error in the calculated proton momentum. Second, part of our goal is to provide an optical model potential useful in other nuclear physics calculations, e.g. DWBA calculations. These calculations are almost always made with the Schrödinger equation; to be useful, we must provide a suitable potential. Third, the microscopically derived potentials for which we wish to provide guidance are non-relativistic.

2.2.1 Potential Geometry

The nucleon-nucleus optical-model potential normally includes central and spin-orbit components; a Coulomb potential must also be included for proton scattering. The form-factors (radial shapes) we use for the nuclear part of the potential are based on the Woods-Saxon (WS) form. This form has two parameters, 'R' the half-value radius and, 'a' the diffuseness. It is sometimes known as the two-parameter-Fermi (2pF) shape. It is used because it is similar to the shape of nuclear density distributions; the short range of the nuclear force suggests that the real parts of the potential should also resemble the nuclear density. The functional form of the Woods-Saxon shape is,

$$f_{ws}(r,R,a) = \frac{1}{1 + \exp\left[\frac{r-R}{a}\right]} \quad . \qquad 2\text{-}1a$$

In addition, a surface-peaked form factor can be generated by taking its derivative,

$$g_{ws}(r,R,a) = -4a\frac{d}{dr} f_{ws}(r) = \frac{4\exp\left[\frac{r-R}{a}\right]}{\left[1 + \exp\left[\frac{r-R}{a}\right]\right]^2} \quad . \qquad 2\text{-}1b$$

Given these form factors, the local optical potential for nucleon-nucleus scattering is usually written as,

$$V(r) = -V_0 f_{ws}(r,R_0,a_0) + -i(W_v f_{ws}(r,R_w,a_w) + W_s g_{ws}(r,R_w,a_w)) \qquad 2\text{-}2$$

$$+ -2(V_{so}+iW_{so}) \left[\frac{-1}{r}\frac{d}{dr} f_{ws}(r,R_{so},a_{so}) \; \bar{\ell}\cdot\bar{\sigma} \right]$$

$$+ \begin{cases} V_{coul}(r), & (p,p) \\ 0, & (n,n) \end{cases}$$

In Eq. 2-2, the successive terms are the real central potential, the imaginary central potential, composed of a volume term and a surface-peaked term, the spin-orbit potential, composed of real and imaginary parts, and, when the scattering of protons is calculated, the Coulomb potential. These components of the optical model potential are described below.

2.2.2 Real Central Potential

The real central part of the potential has a simple, volume-dominated shape, similar to nuclear matter distributions. This is because the real potential is produced largely by short-range nucleon-nucleon interactions between the projectile and the nucleons of the target. In the energy range of this investigation, the real central term is much deeper than any other component of the potential.

2.2.3 Imaginary Central Potential

The imaginary central potential is usually represented as a combination of volume and surface-peaked form factors. The surface peaking of the form factor would be expected in cases where the dominant inelastic and reaction processes occurred in the surface of the nucleus, for example collective excitation and single nucleon transfer reactions (Satc83, pg. 457). Such a form is found in microscopic calculations of the imaginary potential (Oste84, Jeuk77). This peaking is most prominent for low energy (E_p<20 MeV) nucleon scattering. In addition, at these low energies, the nucleon wave function is absorbed at the nuclear surface, preventing it from sampling the nuclear interior; thus low energy scattering is not very sensitive to the interior. For higher energy projectiles which penetrate the nuclear interior, the dominant absorption is from nucleon-nucleon collisions in the nucleus,

related to the finite mean free path of nucleons in the nucleus. This absorption then resembles the bulk distribution of target nucleons and is modeled as a volume type Woods-Saxon form factor.

2.2.4 Spin-Orbit Potential

The non-central part of the optical potential used here is the spin-orbit potential, which appears to originate from the nucleon-nucleon spin-orbit force. This part of the potential may be complex, although calculations and most results from low-energy scattering show it to be essentially real at E≤65 MeV (Brie77). Work with ($\vec{n}$,n) analyzing power data indicates that some small, imaginary spin-orbit potential may help the description of these data (Walt84). The spin-orbit potential is usually taken to have the Thomas radial form (Satc83, pg. 457). This is not correct, since the Thomas form results from relativistic corrections to the motion of a point particle with spin in a potential; this model of the nucleon-nucleus spin orbit potential gives calculated spin-orbit forces which are much too small and of the wrong sign to describe properly the observed shell-model splittings. However, folding model calculations with nucleon-nucleon spin-orbit interactions give shapes easily parameterized by the Thomas form (Satc83, pg. 458).

2.2.5 Coulomb Potential

When the scattering of protons from nuclei is calculated, the potential must include the Coulomb potential. It is a relatively slowly varying (in r-space) part of the total real potential near the nucleus (the average value of V_{coul} in the interior of tin nuclei is 10 MeV). The long-range effects of Coulomb scattering are accounted for by requiring that the scattering wave function far from the nucleus match to linear combinations of wave functions for pure Coulomb potentials. The Coulomb potential used here is modeled as that from a sphere of radius R_c and charge Z_t uniformly distributed throughout its volume:

$$V_{coul} = \begin{cases} \dfrac{Z_p Z_t e^2}{r}, & r \geq R_c \\ \dfrac{Z_p Z_t e^2}{2R_c}\left[3 - \dfrac{r^2}{R_c^2}\right], & r \leq R_c \end{cases} \quad . \qquad 2\text{-}3$$

In applying this approximate potential to proton scattering from realistic nuclei, we use an effective radius parameter, which gives effects at the nuclear surface comparable to those of the true diffuse-edged charge distribution. Sect. 2.6.3 describes our procedure in more detail.

2.2.6 Parameterization Procedure

Given the above potential form, values for the parameters of the optical model for a given nucleus at a particular energy are found by the following procedure. We postulate values for the parameters of the potential, then solve the Schrödinger equation for the scattering wave function, which is used to predict elastic-scattering observables. After comparison with the data, the potential is modified, the equation re-solved, and another comparison made; the procedure is repeated until a good fit is obtained (Hodg71, pg. 151). This iterative procedure is time consuming and subject to considerable ambiguity, especially given the large number of parameters in the usual optical potential parameterization. It is the only general procedure yet found for discovering the best optical parameters. Approaches to inverting the problem (going directly from the data to the potential) have been proposed (Ioan85), but they were not considered here. The principal effort in optical model research has been to find an efficient procedure for choosing the parameters before each calculation, in order to find quickly the best potential. Our approach to fitting the parameters of the global model is described in Sects. 6.2 and 6.4.

2.3 Folding Model of the Optical Potential

The optical potential can be calculated from semi-microscopic grounds. Most of these calculations proceed by means of the folding

model, first used seriously for data analysis by Greenlees et al. (Gree68). In this model the potential is calculated as the superposition of the interactions between the incident nucleon and each of the nucleons in the target. The first-order folding model is (Satc83, pg. 475),

$$V(\bar{r}) = \int v(|\bar{r}-\bar{r}'|)\rho(\bar{r}')\, d\bar{r}' \qquad 2\text{-}4$$

in which $v(|\bar{r}-\bar{r}'|)$ is an "effective" nucleon-nucleon interaction, and $\rho(\bar{r}')$ is the distribution of the nucleons in the nucleus. The nuclear density distribution can be inferred from the charge distribution measured by (e,e) scattering, or calculated from a self-consistent model of the nucleus (Pres75).

The effective interaction is taken to be similar to the free nucleon-nucleon interaction in its spin and isospin structure (Satc83, pg. 638). In the presence of other nucleons it differs from the free interaction for many reasons, among which are the effects of the surrounding nucleons (the mean-field potential) and exchange (Pauli blocking) effects. Attempts have been made to parameterize the effective interaction by fitting elastic scattering data (Gree68, Tarr79). This generally is as successful as standard optical model fitting, but can be more computationally intensive if the integral in Eq. 2-4 must be evaluated for each computation of V(r), rather than simply evaluating Eq. 2-2. This makes the use of a general folding model difficult for large-scale analysis. Parameterizations of the effective interaction from other data are also possible, as are microscopic derivations (Satc83, Ch. 15). Comparison of folded potentials with phenomenologically derived potentials provides a test of the effective interaction.

2.3.1 Volume Integrals and RMS Radii

One result from the folding model in the form of Eq. 2-4 is that optical model potentials are characterized by their volume integrals and RMS radii (Gree68), independent of the details of the density distributions. For most form-factors, like those defined in Eqs. 2-1, we

define the volume integral, J_0, and the RMS radius by,

$$J_0 = 4\pi \int V(r)\, r^2 dr \ , \qquad \langle r^2 \rangle = \frac{4\pi}{J_0} \int r^2 V(r)\, r^2 dr \ . \tag{2-5a}$$

For the spin-orbit form-factor, a different integral is defined,

$$J_2 = 4\pi \int r^2 V_{so}(r)\, r^2 dr \ , \quad \langle r_2^2 \rangle = \frac{4\pi}{J_2} \int r^4 V_{so}(r)\, r^2 dr \tag{2-5b}$$

For our Woods-Saxon form factors, the volume integrals are approximately (in the limit of $a/R \ll 1$),

$$\frac{J_R}{A} = \frac{J_0(V_0,R_0,a_0)}{A} = \frac{4\pi}{3} \frac{R_0^3}{A} V_0 \left[1 + \left[\frac{\pi a_0}{R_0} \right]^2 \right]$$

$$\frac{J_W}{A} = \frac{J_0(W_V,R_{WV},a_{WV})}{A} + \frac{J_0(W_S,R_{WS},a_{WS})}{A}$$

$$= \frac{4\pi}{3} \frac{R_W^3}{A} \left[W_V \left[1 + \left[\frac{\pi a_{WV}}{R_{WV}} \right]^2 \right] + \frac{12 a_{WS}}{R_{WS}} W_S \left[1 + \frac{1}{3} \left[\frac{\pi a_{WS}}{R_{WS}} \right]^2 \right] \right] \tag{2-6}$$

$$\frac{J_{SO}}{A} = \frac{J_2(V_{SO},R_{SO},a_{SO})}{A} = 8\pi \frac{R_{SO}^3}{A} V_{SO} \left[1 + \left[\frac{\pi a_{SO}}{R_{SO}} \right]^2 \right] \ .$$

The significance of volume integrals is that for density-independent effective interactions, the volume integrals in Eq. 2-5 reduce to the integral of the effective interaction multiplied by the A of the nucleus (Satc83, App.C),

$$J_i = A\, J_v = A \int v_i(s) s^2 ds \ . \tag{2-7}$$

The quantity J_i/A (i=R,W,SO) is characteristic of the corresponding underlying effective interaction, and is independent of the specific nuclear densities used. The spin-orbit integral J_2 is constructed to give the integral of the effective nucleon-nucleon interaction for form factors like that of the spin-orbit potential. The RMS radii have similarly simple behavior, if the potential results from the folding of a density distribution with a finite-range interaction:

$$\langle r^2 \rangle_{pot} = \langle r^2 \rangle_{\rho} + \langle r^2 \rangle_{v} \ , \qquad 2\text{-}8$$

where $\langle r^2 \rangle_{\rho}$ is the RMS radius of the density distribution and $\langle r^2 \rangle_{v}$ is the RMS radius of the effective interaction.

Because of the expected simple behavior of the volume integrals and RMS radii, they are often used to compare and characterize potentials.

2.3.2 Microscopic Calculation of Optical Potentials

There are two successful approaches to the microscopic calculation of the optical model potential, commonly known as the nuclear structure approach and the nuclear matter approach. The former technique (Oste84) requires one to specify the nuclear-structure properties of each target-nucleus for which a calculation is desired. This permits the accurate calculation of some parts of the absorptive potential, as well as detailed prediction of the form factors. However, it is difficult to extract global predictions from these models.

Nuclear matter techniques, in contrast, predict the properties of nuclei from the properties of nucleons interacting in (infinite) nuclear matter. They cannot easily predict the optical potential depths and geometries of individual nuclei, because of shell effects, but predict the global behavior of optical potential volume integrals and RMS radii, and so are appropriate to the goals of our analysis. We will only compare our global potential with potentials calculated in nuclear matter approaches to microscopic predictions.

Nuclear matter calculations use as input a realistic parameterization of the nucleon-nucleon interaction. This interaction is converted into an "effective" interaction by solving the Bethe-Goldstone equation,

$$G\Phi = v\Psi \qquad 2\text{-}9$$

in which v is the realistic nucleon-nucleon interaction, Ψ is the wave function of the nucleon in nuclear matter, Φ is a plane wave describing a nucleon in non-interacting nuclear matter, and G is the "G-matrix" effective interaction, defined by Eq. 2-9. This procedure includes many-body effects in the effective interaction so that the nucleon wave functions may be expressed in the non-interacting basis (Pres75, Ch. 8;

Jeuk75, Day67). This effective interaction can be used in a folding model calculation for finite nuclei to produce the nucleon-nucleus potential (Satc83, pg. 635), and in nuclear matter to calculate the average one-body potential experienced by each nucleon.

In the work of Jeukenne, et al. (often referred to as JLM) (Jeuk76, Jeuk77), this latter approach is used. They solve the Bethe-Goldstone equation by directly solving the integral equation for the G-matrix. Then they calculate the total energy of a nucleon in nuclear matter (the "mass operator"), from which the optical potential in nuclear matter is computed. The components of the mass operator have been fitted by JLM
and tabulated as simple polynomial functions of ρ, the nuclear matter density, and E, the nucleon energy. From these tables the potential may be estimated, using empirically determined nuclear densities, at any point in a finite nucleus by inserting the density at that point and the incident energy of the scattering nucleon in the polynomial expression for the mass operator. This is called a "local density approximation" (LDA). It is not possible to extract an effective nucleon-nucleon interaction from the results of Jeukenne, et al., except in a rough approximation (Jeuk77).

The method of Brieva and Rook (Brie77, Gera84), involves computing the effective nucleon-nucleon interaction (G-matrix) in nuclear matter, then using this interaction directly in the folding model. Their technique involves converting the Bethe-Goldstone equation into a set of coupled differential equations and solving them. The calculated G-matrix elements are functions of the density of the nuclear matter, and are used in a slightly different version of the local density approximation, in which the effective interaction in a finite nucleus at a given radial position is taken to be that in nuclear matter of the same density. The optical model potential is computed by folding this density-dependent effective interaction with nuclear density distributions. The difference between this approach and that of JLM is mainly one of mathematical technique and form of the final parameterization of the result.

2.4 Features of Global Optical Potentials

The global optical model analysis of elastic scattering data is the parameterization of the model parameters of Sect. 2.2, as a function of the incident nucleon isospin and energy and the target A, Z, and isospin, in order to obtain a smoothly varying potential that best describes a large amount of data.

2.4.1 Motivations for global parameterization

There are several reasons for this type of analysis:

(1) It is often necessary to postulate an optical potential for nuclei for which elastic scattering is not possible (e.g. for the residual nucleus in some transfer reactions or decay of unstable fission products);

2) There are many "ambiguities" or correlations between the parameters of the model; often these arise from the use of many optical parameters to describe small amounts of data. A global analysis, including much more data and a similar number of parameters, should be less sensitive to such ambiguities;

3) The potentials that fit single angular distributions reflect the nuclear structure of the target. Global potentials should average over these effects, given a sufficiently large dataset, and provide a potential suitable for comparison to microscopic models of the optical potential.

2.4.2 Observed global properties

The study of the average trends of optical model parameters shows that such global analyses are possible. The observed global properties of the volume integrals of empirical potentials have been summarized in several references (Hodg71, Rapa82, Satc83). The most noteworthy properties are that

1) J_r/A decreases almost linearly with increasing E

2) J_r/A is approximately constant with target A in proton potentials, but decreases monotonically with A in neutron

potentials

3) J_w/A is almost constant with target A and incident E in proton potentials (Agra75), but decreases monotonically with target A in neutron potentials

4) J_{so}/A varies slowly with target A and incident E (Coop80).

Most of these properties are qualitatively well determined for proton scattering. The results for neutron scattering are summarized in (Rapa82).

Although volume integrals per nucleon are convenient for summarizing the gross properties of the optical potential, they do not help to elucidate global properties of the potential geometry, nor to deconvolute complicated A- and E-dependent effects. Unfortunately, optical model parameters derived from fits to individual nuclei at single energies vary considerably from nucleus to nucleus (Hodg71). Thus, to extract the global properties of the individual parameters, we must postulate models of nuclear behavior as a function of A and E, which are likely to reproduce the general behavior of the largest amount of data (angular distributions, volume integrals, etc.).

The global behavior of optical model potentials is often postulated from the behavior of,

1) volume integrals of individual fits to scattering data,

2) nuclear matter distributions,

3) properties of nucleon-nucleon interactions.

The radius parameters are usually assumed to be proportional to $A^{1/3}$, the apparent gross variation of the radius of the matter distributions in nuclei. This is not exactly true, as discussed in Sect. 2.5. The diffuseness parameters are usually assumed constant, because shell effects result in variations in the values which are not easily parameterized.

In general, all other functional dependence of the potentials is put into the depth parameters. The energy dependence of the real potential is usually assumed to be linear at these energies, consistent with the volume integral behavior. A more complex E-dependence exists for the absorptive potential, as mentioned earlier (Ch. 2.2.3), in

which the form-factor actually changes with incident nucleon energy. Such a dependence is necessary to explain the behavior of the volume integrals of the absorption with E.

The A-dependence of the real and imaginary potential depths is difficult to extract from volume integrals, but is instead postulated on the basis of nucleon-nucleon scattering properties. The main A-related effect is from isospin dependence of the N-N potential, that is the differences in n-p (neutron-proton) scattering from n-n or p-p scattering. This introduces a term (called the isovector term) in the optical potential which is proportional to (N-Z)/A (Hodg71, Ch. 9), with negative sign for (n,n) scattering and positive sign for (p,p) scattering when N>Z. This term also introduces an apparent A-dependence into the optical potential, since N-Z increases with A for nuclei on the line of stability. There are additional isospin effects because of Pauli blocking (exchange) effects in the scattering from nuclei.

Even when starting with these predetermined forms for the potentials, it is difficult to unambiguously parameterize each term. In particular, it is difficult: (1) to separate surface and volume components of the absorption (as can be seen by the general behavior of the volume integral of the absorption), and (2) to separate A-dependence of the optical potential (as in the radius parameters) from isospin dependence of the depth.

To extract isospin dependence, one must investigate systems in which the isospin changes. This may be accomplished by: (1) studying targets with different isospin using the same projectile, or (2) studying the same target with both neutrons and protons, in which case the isovector potential changes sign. There are difficulties with each approach. In the former approach, the nuclear asymmetry, $\epsilon=(N-Z)/A$ increases with A, from $\epsilon=0$ for ^{40}Ca to $\epsilon=0.21$ for ^{208}Pb, so that A and ϵ are correlated. Of course, A increases monotonically while ϵ fluctuates, but this is apparent only in a very complete dataset. In addition, the contribution of the isovector potential to the total optical model potential is small. For the real central potential, one

has, typically, $\epsilon * V_t/V_0 = 0.04$, that is, the effect of the isovector potential is about 4% of the total real potential for a nucleus like ^{90}Zr. The most effective appearing means of implementing case (1) is to study chains of isotopes, in which A changes very little, but ϵ changes significantly. Unfortunately, nuclear structure often varies significantly across a chain of isotopes, resulting in changes in the optical potential not related to the isovector dependence. This confuses such an analysis, making it almost useless for separating out the isovector components of the optical potential.

The alternative approach is to parameterize (p,p) and (n,n) scattering consistently. Since the isovector contributions to the potential are of opposite sign for the two cases, while the nuclear structure effects and A dependence remain the same, such a procedure should effectively parameterize the isovector potential. Unfortunately, effects of the Coulomb potential in (p,p) scattering, which vanish for (n,n) scattering, can confuse this analysis. These effects occur because the optical potential is momentum dependent (Satc83, pg. 451); in a semi-classical description the repulsive Coulomb force, acting only for (p,p) scattering, reduces the momentum of the incident proton, and thus the average optical potential for a proton at a given asymptotic kinetic energy is different from that of a neutron incident with the same asymptotic kinetic energy.

The best method to account for these Coulomb effects in the optical potential would be to solve the Schrödinger equation with a momentum-dependent potential. This results in an integral equation (Satc83, pg. 450) which is difficult to solve; it is also not clear what form of momentum dependence to choose. If one chooses to solve the momentum-independent equation, an approximation is needed for the effect of the Coulomb potential.

The usual approach is to make a "Coulomb correction" (Pere63) to the depth of the real potential. If the imaginary potential is also momentum dependent, it too should have a Coulomb correction (Rapa80b). In the Perey model, however, there is no Coulomb correction for the imaginary potential. In addition, the Perey model assumes linear

energy dependence of the potential depth on the incident energy, which we will not assume for the imaginary potential components. We use an alternative approach (Patt76), in which we assume that the energy of the incident proton is reduced by the average of the Coulomb potential energy over the nuclear interior. This procedure gives the same Coulomb correction for the real potential as the Perey model, yet can be applied consistently to the absorptive potential. The details of this model are shown in Sect. 2.6.1.

The Coulomb correction may be studied by comparing (n,n) and (p,p) scattering at similar incident energies on N=Z nuclei. The comparisons that have been made are for scattering from ^{28}Si, ^{32}S, and ^{40}Ca (Rapa82); the results of this comparison have significant uncertainties (Rapa80b). The effects of the nuclear structure of these particular isotopes on these results are unclear. Also, it is not possible to deduce the form factor for this correction from this type of study, even though it is expected to differ significantly from the corresponding potential form factors (Jeuk77).

2.4.3 Previous Global Optical Model Analyses

In view of the smooth global properties of the optical potential, and in spite of the apparent difficulties with the analysis, there have been several previous attempts at global optical model analyses of nucleon-nucleus elastic scattering in the range E≤65 MeV. There follows a summary of some of the more comprehensive analyses and some discussion of their strengths and weaknesses.

One of the early and best known global analyses was that of Perey (Pere63). This analysis was of proton scattering, using 32 angular distributions (about 1000 data points) of elastic cross sections for A≥27 and 9≤E≤22 MeV. The analysis explored the ambiguity between the volume- and surface-imaginary potentials, the nuclear asymmetry dependence of the potential, and included a spin-orbit potential. An automatic search (not discussed in the reference) for the optimum parameters was used. Many parameters were constrained in the final searches. For example, the imaginary part was constrained to be purely

surface, the geometries were constrained to be the same as an earlier neutron analysis, and the spin-orbit geometry was constrained to be that of the real central potential. This work was pioneering, illuminating many of the basic properties and ambiguities of optical model analyses.

The Becchetti and Greenlees analysis (Becc69) is the most widely used global parameterization. Their analysis used a database of about 2500 proton data points and 1000 neutron data points for targets of $A \geq 40$ and $E \leq 40$ MeV, dominated by data for $A \leq 90$. This dataset included some reaction and total cross section data, as well as more polarization data than Perey. They performed separate analyses for the proton and neutron data, using the best proton potential as the starting point for the neutron analysis. They tested many different parameterizations of the potential in a purely empirical attempt to fit the data, using an automatic fitting program. The final parameterization chosen included linear energy dependences for all the central components, simple asymmetry dependence for the depths, constant geometry (except for the imaginary diffuseness), and a simple model for the real central potential Coulomb correction (Pere63). The neutron parameters were deduced by using the proton parameters as a starting point. The parameters found by Becchetti and Greenlees were,

for (p,p),

$$V = 54.0 - 0.32E + 0.4Z/A^{1/3} + 24.0\epsilon \quad \text{MeV},$$
$$R_0 = 1.17A^{1/3} \text{ fm}, \qquad a_0 = 0.75 \text{ fm},$$
$$W_V = -2.7 + 0.22E \quad \text{MeV}$$
$$W_S = 11.8 - 0.25E + 12.0\epsilon \quad \text{MeV} \qquad \text{BG(p)}$$
$$R_W = 1.32A^{1/3} \text{ fm}, \quad a_W = 0.51 + 0.7\epsilon \text{ fm},$$
$$V_{SO} = 6.2 \text{ MeV}, \quad R_{SO} = 1.01A^{1/3} \text{ fm}, \quad a_{SO} = 0.75 \text{ fm},$$

and, for (n,n),

$$V = 56.3 - 0.32E - 24.0\epsilon \text{ MeV}$$
$$R_0 = 1.17A^{1/3} \text{ fm}, \qquad a_0 = 0.75 \text{ fm},$$
$$W_V = -1.56 + 0.22E \text{ MeV}$$
$$W_S = 13.0 - 0.25E - 12.0\epsilon \text{ MeV} \qquad \text{BG(n)}$$

$R_w = 1.26A^{1/3}$ fm, $a_w = 0.58$ fm,
$V_{so} = 6.2$ MeV, $R_{so} = 1.01A^{1/3}$ fm, $a_{so} = 0.75$ fm.

The analysis by Rapaport (Rapa79b, Rapa82) was an analysis of neutron cross-sections at "high" energies from "closed" shell nuclei. These data were for A=40,90,92,116,124,208 and 11≤E≤26 MeV, all measured in one laboratory. The analysis explored many issues, particularly the asymmetry dependence of the potentials and more sophisticated parameterization of the real radius. The dataset consisted of about 500 data points. The resulting best fit potential Set B, (Rapa79b) in which V_{so} was fixed during the search at Becchetti-Greenlees values, was

$V = 54.62 - 0.30E - (25.3 - 0.02E)\epsilon$ MeV,
$R_0 = 1.225A^{1/3} - 2.985A^{-2/3}$ fm, $a_0 = 0.668$ fm,
$W_v = 0.0$ MeV
$W_d = 4.27 + 0.4E - 12.7\epsilon$ MeV, E≤15 MeV
$W_v = -3.95 + 0.37E$ MeV,
$W_d = 13.5 - 0.35E - 9.3\epsilon$ MeV, E≥15 MeV Rap(n)
$R_w = 1.295A^{1/3}$ fm, $a_w = 0.59$ fm,
$V_{so} = 6.2$ MeV, $R_{so} = 1.01A^{1/3}$ fm, $a_{so} = 0.75$ fm.

There have been other attempts at global analyses of nucleon-nucleus scattering on smaller scales. Patterson et al. (Patt76) used (p,n), (n,n), and (p,p) data in the Lane model to determine the isovector parts of the optical potential. They found significant differences in the isovector potential components from previous analyses, and were able to describe (p,n) and (n,n) cross section data to high accuracy. The (p,p) "data" were produced by calculation from the Becchetti-Greenlees potential. No polarization data were used in the analysis. At higher energies, for which systematic elastic scattering data with polarized beams are now becoming available, the analysis by Nadasen et al. (Nada81) parameterized an optical model corrected approximately for relativistic effects, using ($\vec{p}$,p) scattering from ^{40}Ca, ^{90}Zr, and ^{208}Pb for $60<E_p<200$ MeV. This model used a logarithmic energy dependence,

and included some data at energies within the range of this analysis.

2.5 Improvements Possible Over Previous Parameterizations

Each of the previous analyses has addressed the question of global optical model parameterizations using data selected by various criteria, the computational techniques available, and the available knowledge of the optical model. The difficulties with these analyses may be categorized as problems with the model, problems with the data, and limitations of the search techniques. Each analysis suffers from a different mixture of these difficulties; this section summarizes some of the major problems facing any analysis in terms of a global optical model.

2.5.1 Problems with previous parameterizations

The models assumed by the analyses summarized in Sect. 2.4 used similar parameterizations. These models include assumptions such as a simple $A^{1/3}$ dependence of the radius of all form factors of the potential, a constant diffuseness, a constant spin-orbit depth in A and E, mixtures of surface and volume components in the form factor for the imaginary potential, and linear energy dependencee throughout. This last condition forces one to postulate an unphysical "cuton" energy for the volume component of the imaginary central potential, and a similar "cutoff" energy for the surface term. In most analyses, the Coulomb correction coefficient estimated by Perey (Pere63) is used. This was based on his estimate of the Coulomb radius and the energy dependence of the real central potential, which generally differed from later analyses. This term contributes as much or more to the real central potential as the isovector potential, which is normally carefully parameterized. In spite of the obvious energy dependence of the absorptive potential, none of these analyses included a Coulomb correction for this potential.

These assumptions were made to reduce the number of free parameters which must be searched upon (when simple radius and spin-orbit parameterizations were chosen), and for simplicity (as when a linear energy

dependence of the absorption was chosen). There is now much phenomenological information about the optical potential, as well as sufficient understanding of microscopic models to predict parameterizations. For the real central and spin-orbit potentials it is possible to make folding-model calculations using realistic nuclear densities and effective interactions, and then to investigate reasonable means of parameterizing the resulting potentials. For the imaginary potential, there is sufficient information about the phenomenological behavior of the potential, as well as some microscopic calculations, that reasonable parameterizations of the E and A dependence may be predicted. The details of these calculations and our parameterization will be discussed in Sect. 2.6.

2.5.2 Limitations of Previous Datasets

The datasets used in Perey and Becchetti-Greenlees analyses were extracted from the literature. The data in the other analyses mentioned were generally limited in scope to a few target nuclei. The proton data were principally unpolarized elastic-scattering cross-section measurements and some absorption cross-section measurements, supplemented by a few polarization data (measured by double scattering). The small number of these polarization data and the severe systematic uncertainties affecting them, compared with the more easily and accurately measured analyzing-power data, limited the reliability of the parameterization of the spin-orbit potential in these earlier works.

The neutron data, particularly in the Becchetti-Greenlees analysis, were almost entirely elastic or total cross sections, many of which were measured at energies below 10 MeV, where compound elastic scattering corrections were required. There were also many fewer neutron datasets than proton datasets. This is unfortunate, since the greatest sensitivity of elastic scattering to the isovector potential occurs only on comparison of neutron and proton scattering.

An additional difficulty with data used in previous analyses is that the data for various targets and energies were measured at many

different laboratories. Under the best circumstances the systematic errors are different, causing variations in the data which could be mistaken for E or A dependencies.

The datasets of previous analyses can be improved in the following ways:

1) Systematic measurements from laboratories engaged in elastic scattering studies can be utilized. These are measurements on large numbers of targets, either at single energies or at a few energies, using the same scattering apparatus and techniques, to make systematic errors among groups of targets similar, and small.
2) Using polarized ion sources, it is possible to measure easily (at least for protons) analyzing powers and cross sections for elastic scattering. Analyses of such data provide strong constraints on the spin-orbit potential and other optical model parameters, since the spin-flip pieces of the scattering amplitude are better determined.
3) The neutron database is now such that only those data for scattering above 10 MeV need be used, avoiding the need for difficult compound elastic corrections.
4) Neutron analyzing power data are becoming available (Walt84), placing the analysis of neutron data on an equal footing with that of proton data.

2.5.3 Previous Search Techniques

Two techniques of global analysis have been employed in the past. The most common was to fit each angular distribution separately, allowing the parameters to take on any values to achieve the best fit. Then, to achieve the global analysis, the geometric parameters were averaged and the individual fitting redone with the fixed geometry. The resulting depths were then parameterized as functions of A, E and isospin, to give a global parameterization (Rapa79b). The second approach, that of Becchetti and Greenlees (Becc69), is to optimize the fit to all the data simultaneously with a postulated global model.

In the first technique, the analysis is usually guided by hand rather than by machine. This is because (1) there are strong parameter correlations in the optical model which tend to confuse many search algorithms and (2) it has been expensive, because of the high cost and slowness of computing, to allow fully automatic searches, which tend to require many iterations to optimize a problem. This is a practical technique when the amount of data is small, but is impractical for a truly global analysis of a large data base. Also, in hand guidance, there is considerable danger of prejudicing the choice of final parameter values.

The second technique seems the better for the analysis of large amounts of data. However, a single analysis of a large database requires a large number of optical model calculations and a search technique that is stable even when searching on 10-15 correlated parameters.

In the previous analyses, confidence limits and detailed parameter correlations were seldom reported. This information is necessary for comparison of the results with microscopic calculations and local parameterizations. Also, to compute the uncertainty in functions of the optical model parameters, such as the volume integrals, the covariances of the parameters are necessary (Smit82).

In the past several years, there have been two types of developments which improve our ability to perform searches on the parameters of a global optical model. These have come through the development of stable searching algorithms (Jame75) and the significant increase in the speed of computing. Algorithms now exist which are capable of stable searches on dozens of parameters, although they require hundreds to thousands of calculations to examine properly the space of the parameters. Use of fast processors, such as a Floating Point Systems FPS-164 (FPS84), computing at a rate of 3 Mflops (million floating point operations per second), allow the execution of a search on a 16-parameter optical model, using 150 datasets (8800 datapoints), in about 3 hours. These algorithms are also capable of providing estimates of the uncertainties in the determination of the parameters (assuming that

the data uncertainties are properly known), and, of making estimates of the linear correlations between parameters.

2.6 Specification of the Semi-Empirical Global Potential

In a global optical model parameterization of this sort, it is possible to arrive at many different parameter sets which give similar overall fits to the data (Becc69). It is necessary to choose forms for the parameterization most likely to describe the data properly and not simply to provide computational convenience. Furthermore, this parameterization must be easily related to microscopic predictions if it is to have value as a test of these predictions.

In the specification of our global potential for the real parts of the potential we used folding-model calculations with realistic effective interactions (Bert77) and measured nuclear charge distributions (Jage74). The calculations are described elsewhere (McAb86). The resulting potentials were parameterized and used to guide our empirical parameterization. For the imaginary part of the potential, previous phenomenological observations were used in arriving at the parameterization.

2.6.1 Real central potential

For the real central potential, it was not expected that the folding model predictions of the depth would be correct. In the folding model, the depth calculated is very sensitive to the type of exchange model used and requires the inclusion of an ad hoc density dependence in the effective interaction to obtain results consistent with previous phenomenological results. The folding-model calculation of the radial form factor should be more accurate. For example, we observed in these calculations that the half-density radius of nuclear density distributions and the resulting folding potentials did not obey the simple $A^{1/3}$ dependence usually assumed in optical model analyses. This effect is a fundamental property of diffuse nuclear form factors (Myer73) and is expected to provide an explanation of several properties of proton elastic scattering (Hodg71, pg. 218, Hodg84). Further, the inclusion

of density dependence in the effective interaction modifies this deviation from $A^{1/3}$ variation (Myer73). It was possible to parameterize the half density radius, R_0, of these folded potentials as,

$$R_0 = r_0 A^{1/3} + r_0^{(0)} \quad . \qquad 2\text{-}10$$

Failure to include this deviation of the potential radius from simple $A^{1/3}$ behavior in a global analysis will affect the determination of other components of the optical model potential. If not modeled correctly, it will appear as an extra A-dependence in the real central depth, thus confusing the parameterization of the Coulomb correction and the isovector potentials.

The diffuseness of the potential was chosen to be constant. The diffuseness resulting from the folding model calculations appeared to vary randomly in A, presumably reflecting shell-dependent effects. A constant diffuseness, representing the average, was selected as the most reasonable compromise. A global analysis with the goal of studying the fine structure of the optical model (variations in the parameters for closed shell nuclei and those between closed shells) would include a more complicated diffusness (Hodg84).

Since we lack sufficient accurate guidance from the folding model for the real potential depth, we use phenomenology as a guide. For the real central depth, we chose the usual parameterization of the form,

$$V_r = (V_0 - V_e E) + (V_t - V_{te} E)\epsilon \qquad 2\text{-}11$$

In this expression, the linear energy dependence of the real potential is consistent with previously observed behavior. As is usually done, the isovector variation of the potential is assumed to affect only the potential depth and not the geometry. This assumption does not necessarily hold (Jeuk77), but, given the small contribution of the isovector terms to the depth (usually 1 to 2 MeV) isovector effects on the geometry are not significant in elastic scattering. The energy dependence of the isovector term (subscripts "t") is included for the sake of completeness. The evidence for energy dependence of the isovector potential is weak: some studies require none (Patt76) and others

require it (Rapa79b).

It is necessary to account for Coulomb effects when the above potential is applied to proton scattering. We do this by reducing the energy at which potentials are evaluated by the spatial average of the Coulomb repulsion experienced by an incident proton (Patt76). In evaluating the Coulomb repulsion we use the same radius parameter as in the Coulomb potential. For linear energy dependence of the potential, this gives equivalent results to the Coulomb correction model first suggested by Perey (Pere63). Thus, in the case of proton scattering, the E in Eq. 2-10 is replaced by,

$$E = E_p - \alpha \frac{6\ Ze^2}{5R_c} \quad . \qquad 2\text{-}12$$

The coefficient, α, is included as an adjustable parameter, since it is not clear that the average Coulomb energy is the correct energy to use.

2.6.2 Spin-Orbit Potential

The parameterization of the spin-orbit potential was guided by folding-model calculations similar to those that guided the real central potential (McAb86). These calculations included exchange effects, and were made for proton scattering at 16 and 65 MeV, using tabulated 2pF nuclear densities (Jage74) and the M3Y effective interaction (Bert77). The results were parameterized as,

for the depth,

$$V_{so} = V_{so0} + V_{soe}E + V_{soA}A^{-1/3}$$

and, for the geometry, 2-13

$$R_{so} = r_{so}A^{1/3} + r_{so}^{(0)}, \qquad a_{so} = \text{constant},$$

with simple linear E dependence and a simple $A^{-1/3}$ dependence in the depth. The parameterization of the spin-orbit radius reflects the behavior of the radius of the underlying density distributions. The diffuseness parameter appeared to vary randomly in A; it was held constant. The predicted parameter values from the folding model were,

(1) V_{soo} / V_{soe} / V_{soA} = 5.1 / -0.0087 / 5.61 MeV, and
(2) r_{so} / $r_{so}^{(0)}$ / a_{so} = 1.24 / -0.82 / 0.66 fm.

2.6.3 Coulomb radius parameterization

Since we had found that the radius of the nuclear charge distribution did not vary simply as $A^{1/3}$, we considered its effects on the Coulomb potential. We would expect that even in the uniformly charged sphere approximation of the Coulomb potential, this radius should be similar to the actual nuclear charge density. Other analyses have used a parameterized radius giving the same RMS radius as the actual charge distribution (Becc69). We were also concerned about the appropriateness of using the diffuse charge distribution radius in a square-well approximation to the Coulomb potential. A prescription exists (Myer73) for the equivalent sharp radius, R_s, for a diffuse nuclear potential, f(r),

$$\frac{4\pi}{3} R_s^3 \, f(r=0) = 4\pi \int_0^\infty f(r) r^2 dr, \qquad 2\text{-}14$$

in which the central sharp depth is chosen the same as that for the actual potential and the R_s is chosen to make the volume integrals equal. This prescription is sufficient for a short-range force, but will not work for the Coulomb force since the integral in Eq. 2-14 does not exist. We desired to make an appropriate approximation for the Coulomb potential.

The approximation we chose was to require that the electric field at the radius, R_c, of our equivalent uniform charge distribution be the same as that at the half-density radius of the 2pF nuclear charge distribution. It would be possible to choose to match potentials at the radii; since the potential is quite long range, either choice should be sufficient. We made this choice because the analytic calculation was more tractable and because over the range of proton energies considered, $E_p \leq 65$ MeV, the scattering is most sensitive to the surface region, $r \approx R_c$.

For this approximation it is necessary to compute,

$$E(r) = \frac{1}{r^2}\int_0^r \rho(r')\, r'^2 dr' = \frac{Q(r)}{r^2}, \qquad 2\text{-}15$$

where $Q(r)$ is the charge contained by a sphere of radius r and $\rho(r)$ is the diffuse (2pF) charge distribution,

$$\rho(r) = \frac{\rho_0}{1 + \exp\left[\frac{r-R_c}{a_c}\right]}, \qquad 2\text{-}16a$$

with normalization,

$$Ze = 4\pi \int_0^\infty r^2 dr\ \rho(r). \qquad 2\text{-}16b$$

To evaluate the integral in Eq. 2-15, we must expand the charge distribution differently in the two regions $r<R_c$ and $r>R_c$. For region (I) $r<R_c$, we expand the form factor in a geometric series expansion as,

$$f(r,R_c,a_c) = 1 + \sum_{n=1}^{\infty} (-\lambda e^z)^n, \qquad 2\text{-}17$$

where $\lambda \equiv \exp(-R_c/a_c)$, and $z \equiv r/a_c$.

This expansion is convergent, since $\lambda e^z < 1$. For the charge integral in Eq. 2-15, this leads to integrals of the type,

$$\int z'^2 dz'\ e^{nz'} = [(1-nz)^2 + 1]\ \frac{e^{nz}}{n^3}, \qquad 2\text{-}18$$

for $n>0$, resulting in the charge contained within radius r:

$$Q(r) = \rho_0 \left[\frac{r^3}{3} + a_c \Sigma\ \frac{(-)^n}{n^3} \left[\exp\left(n\left[\frac{r-R_c}{a_c}\right]\right) \left[2a_c^2 - 2na_c r + (nr)^2 \right] - 2a_c^2 \exp\left(\frac{-nR_c}{a_c}\right) \right] \right]. \qquad 2\text{-}19$$

For region (II), $r>R_c$, the expansion becomes,

$$f(r,R_c,a_c) = \frac{e^{-z}}{\lambda} \quad \frac{1}{\lambda^{-1}e^{-z} + 1} = -\sum_{n=1}^{\infty} (-\lambda e^{z})^{-n} \qquad 2\text{-}20$$

This series is also convergent, since now $(\lambda e^{z})^{-1} < 1$. Inserting this into the integral in Eq. 2-15 for charge, including the previously determined charge for $r<R_c$, we calculate the charge contained within r for $r \geq R_c$,

$$Q(r) = \rho_0 \left[\frac{R_c^3}{3} + a_c \sum_{n=1}^{\infty} \frac{(-)^n}{n^3} \left[\exp\left(-n\left[\frac{r-R_c}{a_c}\right]\right) \left[2a_c^2 + 2na_c r + (nr)^2 \right] \right. \right.$$

$$\left. \left. - 2a_c^2 \exp\left(\frac{-nR_c}{a_c}\right) - 4na_c R_c \right] \right] . \qquad 2\text{-}21$$

Our interest in this region (II) is for the determination of ρ_0, which we obtain from the normalization condition (2.16b) using (2-21), letting $r \to \infty$:

$$\rho_0 = \frac{Ze}{4\pi} \left[\frac{R_c^3}{3} - 2a_c \sum_{n=1}^{\infty} \frac{(-)^n}{n^3} \left(2na_c R_c + a_c^2 \exp\left(\frac{-nR_c}{a_c}\right)\right) \right]^{-1} . \qquad 2\text{-}22$$

To obtain the field at the charge density radius, R_c, we make the approximation $\exp(-nR_c/a_c) \approx 0$ and set $r=R_c$ in either expression for Q(r). Then the series can be summed using the Riemann zeta function (Hayn64, Sect. 23.2) to yield the electric field at R_c,

$$E(R_c) \approx \frac{Ze}{4\pi R_c^2} \left[\frac{1 + 3\alpha \left[(-\ln 2) + 2\alpha \left[\frac{\pi^2}{12}\right]\right]}{1 + 12\alpha^2 \left[\frac{\pi^2}{12}\right]} \right] , \quad \alpha = \frac{a_c}{R_c} \qquad 2\text{-}23$$

The equivalent uniform potential radius is obtained by requiring that the field at the radius of the uniform charge density, R_{sc}, be the same as at the radius of the 2-parameter-Fermi charge distribution. We then make a relation between the diffuse charge distribution radius and the equivalent uniform distribution radius from,

$$E(R_c) = E_s(R_{sc}) = \frac{Ze}{4\pi R_{sc}^2} \qquad 2\text{-}24$$

The equivalent sharp radius may therefore be calculated from,

$$\left[\frac{R_{sc}}{R_c}\right]^2 \approx \frac{1 + \pi^2\alpha^2}{1 - (3\ln 2)\alpha + \frac{\pi^2\alpha^2}{2}} \qquad 2\text{-}25$$

This expression may be evaluated in the limit of $A \geq 40$, assuming that, from the typical values of R_c and a_c, $\alpha \leq 0.15$. Then, to an accuracy of better than 2%,

$$R_{sc} \approx R_c\left[1 + \left(\frac{3}{2}\ln 2\right)\alpha + \left[\frac{3}{2}\left[\frac{3\ln 2}{2}\right]^2 + \frac{\pi^2}{4}\right]\alpha^2\right.$$

$$= R_c(A)\ (1 + 1.040\alpha + 4.089\alpha^2\ ) \qquad 2\text{-}26a$$

or,

$$R_{sc}(A) \approx R_c(A) + 1.040a_c + \frac{4.089a_c^2}{R_c(A)} \qquad 2\text{-}26b$$

In the last term, $R_c(A)$ may be replaced by its average value of 5.03 fm with less than a 2% error ($40 \leq A \leq 208$). We have obtained a parameterization of nuclear charge radii, derived by performing a least squares fit to charge distribution parameters (Jage74) for all 2pF form factors tabulated (McAb86), from which the parameters

$$R_c(A) = 1.238A^{1/3} - 0.721 \text{ fm. and,}$$

$$a_c = 0.56 \text{ fm.}$$

were derived. Inserting this radius into Eq. 2-26b we get,

$$R_{sc}(A) \approx 1.238A^{1/3} - 0.721 + 1.040(0.56) + \frac{4.089(0.56)^2}{5.03} \text{ fm} \qquad 2\text{-}27a$$

or,

$$R_{sc}(A) \approx 1.238A^{1/3} + 0.116 \text{ fm.} \qquad 2\text{-}27b$$

This expression can be used to calculate the equivalent sharp Coulomb radius to model the true Coulomb potential of nuclei. In previous analyses, constant Coulomb radii (R_c = 1.25 fm) were often used, although in some analyses a formula by Elton, derived by equating the

RMS radii of diffuse and sharp-edged charge distributions, was used ($R_c = 1.123A^{1/3} + 2.352A^{-1/3} - 2.070A^{-1}$ fm) (Elto61). The numerical values given by these formulas are quite different, but make only small differences in the final determination of the optical model potential parameters.

2.6.4 Imaginary Central Potential

The imaginary part of the optical model potential is difficult to calculate from semi-microscopic grounds. Accurate calculations of this may be attempted in a nuclear structure framework (Oste84), but these results are specific to the nucleus under study. Nuclear matter calculations result in complex potentials, in which the absorption describes the finite mean free path of nucleons in nuclear matter. This type of calculation neglects absorption effects such as collective excitation and reactions in finite nuclei. Thus, in parameterizing the absorptive potential we must turn to phenomenology for guidance.

There are two well-determined characteristics of the absorptive potential which must be described by our parameterization. First, there is the transition from principally surface-dominated absorption at low energies (E_p<20 MeV) to volume-dominated at high energies (E_p>60MeV). Second, there is the observation that in proton optical potentials the imaginary volume integral per nucleon is approximately constant as a function of A and E (Agra75). In addition, we sought to impose the physically reasonable criterion that the transition from surface to volume form take place smoothly as a function of energy. Such a criterion has not been applied in previous analyses (Becc69, Rapa82).

For the energy dependence of the potentials we have chosen a Fermi shape. This has been used previously (Leeb79,Hono84) and satisfies the criterion of smoothness. In addition, it is possible for the two parts of the potential to satisfy the constancy of volume integral in E, by the appropriate choice of their parameters. The form of this potential is,

$$W(r,E) = W_v(r)\left[1+\exp\left[\frac{W_{ve0} - E_{inc}}{W_{vew}}\right]\right]^{-1} + W_s(r)\left[1+\exp\left[\frac{W_{se0} - E}{W_{sew}}\right]\right]^{-1} \quad 2\text{-}28$$

in which W_s and W_v are the E-asymptotic depths of the imaginary surface and volume potentials. The parameters of the energy dependencies are the half-value energies, W_{ve0} and W_{se0}, for the volume and surface absorptions respectively, and the widths, W_{vew} and W_{sew}, just as for the parameters of Woods-Saxon radial form factors. If these parameters of the volume and surface components are chosen such that $W_{ve0}=W_{se0}$ and $W_{vew}=W_{sew}$, the constancy in energy of the absorption volume integral is satisfied automatically, for any given target A. Examples of these forms may be seen in Fig. 7-11, where the parameters of the final best-fit potential are used.

Our parameterization of the absorptive potential must also describe the observed constant value of the volume integral with A for proton scattering. A conventional parameterization of the optical model yields a total volume integral for the absorption as shown in Eq. 2-6. Note that for the surface terms, a constant value of the volume integral may be maintained if W_s rises in a manner similar to the fall of $A^{-1/3}$. This can be described by including an isovector term in the potential depth. A similar effect can be produced by introducing an A- or ϵ- dependent diffuseness (Becc69, Mene71). Of course, this effect may arise from similar density dependent effects in the effective interaction as for the real potential (Jeuk77). Usually, W_v is assumed to be isoscalar, to satisfy the observed constancy in medium-energy proton scattering (Nada81). It will not be possible to determine the nature of this constancy until significant amounts of accurate neutron elastic scattering data are available in the energy region where the volume absorption dominates, E_n>40 MeV.

In summary, we chose the following parameterization of the imaginary central potential depths:

$$W_v = W_{v0} f_{wv}(E) \qquad R_w = r_w A^{1/3} + r_w^{(0)}, \; a_w = \text{const.} \qquad 2\text{-}29$$
$$W_s = (W_{s0} + W_{st}\epsilon) f_{ws}(E)$$

In the above, the potential radius has an offset from the usual parameterization as a function of $A^{1/3}$, in analogy with the real central and spin-orbit components of the potential. This is necessary if there is density dependence of the imaginary parts of the effective interaction (Myer73). The diffuseness is chosen as constant, in analogy with the other components of the potential.

The Coulomb correction for the imaginary central potential was applied in the same manner as for the real central potential, by adjusting the proton energy at which the potential is evaluated. It is not clear that such a procedure is well justified, since the available channels for absorption will differ for protons and neutrons, even when the energy has been adjusted (Oste84). Nevertheless, we will use this in an attempt to apply at least a consistent Coulomb correction to the full optical potential.

2.7 Conclusions and Proposal

In this chapter, our chosen form of the optical model potential for nucleon-nucleus scattering has been presented and justified. As shown in Sect. 2.3, there has been much recent progress in understanding the origins of the optical potential in the many-body problem of a nucleon scattering from a nucleus. This understanding has arisen from the point of view of the folding model, as well as the more fundamental approach of the nuclear matter many-body calculation. In addition, there is available now a large amount of phenomenological information about those parts of the optical potential which cannot be well predicted from microscopic models (Sect 2.4).

Besides the improvements in our understanding of the optical potential, there has become available a large dataset composed of much larger amounts of polarization data than previously used in global analyses (Sect. 2.5.2), as well as the search algorithms and computational facilities to permit large searches on this extensive dataset (Sect 2.5.3).

In view of these improvements, a new global parameterization of the nucleon-nucleus optical potential is appropriate. This parameter-

ization, specified in Sect. 2.6, includes parameters indicated by both folding-model calculations and phenomenological observations.

The data to be used in determining the values of the parameters are described in Chapters 3, 4, and 5. The search techniques and the facilities for the calculation are described in Chapter 6. The final parameterization is presented in Chapter 7.

III. Data-Acquisition Facilities and Procedures

3.1 Introduction

To understand the strengths and weaknesses of the 16-MeV proton elastic scattering data measured at TUNL, it is necessary to describe the experimental facilities and procedures used. This chapter presents the measurements made and the relevant properties of the ion source, accelerator, and scattering chamber. In addition, the target preparation and the data-acquisition programming performed during this research are summarized.

3.2 Description of Measurement

The experiment at 16 MeV consisted of simultaneous measurement of angular distributions of differential cross section, $\sigma(\theta)$, and analyzing power, $A_y(\theta)$. These measurements were made on 23 targets of varying thicknesses, using essentially the same detector geometry and experimental procedures for each target, at angles between 25° and 170° in 5° steps.

The data were measured, in fact, in two different setups. Six of the targets (^{58}Ni, ^{76,78,80}Se, and ^{63,65}Cu) were measured in a scheme which differed from the rest of the experiments. This earlier experiment will be referred to as NOV80; it will be discussed in the relevant sections of this chapter where it differed from the standard procedures. The differences between NOV80 and the standard setup were that in the former 1) smaller detectors were used, resulting in smaller solid angles and somewhat larger uncertainties in the cross sections; 2) a different polarimeter was used; and 3) the data were measured with a data-acquisition system, based on a Honeywell DDP-224 computer.

The analyzing power was measured in a scheme that required two

runs, with the beam spin up, then down, and with detector pairs placed symmetrically to the left and the right side of the beam. The analyzing power was then calculated as:

$$A_y = \frac{1}{P_b}\left[\frac{r-1}{r+1}\right] \quad ; \quad r = \left[\frac{(NLU)(NRD)}{(NLD)(NRU)}\right]^{1/2} \qquad 3\text{-}1$$

In these equations,

a) NRU is the sum for the right detector during the spin up run,
b) NLU is the sum for the left detector, spin up;
c) NRD is the sum for the right detector, spin down;
d) NLD is the sum for the left detector, spin down; and
e) P_b is the measured beam polarization.

This scheme of measurement has been shown to eliminate most first-order errors in the calculation of A_y(Ohls73), and is the standard scheme at TUNL for vector analyzing power measurements.

Examination of the above equation shows that the uncertainties in the analyzing power arise predominantly from the counting statistics in the detectors, and from uncertainty in the beam polarization. The uncertainties in the beam polarization measurement are discussed in Sect. 3.3. The contributions to the uncertainties in the analyzing power from counting statistics were generally about 0.01 or less.

The differential cross section was measured simultaneously with the analyzing power, and was calculated as the error-weighted mean of the cross sections from the spin-up run and the spin-down run. These are calculated as (e.g. spin up):

$$\sigma(\theta) = \frac{N_s\ DTC\ \cos(\theta_{targ})}{\Delta\Omega\ T\ N_{inc}} \quad mb/sr. \qquad 3\text{-}2$$

The spin-down cross section is computed in a similar fashion. The terms are defined as follows:

a) Ns - the sum of the left and right detector peak counts (NRU + NLU, for example),

b) DTC - the dead time correction ratio. This corrects for the time during the active counting when events are not stored in the computer.

c) $\Delta\Omega$ - sum of the detector solid angles in steradians

d) T - target thickness in target nuclei per millibarn (10^{-27} cm^2)

e) θ_{target} - target angle; 0° angle corresponds to target normal to the incident beam

f) N_{inc} - total number of incident particles, obtained by integration of the beam current.

The statistical uncertainties for the cross sections were ≤ 1%. As for the analyzing power, many possible first-order errors cancel in this scheme. Unlike the analyzing power, there are many contributions to the uncertainty in the normalizations of the cross sections. The uncertainties introduced by each factor are discussed in Sect 4.4.2.

3.3 Beam Preparation

The polarized proton beam used was produced in a Lamb-shift polarized ion source(Cleg74), then accelerated in an FN tandem Van de Graaff electrostatic accelerator(News74). The beam for these experiments had an average polarization of 80% and an average intensity on-target of 80 nA. The operating voltage used, 8 MV, was the highest voltage at which the accelerator could be reliably and stably operated.

After acceleration, the beam was injected into the experimental beamline using a switching magnet regulated by an NMR gaussmeter. After the magnet, the beam passed through momentum-analyzing slits, which were used to regulate the terminal voltage, providing a more stable beam current and energy. This system has been shown to produce an energy spread on target of less than 10 keV in the scattering chamber used, and an absolute energy uncertainty of less than 50 keV

(Burk83), under the operation conditions of this experiment, which included no recycling of the switching magnet.

The beamline used in this experiment had several active and passive optical elements to define and focus the beam on target. The locations of the these elements and the sizes of the defining slits are listed in Table 3-1. Also shown in the table are estimates of the worst-case beam size and divergence on target, as determined by the slits after the last active beam-optics elements.

As can be seen, these divergences and sizes are quite substantial, allowing the beam to scatter from points over a wide area of the target and at angles different from the mean angle selected for the experiment. This causes an apparent variation in the target thickness, because of non-uniformities in the targets, and the measurement of observables at the incorrect scattering angles. In this experimental setup there are two important factors substantially reducing these potential effects. First, the symmetric detector placement around the beam axis at each angle nearly eliminates from the asymmetry measurement the effects of an incorrect angle of beam incidence (Ohls73) and reduces the effects on the cross sections to much less than 1%. Second, an automatic beam-steering feedback system controlling steerers 9-10 and 11-12 was used to hold the beam on the center of the target. This system derived the control signals from the rotating slits and a position-sensitive Faraday cup in the beam-current integration system. It is not quantitatively known how much this system improves the beam stability. No tests of this were made during this research. This system did not operate correctly for all measurements, in part because the small beam deposited on the slits was insufficient to generate a reliable feedback signal and because of problems maintaining isolation between the sectors of the position-sensitive Faraday cup built into the polarization monitor.

3.4 Scattering Chamber and Experimental Details

These experiments were performed within a general purpose cylindrical, aluminum, vacuum scattering chamber approximately 0.6 meters in

Table 3-1

Beam Line Elements

Element	Distance to Target	Apertures Horizontal	Apertures Vertical
Momentum Analyzing Slit	16 m	0.025 cm	----
Quadrupole Doublet (Q4C)	12 m		
Magnetic Steerer (7-8)	11 m		
Quadrupole Doublet (Q7C)	6.7 m		
Magnetic Steerer(9-10)	4.1 m		
Magnetic Steerer(11-12)	1.5 m		
Rotating Slits	1.35m	0.75-0.13 cm	0.75-0.13 cm
Chamber Slits	0.18m	0.25 cm	0.30 cm
Faraday Cup	-0.5 m		

Beam Divergence and Size

(maximum possible)

Horizontal (Chamber slits 0.25 cm)

Rot. Slits	$\theta_{1/2}$	Crossover (from tgt)	Beam Size (at tgt)
0.75 cm	0.24°	47 cm	0.39 cm
0.13 cm	0.09°	95 cm	0.30 cm

Vertical (Chamber slits 0.30 cm)

Rot. Slits	$\theta_{1/2}$	Crossover (from tgt)	Beam Size (at tgt)
0.75 cm	0.26°	51 cm	0.46 cm
0.13 cm	0.11°	100 cm	0.38 cm

diameter. The typical vacuum in the chamber was 7×10^{-6} Torr. A maximum of five targets could be mounted inside the vacuum system. The chamber contained two sets of detectors, one each on its top and bottom rotating plates; each set could be separately adjusted in scattering angle while the chamber vacuum was maintained. The angles could be set to a precision of better than 0.1°; the alignment was checked optically with the actual detector holders used. The chamber had freon cooling lines to which the detector holders were attached, providing the low (less than $0^{\circ}C$) temperatures necessary for low noise/ high resolution operation of the detectors. A schematic picture of the scattering chamber is provided in Figure 3-1.

3.4.1 Detector Mounting and Collimation System

For this experiment, a new detector mounting system was designed for the scattering chamber. Previously, detector holders were mounted on radial tracks smoothly variable in angular position on the chamber baseplate. That system, while very versatile had two problems: 1) difficulty obtaining reproducibility in the radial placement of each detector, and 2) inability to locate adjacent detectors at scattering angles less than 17.5° apart. The present experiment requires precision from run to run and, because of the rapid decline in the elastic scattering cross section with angle, it was inefficient to locate detectors more than 10° apart. For these reasons, a new detector mounting system was designed.

The new design replaced the previous system of radial tracks by two fixed plates, one mounted on the bottom and one on top of the chamber (for left and right symmetric detector placement). These plates were pinned into alignment holes in the rotating baseplates, holes placed there when the chamber was originally designed. The detector holders were in turn pinned into the plates, at one of several radial positions (approximately 1.91 cm apart) along one of four angular positions on the plate set 10° apart. The detector location was thus fixed accurately and reproducibly in angle and radial distance, relative to the rotating baseplate. With this system (designed for 150-mm^2 Ortec-style

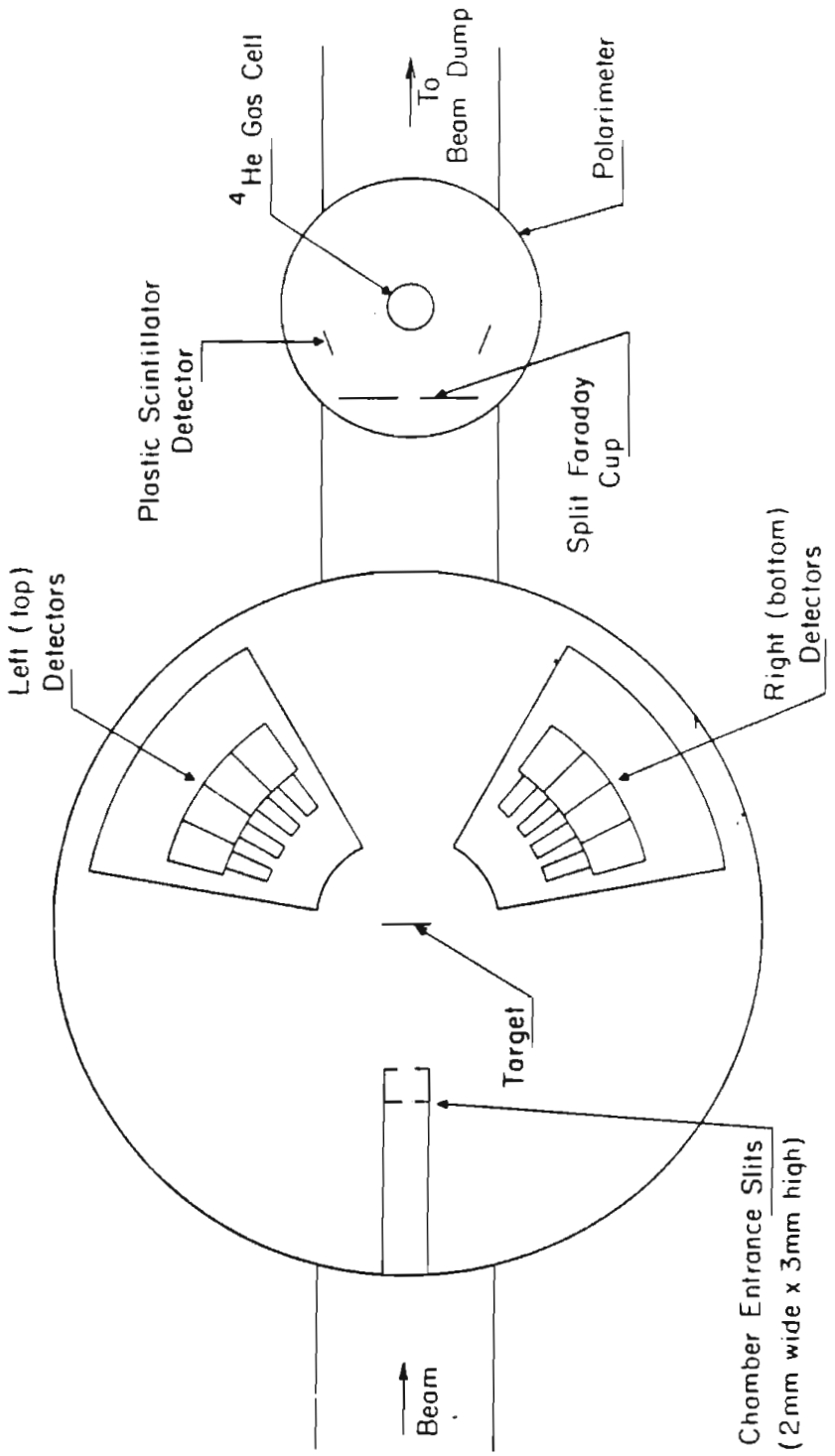

Figure 3-1: Schematic diagram of the scattering chamber used in this experiment. Details of the individual components are given in the text. This figure is not to scale.

TB or BA detectors), four detectors could be mounted 10° apart at a distance of 15.9 cm from the target.

The detector holders themselves were designed to pin the collimators and slits, so that the angular acceptance and solid angle could be reproduced as easily as the radial position and centroid angle. For greater accuracy in the final cross section calculation, the target thickness was usually measured using the same slits as were used in the elastic scattering measurement. This allowed the determination of the product of the solid angle and thickness ($\Delta\Omega T$), making the final normalization independent of the calculated solid angle. The solid angles and angular acceptances ($\Delta\theta$) used in this experiment (except for NOV80) are shown in Table 3-2(a).

In Table 3-2(a), the column labeled $\Delta\Omega_c$ contains the calculated solid angles based upon the slit specifications given to the machine shop. The overall normalization was assured by measuring $\Delta\Omega T$, as mentioned earlier. The exact relative detector normalization was determined by comparing measurements of the yield at some angles with different detector pairs. The pattern of detector placements is shown in Table 3-3; this scheme was used for all the data (except for some middle angles in NOV80). From these overlapping measurements, corrections for the standard setup were estimated using the results for all targets measured during a given run, since the geometry remained unchanged throughout one experiment. The average correction for each detector pair is listed in Table 3-2(a) in the column labeled "Empirical Correction". This correction is the mean of the standard geometry runs, with the stated uncertainty being the standard deviation of this mean. These corrections were applied to the data in the computation of the final cross sections.

In view of the large size of the correction for detectors 3 and 4, the slit dimensions were measured with a travelling microscope and showed significant differences from the specified dimensions. These resulting solid angles are shown in the column labelled $\Delta\Omega_m$. From these measurements, the corrections to the detector normalizations can be calculated. These are tabulated under "Estimated Corrections" in

Table 3-2(a)

Geometric Properties of Standard Setup

Detector	$\Delta\theta$	$\Delta\Omega_c$ (msr)	$\Delta\Omega_m$ (msr)	Estimated Correction	Empirical Correction
R1+L1	0.6°	1.158	1.308±0.06	1.0	1.0
R2+L2	0.6°	1.158	1.290±0.06	0.98±0.07	0.98±0.01
R3+L3	1.2°	2.228	2.358±0.06	0.94±0.07	0.96±0.01
R4+L4	1.2°	2.228	2.358±0.06	0.94±0.07	0.96±0.01

Table 3-2(b)

Geometric Properties of NOV80 Setup

Detector	$\Delta\theta$	$\Delta\Omega_c$ (msr)	$\Delta\Omega_m$ (msr)	Estimated Correction	Empirical Correction	
					(I)	(II)
R1+L1	0.6°	0.994	1.122±0.10	1.0	1.0	1.0
R2+L2	0.6°	0.994	1.108±0.10	0.99±0.13	1.02	1.00
R3+L3	1.2°	1.926	2.038±0.10	0.94±0.10	0.91	0.98
R4+L4	1.2°	2.228	2.380±0.06	0.95±0.09	1.00	0.98

Table 3-3

Detector Settings Used to Check Relative Normalizations

Each column represents a separate setting of the four detector pairs in the scattering chamber. Eleven separate settings were used to measure each angular distribution. As noted in the text, all four pairs were used to measure 55° scattering.

Angle	1	2	3	4	5	6	7	8	9	10	11
25	1										
30		1									
35	2		1								
40		2									
45	3		2	1							
50		3									
55	4		3	2	1						
60		4									
65			4	3	2						
70						1					
75				4	3						
80						2					
85					4		1				
90						3					
95							2				
100						4					
105							3	1			
110									1		
115							4	2			
120									2		
125								3			
130									3	1	
135								4			1
145									4	2	
150											2
155										3	
160											3
165										4	
170											4

Table 3-2(a). The uncertainties in the estimated corrections are large because of limitations on the accuracy of the travelling microscope. Since the empirical corrections will be more exact and take into account factors other than the slit dimensions, these estimates were not used to correct the data.

For the experiment NOV80, the same slits and detector positions were used. For the detector angles 1, 2, and 3, the 50 mm^2 detectors used had active diameters of 0.80 cm, smaller than the height of the slit used. The geometry for this setup is tabulated in Table 3-2(b).

The same procedures for normalization were applied to the NOV80 data. For most of those targets, the 16-MeV cross section was remeasured at forward angles and used to normalize the full angular distribution measured in NOV80. The table shows the calculated and measured solid angles, angular acceptances, and corrections, as in Table 3-2(a). The empirical corrections required were somewhat larger, and differed noticeably from the estimated corrections. In particular, the corrections fell into two groups, (I) for the targets ^{58}Ni and ^{63,65}Cu, and (II) for ^{76,78,80}Se, as shown in Table 3-2b. These differences are not understood, but are probably a result of large deadtime problems experienced during that run. This problem is discussed in the Sect. 4.4.

3.4.2 Target Mounting System

The targets were mounted on a target ladder with 5 positions available for mounting. Typically, only 4 of these positions were used, leaving the fifth position open for beam tuning. The target rod faces were asymmetrically shaped, obscuring 10° on the "front" side and almost 20° on the "back" side. The target angle was continuously variable from 0° to 180°, and could be set reliably to within ±0.5°. For measurements at scattering angles between 70° and 105°, the target had to be rotated to 45° so that the detectors placed symmetrically on both sides could see the target. For target angles of 0°, the error in the cross-section caused by the maximum 0.5° error goes as $\delta(\cos\theta_T)/(\cos\theta_T) = 1.0\times10^{-5}$. For the target angle of 45°, $\delta(\cos\theta_T)/(\cos\theta_T) = 0.009$. Thus, an error of, at most, 1% might exist in the data, caused

by the incorrect setting of the target angle.

3.4.3 Polarization Monitor

Since this experiment required the measurement of polarization observables, it was necessary to monitor the beam polarization. A commonly used method, the quench ratio (Ohls71), requires that the beam be stable on target during both the full beam measurement and the quenched measurement. At the terminal voltages for this measurement, it was difficult to maintain stable machine operation with the small amount of beam on the analyzing slits during the quenched measurement. In addition, there are several circumstances where a measurement of the quench ratio can indicate a beam polarization significantly different in magnitude from the actual polarization. The quench ratio is incapable of providing information about the sign of the spin-quantization axis. Thus we decided to monitor the beam polarization.

Two different monitors were used at separate times during these measurements. In both cases the monitor used the well-determined analyzing power of the ^{4}He($\vec{p}$,p) reaction (Schw71, Dodd77), placing left and right detectors at $\theta_{cm} = 125^\circ$, where the analyzing power is at a maximum. Also, both monitors were placed after the scattering chamber and were part of the beam current integration system.

The first polarization monitor was designed for maximum efficiency and minimum background in the presence of small beam currents(Hard72). The detectors and slits were housed in the gas cell so the scattered protons did not have to exit through a foil. The detectors were large-area, solid-state surface barrier detectors. The beam current integration was performed by connecting the beam current integrator directly to the monitor body, which was insulated from ground. Suppression of secondary electrons was performed by integrating through a 45-volt battery whose positive terminal was connected to the monitor. The analyzing power of this monitor was calculated using careful measurements of the geometry of the scattering slits, and the phase shifts of Schwandt, et al. (Schw71). It was found to be Ay=0.97±0.01; the uncertainty includes only uncertainties in the phase shifts.

The principal disadvantage of this monitor was the proximity of the detectors to the Faraday cup, exposing them to a considerable flux of radiation which caused degradation of their resolution, large backgrounds, and ultimately, detector breakdown. Worse, these problems increased rapidly in time, causing the background shapes and detector resolution to vary significantly from measurement to measurement. The measured beam polarization thus had a large uncertainty.

The second monitor used was designed to try to overcome these problems (Kend81). It used detectors and collimators separated from the gas cell, plastic scintillation detectors which would not experience radiation damage as severely as the solid-state detectors, and a beam dump well separated from the monitor. It also incorporated a "split Faraday cup" with a biased (-50V) cylinder for secondary electron suppression in front of the monitor. This provided beam position information to the steering feedback system (Tons80).

This monitor was calibrated (Kend81) using solid-state detectors in place of the scintillators. Because of the poor resolution of the scintillators, they were not useful for incident bbeam energies below 14 MeV. As a check upon the calibration, the analyzing power was calculated from the known geometry of the detection system, using cross-sections and analyzing powers calculated from phase shifts fitted to ^{4}He($\vec{p}$,p) elastic scattering(Schw71). For the 16-MeV beam used in this work, the two results agreed very closely, Ay(calib)=0.98±0.02 and Ay(calc)=0.98±0.01, with the uncertainty shown in A_y(calc) coming only from the estimated uncertainty in the phase shifts.

There was a problem with the spectra given by the scintillation detectors, which resulted in the degradation of the observed analyzing power of the monitor. The background under the peaks was large and had been poorly approximated as the tail of a Gaussian peak shape. This background appeared to result from neutrons, presumably emitted in (p,n) reactions on the upstream slits, the target and especially the split Faraday cup.

During investigation of this problem a spectrum was measured with the monitor gas out, which appeared to be an excellent approximation to

the background. This was tested by using the gas-out spectra as the backgrounds for the previous gas-in polarization measurement. The resulting calculated beam polarization agreed with quench ratio measured immediately following the polarimeter measurement to within 1%. Subsequent tests showed, however, that the shape of this background was sensitive to the target thickness and angle, as well as to other factors we could not identify. In addition, the background in the region of the proton peaks could not be fitted with an analytic function which could be extrapolated from above or below the peaks.

After many attempts to fit the backgrounds, a compromise was reached which consisted of fitting the sum of two extrapolated backgrounds, one from below the peak (Gaussian tail) and one from above the peak (linear). The details may be seen in Fig. 3-2. The procedure was,

1) set a background defining gate (I) above the peak and a similar gate (III) below the peak in the small-count spectrum (Left-spin-down or Right-spin-up);
2) Calculate the linear component of the background with the gate above the peak, extrapolating it to below the peak (into region III);
3) Subtract this from the spectrum. This is to prevent the Gaussian fit from being biased by the linear component;
4) Now calculate the Gaussian component from the gate below the peak, extrapolating to the region above the peak (region I);
5) Add the two backgrounds together to obtain the approximate spectrum background.

This procedure consistently underestimates the background and causes the computed asymmetry to be smaller than that determined with correct experimental backgrounds (see Fig. 3-2). This background fitting procedure was tested on a dataset where several polarization measurements were made without any target in the chamber, alternating monitor

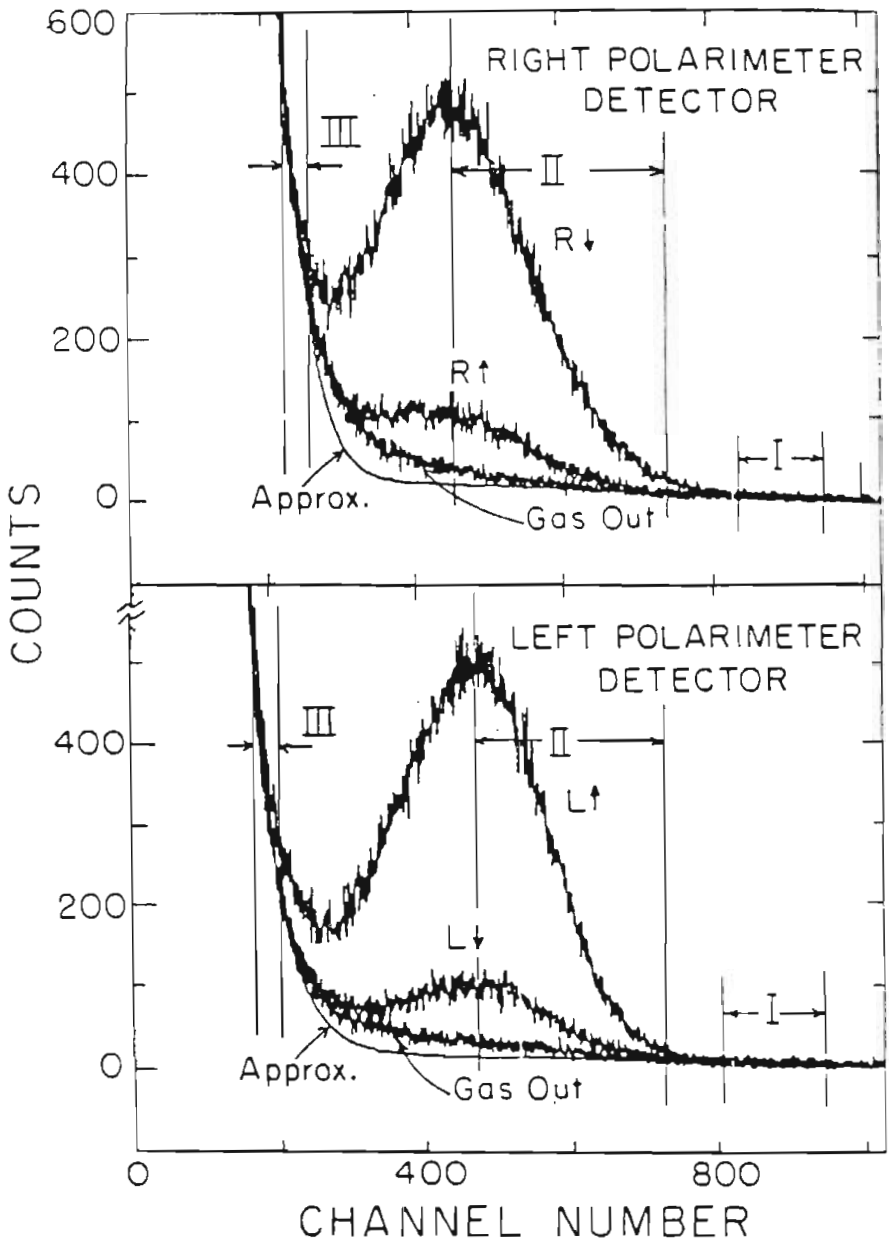

Figure 3-2: Examples of spectra from plastic scintillation detectors used in the polarimeter(Kend81). Shown are both the right and left detector spectra, for the spin up and down measurements, and the ^{4}He gas out specttra used as backgrounds. The smooth line is the analytic approximation used. These spectra were acquired with no target in the main scattering chamber.

gas-in runs with gas-out measurements. It was found that the average ratio of the asymmetry calculated with the approximate background to that calculated with measured gas-out backgrounds was $P_b(\text{approx.})/P_b(\text{meas.})=0.95\pm0.03$. This was used to correct the calibrated monitor analyzing power when calculating the beam polarization in this procedure.

In summary, the monitor background was computed using the approximation procedure described above. The lower limit of the peak sum gate was set high on the peaks, usually at the centroid, (see the gate marked II in Fig. 3-2), to avoid the region where the background was least well determined. Since the background appeared to be unpolarized, it was estimated using the spectra having the smallest peaks, then used for both the spin-up and spin-down spectra. The effect of this procedure was to reduce the monitor analyzing power at E_p = 16 MeV, to a value of $A_y(\text{effective})= 0.92\pm0.04$, using the results of the comparisons in the last paragraph. The uncertainty in this effective analyzing power entered into the overall normalization of the analyzing powers rather than as a point-to-point uncertainty, since the background seemed to be determined predominantly by the small-angle scattering from the target in the main scattering chamber and was relatively constant during the measurement of any one angular distribution.

3.4.4 Beam Current Integration

The present arrangement of polarimeters as part of the integration system caused some concern about the efficiency of beam-current integration. The possible sources of error include:

1) failure to capture all the beam because of the small size of integration surfaces,
2) inadequate suppression of secondary electrons,
3) loss of captured beam current because of leakage current to ground,
4) inaccuracies in the beam current integrator.

Tests and calculations have been made to determine the magnitude of these uncertainties.

The beam current integrator was a Brookhaven Instruments Co. Model 1000, with a calibrated accuracy of 0.1%. This integrator served as a current-to-frequency converter. Tests were made of the relative accuracy of the integrator alone (between scales). This accuracy was found to be 0.5%. The current collection path included a current-to-voltage-to-current amplifier to allow current collection from the split Faraday cup and a voltage feedback signal for steering control(Tons80). This system has been tested and used extensively, and was tested again for this experiment. A current source was connected to the current collection system and integrated, then attached directly to the integrator and the integration performed again. There was no measureable difference in the currents.

The suppression of secondary electrons was accomplished differently for the two monitors used, as mentioned above. The integration system of the newer monitor was tested relative to a standard, suppressed, flat-plate Faraday cup in an experiment where first the Faraday cup was used to measure a cross section (for ^{58}Ni) with and without the steering control system in the current integration circuit. The monitor was then installed and the cross section remeasured, with the same beam intensity and for the same integrated charge. The results from this test all agreed within 0.2%. No test of this type was performed with the NOV80 monitor.

The final concern was that the size of the NOV80 monitor body was too small to collect all the beam. This was checked by performing multiple scattering calculations to discover the divergence introduced by small-angle scattering in the target (Mari68). In all cases, the beam size was small enough that the beam lost was much less than 0.1%.

In summary, several possible problems with the beam current integration system were investigated, and none appears to be able to contribute even a 1% uncertainty to the cross-section measurements.

3.5 Target Preparation and Thickness Determination

The 16-MeV experiment involved the use of 23 targets. The majority of these were made at UNC in a vacuum evaporation system using resis-

tive heating in a variety of boats. Most of the techniques used were standard and are well documented elsewhere. The thicknesses were usually between 100 $\mu gm/cm^2$ and 800 $\mu gm/cm^2$. Most of the targets were self-supporting, the rest being supported on thin films of carbon. All targets were mounted on standard target rings which have an opening approximately 0.7 cm to 0.95 cm in diameter. For further information about the target production, consult Table 3-4 and the associated references.

It is important to measure accurately the thickness of each target. This was monitored during evaporation with a vibrating-quartz-crystal thickness monitor, a device which usually was accurate to about 20%. For the ultimate determination of the target thickness, Rutherford or near-Rutherford scattering was used.

This low-energy scattering was performed using proton scattering at an incident energy chosen to be low enough that an optical-model description of the cross section at forward angles was relatively insensitive to details of the parameterization. This energy was generally between 4 and 6 MeV, the principal tradeoff being between smaller dead times for smaller count rates at the higher energies and more nearly Rutherford scattering at lower energies. This scattering was performed in the same experiment as the 16-MeV scattering in almost every case, and with the same detector geometry. Thus, the measured thickness is the product of the thickness and the solid angle, divided by the calculated solid angle. Any scaling error in the calculation of the solid angle is included in the target thickness, as discussed earlier.

The target thickness measurement contributed the largest errors and uncertainties to the cross section determination. Overlapping measurements of the thickness usually differed by 2% to 5%. In addition, comparison with optical-model calculations and other elastic scattering data measured at 16 MeV, show discrepancies as large as 8%, but averaging 4% or less.

In general, the technique of low energy normalization of the target thickness should be quite accurate, if the beam can be properly integrated at the relatively low intensities necessary for these high

Table 3-4

Target Preparation Summary
(A general reference is Mugg79)

Target	Chemical Form	Boat or Crucible	Thickness ($\mu gm/cm^2$)	Release Agent	Notes	Reference
^{40}Ca	Ca metal	W dimple	150.	----	Handled under He and Ar gas only. Scraped from glass slide, glued to target ring. Excellent.	Benn80
^{48}Ti	Ti(foil)	-------	300.	-----	Rolled from ORNL supplied foil (by R.E. Anderson)	
$^{54,56}Fe$	Fe_2O_3	Al_2O_3 on Mo dimple	150 - 250	NaCl on Ferroplate	Reduction in H_2 gas and vacuum evap. of Fe metal Poor release, good films, but NaCl contaminated.	Heag76
^{58}Ni	Ni metal	Al_2O_3 on Mo dimple	600	$BaCl_2$ on Glass	(prepared by J.F. Wilkerson)	
^{60}Ni	Ni metal	Al_2O_3 on Mo dimple	200	NaCl on Ferroplate	Slow rate best for smooth films.	
^{63}Cu	CuO	Mo dimple	400	$BaCl_2$ on Glass	Reduction in H_2 gas and vacuum evap.	Heag76
^{65}Cu	CuO	Vitreous Carbon	150	$BaCl_2$ on Glass	Simultaneous reduction and evap with electron beam gun. Poor technique. (by J.F. Wilkerson and D. Sanderson)	
$^{76,78,80,82}Se$	Se metal		75 - 200	Carbon films (10 $\mu gm/cm^2$)	Resistive heating. Small distances. (by Y. Tagishi and D. Sanderson)	
$^{116,120,124}Sn$	SnO_2	Mo dimple	300	NaCl or none on Glass	Best targets scraped from bare glass. Reduced in H_2 gas. Poor sticking to glass substrate during evaporation.	
$^{134,136}Ba$	$BaNO_3$	Ta tube crucible	150	Carbon films (20 $\mu gm/cm^2$)	Reduction and distillation. Wet chemistry Poor sticking when exposed to air. Kept in Ar as much as possible. Allowed to	Gurs83
^{138}Ba	$BaCO_3$	Ta tube crucible	150	" "	oxidize in bell jar under vacuum.	
^{209}Bi	Bi metal	W dimple	670	NaCl on Glass	Straightforward target. Simple, resistive heating Yields thick uniform films.	

References

Mugg79 - A.H.F. Muggleton, Journal of Physics E(Scientific Instruments) 12(1979)780. (General reference to target making).
Benn80 - A.H. Bennink and T.W. Tuintjer, KVI Annual Report 1980, Groningen, Netherlands (unpublished).
Heag76 - J.M. Heagney and J.S. Heagney, Proceedings of the 5th International Conference of the Nuclear Target Development Society, LASL Document LA-6850-C(1976)94
Gurs83 - J. Gursky, LANL, private communication.

cross-section measurements. I believe that the technique as applied here and as seen in Chap. 4 is accurate to 5%. However, the measurement could be improved in several ways. There are several uncertainties in the procedure, among which are the cross section, the target uniformity, and possibly the dead-time correction.

There is some danger to choosing an arbitrary energy for the low energy measurement, largely because many non-direct processes can contribute to the cross section, e.g. isobaric analogue resonances for the lighter nuclei measured here. A reasonable but time consuming procedure for checking for this problem is to measure an excitation function around the chosen energy to check for resonant behavior. This is probably the only generally reliable procedure, unless, of course such data can be found in the literature. It was difficult to locate detailed excitation function data for our variety of targets, in the energy region where we wished to measure.

The most worrisome problem is that of target uniformity. In particular, it is necessary to attempt to measure the target thickness over the same region of the target as the original elastic scattering. It is likely, within the constraints of the angles and positions shown in Table 3-1, that the same position was measured to within 3 mm. If there are target non-uniformities over this spot, however, it is necessary to attempt to better locate the beam position. This might be done, for example, by using a quartz or phosphor to locate the beam position during the elastic scattering, then tuning the thickness measurement to reproduce that position. It is advisable to at least perform a test with this procedure to see if there is any such problem.

The last potential problem with this normalization procedure is the accuracy of the dead-time correction measurement. The pulser based procedure, described in Sect. 3.6.1, is undoubtedly very accurate, if it is sampling the data rates at representative times. If the pulser, with its very low rate, samples the data more often at low rates than at high (assuming that the rate is varying) then the deadtime will not be properly measured. Especially when the pulser samples are only a very small fraction of the total number of events, the likelihood of error rises. The pulser procedure could be changed to 1) sample at

some fixed percentage of the measured rate, e.g. 0.1%, and 2) to trigger randomly, based on the ADC gates, for example. This is not likely to be much of a problem, but it does appear that at the higher count rates (DTC >1.15) that the estimated DTC's are generally too small. The procedures described above might permit reliable measurements at dead times much larger than the restriction required here (10%).

As a final note, the best means for getting around the normalization problems might be to devise techniques for reliably measuring forward angle scattering to angles of 10° or less. At these angles, for all the targets measured here, the scattering at $E_p \leq 20$ MeV is close enough to Rutherford scattering to provide a strong constraint on the optical-model calculation. Unfortunately, the inherent difficulties of such measurements, with high count rates and cross sections which change rapidly in angle, make it unlikely that they could be performed on a regular basis. It is more likely that one experiment, devoted only to this kind of measurement, taking care to cross normalize to other data, would be successful.

3.6 Data Acquisition System

The data acquisition system consists of the detector pulse shaping electronics, computer interface, and software for sorting and converting the resulting data into cross sections and analyzing powers. The computer system at TUNL was replaced during the time of this research; this provided an opportunity to revamp the data acquisition software for our experimental group. In particular, this allows online computation of the final observables, a step which greatly enhances the experimenters' ability to monitor data taking and correct possible problems.

This section will summarize the components of the data acquisition system such as signal shaping electronics, VAX/XSYS interface, and the software used to sort the data.

3.6.1 Signal-Shaping Electronics

The signal-shaping electronics used in these experiments were relatively standard. Solid-state surface-barrier detectors of 2000 μm thickness were used in the scattering chamber. For some measurements at some angles, this thickness was obtained by using a telescope of two 1000 μm detectors, combining the signals before the preamplifier. This procedure was generally satisfactory for elastic scattering when the two detectors could be matched in bias voltage. The resolution of such a pair was generally poorer than a single detector, and for inelastic scattering this caused a gap in the spectrum for particles whose energy was such that they just barely penetrated the front detector but could not penetrate the rear detector. Consequently, this scheme was used as little as possible.

The pulse height signals were processed as in Fig. 3-3 and stored into a VAX 11-780 computer running the TUNL XSYStem (Goul83). The unusual features of these electronics were the pileup rejection and the active dead time test. The pileup rejection signal was generated by an Ortec 572 amplifier in each of the left and right detector electronics setups. These were summed and used as the gate for an Ortec 444 gated biased amplifier in anti-coincidence mode, to reject the piled-up pulses. Since the pileup rejection introduces dead time, and so that the dead time could be more accurately measured for the entire electronics setup, a slow (10 Hz) pulser was injected into the test input of the right detector preamplifier of each right-left detector pair. The pulse height was adjusted to place the resulting peak in an innocuous place in the spectrum above the elastic peak. This peak could be summed and compared to a scalar storing the count of pulses injected. This technique proved quite reliable. It was not used for the NOV80 data, in which pileup rejection was not used. Here, only the ADC and computer deadtime were measured by gating off a scalar counting the current integrator pulses while the ADC router was dead. In both of these experiments, the right and left detectors of a pair were stored through the same biased amplifiers and ADC's to impose the same dead time on each. In this way, the effects of dead time on the asymmetry were minimized.

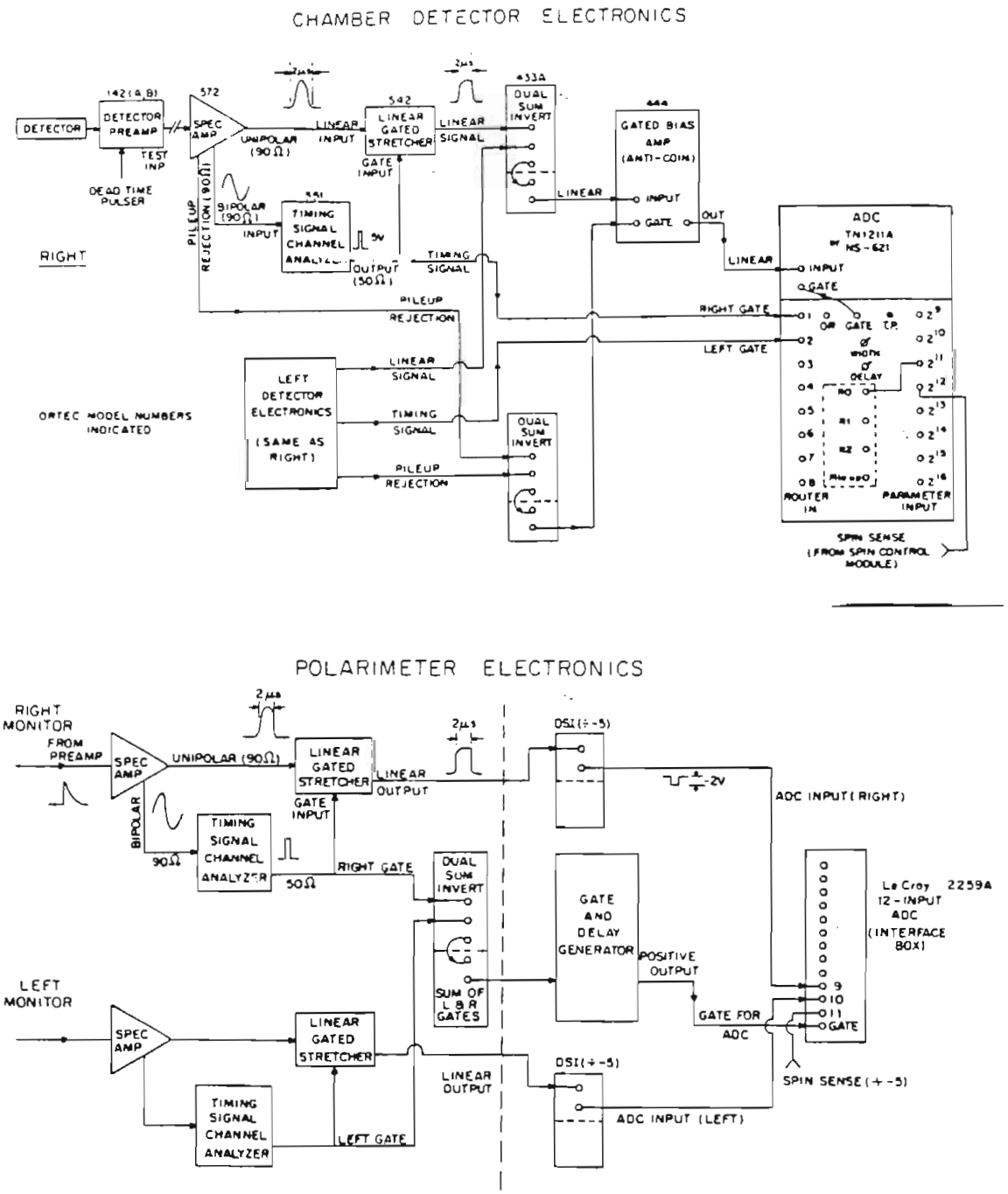

Figure 3-3: Diagrams of the signal processing electronics. The upper diagram shows the electronics for a typical left and right detector pair, each set to the same scattering angle. The second diagram is for the polarization monitor electronics. The same types and model number modules were used for the monitor as for the chamber detectors, wherever possible.

The pulse-height signals were processed by fast ADC's (Northern Scientific NS-621 or TN1211) operating in conjunction with in-house designed routers. These signals were digitized into 1024 channels. In addition, a routing bit was inserted into bit 11, and a spin direction sense bit was inserted into bit 12 since these bits were unused by the ADC. The resulting 16 bit word was sent to the VAX via a CAMAC input register, serviced by an MBD-11(Goul83). The sorting program running in the VAX then sorted the event into left and right spectra based on the value of the router bit, and into spin-up and spin-down spectra based on the spin bit. There were four ADCs used in the data acquisition for the chamber detectors, a separate one for each detector pair.

The maximum event rate that the system could handle within our dead-time requirements of 10% or less was 2 kHz in any one detector pair. This dead time was in the signal shaping electronics, largely resulting from the pile-up rejection. The system was very stable, exhibiting obvious gain changes of less than 1 channel in 800 over the period of the measurements (up to 4 hours per measurement). The energy linearity of the system was also good to better than 1%.

3.6.2 Polarimeter Electronics and Interface

The electronics for storing the polarimeter detector signals were similar to the chamber detectors. The details are given in Figure 3-3. Pileup rejection was not used, nor were any dead-time corrections made, since in our measuring scheme of left and right detectors the determination of the asymmetry was independent of the dead time, and we had insufficient electronics for the pileup rejection.

In the interface at TUNL there are only four ADC's with routers. Since we run four pairs of detectors in the chamber, we had no routing ADC's left for the polarization monitor detectors, so we used a LeCroy 2259A 12-input ADC. This required somewhat different signal processing than the routing ADC's, since this module has 12 linear inputs and only one gate input. The logic for this setup was to sum the gates from the monitor detectors, and put each linear signal into its own input. This

resulted in the spectra for each of the left and right detectors registering a count in channel zero for each count occurring for the other detector. This occurrence has no consequence in the analysis of the polarization.

3.6.3 Miscellaneous Signal Inputs

Some information was available to the experiment in digitized form. This included the integrated beam current (digitized by the Brookhaven Instruments Corp. current integrator), the "clock" (a 10-Hz oscillator), the dead-time-correction pulser, and the external gate for events presented to each router. These counts were summed by LeCroy 3610 scalers. In addition, each run was halted after a predetermined integrated charge; this was controlled by a Borer 1008 preset counter/timer (XSYS84).

The VAX/XSYS interface permitted some degree of sensing and control, which was utilized in this experiment. The system was used to control and sense the spin direction at the polarized ion source, and monitor the status of the Faraday-cup suppression.

3.6.4 Data Acquisition and Analysis Programming

A considerable portion of the work for this thesis was involved in data acquisition and analysis programming within the TUNL XSYStem (XSYS84, Goul83). This section is a summary of this programming. More details can be found in the **UNC XSYSTEM Programming Guide** (Varn85) and the **XSYSTEM Manual** (XSYS84).

The XSYS was planned to be an environment to give each user flexibility in the design of a data acquisition scheme. The majority of the experiments run by the UNC group use polarized beams of charged particles and detect the outgoing charged particles with silicon surface barrier detectors. The many common elements of these experiments led us to design and write a set of data processing modules, using similarly organized data structures. This experiment and others by the UNC group required first the implementation of the basic sorting and control programs which were necessary for any data measurement. These

sorting codes were written in the DAP and EVAL languages of XSYS; the control programs were written in the Digital Command Language (DCL). The large computing power of the VAX 11-780, which is able to support more than a dozen separate, active, time-sharing tasks and which has 4 megabytes of memory, as well as 700 megabytes of online storage, suggested that it would be possible both to implement a system of computer recording of experimental parameters and to automate the computation of observables.

The calculation system was designed with two principal goals. The first was automatic online calculation of the observables. This was necessary to help the experimenters to identify problems with the measurement immediately and to take corrective measures. The previous system, one of hand calculation, was often neglected since the experimenter was required also to monitor the ongoing experiment. The second goal was to design a system which could be used offline as well in a flexible manner, retaining the automatic features of the online system. This would permit the analyzer to concentrate on those aspects of the analysis which require human attention, the setting of peak gates and the judgement of backgrounds. Further, it would permit immediate checking of calculations for consistency, since the plot of final observables would be quickly available.

This second goal was particularly important in view of the large amount of data collected in this project, about 1600 data points. The automatic scheme reduced the likelihood of calculation errors in processing the data, and permitted the straightforward recalculation of the observables from peak sums when, for example, the problems with the polarization monitor background subtraction (Sect. 3.4.3) were discovered.

This system of calculation was implemented by first dividing the basic functions of these calculations into relatively small and coherent modules. Then FORTRAN programs were written to implement these modules within the environment of the XSYStem. These modules were:

1) Background calculation, XBACKGRND

2) Peak summing and background subtraction, VSUM
3) Calculation of the normalization, VNORM
4) Calculation of the beam polarization, VMON
5) Calculation and tabulation of the final observables, VCALC.

The modules named above are examples for vector polarized beam data acquisition. For other types of beams, some of these modules, each of which is a separate FORTRAN program, are replaced by more appropriate programs.

These basic functions already existed in the XSYS, but needed to be rewritten to include the storage of intermediate results and pertinent auxiliary data into XSYS data areas. These data areas are saved as part of the online and offline data record, together with the regular spectra. These data areas are of 3 types:

1) Master Data Area - for the storage of general information about the experiment, e.g. detector solid angles, detector angles, etc;
2) Scaler Data Area - for storage of scalers and pulser-computed-dead-time corrections for multiple-step runs;
3) Sum Data Areas - for each detector pair, to save the sums, backgrounds and computed errors for each detector peak and each step of the data measurement sequence.

These data areas serve also as a fixed record, attached to the measured spectra, of the experiment. This record is independent of the quality of the manual log book recording, at least in principle.

In addition to the storage of the intermediate results, the final calculations were stored in external files. This was chosen as the medium for storage because of the ease with which these results could then be manipulated by post-processing programs, which, for example, convert the data to center-of-mass cross sections and analyzing powers. Also, these results were considered more volatile than the data stored in data areas, since these could change with changing assumptions about

the data analysis, and were less important than other information stored with the spectra.

Once these basic functions and storage systems had been determined, it was necessary to write control programs in DCL to link the functions together, to convert peaks in spectra to the final observables. This system was designed to be relatively flexible, yet to require the average user to know only a few commands. A scheme of data-area organization was designed to permit maximum use of DCL capabilities for symbol manipulation, so that the command files could compose the arguments for the basic functions given only the detector pair number and the appropriate step numbers. Furthermore, the system was made as modular as possible so that many pieces could be reused in other schemes of data taking, and so that the changes necessary to support the current mode might be made at as high a level as possible, that is at the most simply organized level. For more information, consult the UNC XSYStem Programming Guide(Varn85).

The system for data acquisition outlined above has been in use for about 3 years. It has changed considerably from the first conception, and the description above represents the current state of the system. The most important quality to maintain in these programs is flexibility: program systems should be easily modified to accommodate changes in the data-taking procedures. This already exists to a considerable extent in the current system, but it can be enhanced at several levels.

The FORTRAN programs could be enhanced by increasing their modularity. Most of the programs are expected to perform the mapping and extraction of data from the Master, Scaler and Sum data areas on their own. This should be replaced by a set of subroutines for management of these data areas. This accomplishes two goals: first, it makes the programs more readable, since they would then obtain values from the data areas by calling a subroutine which knows the structure of the particular data area; second, it allows the structure of data areas to be modified easily, since only one program must be changed to accommodate the change. All other routines must be merely relinked to the

changed subroutine.

Another change which should be implemented for future ease of modification is the inclusion of version numbers into the data areas, numbers which indicate what versions of the programs were used to write the data area. This allows programs to recognize automatically an old version of the data and take some action, either to warn the user, or use the correct structure to read the data. Currently, with no version numbers, there is no way for the user to determine that there is a problem until a calculation fails. At that point the user is on his own in finding a solution.

The command files could also be improved. There is currently some division among users about how to implement the many different modes of data acquisiton within the command files. One possibility is to create command files which execute all possible modes of data acquisition simply by altering the values of certain control symbols. The other possibility is to maintain different versions of the higher level command files for the different modes of data taking. To change modes would be as simple as copying in the appropriate set of command files for the new mode. The latter is to be preferred for one essential reason, that it allows the structure of the command files to be simpler, without the continuous testing for modes. These sets of command files will often share the same lower-level routines, routines whose arguments are modified by the calling routine to suit the current mode. A simpler routine is easier to understand, and thus to use and modify.

Finally, more daring changes might be explored, such as the use of alternative programming languages, in which the handling of the data might be made more convenient through such modern language features as data structures and enumerated types. The task of data processing is largely one of moving numbers and characters around, with only a small part involving actual calculation. Most modern computing languages have better facilities for these type of manipulations than does FORTRAN. These other languages often employ the concept of a "structure" of logically related data of possibly different types. Use of structures in XSYStem programming would provide a more intuitive way

to represent such XSYStem concepts as the data area, which is composed of integers representing the size, characters for the names and types, and real numbers for the calibrations, for example. On the VAX, such experimentation should be straight-forward, since most VAX programming languages have common interfaces, allowing non-FORTRAN routines to communicate with the FORTRAN routines remaining in the XSYStem libraries.

IV. Summary of 16-MeV Proton Elastic Scattering

4.1 Introduction

The procedures used to measure $\sigma(\theta)$ and $A_y(\theta)$ for 16-MeV elastic scattering have been described in Chap. 3. This chapter is concerned with the specific targets chosen for this research, the reasons for these choices, and the strengths and weaknesses in the measured data sets. In addition, this chapter describes the estimated uncertainties in these data.

4.2 Selection of Targets

Several criteria were used to select the 16-MeV dataset desired for our global optical model analysis. These include:

1) wide range of target mass ($40 \leq A \leq 238$);
2) many chains of isotopes for the investigation of isospin properties of the optical model potential(OMP);
3) matching of targets to proton datasets at other energies and to the neutron datasets.

In the course of the experiment several compromises were made in the above criteria, primarily for two reasons. First, the detector system and electronics had a resolution of $\geq$ 50 keV (FWHM). This effectively prevented our measuring elastic-scattering data with targets for which the excitation energy of the first-excited state is smaller than about 100 keV. Most rare-earth-region targets, for example, fall into this category. On the other hand, nuclei near closed shells have relatively high-lying first-excited states, so the targets selected tended to emphasize nearly-closed-shell nuclei, as in previous datasets (Becc69).

Second, many potentially useful target materials required target

making techniques beyond our capabilities, or were provided by Oak Ridge National Laboratory in chemical forms which were not easily usable without complicated reduction procedures.

4.3 Summary of Data

The nuclei measured are listed in Table 4-1. These targets were chosen to fulfill the selection criteria given above, although some were included because of their availability. The table contains information about the isotopes used, the energy of the first-excited states, and the measured target thicknesses, whose uncertainties are standard deviations of an average from multiple measurements. The data are plotted in Figures 4-1 to 4-4. These are shown as the cross section divided by the Rutherford cross section (σ/σ_R) and the product of the cross section and the analyzing power divided by σ_R, $(\sigma A_y)/\sigma_R$. These were the forms of the data searched upon, and to which fits are shown. The justification for the $(\sigma A_y)/\sigma_R$ is discussed in Chapter 6. The curves shown are the best global optical model fits we obtained. The differences between solid and dashed curves are described in Sect. 7.2.1. The 16-MeV $(\bar{p},p)$ data measured at TUNL are tabulated in the Appendix.

4.4 Discussion of the Data Set

The noteworthy feature of the 23 targets is that 19 of them are within one nucleon of a closed shell, which causes this dataset to reflect the properties of nuclei with closed shells, rather than nuclei at large. This is generally a property of elastic scattering databases (Becc68, Rapa82), which tend to be dominated by these closed-shell nuclei because of similar constraints to ours. Our targets overlap significantly with those of other data sets used in our global analysis, as described in Chap. 5.

4.4.1 Nuclear Structure Problems

Being near closed shells, these nuclei generally exhibit simple vibrational collective excitations for their lowest-lying states.

Table 4-1

Target Nuclei for 16 MeV Elastic Scattering

Target	Enrichment (%)	Thickness (μgm/cm^2)	First Excited State J^π(MeV)
^{40}Ca	97 (natural)	434± 6	0^+ (3.352)
^{48}Ti	≈99	349± 8	2^+ (0.983)
^{50}Ti	≤88	311±30	2^+ (1.555)
^{54}Fe	97.2	570±25	2^+ (1.408)
^{56}Fe	99.9	206± 2	2^+ (0.847)
^{58}Ni	99.8	722± 9	2^+ (1.454)
^{60}Ni	99.08	387± 7	2^+ (1.333)
^{63}Cu	99.89	607±24	$1/2^-$ (0.670)
^{65}Cu	99.69	108± 6	$1/2^-$ (0.771)
^{76}Se	96.88	302±12	2^+ (0.559)
^{78}Se	97.27	372± 7	2^+ (0.614)
^{80}Se	99.45	742±26	2^+ (0.666)
^{82}Se	96.66	400± 4	2^+ (0.654)
^{90}Zr	≈97	1119±24	0^+ (1.761)
^{116}Sn	95.6	356± 6	2^+ (1.294)
^{120}Sn	98.4	362± 6	2^+ (1.171)
^{124}Sn	97.0	427± 9	2^+ (1.131)
^{134}Ba	86.2	152± 4	2^+ (0.605)
^{136}Ba	92.9	157± 3	2^+ (0.819)
^{138}Ba	99.7	332± 4	2^+ (1.436)
^{208}Pb	≈95	414± 9	3^- (2.615)
^{209}Bi	100 (natural)	673± 7	$7/2^-$ (0.897)
^{238}U	99.3 (natural)	72.5±2.5	2^+ (0.045)

(The uncertainties in the thicknesses are the standard deviations of the mean of several measurements with different detectors.)

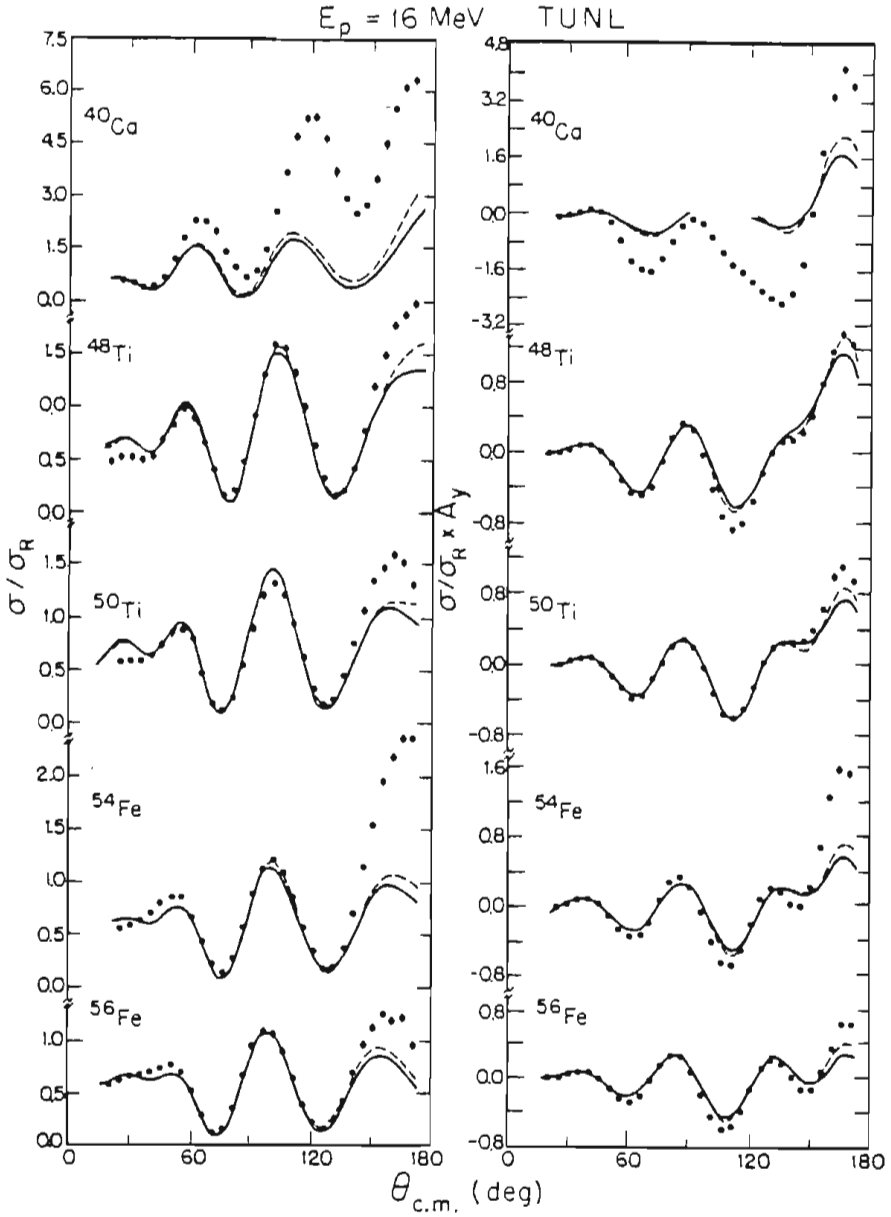

Figure 4-1: Elastic scattering data measured at 16 MeV. Shown are angular distributions in σ/σ_R and $(\sigma A_y)/\sigma_R$ plotted as a function of the center-of-mass scattering angle. The relative uncertainty is shown by the vertical bars through the data points. When not visible, they are smaller than the dots. The curves are from the best-fit optical-model potential, as described in Chap. 7.

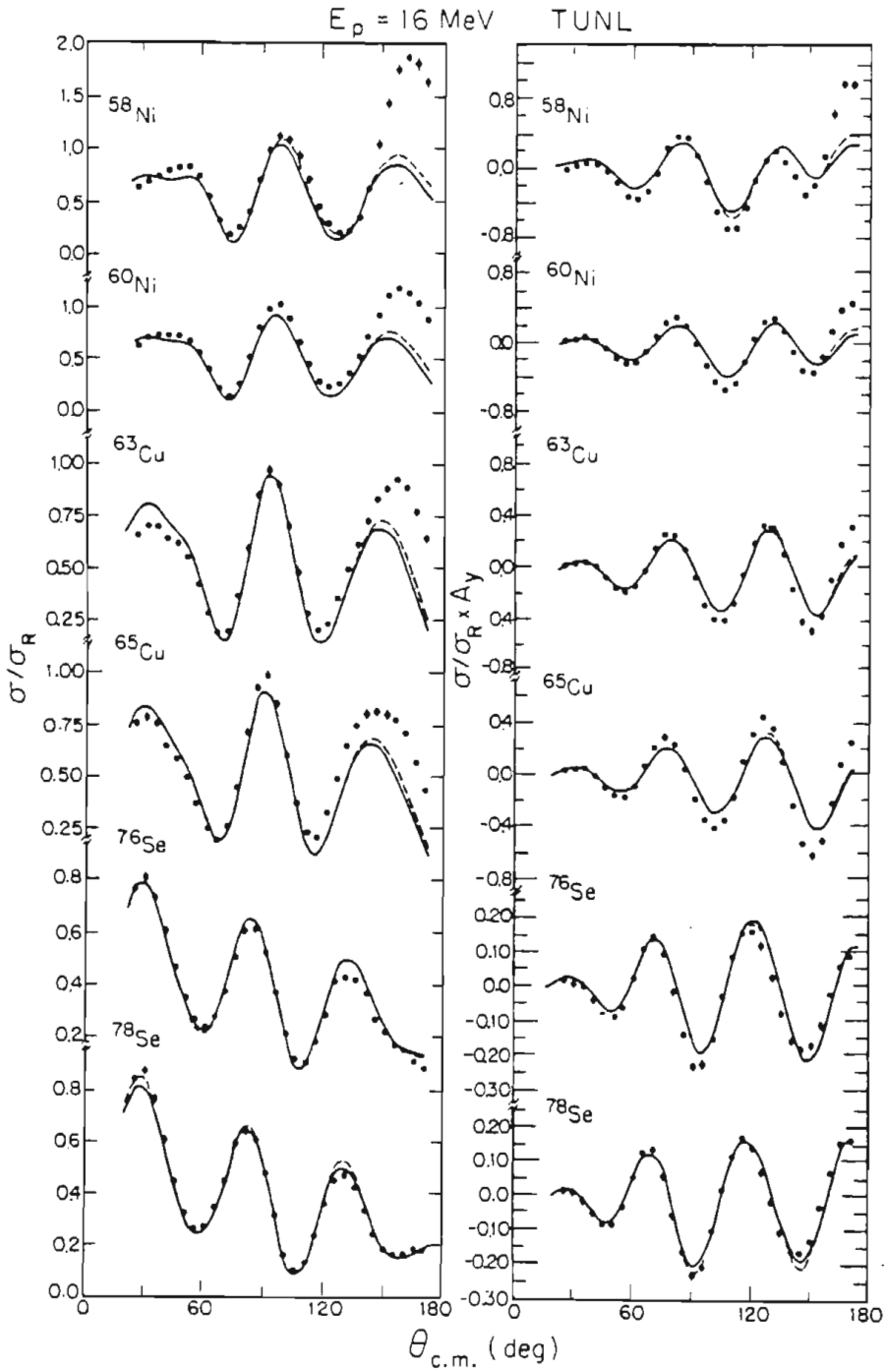

Figure 4-2: Elastic scattering data measured at 16 MeV. Shown are angular distributions in σ/σ_R and $(\sigma A_y)/\sigma_R$ plotted as a function of the center-of-mass scattering angle. The relative uncertainty is shown by the vertical bars through the data points. When not visible, they are smaller than the dots. The curves are from the best-fit optical-model potential as described in Chap. 7.

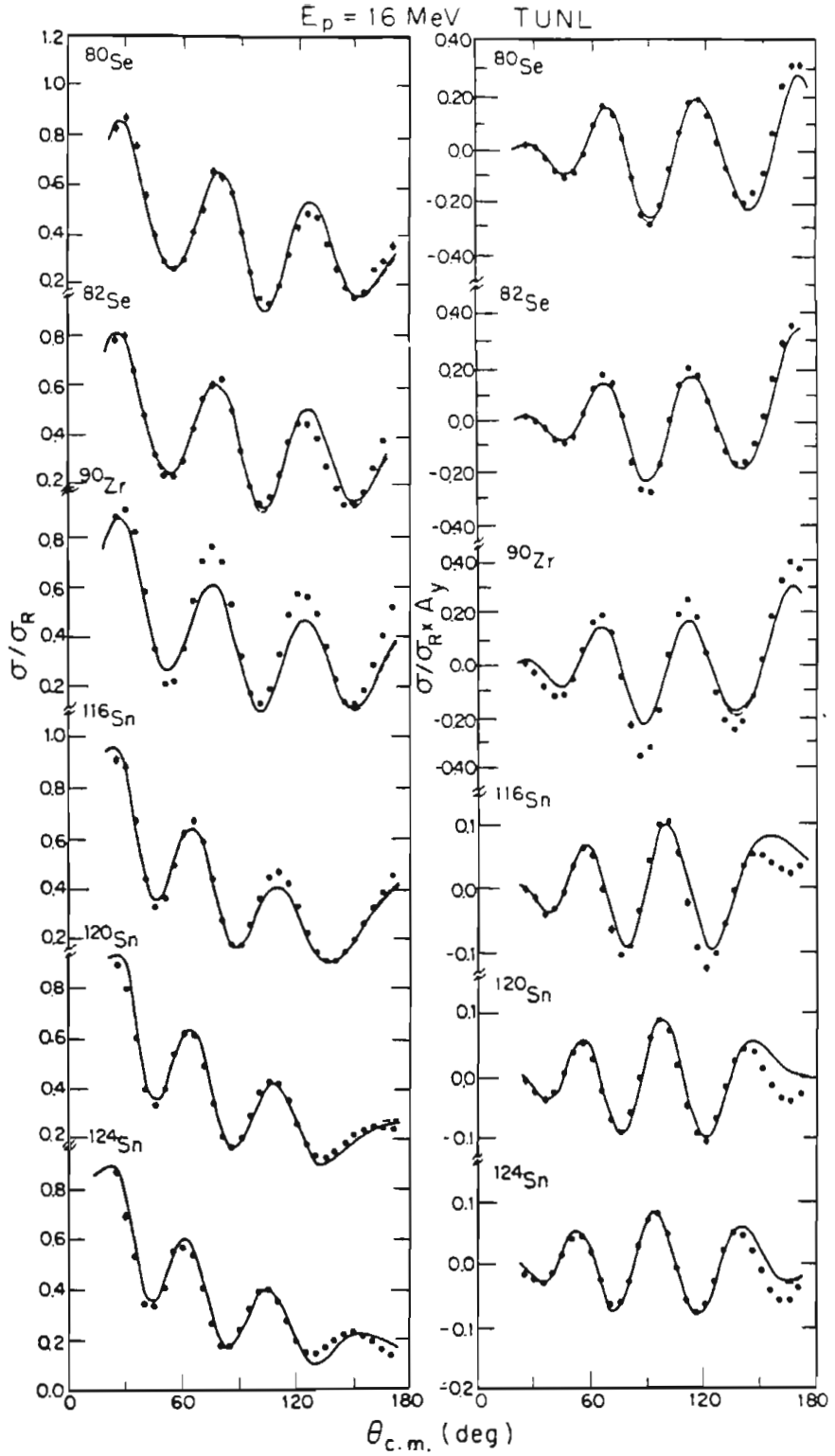

Figure 4-3: Elastic scattering data measured at 16 MeV. Shown are angular distributions in σ/σ_R and $(\sigma A_y)/\sigma_R$ plotted as a function of the center-of-mass scattering angle. The relative uncertainty is shown by the vertical bars through the data points.

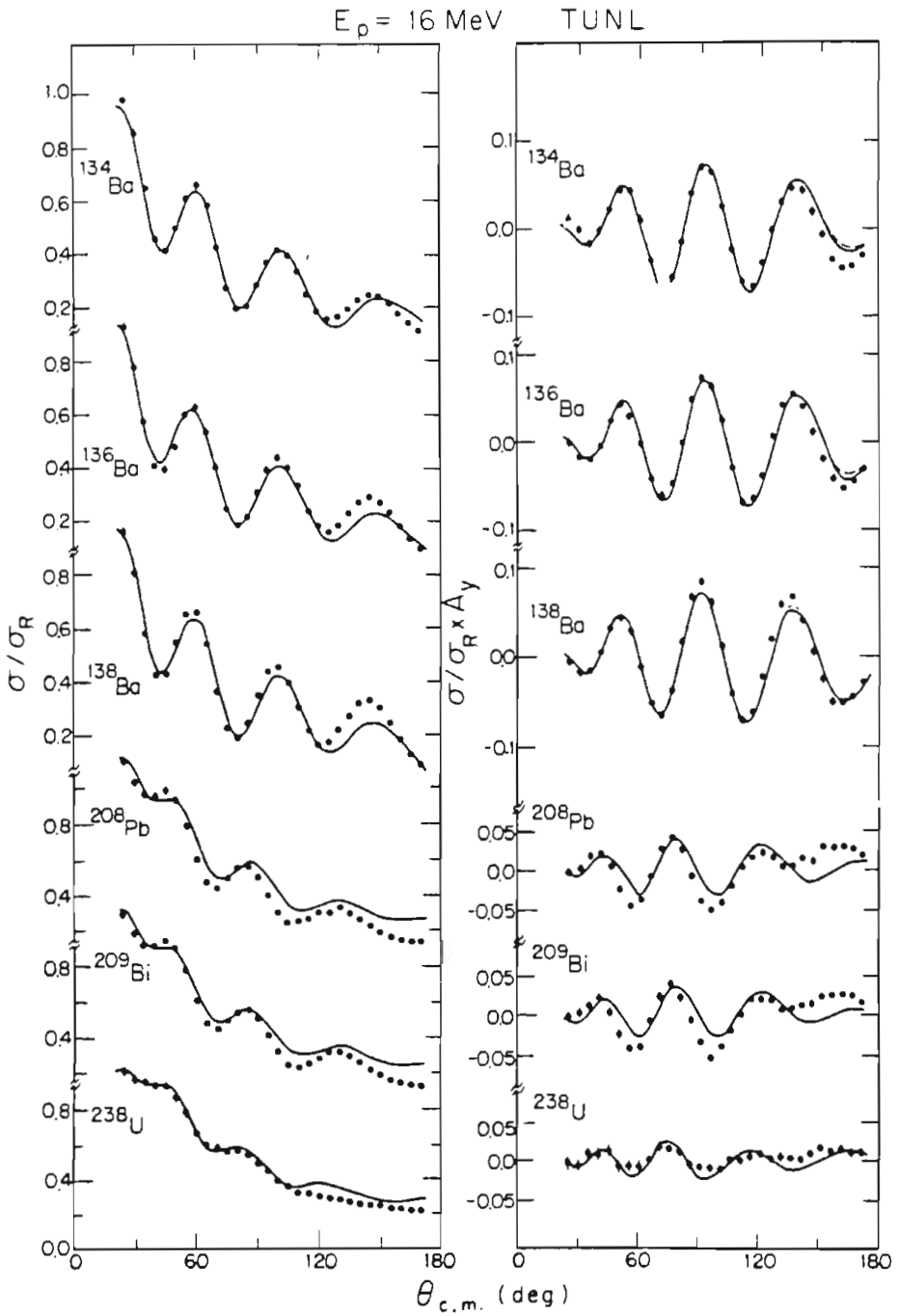

Figure 4-4: Elastic scattering data measured at 16 MeV. Shown are angular distributions in σ/σ_R and $(\sigma A_y)/\sigma_R$ plotted as a function of the center-of-mass scattering angle. The relative uncertainty is shown by the vertical bars through the data points. When not visible, they are smaller than the dots. The curves are from the best-fit optical-model potential as described in Chap. 7.

There are several exceptions to this observation. The Se isotopes have been shown to exhibit more complex behavior, showing a transition from complex rotational structure to more vibrational character (Dela84). More significantly, and unfortunately for this research, three of the targets exhibit significant resonant behavior for scattering at this incident energy (16 MeV). The isotopes ^{208}Pb and ^{209}Bi exhibit strong isobaric analogue resonances (Melz85) in the vicinity of 16 MeV. This was noticed first after the experiment had been performed; the data for these two targets could not be described successfully even with reasonable individual optical model parameterizations. Some previous optical model analyses had included ^{208}Pb scattering near 16 MeV and ignored the inconsistency of the OMP at this energy with parameters from other energies (Mako72, Oers74).

Similar problems were experienced in performing an individual fit to the ^{40}Ca data. An attempt to describe the present data with an energy-dependent optical model for ^{40}Ca over a wide range of energies above and below 16 MeV showed that these data could not be described consistently with most other ^{40}Ca data (Hono84). Other attempts at such analyses experienced serious difficulty with ^{40}Ca elastic scattering data near the (p,n) threshold (Dice71). In addition, reaction cross section measurements show some oscillatory behavior near 16 MeV, prior to the onset of the (p,n) threshold at 16.2 MeV (Dice71). These effects most likely arise from compound-elastic scattering, since there is no (p,n) reaction to depopulate compound nuclear states formed in this reaction.

These problems with the distinctly non-direct scattering in these three nuclei forced us to exclude these data from the search database. They are shown with calculations only for comparison and completeness.

4.4.2 Technical Problems

Several technical problems have been mentioned previously, in particular the problems with polarization monitors (Sect. 3.4.3). Several others affected only one or two targets. These problems and the procedures used to compensate for them will be discussed below.

The most difficult problem was that of determining the appropriate dead-time correction for the NOV80 experiment. This experiment measured only the ADC and computer dead-times; many runs were made with the apparent dead-time well above acceptable limits (10%). This affected chiefly the target thickness measurements (performed with high count rates even when using small beams) and the measurement of forward-angle cross sections. As a result, the target thicknesses measured during the NOV80 experiment were found by comparison with later measurements to be inaccurate by as much as 13% (for ^{65}Cu). For all the targets, except ^{63,65}Cu, the scattering at angles with excessive dead-time corrections was remeasured in a later experiment. Additionally, the target normalizations for ^{76,78,80}Se were redetermined, since new targets had to be used.

The ^{63,65}Cu targets were all destroyed prior to remeasurement. For the ^{63}Cu target no additional dead-time corrections seemed to be needed. For ^{65}Cu an additional correction of 6% was estimated for the most forward-angle measurement. This correction was deduced from the fact that the same dead-time was imposed on the first and second detector pairs in the NOV80 system. We used the detector cross normalization measurements described in Sect. 3.4.1, comparing runs made with high dead-time with those at low dead-time, assuming that the detector cross normalization was known from other measurements. For example, we made a measurement with high dead-time using detector 1 set at 25° and detector 2 at 35°. The cross normalization measurement was made with detector 1 at 35° and a much lower dead-time. If we assume that the smaller dead-time at 35° was measured accurately, and that the relative normalizations of detectors 1 and 2 are known independently, then the dead-time for detector 2 at 35° can be estimated. Since this is the same dead-time imposed by the electronics on detector 1 at 25°, we could estimate the needed corrections.

The thickness of the ^{58}Ni target was not remeasured. The resulting normalizations (compared to other data and OMP estimates) do not seem to be significantly in error.

A different problem was experienced with the measurement of the

^{50}Ti angular distribution. The suppression of secondary electrons from the Faraday cup was not switched on, causing an incorrect measurement of the beam current. This was the case for the entire measurement, including the measurement of the target thickness. Past experience has shown that the lack of suppression causes the beam to appear 30% higher than it truly is, but this number can fluctuate with the experimental conditions. We have no quantitative measure of the point-to-point fluctuations possible under these conditions, but the smoothness and good overlaps within the angular distributions suggests they are small. The calculated cross section, using the thickness determined during that run, appears to be too large (in comparison with ^{48}Ti and optical model predictions). The target thickness was finally chosen by normalization to the forward angle calculations of the best fit global optical model potential. This OMP differed little from most other good fit OMP's at the forward angles, and is believed to give an estimate of the target thickness accurate to 10%.

As can be seen from Table 4-1, a few of the target materials were significantly contaminated by other isotopes, namely ^{50}Ti and ^{134,136}Ba. Also, ^{54}Fe was contaminated by significant amounts of NaCl during the target production. These angular distributions were corrected for these contaminants, as described below.

The contamination in the ^{54}Fe target was most difficult to correct. The problem was that at forward angles the Na and Cl peaks could not be resolved from the Fe elastic scattering. The contributions from contaminants were estimated by first extracting an angular distribution for the resolved Na and Cl peaks and then by fitting these data with an optical model calculation, using the best estimate of the renormalization given by the optical model predictions to gauge the thickness of the contaminants. This optical potential was then used to predict the forward-angle scattering, weighted by the estimated thickness; the estimated contribution was subtracted from the data. The contaminations were estimated to be 3.6 atom-percent for Cl and 4.5 atom-percent for Na, such that errors of 20% in the predicted cross sections affected the ^{54}Fe data by less than 1%.

For the other isotopes, a sample analysis performed at ORNL prior to shipment was used in determining the amount of contamination to be subtracted. For the ^{50}Ti target the difficulty of estimating the thickness of the target has been discussed. In addition, it was clear from optical-model analysis that the measured thickness for the ^{48}Ti target was incorrect by more than 10%. Since the ^{50}Ti target was about 12% ^{48}Ti (Hall84), a 10% error in the measured cross-section for ^{48}Ti introduces a significant error in the contamination correction. As a result of these uncertainties, renormalizations of both the ^{48}Ti and ^{50}Ti data were made, using a global optical model optimized to best describe both sets of angular distributions. After these renormalizations were performed, the contamination contribution of ^{48}Ti was subtracted from the ^{50}Ti data. There remains in the ^{50}Ti data a contamination by other Ti isotopes of much less than 10%. No attempt was made to correct for this.

The correction for the Ba isotopes was the most straightforward, since there were no apparent problems with the target thicknesses. The ^{136}Ba was first corrected for ^{138}Ba contamination, then the resulting angular distributions were used to correct the ^{134}Ba data.

For the measurement of ^{238}U scattering, it was necessary to place thin pieces of mylar in front of the detector to stop fission fragments from entering the detector. These fragments, from proton induced fission in the target, have masses of about 100 amu, and energies of over 100 MeV. In large numbers,they can seriously damage solid-state detectors (Orte80). The use of these mylar windows degraded our energy resolution in the detectors to greater than 100keV. Thus the first excited state in ^{238}U, (2^+ at 45 keV) was not generally resolved. Some excitation of the 4^+(148 keV) and 6^+(307 keV) states was seen. In addition to this physics problem, one of the detector holders was incorrectly installed in the scattering chamber, causing it to subtend a smaller solid angle, which varied through the measurement (apparently it was slightly loose). The data taken with this detector were unnecessary at most angles. In addition, the unresolved excited states cause these data not to be useful, especially at backward angles where

the 2^+ yield may be significant in comparison with the elastic scattering.

4.4.3 Uncertainties Assigned to the Data

The uncertainties normally reported with scattering data are of two types. Relative uncertainty is the precision with which points in an angular distribution can be remeasured, giving the same shape, but not necessarily the same absolute magnitudes. Normalization uncertainty is the accuracy with which the absolute magnitude of the data is determined. Each type of uncertainty is reported for these data. Our means of estimating them are discussed below.

Relative uncertainty arises from any factors in the calculation of the cross section or analyzing power which vary with angle. The principal factor normally considered is statistical uncertainty in the counting process. There are, however, other factors which can contribute. These include statistical uncertainties in the dead-time-correction estimate, which occur only in the pulser-based measurement used here, and less easily measured fluctuations, such as the apparent change in target thickness resulting from beam motion on a non-uniform target, or effects from fluctuations in the incident beam angle, an effect which is very small for this experiment (as discussed in Chapter 3). Other contributions to the relative uncertainty arise in the determination of the relative detector solid angles, or uncertainties in the angle of the target, each of which are discussed in Chap. 3. Furthermore, there will be uncertainty from the larger area of the beam spot on the non-uniform target when the target is rotated away from 0°.

The uncertainty from the counting statistics was 1% or less in the cross section; the corresponding uncertainty in the analyzing power was generally 0.01 or less. The dead-time correction uncertainties were always less than 1% and affected only the cross sections. Other uncertainties, resulting from imprecise determination of instrumental parameters, were kept to a minimum and were not included in this estimate of the uncertainties of the data.

The estimate of the cross-section uncertainties based on statistics

alone appears to be insufficient for the 16-MeV scattering. This conclusion is based on the overlapping measurements used to compute the relative normalizations of the different detector pairs. Even after these corrections had been applied (as discussed in Chapter 3), the average standard deviation of $\sigma(\theta)$ at the overlapping points was significantly larger than any of the statistically derived uncertainties. It was decided to use the mean of these standard deviations, determined mainly from forward-angle-scattering detector overlaps, as an estimate of the relative uncertainty of the cross section data arising from non-statistical effects. These values are listed in Table 4-2. They were incorporated by adding them in quadrature with the statistically derived uncertainties, as:

$$\left[\frac{\Delta\sigma}{\sigma}\right]^2 = \left[\frac{\Delta\sigma}{\sigma}\right]^2_{\text{statistical}} + \left[\frac{\Delta\sigma}{\sigma}\right]^2_{\text{estimated}} . \qquad 4\text{-}1$$

This procedure was chosen because the overlapping measurements used to estimate the uncertainties were at forward angles where the uncertainties from statistical effects were negligible compared to the estimated instrumental uncertainties. It is necessary to account at the more backward angles for statistical effects, which should enter independently of the instrumental effects.

A similar procedure was followed for the analyzing-power data. The mean used was the mean of the standard deviations, rather than the relative standard deviation, as for the cross-section data. For these data the corrections were generally smaller than the calculated statistical uncertainties. The analyzing-power uncertainty estimates are also listed in Table 4-2. These were combined with the statistical uncertainties as:

$$\Delta A_y^2 = \Delta A_y^2(\text{statistical}) + \Delta A_y^2(\text{estimated}). \qquad 4\text{-}2$$

There are several contributions to the normalization uncertainty for these data. The cross-section uncertainty is composed of uncertainty in $\Delta\Omega T$, uncertainty in the absolute angle, and uncertainty in the average efficiency of the beam current integration. As mentioned

Table 4-2

Estimated Uncertainties For Elastic Scattering Targets

Target Name	Estimated Relative Uncertainties		Target Thickness	Renormalizations		
				$\sigma(\theta)$		$A_y(\theta)$
	σ(%)	A_y	Uncertainties (%)	Expts.	OMP	OMP
^{40}Ca	2	0.006	1		*	*
^{48}Ti	2	0.010	2		1.07	0.88
^{50}Ti	2	0.007	-		1.03	0.95
^{54}Fe	1	0.006	5		1.04†	0.90†
^{56}Fe	2	0.009	2		1.01	0.97
^{58}Ni	3	0.013	1	1.06±0.05	1.01†	0.86†
^{60}Ni	1	0.009	2	1.02±0.04	1.01	0.93
^{63}Cu	2	0.013	4		1.01	0.97
^{65}Cu	2	0.008	6		1.00	1.00
^{76}Se	2	0.012	4		1.00	1.01
^{78}Se	2	0.012	3		1.00	1.00
^{80}Se	2	0.011	4		1.00	1.00
^{82}Se	2	0.012	2		1.01	1.02
^{90}Zr	1	0.009	3	0.99±0.01	1.00	1.03
^{116}Sn	2	0.007	1		1.01	1.00
^{120}Sn	1	0.005	1	1.05±0.02	1.01	1.00
^{124}Sn	1	0.005	1		1.02	1.01
^{134}Ba	1	0.006	1		1.00	1.00
^{136}Ba	2	0.005	2		1.02	1.00
^{138}Ba	1	0.005	2		1.00	1.01
^{208}Pb	2	0.004	1	0.92±0.04	0.90**	*
^{209}Bi	1	0.005	1		0.95**	*
^{238}U	2	0.008	4		1.02**	*

* The OMP estimate is not useful due to the poor quality of the fit
** The OMP estimate is based only on forward angle scattering($\theta \leq 55^\circ$)
† The fits to these datasets were of lower quality. The estimated normalization may be incorrect.

in Sect. 3.3, most of these quantities were checked and found to contribute only negligibly to the uncertainty in the measured cross section. The uncertainties in the measured target thickness, based on the standard deviations of multiple measurements, are shown in Table 4-2 and range from 1% to 6%. In view of the investigations of Chapter 3, only the uncertainty in the thickness should contribute significantly to the uncertainty in the normalization.

For the analyzing power measurements, the only significant uncertainty in the normalization is from the uncertainty in the beam-polarization determination. As discussed at length in Sect. 3.3, except for statistical uncertainties from the polarimeter peak sums (which were kept to less than 1%) the only uncertainty in the polarization was in the determination of the effective monitor analyzing power, about 4%.

There are two ways to investigate these uncertainties. The first is to compare with other measurements of elastic scattering at 16 MeV. This was done for the cross-section data measured on ^{58,60}Ni, ^{90}Zr, ^{120}Sn, and ^{208}Pb (Mako72). The measurements of the cross section with which we compare have a stated accuracy of about 2%. The resulting average ratio of the TUNL measurements to these from the literature are shown in Table 4-2. The uncertainties are standard deviations of the mean. From these numbers, it is clear that all the TUNL data are within 8% of being consistent with the cross-section data of Makofske, et. al, and are usually within 5%. The disagreement is usually larger than the size of the TUNL target thickness uncertainty. Including the 2% uncertainty in Makofske's work and the standard deviations of the comparisons (see Table 4-2), the TUNL cross-secction data are not inconsistent with the earlier measurements. The uncertainties of these comparisons are large, as shown in Table 4-2.

No such comparison was made for the analyzing-power data, because we were unable to locate any measurements with which to compare.

Another technique for checking the reliability of the normalization is the renormalization estimated from comparison of the data with calculations of the optical model. The optical-model prediction of the

cross section is sensitive to the normalization of the data. For small renormalizations, studies with synthetic data (see Sect. 6.3), show that this normalization factor can be estimated successfully in optical-model calculations. This technique has its limitations, as shown in Sect. 6.3 and 6.4, but serves as a check on the normalizations used in this work. Estimates of the renormalizations by optical-model fits to each of the target data sets are shown in Table 4-2 (under OMP renormalizations) and can be seen to be generally small, on the order of 1%.

4.5 Summary of 16-MeV Proton Scattering

The TUNL proton elastic scattering data have been discussed and shown in Fig. 4-1 to 4-4. Some of these data have problems with nuclear structure effects in the scattering, as well as technical problems with the measurements. Most of the technical problems have been corrected; the data with nuclear physics difficulties were eliminated from the database for the search (which is summarized in Table 6-2).

We have estimated both relative and absolute uncertainties in our data. Our determination of the relative uncertainties includes an estimate of instrumental and statistical effects; these are the uncertainties reported with each data point. The sufficiency of this estimate is discussed further in Sect. 6.4.

The estimation of normalization uncertainties is more difficult. We have seen that the uncertainties in the cross sections from the target-thickness determination range from 1% to 6%, and are not always consistent with the comparison to other data; those comparisons show differences of 1% to 8%. The nature of these estimated uncertainties was such that we were unable to identify the factors which distinguished the small uncertainty data from the large uncertainty data nor to understand the variation in agreement with previous measurements. To assure that unreasonable accuracy was not assumed for the data, an uncertainty of 5% was uniformly assigned to the normalization of the cross-section data.

For the analyzing power data, the individual optical-model fits

provide the only comparison with which to check the uncertainties in the normalization. The renormalizations found from this method are within the calculated uncertainty of about 4% in the polarization monitor analyzing power, which is the only significant factor in the normalization of the analyzing powers.

V. Summary of Other Data in the Optical-Model Parameterization

5.1 Introduction

As discussed in Chap. 2, an analysis of this scope requires a considerable database, composed of elastic-scattering data from a wide variety of isotopes, at many energies, and with both neutrons and protons. It is beyond consideration that any one experimenter or even any one laboratory be equipped to perform all these measurements. To augment our ($\vec{p}$,p) scattering we turned to other experimental groups working at several facilities. Much of the data we are using has been published in the literature; those works will be cited herein. Some data have been provided prior to publication, particularly the Eindhoven data set. We gratefully acknowledge Dr. P.J. Van Hall for providing the Eindhoven data and Dr. H. Sakaguchi for providing the 65 MeV data.

The proton data used in this analysis come from three sources outside TUNL. These facilities are the Phillips Cyclotron Laboratory at Eindhoven, Netherlands (17 to 25 MeV), the Oak Ridge National Laboratory (ORNL) (40 MeV), and the Research Center for Nuclear Physics (RCNP) of Osaka, Japan (65 MeV). All the proton data were measured with polarized beams, and in most cases, the cross-section data were measured simultaneously with the analyzing power data.

The neutron data come from two facilities, the TUNL neutron time of flight facility and the Ohio University Accelerator Laboratory (OUAL). The former facility is capable of measuring neutron analyzing power data; the latter measures only cross-section data.

This chapter will briefly describe the above sources of data and the references available concerning the data and their source. In

addition, figures of the data will be presented, showing calculations from the final parameterization.

5.2 Data from polarized neutron scattering (TUNL)

The polarized neutron scattering data were obtained from the neutron time of flight facility at Triangle Universities Nuclear Laboratory, Duke University, Durham, NC (Floy81, Guss82, Hono84). This facility is unique in its capability for measuring polarized neutron scattering in the 10 to 17 MeV energy range. The techniques used to measure elastic and inelastic scattering at this facility have been documented in the literature, especially the data corrections needed to correct for the large sample size required with the small incident flux (ElKa82, Guss85).

The techniques and instrumentation at this facility are continually developing, so any summary of the experimental conditions is at best an average over time. The average conditions of the measurements were (Guss85, Floy83):

Beam energy spread - (beam energies of 10 to 17 MeV)
- Cross section measurements: 0.1 MeV
- Analyzing power measurements: 0.3 to 0.5 MeV

Relative uncertainties -
- Cross sections: 5% to 20%
- Analyzing powers: 0.01 to 0.07

Normalization uncertainties -
- Cross sections: 5%
- Analyzing powers: 2.5%

Angle accuracy: 0.3°

Targets: Isotopic, enriched to $\geq 97\%$

In order to fit the cross-section and analyzing-power data into the small storage space available in the database system on the VAX, the analyzing power data were interpolated, where possible, to the angle of the nearest cross section measurement. This interpolation, made using cubic splines, was performed only where the angle shift was smaller

than 2° and the interpolation was visibly reasonable. In cases where the shift required was larger than 2°, the data point was left in its original form.

The data are listed in Table 5-1, along with the incident neutron energy and references to the data collection and analysis. The data are shown in Figs. 5-1, 5-2, and 5-3.

Table 5-1

TUNL Neutron Time-of-Flight Data

Target	E_{inc} (MeV)	Notes	References
^{40}Ca	10,14,17		Hono84
^{54}Fe	10,14		Floy81, Floy83
^{58}Ni	10,14		Guss82, Guss85
^{60}Ni	10,14	No A_y data	Guss82, Guss85
^{65}Cu	10,14		Floy81, Floy83
^{116}Sn	10,14		Guss82, Dela83a
^{120}Sn	10,14,17	(No A_y data with 17 MeV)	Guss82
^{208}Pb	10,14,17	(No A_y data with 17 MeV)	Floy81, Dela83b

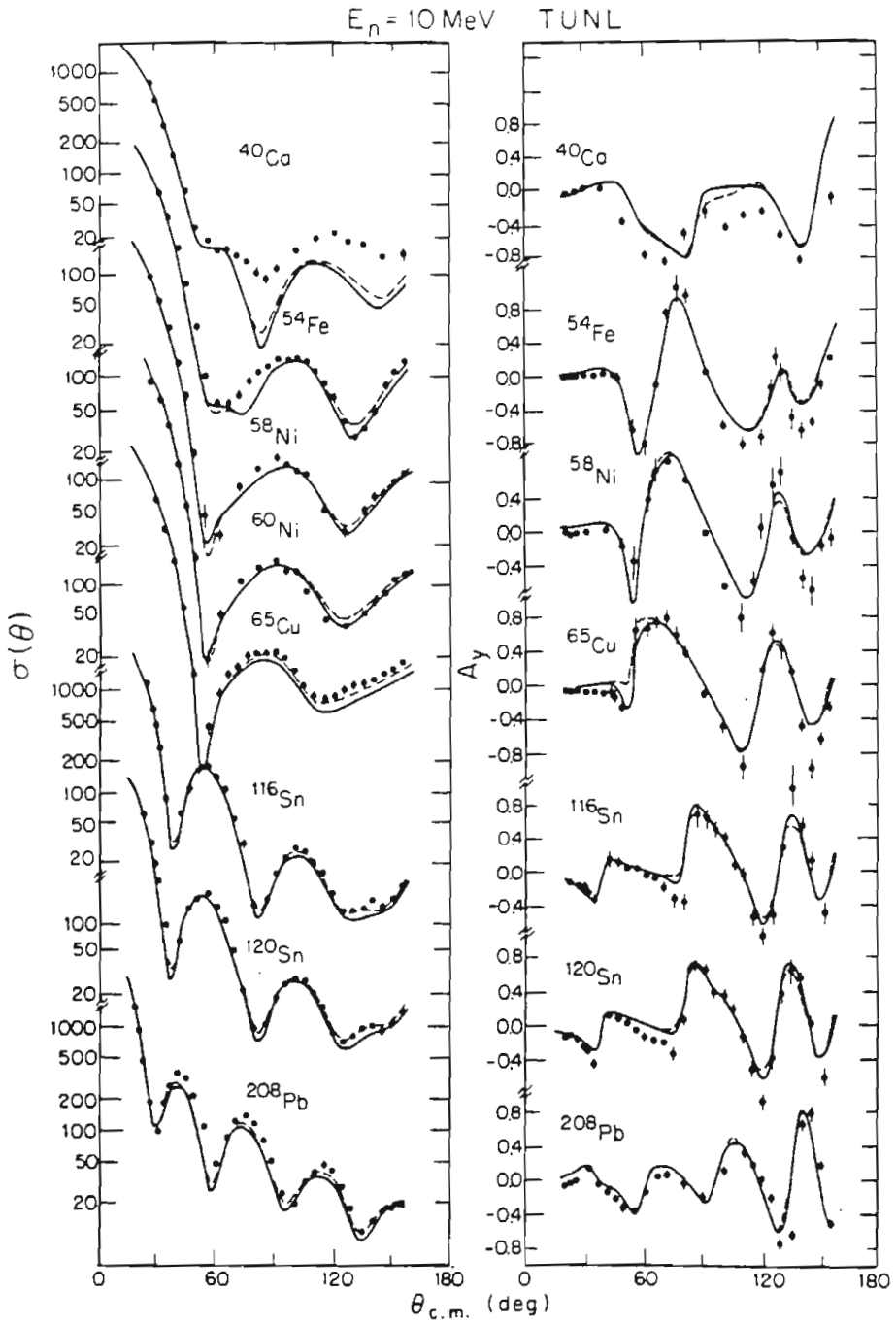

Fig. 5-1: TUNL cross section and analyzing power data for ($\vec{n}$,n) scattering at 10 MeV. The curves are calculated with the best-fit optical potential as described in Chap. 7.

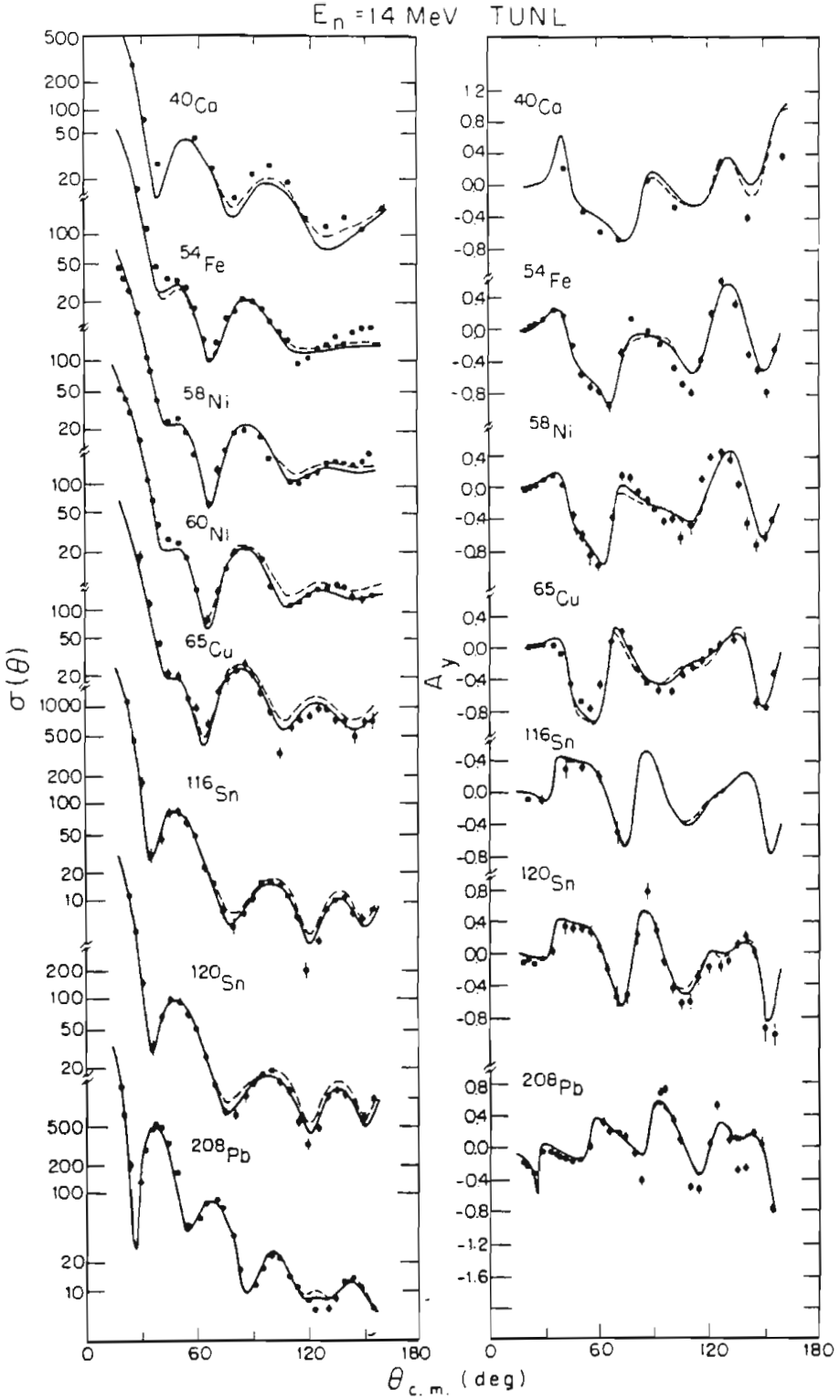

Fig. 5-2: TUNL cross section and analyzing power data for ($\vec{n}$,n) scattering at 14 MeV. The curves are calculated with the best-fit optical potential as described in Chap. 7.

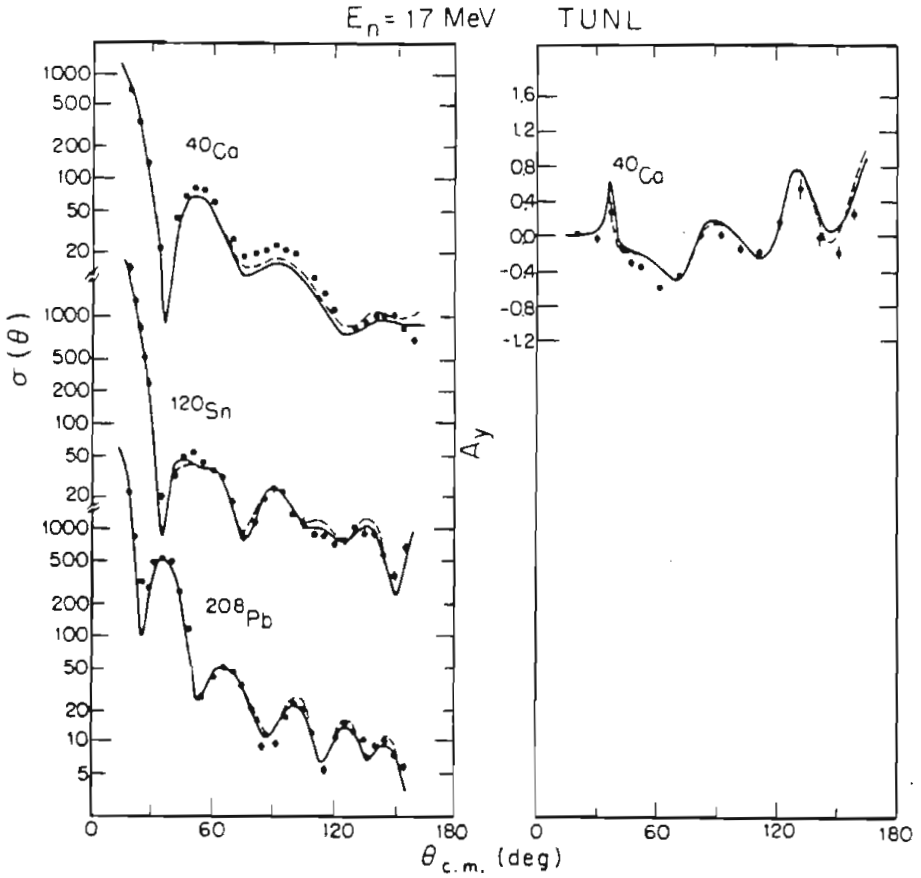

Fig. 5-3: TUNL cross section and analyzing power data for ($\vec{n}$,n) scattering at 17 MeV. The curves are calculated with the best-fit optical potential as described in Chap. 7.

5.3 Unpolarized neutron scattering from 11 to 26 MeV (OUAL)

The unpolarized neutron elastic scattering data used here were measured at the Ohio University Accelerator Laboratory, Athens, Ohio. These data were obtained from the National Nuclear Data Center at Brookhaven National Laboratory, Upton, NY. The energy range of these data is from 10 MeV to 26 MeV. These data have been published previously and some have been used in another global optical analysis (Rapa82).

The average conditions for these measurements were (as summarized in the references in Table 5-2):

Beam energy accuracy: 0.1 MeV (at 11.0 MeV)

Energy resolution: 2%

Relative uncertainties: 3 to 5% (more in some data)

Normalization uncertainies: 5%

Angle accuracy: 0.3°

Targets: Isotopic (usually)

The data sets and their sources are listed in Table 5-2. The data are shown in Figs. 5-4 to 5-7.

Table 5-2

Ohio University Neutron Elastic Scattering Data

Target	E_{inc}(MeV)	References
^{40}Ca	11	Bain77
^{51}V	11	Ferr77
^{55}Mn	11	Ferr77
^{54}Fe	11,20,22,24,26	Mell83
^{56}Fe	11,20,26	Mell83
^{59}Co	11	Ferr77
^{88}Sr	11	Bain78
^{89}Y	11	Yimi82
^{90}Zr	11	Bain78
^{93}Nb	11	Ferr77
^{92}Mo	11,20,26	Rapa79a
^{96}Mo	11,20,26	Rapa79a
^{98}Mo	11,20,26	Rapa79a
^{100}Mo	11,20,26	Rapa79a
^{116}Sn	11,24	Rapa80a
^{118}Sn	11,24	Rapa80a

Table 5-2(con't)

Target	E_{inc}(MeV)	Reference
^{120}Sn	11	Rapa80a
^{122}Sn	11	Rapa80a
^{124}Sn	11, 24	Rapa80a
^{165}Ho	11	Ferr77
^{206}Pb	11	Ferr77
^{208}Pb	11,20,26	Rapa78
^{209}Bi	11	Ferr77

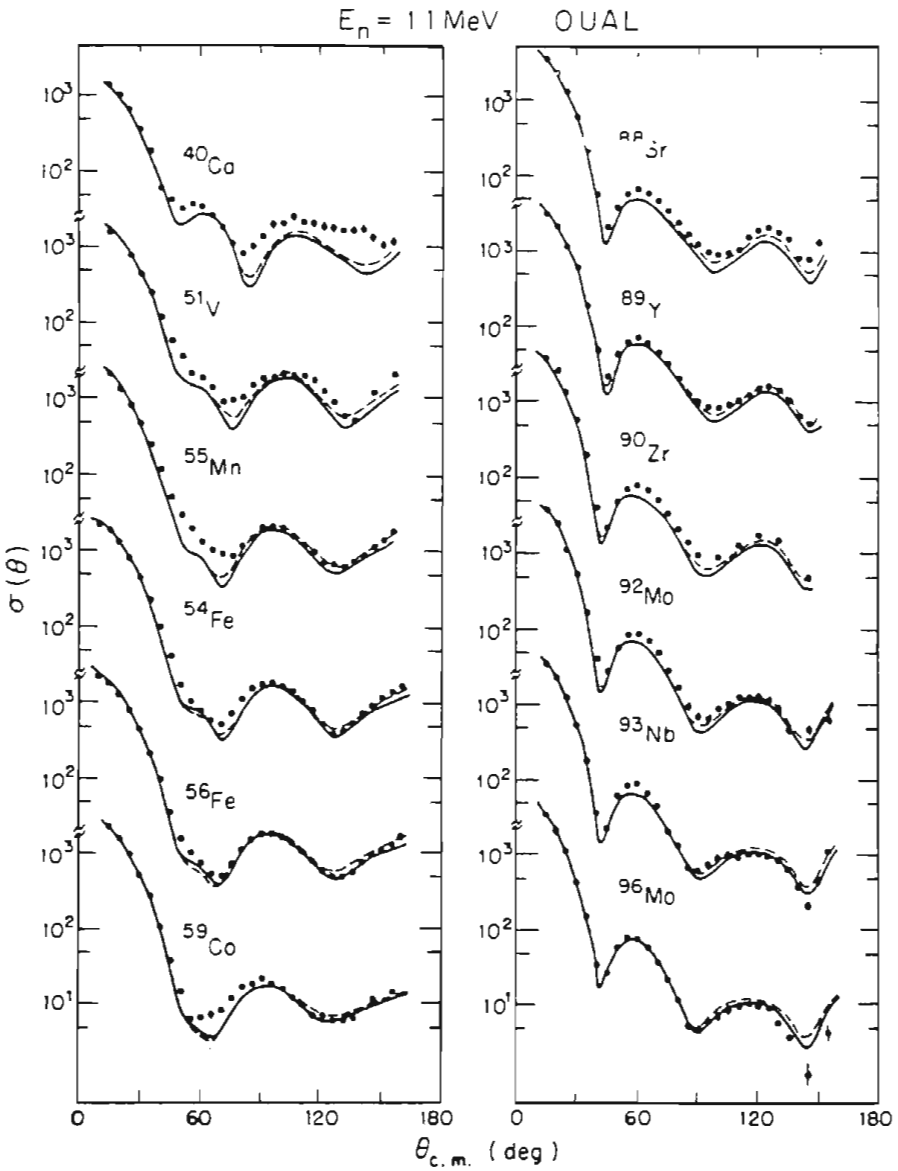

Fig. 5-4: OUAL cross section data for (n,n) scattering at 11 MeV. The curves shown are calculated with the best-fit global optical model, as described in Chap. 7.

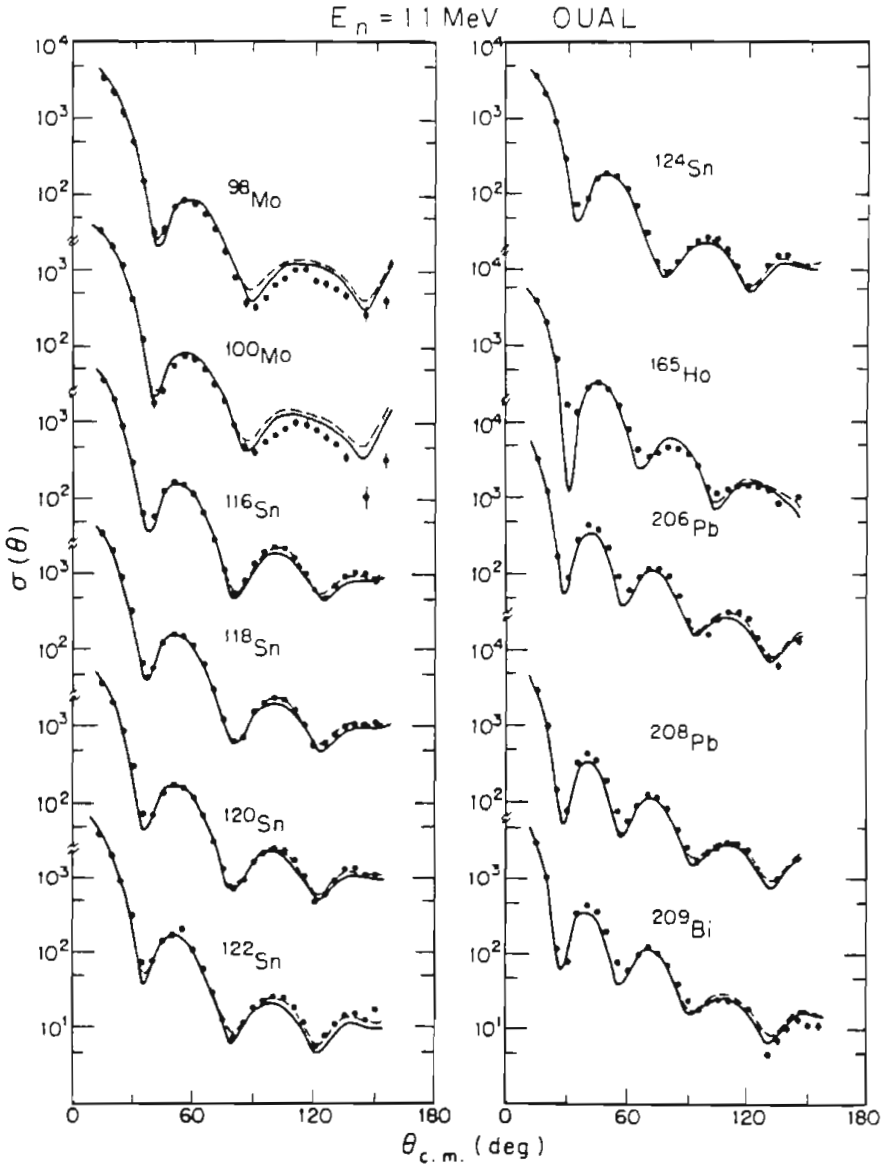

Fig. 5-5: OUAL cross section data for (n,n) scattering at 11 MeV. The curves shown are calculated with the best-fit global optical model, as described in Chap. 7.

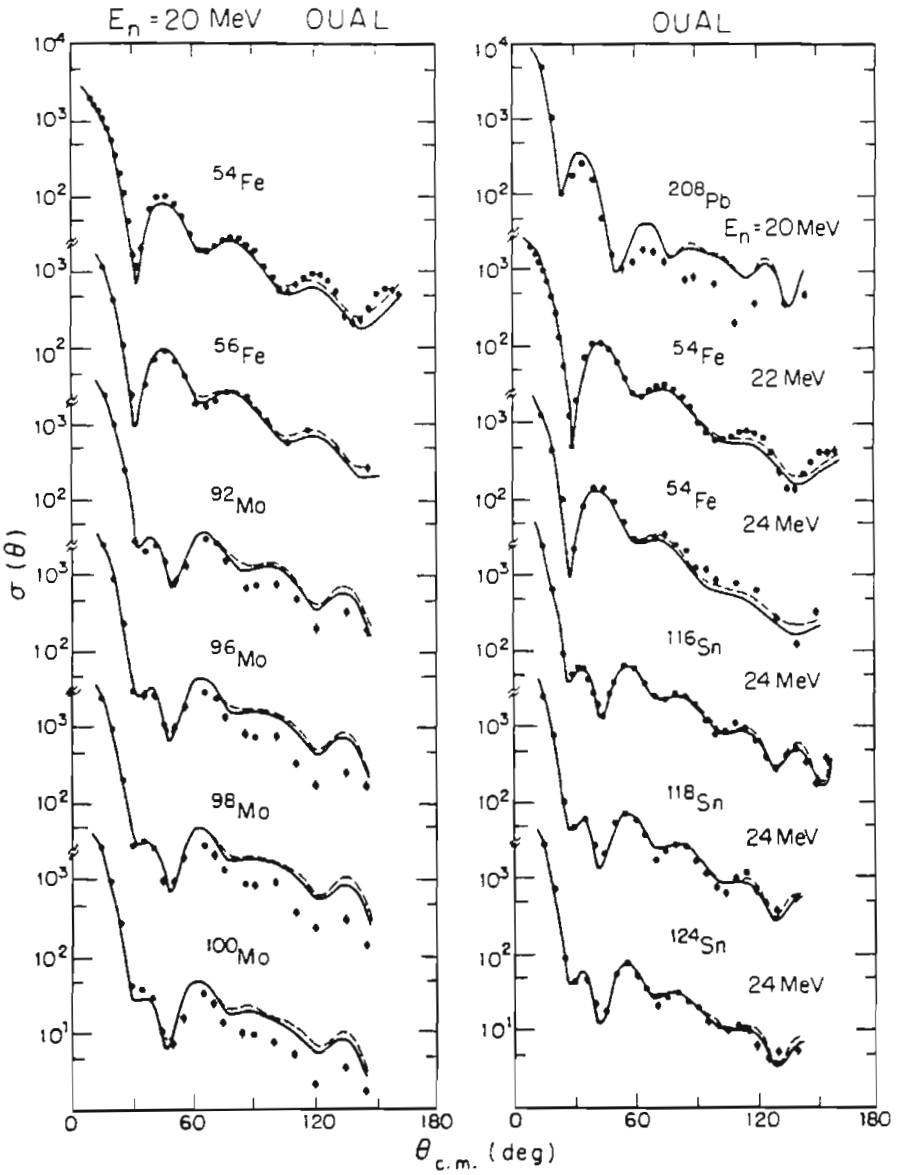

Fig. 5-6: OUAL cross section data for (n,n) scattering at 20 and 24 MeV. The curves shown are calculated with the best-fit global optical model, as described in Chap. 7.

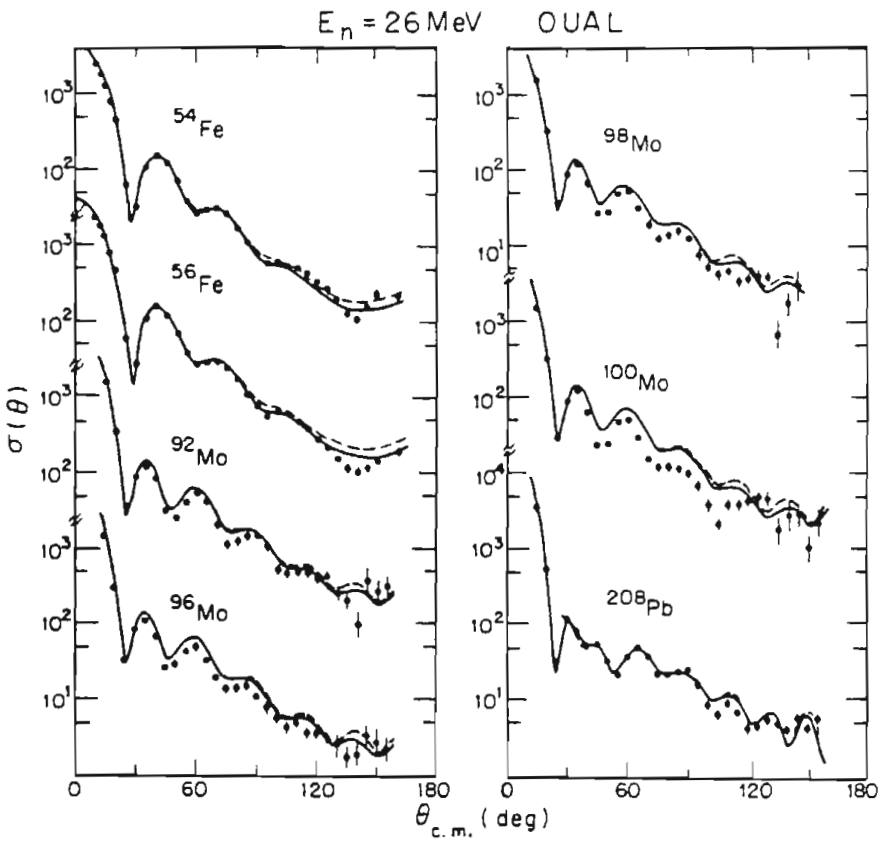

Fig. 5-7: OUAL cross section data for (n,n) scattering at 26 MeV. The curves shown are calculated with the best-fit global optical model, as described in Chap. 7.

5.4 Data for 17 to 25 MeV proton scattering (Eindhoven)

The data for 17 to 25 MeV ($\vec{p}$,p) scattering were obtained from the extensive elastic and inelastic scattering data set of the Eindhoven University of Technology, Eindhoven, the Netherlands (Hall85). These data were measured with a polarized proton beam, and consist of simultaneously measured angular distributions of cross section and analyzing power. The facilities and procedures used in measuring these data are described in published literature (Hall77, Mels82) and in unpublished dissertations (Wass82, Mels78).

The conditions for the measurements were (Mels78):

Energy accuracy: ±0.1 MeV

Average relative uncertainty -

Cross section: 2 to 3%

Analyzing Power: 0.01

Average normalization uncertainty -

Cross section: <10%

Analyzing Power: 5%

Angular acceptance: $\pm 1^{\circ}$ to $\pm 2^{\circ}$

Angle accuracy: $\pm 0.1^{\circ}$

Targets: Isotopic, enriched to ≥97%

The cross section data were normalized by comparison with optical model calculations (Wass82). This technique was estimated (Wass82) to be accurate to 5%. Some of the data we received were un-normalized or only approximately normalized, which required us to estimate the normalization for those data using optical model calculations. It is not clear to us that this procedure is sound for all datasets. We fitted the data for ^{110}Pd and several Sm isotopes, using data renormalized by factors which differed from 1 by 10% to 20%, in an attempt to find the correct normalization factor. The fits with the different factors differed significantly in the minimum value of the least squares function. The optical model programs, however, consistently estimated a renormalization factor of 1, regardless of the normalization of the data used in the calculations. Thus, for these nuclei, the estimate of the normalization from the optical model program was accurate to only

about 20%. The normalization estimates were given by formulas as in (Wass82, East73). The full technique of Wass82 is to recalculate the normalization of the data after each iteration of the search routine. This is not possible for us, given our search techniques, for reasons described in Sect. 6.2.2. The only means we found to estimate the renormalization was to make individual fits to the data, then to estimate the correct normalization from the forward angle cross section data. This was insufficiently precise, for the case of the ^{110}Pd and the cases of ^{152,154}Sm, and so we excluded these data from the search.

The Eindhoven data sets used are listed in Table 5-3, and shown in the Figs. 5-8 to 5-16.

Table 5-3

Proton Data Sets from Eindhoven

Target	E_p	UnNormalized	Reference
^{54}Fe	17.2,20.4,24.6		Mels78
^{56}Fe	17.2,20.4,24.6		Mels78
^{58}Ni	20.4,24.6,27.2		Mels78
^{60}Ni	20.4,24.6		Mels78
^{62}Ni	20.4,24.6		Mels78
^{64}Ni	20.4		Wass82
^{64}Zn	20.4		
^{66}Zn	20.4		
^{68}Zn	20.4		
^{70}Zn	20.4		
^{72}Ge	22.3		
^{74}Ge	22.0		
^{78}Se	22.0		
^{80}Se	22.3		
^{86}Sr	24.6		Wass82
^{88}Sr	24.6		Wass82
^{110}Pd	20.4	Yes †	
^{106}Cd	22.3	Yes	
^{108}Cd	22.3	Yes	
^{110}Cd	20.4,22.3	22.3	Wass82
^{112}Cd	20.4,22.3	"	Wass82
^{114}Cd	20.4,22.3	"	Wass82
^{116}Cd	22.3		
^{116}Sn	20.4		Wass82
^{118}Sn	20.4		Wass82
^{120}Sn	20.4,24.6		Wass82

Table 5-3 (con't)

Target	E_p	UnNormalized	Reference
^{122}Sn	20.4		Wass82
^{124}Sn	20.4		Wass82
^{142}Nd	17.2	Yes	
^{148}Sm	20.4	Yes	
^{150}Sm	20.4		
^{152}Sm	20.4	Yes †	
^{154}Sm	20.4	Yes †	

† These data were not used in the global search.

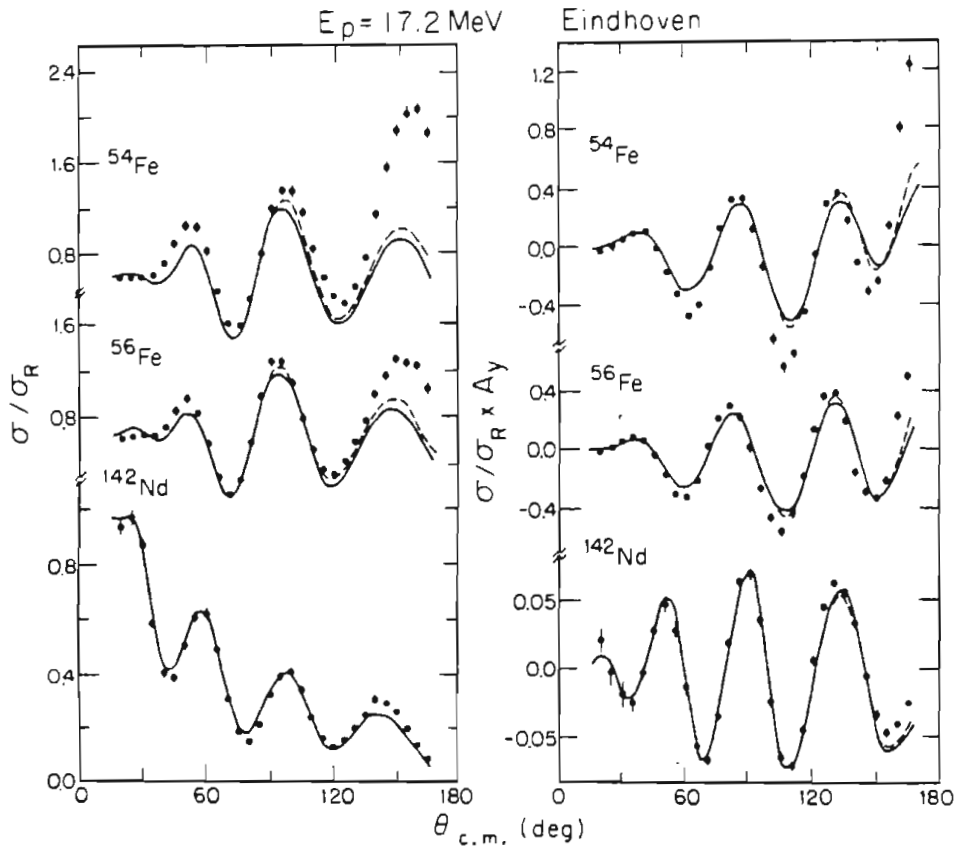

Fig. 5-8: Data for 17.2 MeV ($\vec{p}$,p) elastic scattering from Eindhoven. The curves shown are calculated with the best-fit global optical model, as described in Chap. 7.

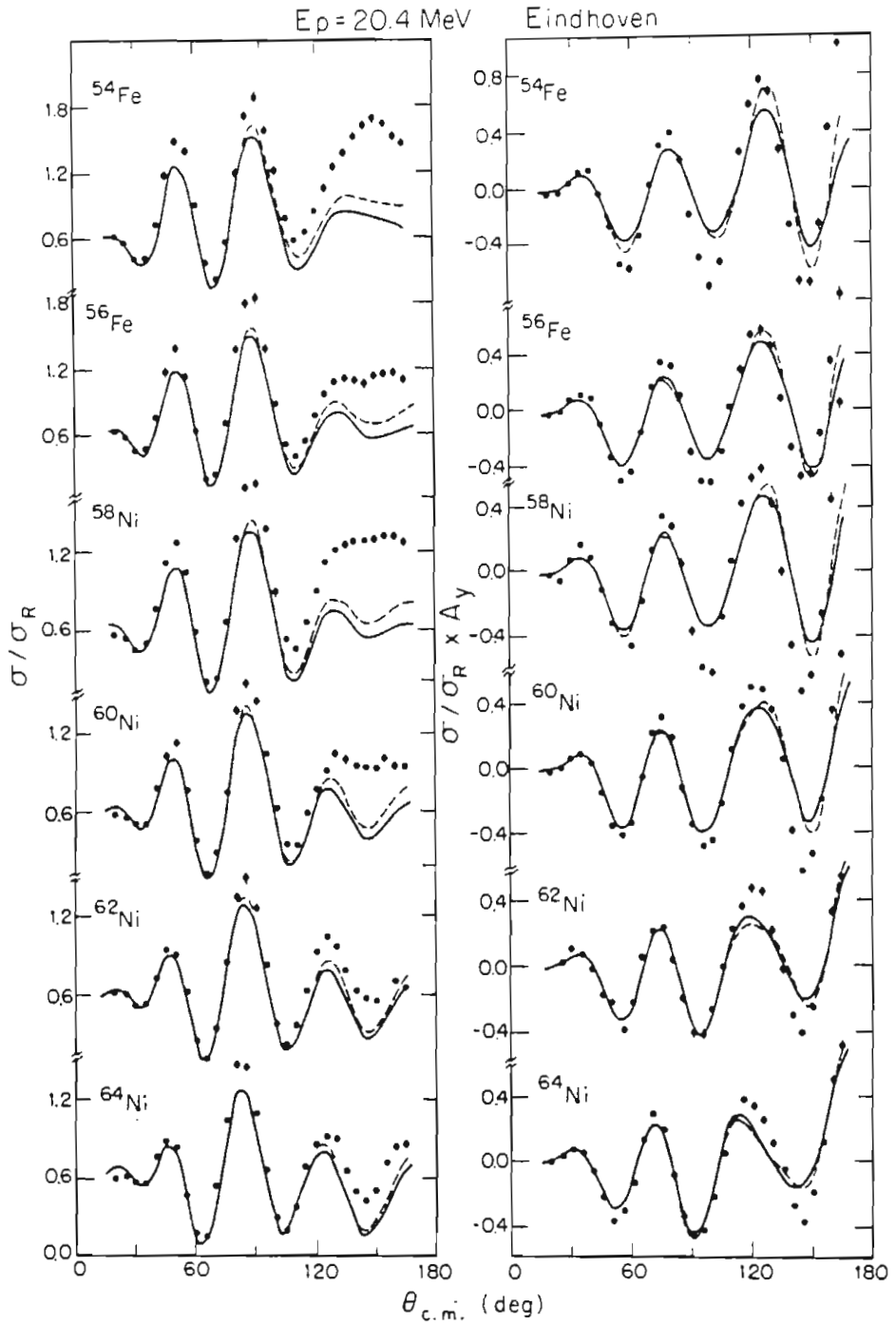

Fig. 5-9: Data for 20.4 MeV ($\vec{p}$,p) elastic scattering from Eindhoven. The curves shown are calculated with the best-fit global optical model, as described in Chap. 7.

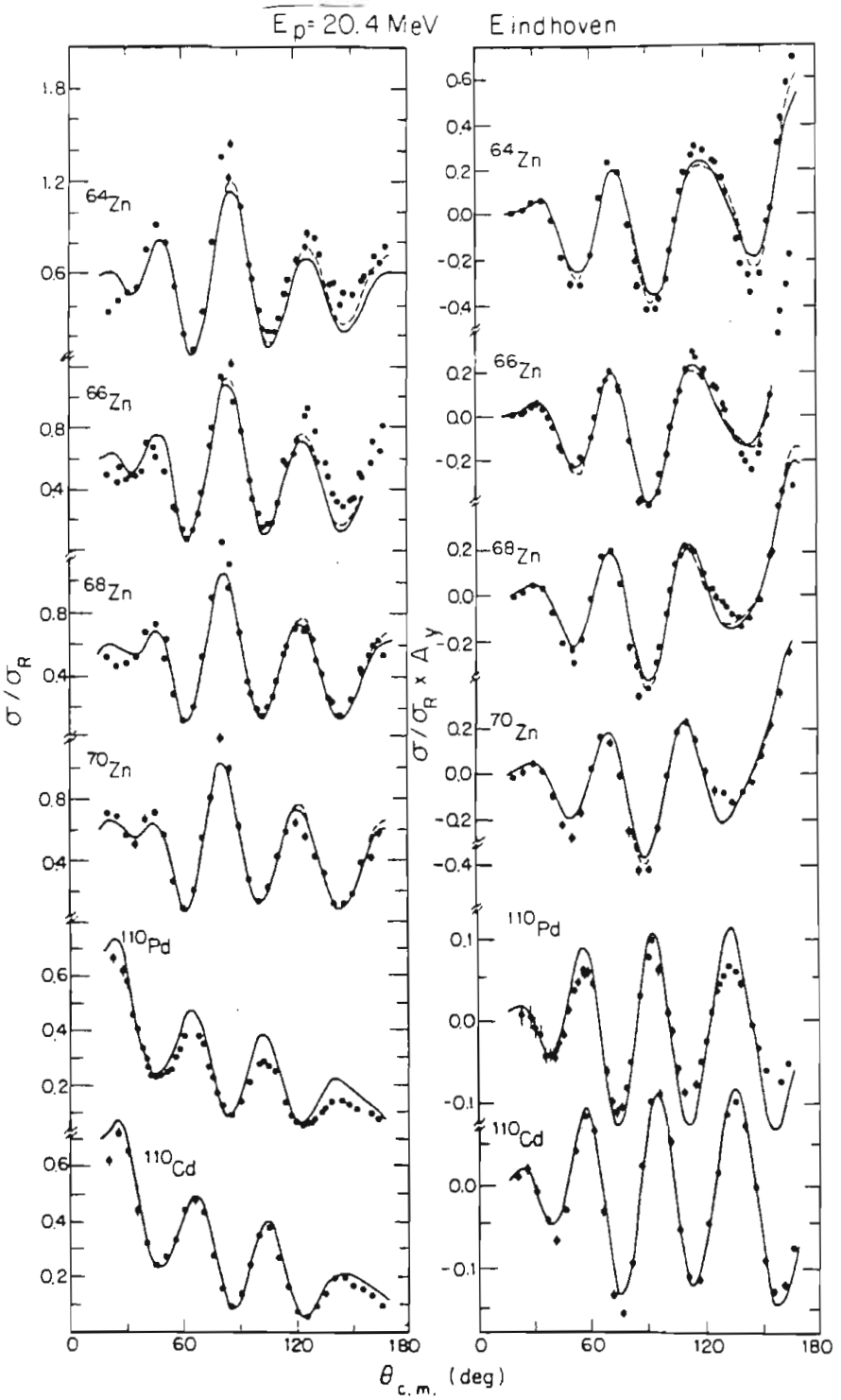

Fig. 5-10: Data for 20.4 MeV ($\vec{p}$,p) scattering from Eindhoven. The curves shown are calculated with the best-fit global optical model, as described in Chap. 7.

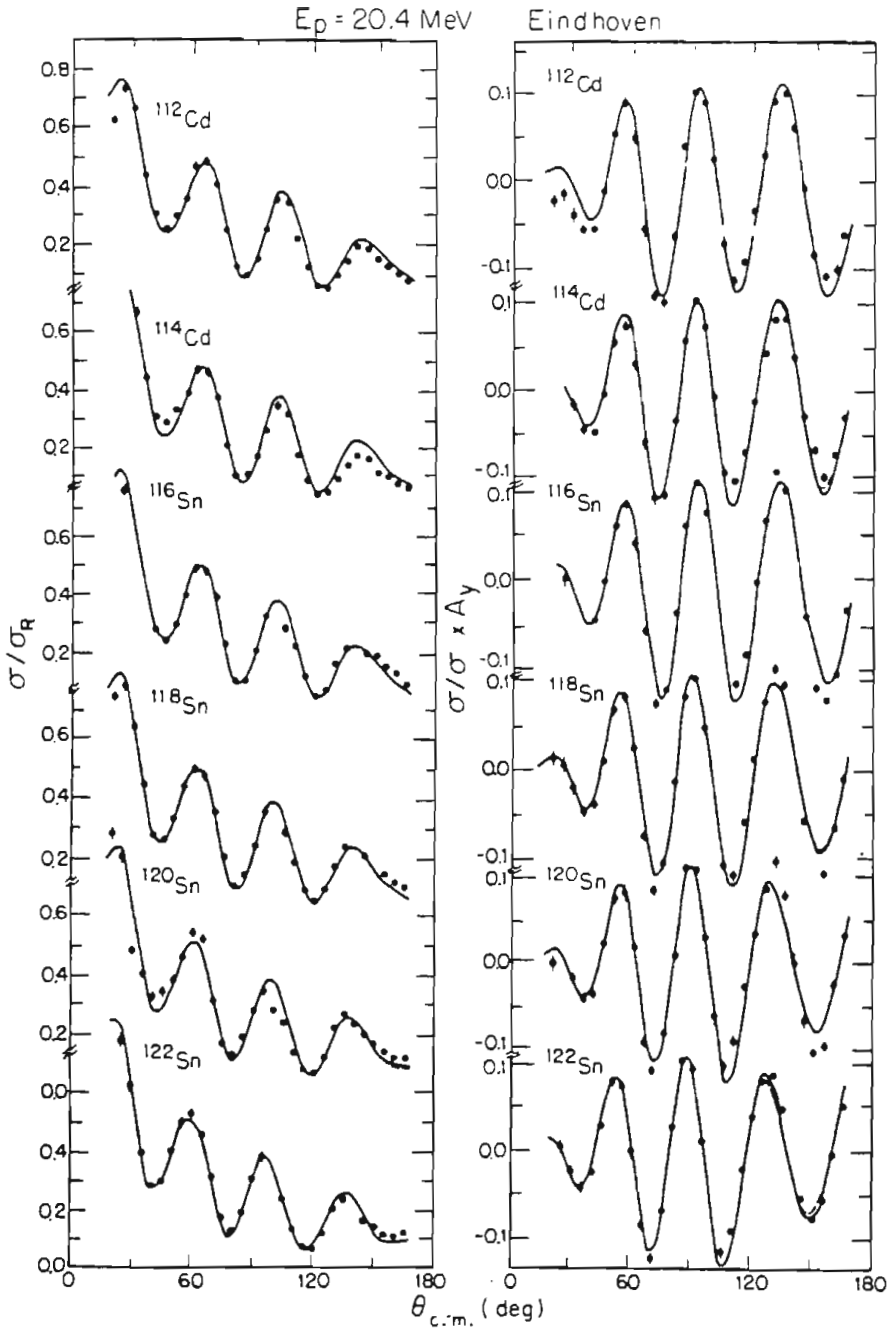

Fig. 5-11: Data for 20.4 MeV ($\vec{p}$,p) scattering from Eindhoven. The curves shown are calculated with the best-fit global optical model, as described in Chap. 7.

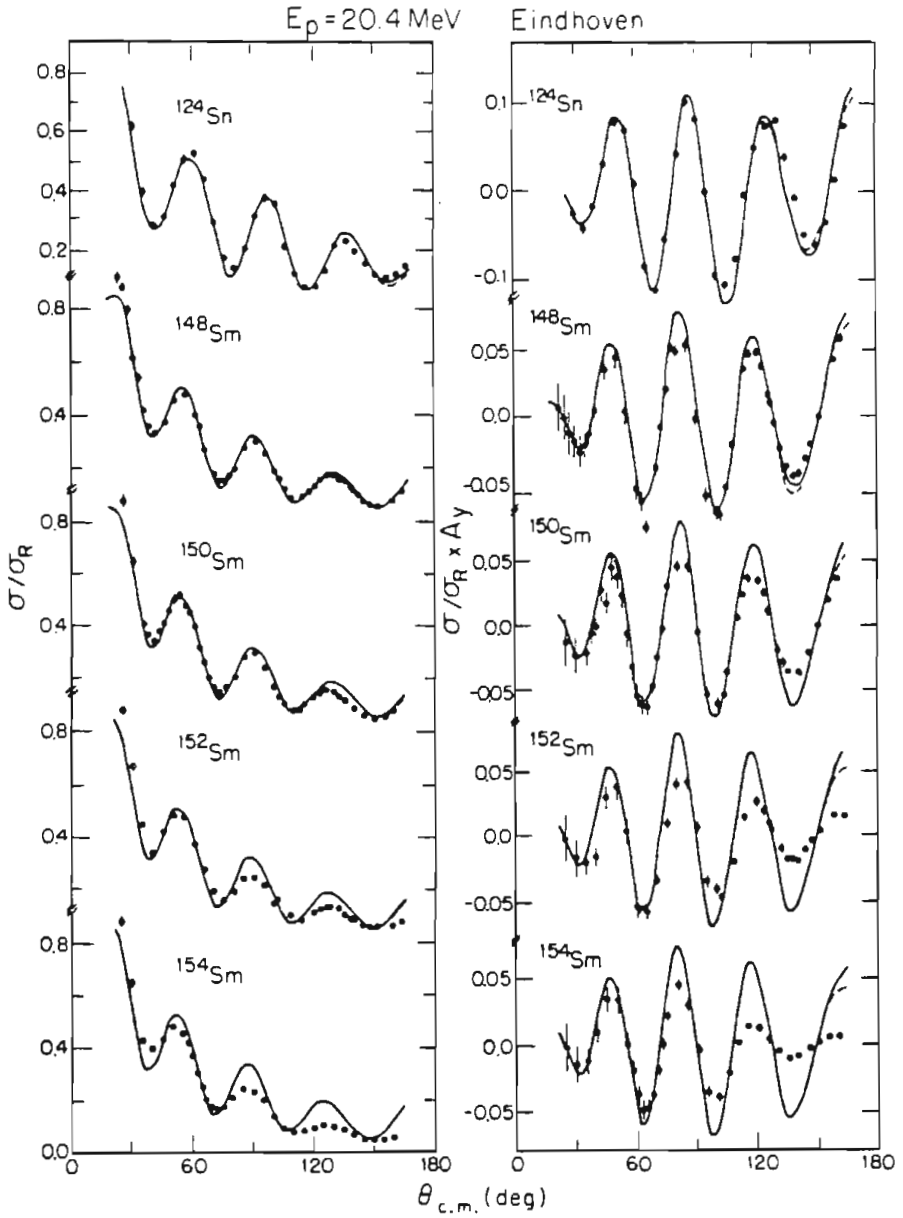

Fig. 5-12: Data for 20.4 MeV ($\vec{p}$,p) scattering from Eindhoven. The curves shown are calculated with the best-fit global optical model, as described in Chap. 7.

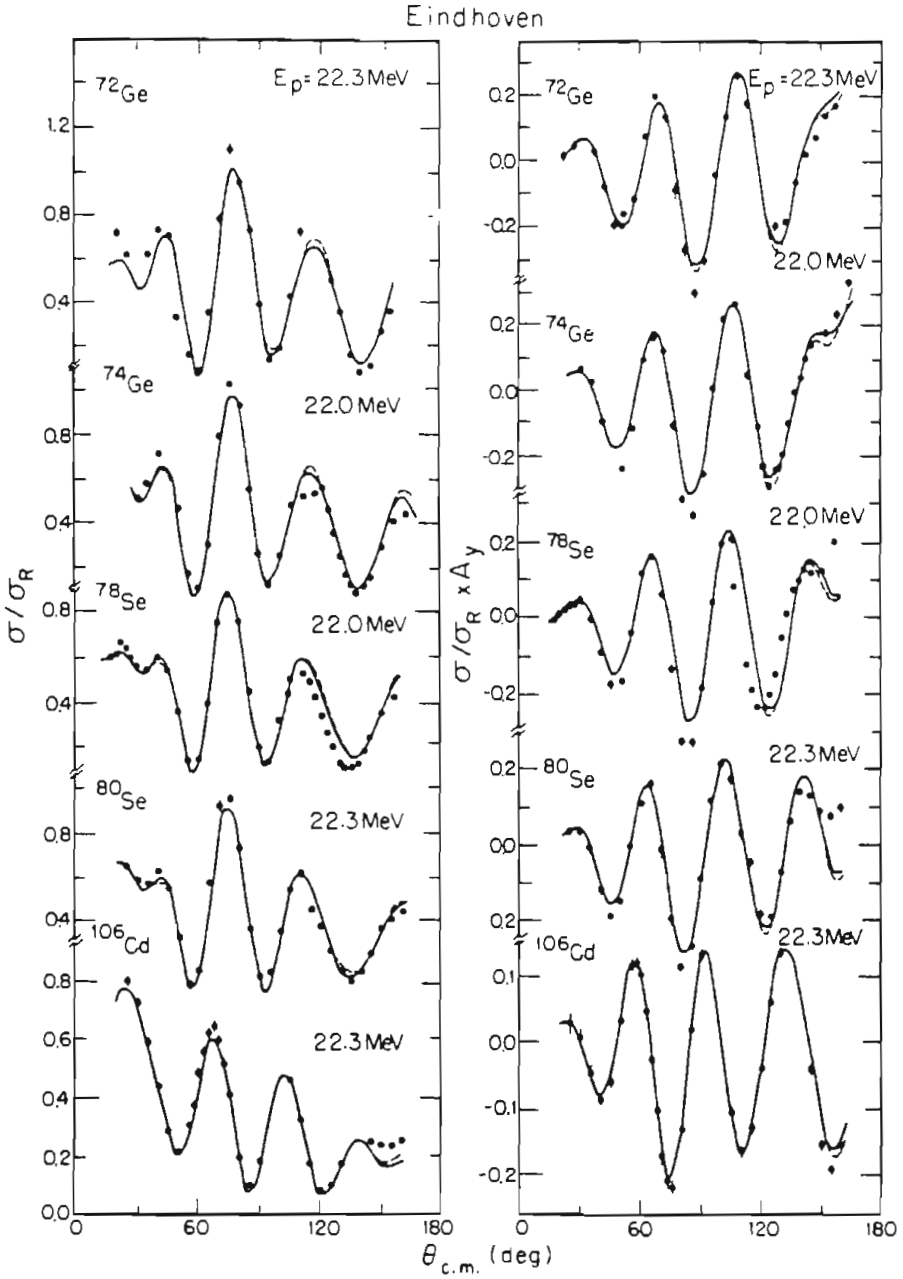

Fig. 5-13: Data for 22.3 MeV ($\vec{p}$,p) scattering from Eindhoven. The curves shown are calculated with the best-fit global optical model, as described in Chap. 7.

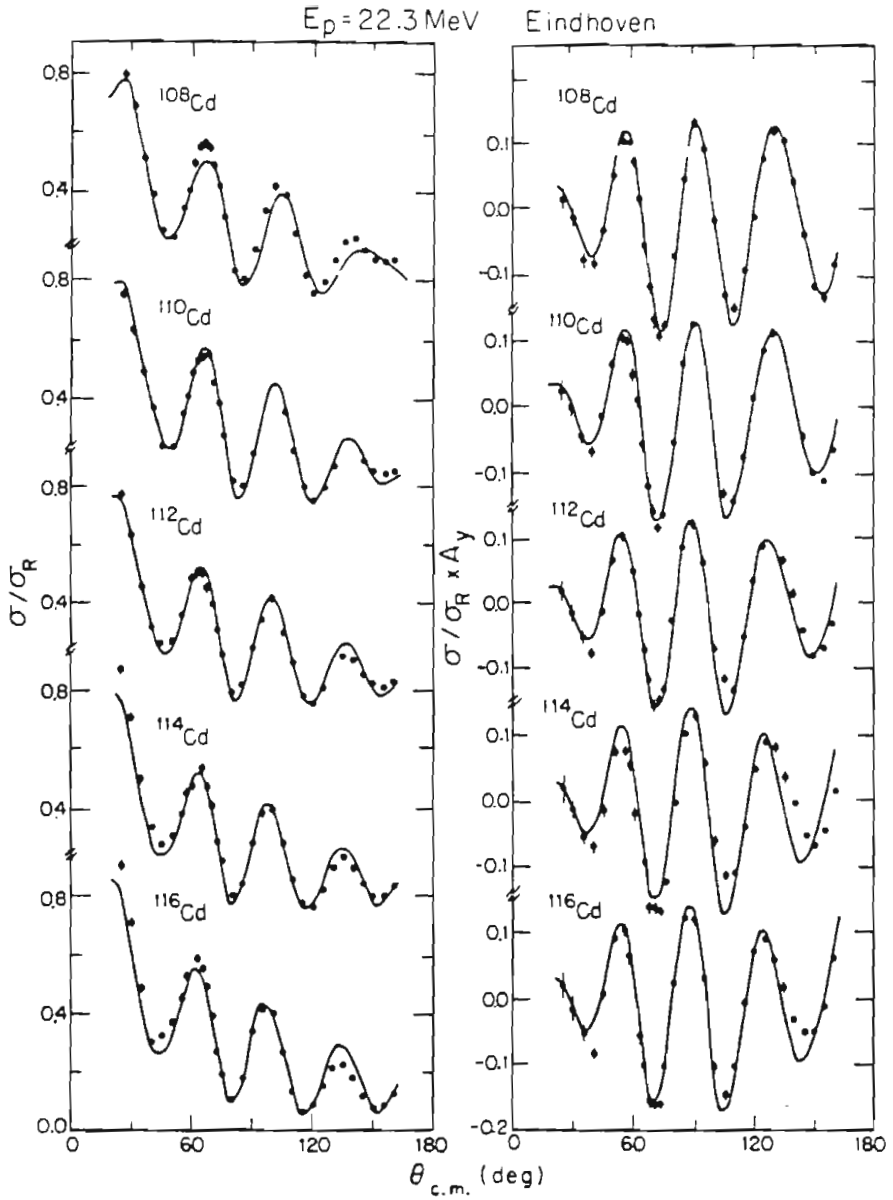

Fig. 5-14: Data for 22.3 MeV ($\vec{p}$,p) scattering from Eindhoven. The curves shown are calculated with the best-fit global optical model, as described in Chap. 7.

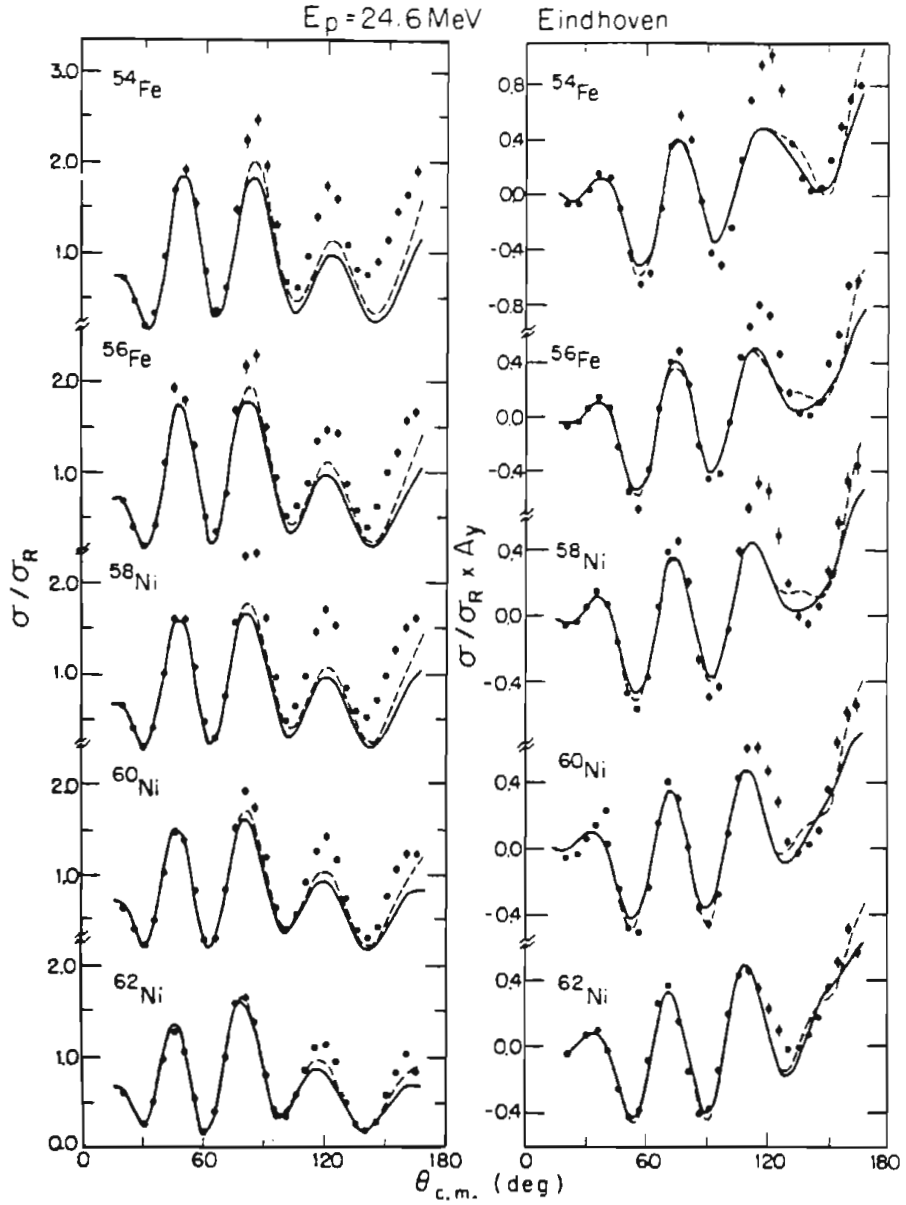

Fig. 5-15: Data for 24.6 MeV ($\vec{p}$,p) scattering from Eindhoven. The curves shown are calculated with the best-fit global optical model, as described in Chap. 7.

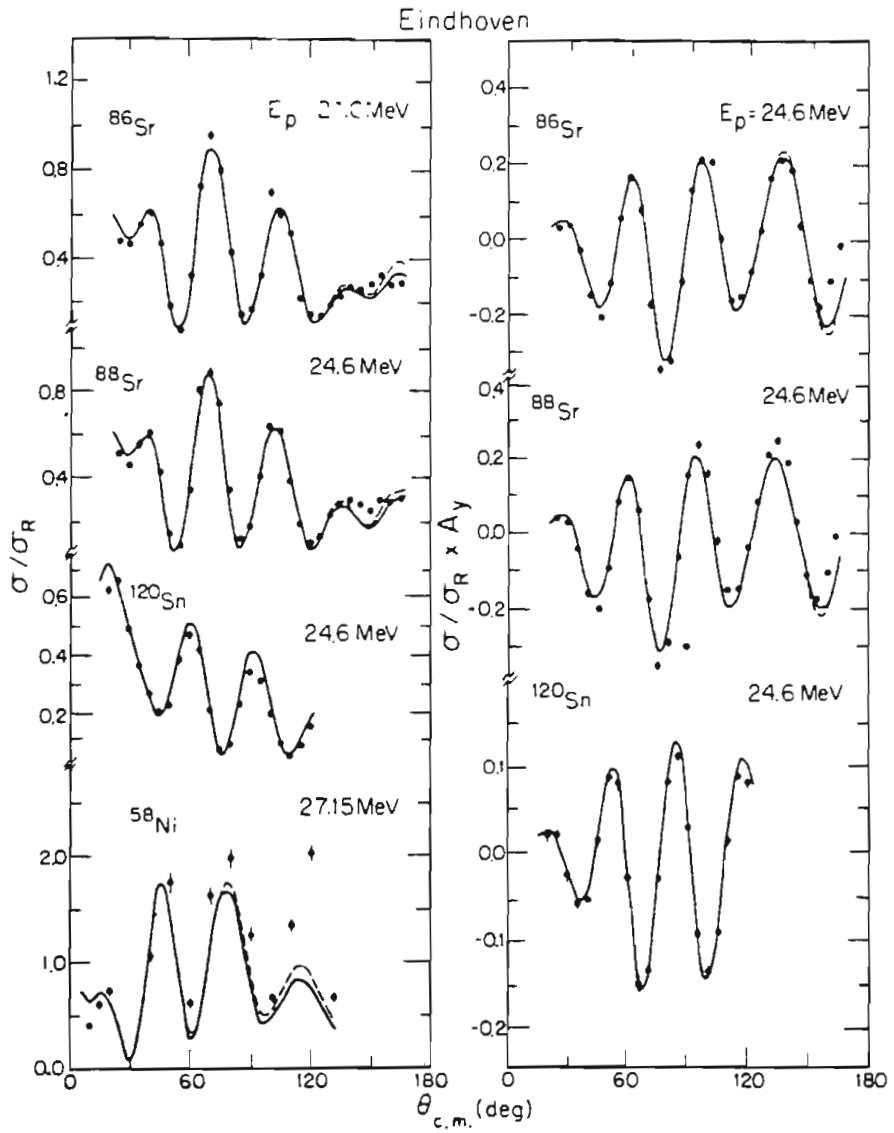

Fig. 5-16: Data for 24.6 and 27.15 MeV (p,p) scattering from Eindhoven. The curves shown are calculated with the best-fit global optical model, as described in Chap. 7.

5.5 Data from 40 MeV proton scattering (ORNL)

The data for 40 MeV proton scattering were obtained from Oak Ridge National Laboratory, Oak Ridge, TN (Fric67 and references therein). These data are composed of 6 angular distributions of cross section and analyzing power measured at E_p of 40 MeV. The polarized proton beam was produced by scattering an unpolarized alpha beam (E_α=81 MeV) from an H_2 gas target, using the recoil protons at at an angle of 25.5° (P_{beam} = 0.89), or by scattering an unpolarized proton beam (E_p=41 MeV) from a ^{40}Ca target at an angle of 25° (P_{beam} = 27.4%). The advantage of the Ca polarizer was the higher P^2I efficiency and the convenience of the solid target, which provided a beam with better resolution. Most measurements were made with the Ca polarizer. In each case the incident energy of the unpolarized beam was adjusted to produce a beam of 40 MeV polarized protons at the scattering chamber. The cross-section and analyzing-power data were measured in separate experiments because of the low intensity of the polarized beam. The cross-section measurements were made in steps of 2.5°, while the analyzing powers were measured with left and right detector pairs in angle steps of about 5° (Blum66).

The conditions of the measurement were (Fric67):

Beam energy: 40±0.4 MeV

Energy spread: 0.6 MeV (Ca(p,p) beam)

Relative uncertainty -

Cross section: 1 to 10%

Analyzing power: 0.1 to 0.15

Normalization uncertainty -

Cross section: 5%

Analyzing power: 2%

Angular acceptance: ±1.2° (A_y) or ±0.4° (*5V)

Angle accuracy: ±0.1°

Targets: Isotopic, enriched to ≥97%.

The target thicknesses were determined by energy loss measurements with a 20 MeV ^3He beam, normalizations determined after the initial publication of the data (Mene71). Because of the difficulties in the

determination of the beam polarization, these data have been assumed to have a 5% normalization uncertainty in both the cross section and the analyzing power.

The ORNL data sets used are listed in Table 5-4 and shown in Fig. 5-17.

Table 5-4

Datasets Provided by ORNL (E_p = 40 MeV)

Target	Reference
^{40}Ca	Fric67
^{54}Fe	Fric67
^{58}Ni	Fric67
^{60}Ni	Fric67
^{90}Zr	Fric67
^{208}Pb	Fric67

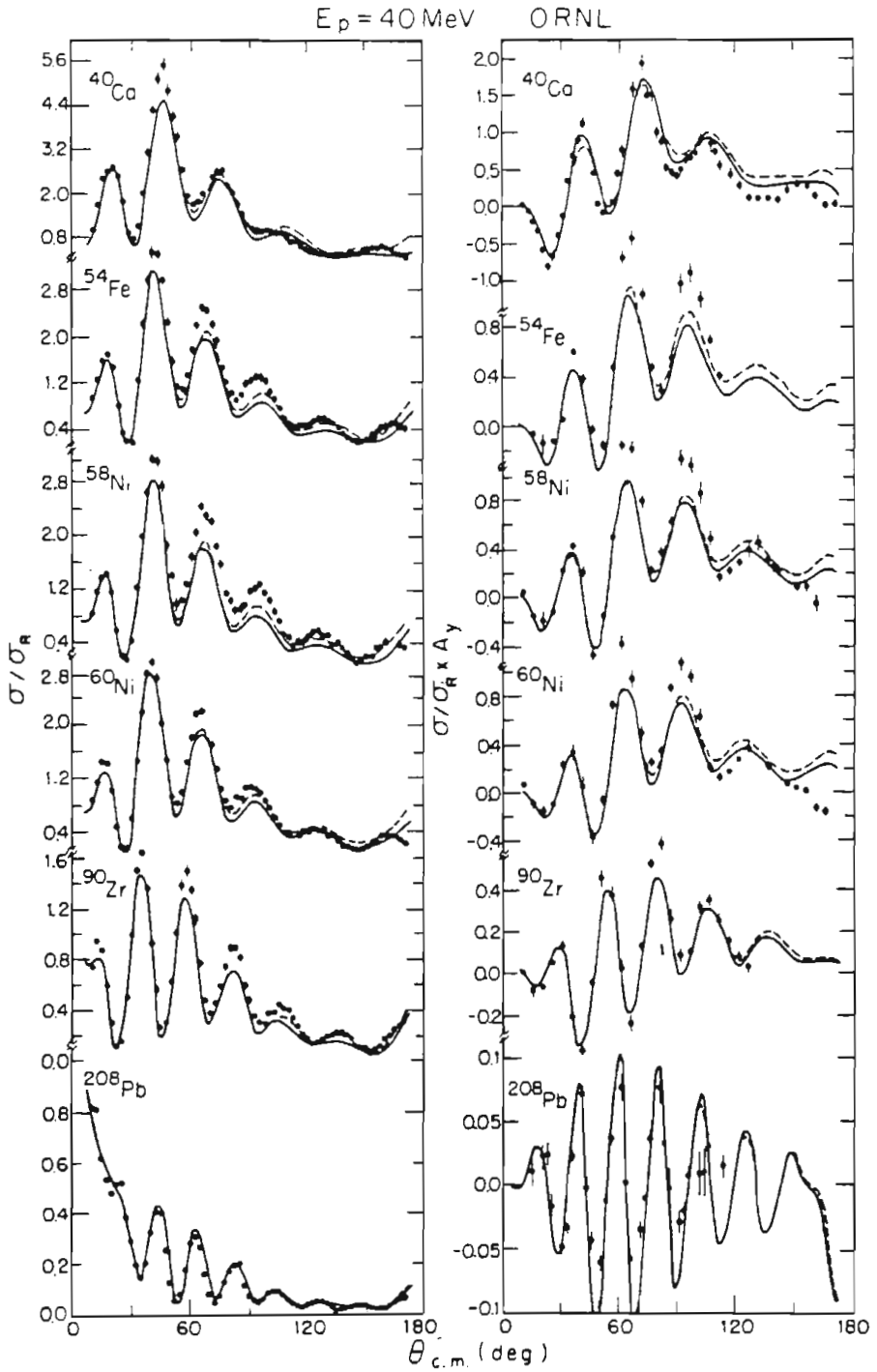

Fig. 5-17: Elastic ($\vec{p}$,p) scattering at 40 MeV from ORNL. The curves shown are calculated with the best-fit global optical model, as described in Chap. 7.

5.6 Data for 65 MeV proton scattering (RCNP)

The data for 65 MeV proton scattering were obtained from the large elastic scattering data set measured at the Research Center for Nuclear Physics in Osaka, Japan (Saka83). The cross section and analyzing power were measured simultaneously with a polarized proton beam, using left-right detector pairs.

The conditions for the measurement were (Saka82):

Energy resolution: (not reported)

Relative uncertainty -

Cross section: <1% to 5%

(Minimum of 3% assumed in Saka83)

Analyzing power: 0.003 to 0.04

(Minimum of 0.03 assumed in Saka83)

Absolute uncertainty -

Cross section: 1% to 20%

Analyzing power: 1%

Angular acceptance: (not reported)

Angle accuracy: $\pm 0.05^{\circ}$

Targets: Isotopic, enriched to ≥97%, except for ^{46,48}Ti with about 82% enrichment.

These data were normalized by weighing the targets to obtain the target thickness, and by measurement of the detector geometry to compute the solid angle (Saka82). Given the uncertainties in the target weighing, the target normalization seems very uncertain, as estimated by the original authors by comparison with optical model calculations.

In general, the normalizations estimated by the authors (Saka82) were used in our search procedure, and we assumed a 10% uncertainty to these normalizations. The data are presented in Fig. 5-18 to Fig. 5-21, as σ/σ_R and $\sigma A_y/\sigma_R$.

Table 5-5

Proton Scattering Data from RCNP (E_p = 65MeV)

Target	Renorms for σ Estimated by RCNP
^{40}Ca	1.24
^{44}Ca	1.05
^{48}Ca	0.97
^{46}Ti	0.97
^{48}Ti	1.05
^{50}Ti	1.02
^{54}Fe	0.90
^{56}Fe	0.99
^{59}Co	1.04
^{58}Ni	0.93
^{60}Ni	0.90
^{62}Ni	0.96
^{64}Ni	0.98
^{89}Y	0.94
^{90}Zr	1.07
^{98}Mo	1.05
^{100}Mo	0.93
^{144}Sm	0.91
^{208}Pb	0.88
^{209}Bi	0.92

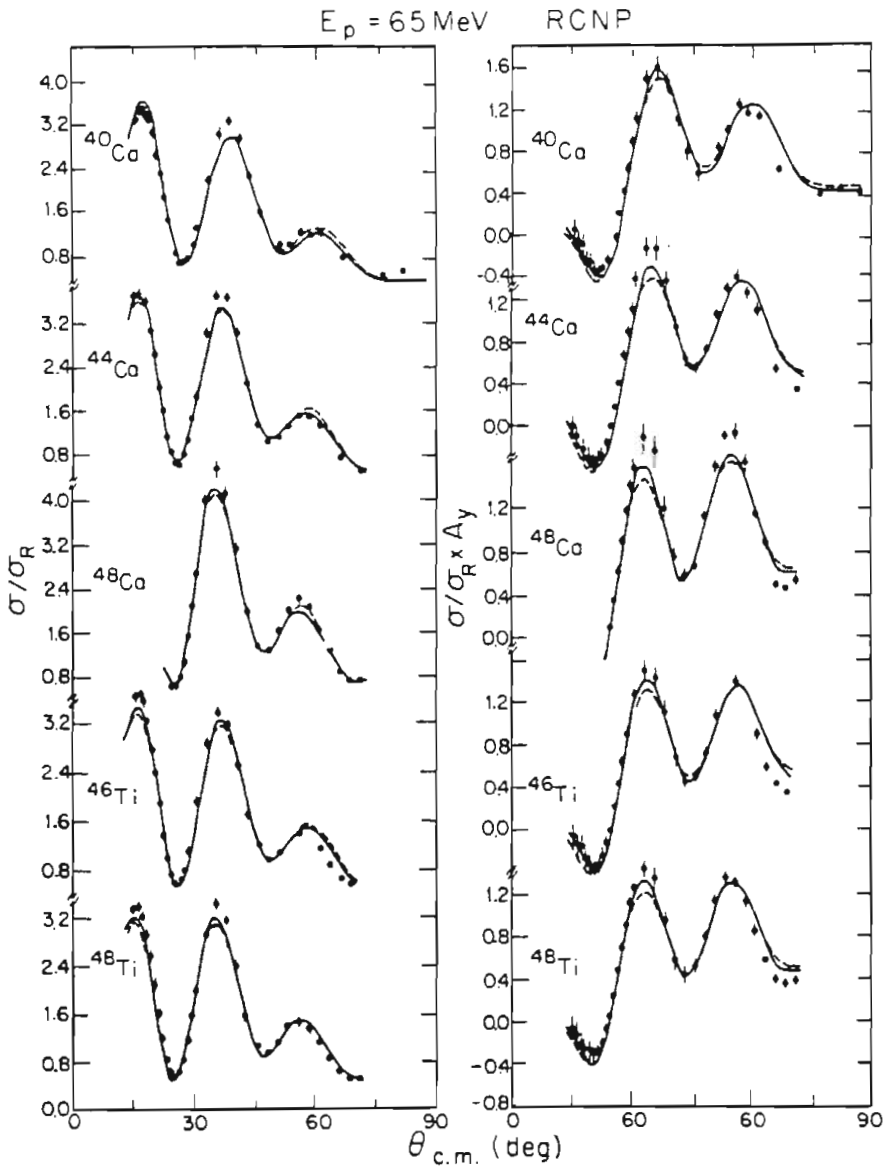

Fig. 5-18: Elastic ($\vec{p}$,p) scattering at 65 MeV from RCNP. The curves shown are calculated with the best-fit global optical model, as described in Chap. 7.

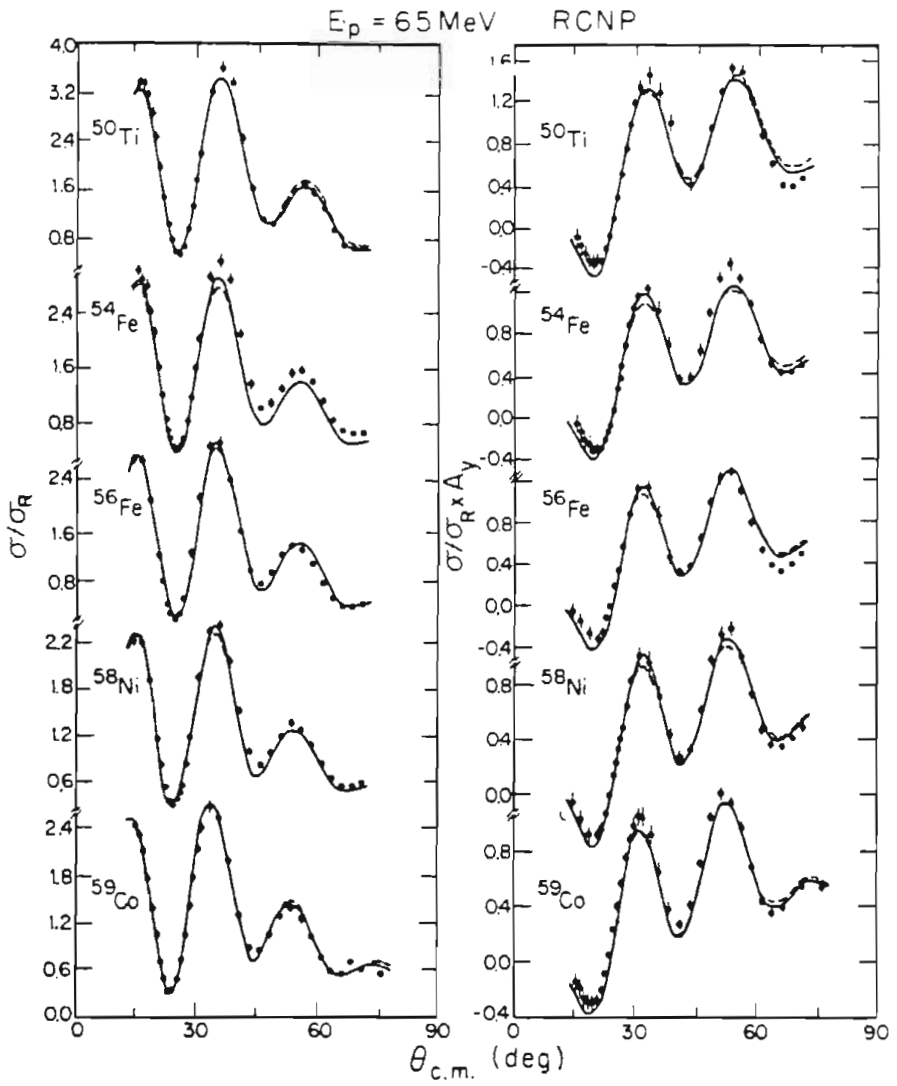

Fig. 5-19: Elastic ($\vec{p}$,p) scattering at 65 MeV from RCNP. The curves shown are calculated with the best-fit global optical model, as described in Chap. 7.

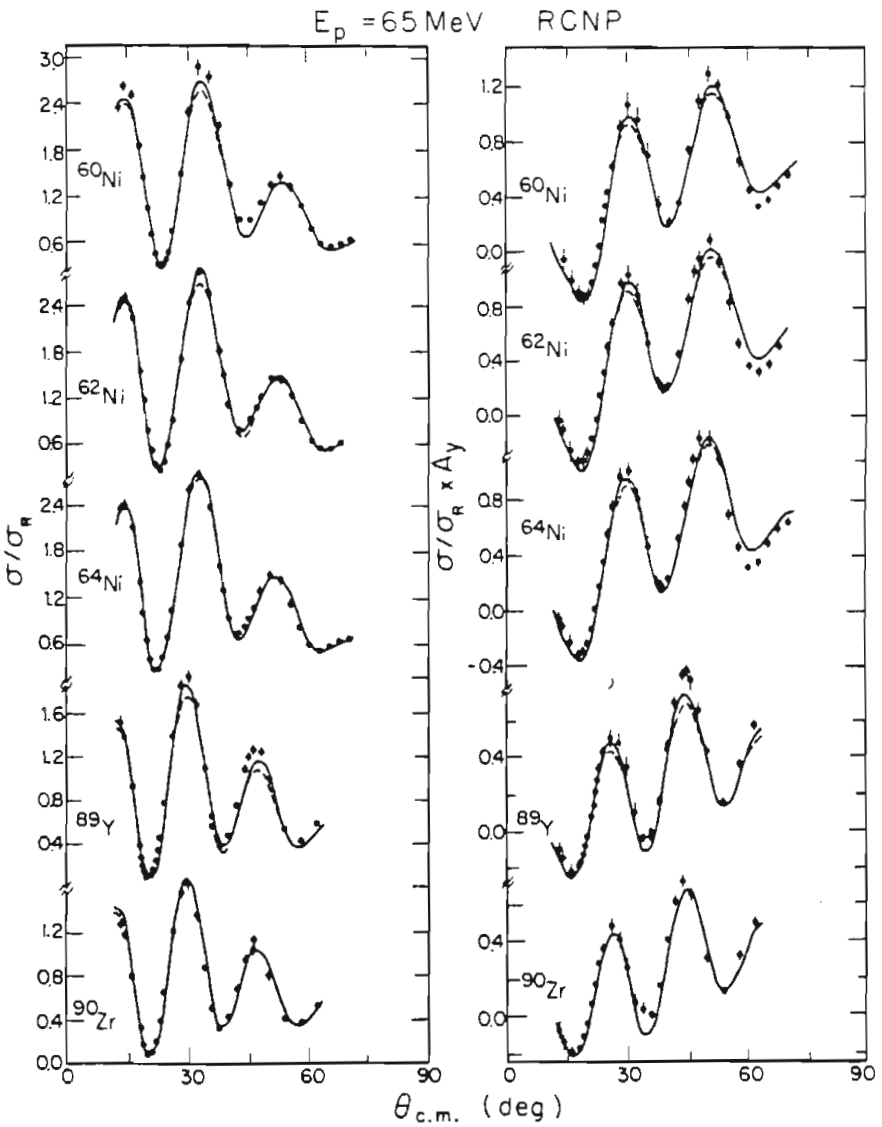

Fig. 5-20: Elastic ($\vec{p}$,p) scattering at 65 MeV from RCNP. The curves shown are calculated with the best-fit global optical model, as described in Chap. 7.

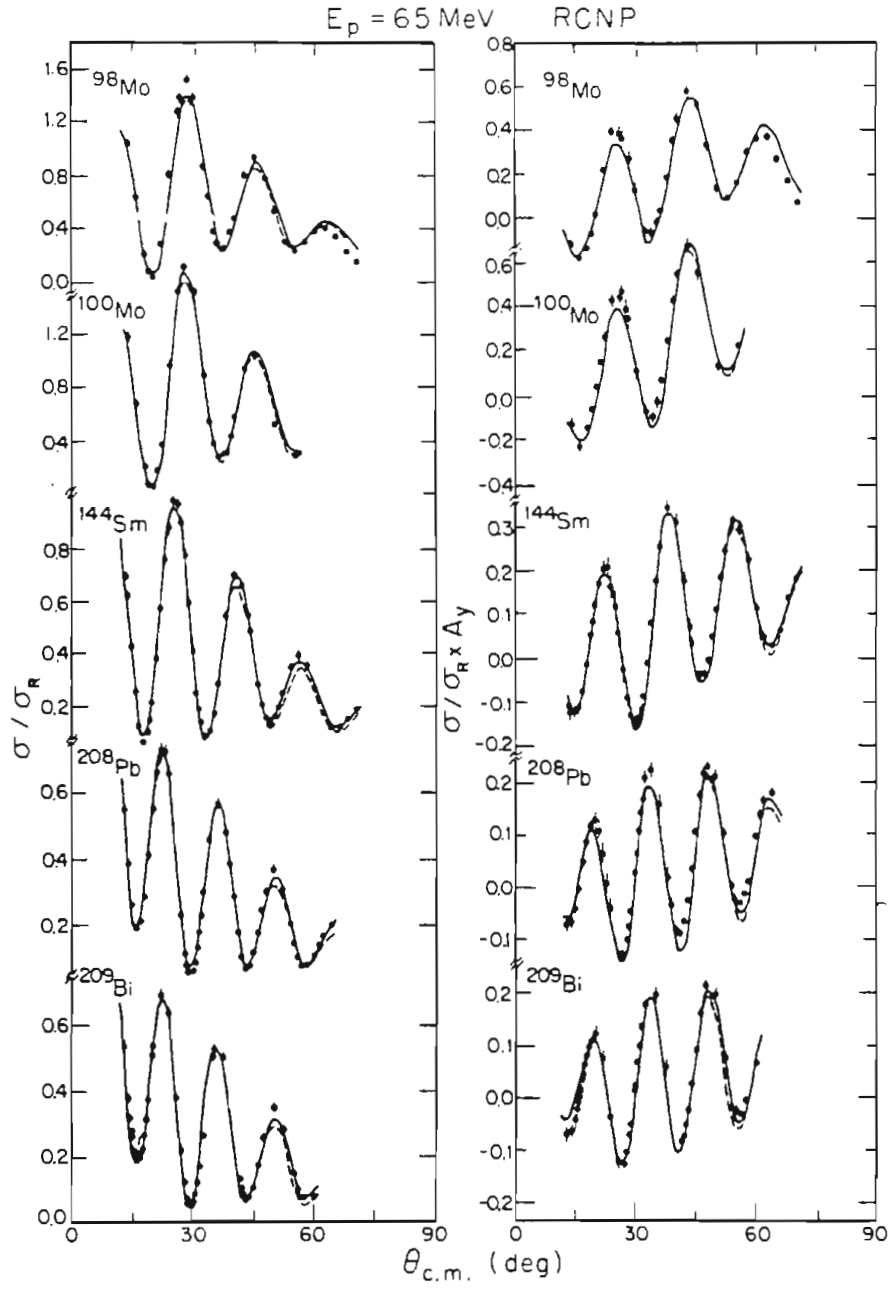

Fig. 5-21: Elastic ($\vec{p}$,p) scattering at 65 MeV from RCNP. The curves shown are calculated with the best-fit global optical model, as described in Chap. 7.

VI. Procedures in the Semi-Empirical Global Analysis

6.1 Overview of Global Analysis

In previous chapters the need for a new global parameterization and the data available for this analysis have been described. The details of the parameter search are described in this chapter. We review the parameterization and dataset, then describe the optical model tools and the search procedure.

6.1.1 Review of the Parameterization

The parameters of our global model are shown in Table 6-1. This model features a radius for the potentials, $R = r_0 A^{1/3} + r_0^{(0)}$, which contains a constant term in addition to the usual simple $A^{1/3}$ dependence, as discussed in Sect. 2.6.1. It also has a smooth energy dependence for the surface and volume components of the absorption, as discussed in Sect. 2.6.4. We also make adjustments to the potential for Coulomb effects in proton scattering in both the real and imaginary potentials, computed by reducing the incident proton energy by the average Coulomb energy in the nucleus, as discussed in Sect. 2.6.1 and 2.6.4.

This parameterization has been chosen to represent current knowledge of the optical potential, as described in Chap. 2, while still being reducible to the form of usual phenomenological potential. The correspondence with the usual potential, particularly in the choice of form factors, entails some compromise between the best forms of the optical potential (as might be generated from the folding-model and realistic nuclear densities) and utility of the Woods-Saxon form factors, both for speed of calculation and application to distorted wave function calculation (e.g. DWBA programs like PTOLEMY (Mcfa76)). In addition, the assumption that the isovector and Coulomb correction

Table 6-1

Global Optical Model Parameterization

(See Sect. 2.2.1 for definitions of the basic parameters)
(See Sect. 2.6 for the definition of the global potential parameters)

Real Central Potential:

$$V_r = (V_0 \pm V_t \frac{N-Z}{A}) + V_e(E-V_c) \quad \text{MeV} \qquad \begin{matrix} + : \text{protons} \\ - : \text{neutrons} \end{matrix}$$

$$R_r = r_0 A^{1/3} + r_0^{(0)} \quad \text{fm},$$

$$a_r = a_0 \quad \text{fm},$$

Imaginary Central Potential: †

$$W_v = W_{v_0} f_v(W_{ve_0}, W_{vew}, (E-V_c)) \quad \text{MeV},$$

$$W_s = (W_{s_0} \pm W_{st} \frac{N-Z}{A}) f_s(W_{se_0}, W_{sew}, (E-V_c)) \quad \text{MeV},$$

$$R_w = r_w A^{1/3} + r_w^{(0)} \quad \text{fm},$$

$$a_w = a_w \quad \text{fm},$$

†Energy dependence of imaginary potential:

$$f_i(W_{i0}, W_{iw}, E) = \left[1 + \exp(\pm \frac{E - W_{i0}}{W_{iw}}) \right]^{-1}$$

Choose the "-" for f_v, the "+" for f_s.

Spin-Orbit Potential:

$$V_{so} = V_{so} \quad \text{MeV},$$

$$R_{so} = r_{so} A^{1/3} + r_{so}^{(0)} \quad \text{fm},$$

$$a_{so} = a_{so} \quad \text{fm},$$

Coulomb Potential Radius:

$$R_{Coul} = r_c A^{1/3} + r_c^{(0)} \quad \text{fm}$$

Note: In the expressions for the energy dependence,

$$V_c = \frac{1.73 \, Z_p Z_t}{R_{Coul}} \quad \text{MeV},$$

which is the spatial average of the Coulomb potential in the target.

terms of the potential have the same form factor as the isoscalar terms is probably not correct (Jeuk77). Yet, it is not clear that there is any alternative way to parameterize these forms in a simple fashion. Thus we choose the more straightforward approach because it will parameterize the data. This analysis is not likely to be sensitive to form factors that are more complicated.

6.1.2 Review of the Elastic Scattering Dataset

One of the important ingredients in a global parameterization is a properly global dataset for the analysis. Since this is a nucleon-nucleus parameterization the dataset must be broad in (n,n) scattering as well as (p,p) scattering. The data for this analysis have been presented in Chaps. 3 to 5. The breadth of the dataset is shown in two figures: Fig. 6-1 shows the distribution of (p,p) elastic scattering data in A and E; Fig. 6-2 similarly shows the (n,n) data. The datasets shown are each composed of angular distributions of both $\sigma(\theta)$ and $A_y(\theta)$, except for the data from Ohio University (OUAL) which consist solely of $\sigma(\theta)$.

In addition to the graphical summary of the data, Table 6-2 presents a tabulation of the datasets and the minimum value of the least squares goodness-of-fit function for each of the observables, derived from a local (non-global) optical model fit. These numbers are used later to establish a relative weighting of the various datasets. Included in this table are notations about data quality or reasons why particular datasets have been excluded from the search.

For the purpose of the search, alternative representations of some of the data were used. For the proton data, the cross sections were represented as the ratio of the cross section to the Rutherford cross section. This was done principally to allow plotting on a linear vertical scale, to enhance the discrepancies between calculations and the data.

The analyzing-power data were converted into the form of cross section multiplied by the analyzing power, σA_y, which is half the difference between the left and right scattering cross sections. This

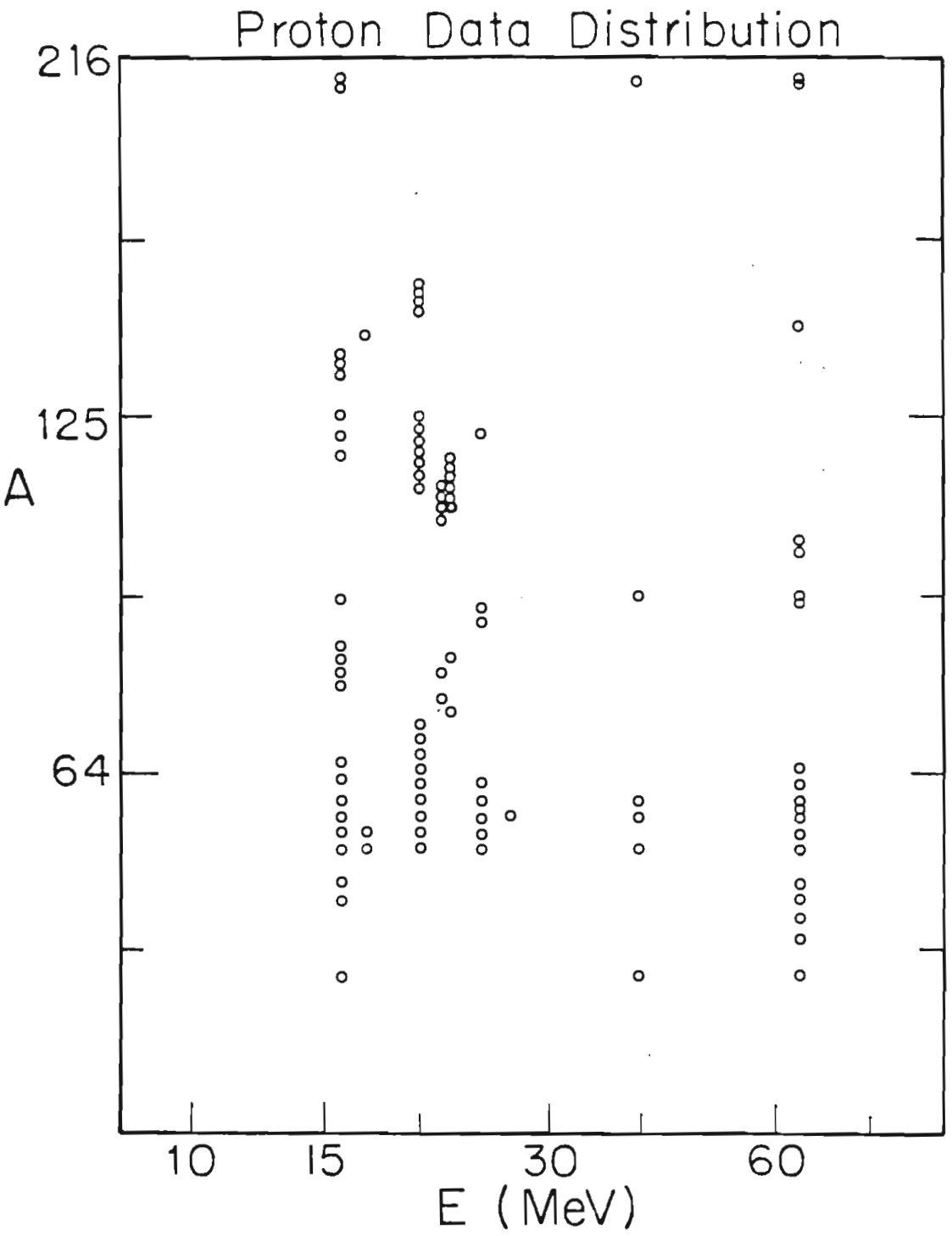

Fig. 6-1: Distribution of cross section and analyzing-power datasets in A and E for proton scattering data. Note that the vertical axis is $A^{1/3}$ (increasing like the nuclear radius) and that the horizontal axis is log E_{inc}, proportional to the the observed long-range energy dependence of the real depth of the optical potential (Nada81).

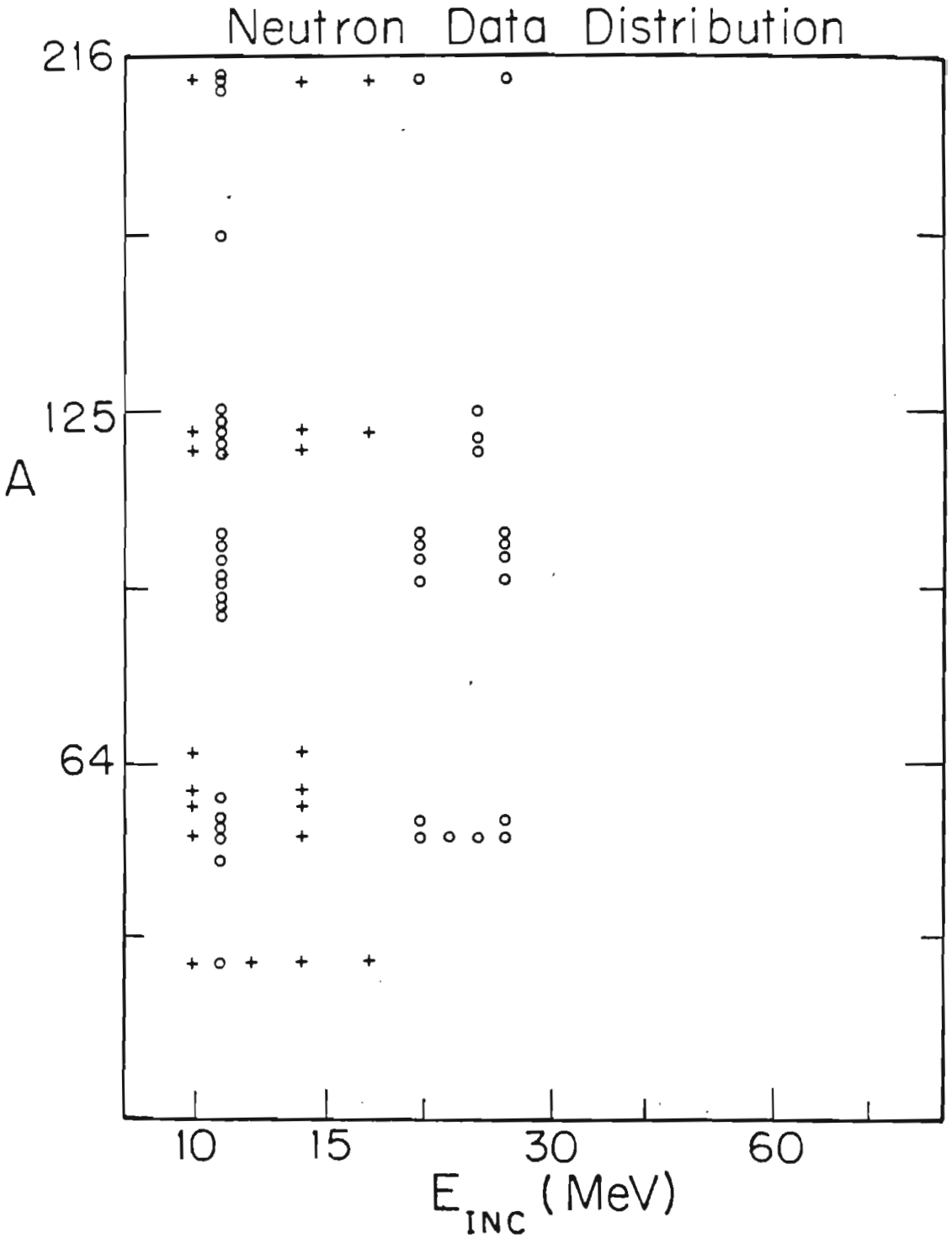

Fig. 6-2: Distribution of datasets in A and E for neutron scattering data. The circles represent the unpolarized data from OUAL, the crosses the data from TUNL polarized-neutron facility.

Table 6-2a

List of (p,p) Scattering Datasets

Name	E	Lab	LSQ_{min}(renorm) σ	A_y	Comments (Data marked with > were omitted from search)
Ca40	16	TUNL			>Severe nuclear structure problems
Ti48	16	TUNL	25(1.07)	10(0.88)	Thickness not well determined
Ti50	16	TUNL	26(1.03)	4(0.95)	Experimental problems
Fe54	16	TUNL	188(1.04)	15(0.90)	Probable nuclear structure effect
Fe56	16	TUNL	20(1.01)	3(0.97)	
Ni58	16	TUNL	21(1.01)	10(----)	A_y renorm outside limits
Ni60	16	TUNL	53(1.01)	12(0.93)	
Cu63	16	TUNL	18(1.01)	6(0.97)	
Cu65	16	TUNL	9	5	
Se76	16	TUNL	6	4	Collective nuclei, Dela84.
Se78	16	TUNL	6	3	"
Se80	16	TUNL	7	4	"
Se82	16	TUNL	14(1.01)	5(1.02)	"
Zr90	16	TUNL	28	19(1.03)	
Sn116	16	TUNL	2(1.01)	2	
Sn120	16	TUNL	8(1.01)	4	
Sn124	16	TUNL	11(1.02)	5(1.01)	
Ba134	16	TUNL	5	1	
Ba136	16	TUNL	3(1.02)	2	
Ba138	16	TUNL	3	5(1.01)	
Pb208	16	TUNL			>IAR resonance effects
Bi209	16	TUNL			>IAR resonance effects
U238	16	TUNL			>Unresolved ground stated
Fe54	17	EIN	16(0.98)	3(1.04)	All EIN data normalized with OMP
	20		10(1.01)	9(0.94)	
	24		7	3(1.01)	
Fe56	17	EIN	8(0.99)	2(1.03)	
	20		4	6(0.96)	
	24	EIN	5	2(0.99)	
Ni58	20	EIN	18	18(0.93)	
	24		10	5	
	27		11		>Sparse angular distribution
Ni60	20	EIN	14(1.01)	10(0.98)	
	24		8	10(0.98)	
Ni62	20	EIN	10(0.99)	19(1.04)	
	24		6(1.01)	11(0.98)	
Ni64	20	EIN	21	9	
Zn64	20	EIN			>Highly scattered data
Zn66	20	EIN			> Same as Zn64
Zn68	20	EIN			> Same as Zn64
Zn70	20	EIN			> Same as Zn64
Ge72	22	EIN	24(0.98)	20(1.08)	

Table 6-2a (cont'd)

Name	E	Lab	LSQ_{min} (renorm) σ	A_y	Comments
Ge74	22	EIN	29	15	
Se78	22	EIN	92	32	Highly scattered data
Se80	22	EIN	13(0.98)	8(----)	A_y renorm outside limits
Sr86	24	EIN	26(1.01)	26(0.99)	
Sr88	24	EIN	17(1.01)	19(0.99)	
Pd110	20	EIN	5(1.20)	3	
Cd106	22	EIN	4(0.90)	6	
Cd108	22	EIN	4(0.94)	4	
Cd110	20	EIN	8	16	
Cd110	22	EIN	4	2	
Cd112	20	EIN	5	7	
Cd112	22	EIN	3	3	
Cd114	20	EIN	9	8(0.98)	
Cd114	22	EIN	8	7	
Cd116	22	EIN	9	6	
Sn116	20	EIN	9(1.05)	5	
Sn118	20	EIN	6	6	
Sn120	20	EIN	15	8	
Sn120	24	EIN	5	3	
Sn122	20	EIN	10	7	
Sn124	20	EIN	11	8	
Nd142	17	EIN	2	1	
Sm148	20	EIN	5	3	
Sm150	20	EIN	5	2	
Sm152	20	EIN			>Strong collective effects
Sm154	20	EIN			>
Ca40	40	ORNL	9(0.99)	6(0.96)	
Fe54	40	ORNL	15(0.98)	14(0.98)	
Ni58	40	ORNL	5(0.99)	7(0.97)	
Ni60	40	ORNL	8(0.99)	11(1.03)	
Zr90	40	ORNL	15(0.97)	12(----)	Estimated renorm outside reasonable
Pb208	40	ORNL	23(1.02)	6(----)	limits
Ca40	65	RCNP	3	1	
Ca44	65	RCNP	1	1	
Ca48	65	RCNP	2	1	
Ti46	65	RCNP	1	0.5	
Ti48	65	RCNP	1	1	
Ti50	65	RCNP	1	1	
Fe54	65	RCNP	3	2	
Fe56	65	RCNP	3	1	
Co59	65	RCNP	2	1	
Ni58	65	RCNP	3	1	

Table 6-2a (cont'd)

Name	E	Lab	LSQ σ_{min}	(renorm) A_y	Comments
Ni60	65	RCNP	3	1	
Ni62	65	RCNP	3	1	
Ni64	65	RCNP	2	1	
Y89	65	RCNP	1	1	
Zr90	65	RCNP	1	2	
Mo98	65	RCNP	1	0.5	
Mo100	65	RCNP	0.2	0.3	
Sm144	65	RCNP	4	1	
Pb208	65	RCNP	4	1	
Bi209	65	RCNP	6	3	

Table 6-2b

List of (n,n) Scattering Datasets

Name	E	Lab	LSQ σ_{min}(renorm) A_y	Comments (Data marked with > were omitted from search)
Ca40	11	OUAL	8	No Analyzing Power data from OUAL
V51	11	OUAL	2	
Mn55	11	OUAL	5	
Fe54	11	OUAL	5	
	20		2	
	22		2	
	24		2	
	26		2	
Fe56	11	OUAL	6	
	20		3	
	26		4	
Co59	11	OUAL	2	
Sr88	11	OUAL	8	
Y89	11	OUAL	10	
Zr90	11	OUAL	4	
Mo92	11	OUAL	3	
	20		2	
	26		1	
Nb93	11	OUAL	9	
Mo96	11	OUAL	5	
	20		4	
	26		1	
Mo98	11	OUAL	2	
	20		2	
	26		2	
Mo100	11	OUAL	3	
	20		1	
	26		2	
Sn116	11	OUAL	3	
	24		3	
Sn118	11	OUAL	3	
	24		2	
Sn120	11	OUAL	5	
Sn122	11	OUAL	6	
Sn124	11		4	
	24		1	
Ho165	11	OUAL	13	
Pb206	11	OUAL	12	
Pb208	11	OUAL	1	
	20		4	
	26		2	
Bi209	11	OUAL	7	

Table 6-2b (cont'd)

Name	E	Lab	LSQmin(renorm) σ	LSQmin(renorm) A_y	Comment
Ca40	10	NTF	18	14	NTF is the TUNL Neutron Time-of-Flight dataset.
	14		41	41	
	17		41	32	
Fe54	10	NTF	9	3	
	14		154	6	
Ni58	10	NTF	3	3	
	14		20	3	
Ni60	10	NTF	5	---	No A_y data available
	14		5	---	
Cu65	10	NTF	11	5	
	14		2	7	
Sn116	10	NTF	3	2	
	14		3	0.5	
Sn120	10	NTF	8	5	
	14		3	4	
	17		2	---	
Pb208	10	NTF	32	12	
	14		11	19	
	17		14	---	

observable was preferable to the analyzing power since this is what optical model programs calculate; from this the analyzing power is computed by dividing it by the cross section. Any error in the calculation of the cross section would be reflected in the analyzing power. Where cross section minima occur, significant enhancements in A_y occur, not directly related to effects of the spin-orbit potential. We have also observed that the contribution to the least-squares estimate of fit quality from σA_y is closer in magnitude to that from the cross section than that from A_y. Thus, the polarization observables in this form will influence more strongly the fitting process. The uncertainty for σA_y was computed by using the simple propagation of errors form,

$$\Delta(\sigma A_y) = \left[A_y^2 \Delta\sigma^2 + \sigma^2 \Delta A_y^2 \right]^{1/2} \qquad 6\text{-}1$$

We have investigated correlations between σ and A_y which might significantly alter the magnitude of this uncertainty, when these are measured simultaneously, since they are computed from the same independent variables, the detector sums. To estimate the correlation contribution to the uncertainty, the product σA_y was reexpressed in terms of the original sums, and the propagation of errors performed with respect to the original sums, assuming that those sums were uncorrelated. The resulting expression is,

$$\left[\frac{\Delta(\sigma A_y)}{\sigma A_y}\right]^2 = \left[\left[\frac{\Delta\sigma}{\sigma}\right]^2 + \left[\frac{\Delta A_y}{A_y}\right]^2 + \frac{2}{(LU + LD + RU + RD)}\left[\frac{r}{r^2-1}\right]\left[\frac{\delta LU^2}{LU} - \frac{\delta LD^2}{LD} + \frac{\delta RU^2}{RU} - \frac{\delta RD^2}{RD}\right]\right] \qquad 6\text{-}2$$

where the variables r, Lx, and Rx are defined as in Sect. 2.1. The first two terms of Eq. 6-2 are identical to the simple expression for the uncertainty in Eq. 6-1. In the case of purely statistical uncertainties in the sums and no backgrounds subtracted, the last term in the Eq. 6-2 is identically zero. For finite backgrounds, where the

uncertainty is,

$$(\delta Lx)^2 = Lx + 2LBx \qquad 6\text{-}3$$

the last term of Eq. 6-2 can be seen to reduce to sums and differences of the ratio of the backgrounds to the net peak sums. In most elastic scattering, the background is only a few per cent of the peak sum and is unpolarized. For the worst case background in the TUNL proton elastic scattering, this term contributes less than 1% to the uncertainty.

The neutron data are represented as absolute cross sections. There is no straightforward means of displaying these data in a linear form, unlike the case of protons. The ($\vec{n}$,n) analyzing-power data, too, have been left in the original form, because the neutron cross-section data were not often measured at the same center of mass angle as the analyzing-power data, preventing the accurate conversion of A_y to σA_y.

From Figs. 6-1 and 6-2 many of the weaknesses of this dataset may be seen. The distribution of the proton data in energy has a sparsely populated gap between 25 and 65 MeV. This is the region where the transition from surface-dominated to volume dominated absorption probably occurs. For the neutron data the problem is more severe - there is virtually no large, systematic dataset above 26 MeV in incident energy. In addition, there is a large gap between A=124 and A=208 that is not well covered by any dataset, at any energy. There are additional problems with individual datasets, which have been discussed in Chaps. 4 and 5. Most significant of these are problems with the normalization techniques, since many of the proton data have been normalized with respect to an optical-model calculation (Chap. 5). Some of the inaccuracies possible with these techniques have been discussed in Chap. 5; the problems these cause for the minimization program are discussed in Sect. 6.2. The effects of improper normalization on the parameter fitting are discussed in Sect. 6.3, using synthetic data. There is some evidence that this can be a serious problem at higher energies (Fulm69), where the same dataset with different normalizations can be fitted equally well by different optical potentials.

This dataset, however, is one of the largest bodies of data ever assembled for an analysis of this type. There are approximately 6000

proton data points, about half cross section and half polarization data, in about 90 datasets. All these data are in the direct-reaction energy region. For the neutron data, there are about 2000 data points, in about 60 datasets. These are mostly elastic cross-section data, with about 15 sets of analyzing-power data. These data are also for energies where the compound-elastic contributions are negligible. The data were measured at only a few laboratories, so that we might identify systematic problems and distinguish them from effects in the parameterization. In this way, we can be aware of those properties of the optical potential that may not be well determined because of errors in the data.

6.2 Tools for the Global Analysis

A global optical model analysis presents many unusual problems to the nuclear physicist. The analysis requires the optimization of the model parameters for a large number of angular distributions (≈150) for elastic scattering of several projectiles from many targets at a wide variety of energies. This must be done very many times for the entire dataset as well as for subsets of the data, to study the local consistency of the global potentials.

These needs may be reduced to two kinds of requirements. First, there are requirements for the optical model program. It must, above all else, be fast in the calculation, since it may need to calculate more than 10,000 angular distributions during the course of a single optical model optimization. It should also be capable of adjusting the calculation to the minimum required accuracy for the dataset at hand, to maximize that speed. The second kind of requirements are for the optimization procedure. This procedure should be able to search stably on 10 to 20 correlated parameters without human guidance, since most parameters in the optical model are strongly correlated with at least one other. In addition, when the minimum LSQ is found, the program should be able to estimate the correlations of the parameters, as well as reasonable confidence limits on the parameters. These kinds of estimates have been largely absent in past analyses, yet they can serve as

a valuable guide to users of the resulting parameter set.

Our response to the above requirements was the construction of the program **MINOPT**. It was assembled from the programs OPTICS (a nuclear optical model program) and MINUIT (a minimization program). Each of these will be described briefly. The combination of them into MINOPT is described in more detail below.

6.2.1 OPTICS - the optical-model program

OPTICS is a small, fast nuclear optical-model program for computing elastic scattering observables for light projectiles of spin ≤1. The fundamental algorithms of the program are well documented in the literature (East73). The version described in that reference is a version for a very small minicomputer, the Honeywell DDP-224. The version used in **MINOPT** was converted to run on a DEC VAX 11/780 or an FPS-164.

OPTICS numerically solves a Schrödinger equation containing the optical-model potential described in Sect. 2.1, then computes the elastic-scattering differential cross section and analyzing powers consistent with the spin of the incident particle. If data are present, it computes the least squares goodness of fit function. The technique for the numerical integration used is a modified Numerov technique (Thom84), discarding the wave function except at two asymptotic matching radii. The most time-intensive parts of the program have been piecewise optimized for maximum speed, compared to the DDP version which had been designed for minimal usage of storage. These optimizations include precomputing arrays of commonly used numbers (e.g. $1/r^2$) and computing the optical potential only out to the matching radius. For the DEC VAX 11/780 execution speed was increased by forcing the variables in the numerical integration kernel into arithmetic registers. OPTICS has one feature which is especially useful for this search - it automatically adjusts the matching radius and the maximum L-value of the calculation for the minimum calculation time consistent with user specified accuracy parameters. Thus, the user can set the parameters for a fast calculation which is only slightly more accurate than the data, or choose precise calculations for the final output.

OPTICS can plot and tabulate the calculated angular distributions, as well as summarize the potential and numerical accuracy parameters.

6.2.2 MINUIT - the minimization program

MINUIT is a modern minimization program developed at CERN. It, like OPTICS, is documented (Jame75). It is a package of minimization algorithms, connected by a command processor. The function to be minimized is linked to the package as a subroutine named FCN. The command processor reads in the model parameters, initializes the common blocks used for information passing, then processes user commands to invoke the optimization routines, adjust the convergence or error criteria, or perform estimates of the parameter confidence limits.

Much has been written on the problem of optimization (function minimization or point estimation) and determination of confidence limits (interval estimation). The procedures used in MINUIT for solving these problems use a variety of mathematical techniques; further information may be found in several references (Jame72, Jame75, Eadi71. Gree78). A summary of results necessary for interpretation of the MINUIT searches follows.

To determine the best values of the optical model parameters, we use a function of the parameters which has its minimum value when the best set of parameters is used. The function most commonly used for this is the sum of error-weighted residuals squared ,

$$LSQ = f(\bar{x},\bar{p}) = \frac{1}{N-d} \sum_{i=1}^{N} \frac{(x_i - T_i(\bar{p}))^2}{\Delta x_i^2}, \qquad 6\text{-}4$$

in which $\bar{x}$ is a vector of N data points, $T_i(\bar{p})$ is the optical model prediction for data point x_i, based on the parameter vector $\bar{p}$, and Δx_i is the standard deviation estimate of the measured x_i. In this expression, d is the number of parameters determined during the current optimization, and N-d is called the "number of degrees of freedom" of the fit. The best estimate of the correct values of the model parameters are those values which minimize the value of this function, which is related to the more general class of estimation formulas known as maxi-

mum likelihood functions (Eadi71, pg. 165). Estimation of the best values of the parameters by minimizing the value of $f(\bar{x},\bar{p})$ is usually called the "method of least squares". In this work, $f(\bar{x},\bar{p})$ will be referred to as the least-squares function (LSQ). This particular form will also be referred to as the "reduced" LSQ, because it is divided by the number of degrees of freedom. The LSQ function has many statistically desirable properties as a means to estimate the best values of the parameters (Gree78, Sect. 5.3). We have experimented with the possibility of augmenting or replacing least squares. These experiments, made with the synthetic data described in Sect. 6.3.4, indicated that least squares was to be preferred over the alternatives we considered.

The techniques for finding the optimal parameter values using MINUIT are in one of two classes, those that use the gradient of LSQ with respect to the parameters and those that do not. The strategy of MINUIT combines algorithms from both classes, depending on the amount of information available about the function, and the proximity of the minimum to the starting point. The algorithms used were SIMPLEX (non-gradient) and MIGRAD (gradient).

The SIMPLEX algorithm is a well-known technique from linear programming (Jame72). It is basically geometric in nature, using the value of the function at n+1 points in the parameter space, which form a simplex, in a search on n parameters, to determine an estimate of the direction and distance of the current simplex from the function minimum. The method is best used far from a minimum, where the gradient is not likely to provide useful information about the location of that minimum. It tends to take the largest possible steps toward a minimum, though, and is not sensitive near the minimum. This technique is said to have converged when the the estimated distance to the minimum, judged by the size of the next step to be taken, is less than a user-specified tolerance.

For searches started near a minimum (or continued after a coarse technique like SIMPLEX), the best technique available in MINUIT is MIGRAD, a gradient-based technique. This technique is a modified

Newton's method, belonging to a class of techniques known as "variable metric methods" (Jame75), which find roots of the gradient of the least-squares function. This is done by using a quadratic approximation of the least-squares function (Jame72), from which an estimate for zeros of the gradient may be found with the expression,

$$\bar{p}_{min} = \bar{p}_0 - \underline{G}^{-1} \bar{g} \quad , \qquad 6\text{-}5$$

in which $\bar{p}_0$ is a starting set of model parameter values, $\underline{G}$ is the matrix of second derivatives of the least squares function with respect to the parameters (assumed locally constant everywhere in the quadratic approximation), $\bar{g}$ is the gradient of the function (evaluated at $\bar{p}_0$), and $\bar{p}_{min}$ is the predicted minimum. The MIGRAD algorithm does not directly evaluate the covariance (the inverse of $\underline{G}$) at each iteration, which would be time consuming and not always useful at any significant distance from the minimum, since this is a quadratic approximation. Instead, it makes an initial approximation to the covariance, exactly evaluates the gradient, then searches for a minimum along the direction predicted by Eq. 6-5. The approximate covariance is corrected after each iteration to reflect the new information about the location of the minimum. This technique is generally very stable, and has the advantage of producing a covariance matrix at the end of the search, which may be used to estimate the parameter confidence limits and the parameter correlations (Jame75). This technique is said to converge when both the estimated distance to the minimum is less than a user-determined constant and the average fractional change in the covariance is less than another constant.

MINUIT is capable of providing estimates of confidence limits on the parameter values. We desire to provide uncertainties or confidence limits for several reasons. We know that given the data, we can at best determine a parameterization near the best parameterization. A confidence limit gives future users knowledge of the range of most likely values of the parameters. In particular, knowledge of the sensitivity of the parameters to the dataset, reflected in the confidence limits, is necessary for the intelligent application of this model.

Also, in the calculation of composite quantities such as the volume integral, the estimation of the composite uncertainty requires knowledge of the uncertainties and the correlations of the components.

By uncertainties we mean a range of values of a parameter within which the "true" value of the parameter lies (Eadi71, pg. 190). For a parameter determined alone and assumed to have normally distributed uncertainties (Eadi71, pg. 190) this is usually taken to be the 1-standard-deviation uncertainty, for which there is a 67% probability that the true value is within the interval. For several parameters determined simultaneously, this interval is often larger than for single estimation, since in this case the probability is the joint probability of the entire parameter set. When the parameters are correlated, the uncertainties are larger still.

In calculating the confidence limits for the parameters, the criterion chosen is usually based on an increase in the value of the LSQ function from its minimum. The choice of an arbitrary relative change has the virtue of simplicity; it provides little information for the user of the parameter set, however, since one must evaluate the significance of the chosen change. We would prefer to specify a confidence interval which has a certain probability of containing the "true" values of the parameters. The connection of confidence intervals with probability is usually made by noting that the LSQ function has a χ^2 probability distribution if the parameter uncertainties are normally distributed (Eadi71, pp. 193). Unfortunately, in a global optical model, we do not know that the parameter uncertainties are normmally distributed, and we know that the model is not sufficient to describe the data exactly (for example, by not accounting for shell effects in the potential parameters). The mathematics of interpreting the LSQ in terms of probability requires that the model be able to describe the data exactly, barring any "noise" superimposed on the data.

Our estimation of uncertainties must proceed from some arbitrary, but well-defined procedure to determine a "reasonable" interval for LSQ, the interval which defines the uncertainties. For our purposes, a

10% increase from the minimum LSQ value was used to estimate the parameter uncertainties.

The estimation of confidence limits also requires that the variances for each data point used in calculating LSQ should represent the true variances of the data (Jame78). This is required so that the contribution of each dataset to the total LSQ is consistent with that of all other datasets. An angular distribution with very small statistical uncertainties has a larger contribution to the LSQ (when the visual quality of the fits are similar) than data with larger statistical uncertainties, even though each may have similar instrumental uncertainties. Thus, the calculated variance for a data point must include contributions from counting statistics and contributions resulting from instrumental effects not normally included in elastic-scattering uncertainties. If there is a constant overall renormalization to the data variances, it is reflected in the ultimate estimate of the parameter uncertainties. The correct parameter variance can be estimated from (Eadi71,pg.164)

$$\sigma_i^2(\text{true}) = \sigma_i^2\ (\text{est.})\ LSQ_{min}, \qquad 6\text{-}6$$

where σ_i^2(est.) is the variance estimated for paramter i by MINUIT with the minimum LSQ of LSQ_{min} and σ_i^2(true) is the variance one would get if the normalization factor were removed. This procedure is equivalent to renormalizing the LSQ to 1, and is the basis for our procedure for estimating the correct variance of each dataset.

Some of the datasets used in this analysis tend to have significant LSQ_{min} values even when individually fitted by an optical-model potential (as may be seen in Tables 6-1 and 6-2). An example is the $^{90}Zr(\bar{p},p)$ data set measured at 16 MeV. The best individual optical model fit to these data is visually quite good, but the LSQ_{min} is 28, much larger than the average (11). This comes from unusually small calculated uncertainties in these data. For the 16-MeV data, an estimate of the instrumental uncertainties has been included in the variances, as discussed in Sect. 4.4. However, these adjustments were insufficient, as seen in the LSQ_{min} of the best individual optical

model fits to these datasets, as shown in Table 6-2. For other datasets, excepting the RCNP data, the uncertainties are purely statistical, as described in Chap. 5. To investigate the bias introduced into our fits by the different estimates of the uncertainties, we made calculations with a renormalized LSQ. Our procedure for normalizing the LSQ function in this parameterization is discussed with the search procedure in Sect. 6.4.2.

Given a magnitude of the change in LSQ which represents our uncertainty, MINUIT can estimate parameter confidence limits in two ways. In either case, the uncertainty quoted is that change in the parameter value which causes a change in the LSQ value of UP, where UP is a MINUIT parameter set by the user.

The first kind of estimate is simply the standard deviation of the parameter, computed as the square root of the corresponding diagonal element of the covariance matrix. The covariance is estimated by a MIGRAD minimization, or is calculated directly by the HESSE command, as the inverse of the matrix of all second derivatives of the LSQ function with respect to the model parameters (Eadi71, pg. 126). Its elements are (Eadi71, pp. 198),

$$\underline{G}^{-1}(\bar{p}) = \underline{V} = \begin{bmatrix} \sigma_1^2 & \cdot & \cdot & \cdot & & \\ \rho_{12}\sigma_1\sigma_2 & \sigma_2^2 & & & & \\ \rho_{13}\sigma_1\sigma_3 & & \sigma_3^2 & & & \\ \vdots & & & \ddots & & \\ & & & & \sigma_m^2 & \end{bmatrix} \qquad 6\text{-}7$$

Here, σ_i^2 is the estimated variance of the ith parameter, and ρ_{ij} is the linear correlation coefficient between parameters i and j. The useful information in the covariance matrix is contained in the variances and the correlation coefficients. The correlation coefficients represent the extent to which pairs of parameters, p_i and p_j, are linearly correlated, $-1 \leq \rho_{ij} \leq 1$. Extreme values of ρ_{ij} indicate that the two parameters are so closely correlated that the problem is not well posed, i.e. that, in the calculation of LSQ, a change in one parameter can be essentially compensated completely by a change in the other, in

the same direction if $\rho_{ij} = 1$ and in opposite directions if $\rho_{ij}=-1$. In Table 6-3 typical covariance-based uncertainties and correlations are shown for a search on a single dataset. These reflect the typical correlations (ambiguities) reported in optical model searches, as well as some less well known ones. This estimate of the uncertainty as the standard deviation is reasonable if the LSQ function is an approximately quadratic function of the parameters and the parameters are normally distributed. Note that these estimated uncertainties include the effects of the correlations with the other parameters (Eadi71, pg. 198).

For the best estimates of the confidence limits, the function MINOS may be used. This is a very general procedure for establishing confidence limits, making no assumptions about the behavior of the LSQ function. For a given parameter, it predicts, using the covariance, the value of the parameter which should give a value for the LSQ function equal to the desired confidence limit. It then performs a minimization on the other parameters. If the minimum found does not have the desired value of LSQ, MINOS estimates a new value and tries again, until the correct LSQ is found or the maximum allowed number of attempts is exceeded. This procedure is performed separately for positive and negative confidence limits on the parameter, allowing for asymmetric uncertainties in the parameters (highly non-quadratic behavior). An example of the uncertainties resulting from MINOS may be found in Table 6-6, in the discussion of synthetic data testing.

6.2.3 MINOPT Function

In the merging of OPTICS and MINUIT into MINOPT, we chose to retain the command structure of MINUIT, including OPTICS as an unusually complex form of the FCN subroutine used by MINUIT. The set of global optical model parameters is specified as the model parameters on which MINUIT is to search. The FCN routine then serves as a driving program for OPTICS, reading in the initial data and performing the individual calculations, translating the global parameters into local parameters. It also creates the final output and plots, when required. The func-

Table 6-3

Typical Parameter Uncertainties and Correlations for Individual Optical Model Search

Target: ^{116}Sn E_{inc}: 16 MeV Projectile: $\vec{p}$

Least Squares per degree of freedom:
$LSQ_{min}(\sigma)=2.3$, $LSQ_{min}(\sigma A_y)=2.4$, $LSQ_{min}(total)=2.3$.

V	52.9±3.2;	r_0	1.23±0.05;	a_0	0.68±0.03
W_s	11.8±2.6;	r_w	1.27±0.03;	a_w	0.56±0.11
V_{so}	5.84±1.1;	r_{so}	1.06±0.14;	a_{so}	0.54±0.09

(Uncertainties correspond to change in $LSQ_{min}(total)$ of 2.3)

Correlation Matrix: (this is symmetric by definition, thus only the half of the matrix is shown).

	V	r_0	a_0	W_s	r_w	a_w	V_{so}	r_{so}	a_{so}
V	1								
r_0	-1.0	1							
a_0	0.3	-0.4	1						
W_s	-0.6	0.7	-0.1	1					
r_w	-0.7	0.6	0.3	0.4	1				
a_w	0.7	-0.8	0.1	-1.0	-0.6	1			
V_{so}	-0.3	0.3	-0.4	0.0	0.0	0.0	1		
r_{so}	-0.5	0.6	-0.6	0.2	0.3	-0.2	0.7	1	
a_{so}	0.2	-0.3	0.4	-0.4	0.3	0.2	-0.3	0.0	1

Note: Strong correlations are underlined.

tions implemented in MINOPT are shown in Table 6-4 and briefly described below.

The FCN/OPTICS subroutine in MINOPT implements all the standard functions required by MINUIT (Jame75). These include initialization, standard calculation, and final wrapup.

The initialization prepares OPTICS for calculation of the observables and the calculation of the least squares function. This process includes reading the selected angular distributions from the appropriate database, establishing the correspondence between the MINUIT parameter list and the MINOPT global parameter set, and performing the initial calculation, to be saved for later comparison with the final calculation.

The standard calculation simply performs the optical model calculation for each dataset, translating the global parameters into OPTICS local parameters and returning the LSQ value for the complete dataset.

The final calculation generates tables summarizing the results. These tables include a target-by-target summary of the OPTICS calculation parameters, a table comparing the initial with the final global potentials, a table showing the distribution of the final least squares on a target-by-target basis, and, in the version for the VAX 11/780, plots of the final angular distributions.

The FCN subroutine for MINOPT also provides additional optical model and data processing functions. It allows the cross section and polarization data to have different weights in the calculation. Another option renormalizes the data according to an estimate from the current optical model potential. The estimate used is a simple minimization of least squares with respect to the normalization of the daata (East73). This option is an alternative to the technique used in some optical model programs, in which the normalization is adjusted after each iteration of the search program (Wass82). Adjustment of the normalization in this fashion reduces considerably the value of a technique like MIGRAD, in which the covariance is estimated assuming that there is at most a slow variation of the covariance in the parameter space and no change in time. The net effect is to confuse the search

Table 6-4

FCN/OPTICS Functions

Function Code	Description
1	Initialize OPTICS for global calculations. Includes decoding global parameters from MINUIT input list, reading datasets requested, performing initial calculation to save initial value of LSQ function.
3	Final calculation and output of tables summarizing search results and optical model calculation with final potential. Includes plots and tables of angular distributions, if requested. (See options below).
4	Standard OPTICS calculation. Most calls to FCN are this type.
6	Set relative weights of cross section and polarization data. One weight is applied to all cross section data, the other to all polarization data.
7	Calculate and apply renormalization estimated from least squares. Requires minimum improvement in LSQ before allowed. Calculated for all datasets.
8	Set/Unset output of tables of angular distributions.
9	Set/Unset output of OPTICS calculation summary for last calculation.
10	Set/Unset plotted output flag
11	Set/Unset flag for Mott-Schwinger corrections to neutron scattering
12	Select 1) slow, accurate calculation or 2) fast, not quite as accurate calculation (1% for 65 MeV protons).
15	Generate tables of angular distributions in format for external programs to plot.

and slow the convergence significantly. Thus, MINOPT/FCN allows renormalization only between other MINUIT commands.

Another option is the choice of calculation parameters for OPTICS to optimize the speed or the accuracy of the program. Two choices are allowed, 1) calculation parameters set to produce a very accurate, but slow calculation and 2) calculation parameters chosen to produce a faster calculation accurate to about 1% for 65-MeV proton scattering. This latter calculation is usually about 30% faster than the very accurate calculation, mostly because of the reduced number of partial waves. Other options generally select final output options, to increase or reduce the amount of final information, or select some features of the calculation, such as the inclusion of Mott-Schwinger corrections to neutron elastic scattering calculations (Hoga69). We found that Mott-Schwinger corrections have no significant effect at most angles where neutron analyzing powers are measured, and thus were not included in this analysis.

For flexibility in the implementation of the global potential, and in the creation of input files for the searches, the global potential is processed by means of three separate routines. The parameters are given to MINUIT with assigned specific names (Varn85). The initial call to FCN calls a routine which reads these names to get the ordering of the parameters in MINUIT, comparing them to a table of allowed names, and creating a table of this ordering, which does not change during the course of the search. During each call to FCN, any defaults for the unspecified global parameters are set in another subroutine. Prior to each calculation, the global parameter set is passed to a subroutine which then calculates the local potential for the currently selected dataset. In this fashion, a modification of the global potential parameterization requires only an addition to, or modification of a table, the correct initialization, and the insertion of the algorithm for including the extra term in well localized points of the code.

The program MINOPT was implemented on two computers. The initial development and searching was on a VAX 11/780 equipped with a floating point accelerator (DEC77). This machine provides a very pleasant dev-

elopment environment, including a flexible and fast FORTRAN compiler. The principal drawback to this machine is its relatively slow floating-point operation time. For the OPTICS FCN in MINOPT, the average time per calculation (over our current dataset) in double precision (required by MINUIT for reasonable convergence) was 0.9 sec. For a search on 75 target distributions, with 10 parameters, this can result in a total search time of 14 hours of CPU time. On a heavily used VAX, this can result in turnaround time in excess of 30 hours.

To increase the rate at which we could perform searches, a problem which has constrained previous global searches, MINOPT was also implemented on a Floating Point Systems FPS-164 attached processor, installed on the Triangle Universities Computation Center IBM 3081-K computer (TUCC84, FPS84). The FPS-164 processor has a pipelined architecture, with parallel floating point multiplication and addition processors. It has a theoretical maximum processing rate in excess of 5 Mflops (million floating point operations per second), as compared with the VAX speed of about 0.3 Mflops. The FORTRAN for this machine conforms to the ANSI-77 standard, so it was relatively easy to convert the VAX version of MINOPT to run on the FPS. The time per angular distribution calculation on the FPS is 0.09 sec, a factor of 10 gain over the VAX, reducing the calculation time from 14 hours to 1.5 hours. As it was not economical to use the FPS for principally I/O bound tasks, some options of the VAX version were omitted, principally the plotting I/O and some tables of output.

For flexibility in the specification of datasets, given the large number (≈150) used in this research, a database system was established to store the actual angular distributions. The specification of the data for MINOPT is accomplished by giving the name of the database, followed by a list of dataset names with vital statistics for each dataset. MINOPT reads the list, retrieves the data from the appropriate database, and stores it in a large common storage block. There were different versions of the database on the different computers used. The VAX database is described in detail in (Vaug81). The IBM version is described in (Varn85).

The VAX database is a relative record file. The first few records of the database (the number depends on the capacity of the dataset) contain information about the size of the data base, a bit map of the records used, and a directory of the target datasets and the location of the data. Each set of target angular distributions is written as one record, thus minimizing the overhead of reading the data. Each record holds a maximum of 46 angles, each composed of a pair of σ and σA_y measured at the same angle. Each dataset is identified during access by the incident nucleon energy, target A, target Z, and laboratory identification. Separate datasets are maintained for the proton and neutron data.

For the FPS, a different database structure was required. The FPS is a single-user machine, requiring a host machine for control. The local host machine is an IBM 3081K running under the MVS operating system. The most straight-forward database structure was a partitioned dataset(PDS) (IBM76), in which each member of the file is equivalent to the records of the VAX database. Each target dataset is identified by a name, instead of by separate E, A, and Z. As on the VAX, two datasets are maintained, one for proton scattering data, one for neutron scattering data.

6.3 Experiments and Tests Using Synthetic Data

Early in the design and construction of MINOPT, we wanted to test the suitability of MINUIT for the problem of optical model fitting. In particular, we desired to test the consistency and stability of the search program. We also wished to investigate the intrinsic limitations of this investigation on optical-model parameters, particularly the confidence-limit estimation, and the effect of ambiguities on the search. Later, these same tests were used to compare alternatives to the least squares function. To best carry out these tests, a global dataset which could be well described by the optical model was needed, for which the best possible fit was known without question.

The test set we developed was a set of synthetic data, generated from an arbitrary, global optical-model potential. This potential is

given in Table 6-5; it represents a realistic potential. The "targets" were chosen to span the mass region of this search. These were "^{60}Ni", "^{90}Zr", "^{120}Sn", "^{138}Ba", "^{208}Pb". The incident projectile chosen was a proton scattered at an energy of 16 MeV. For each "target" nucleus, angular distributions of $\sigma(\theta)$ and $\sigma A_y(\theta)$ were generated in 5° steps from 25° to 170°. This was to emulate the 16-MeV TUNL proton scattering data closely, thus facilitating later comparison of the tests with the actual fitting. For the calculation of the LSQ function, arbitrary, uniform uncertainties were assigned to the individual data points. These were 2% of the "data" value for the $\sigma(\theta)$ data and 0.01 for all the $A_y(\theta)$ data; these were then combined in the same manner as the uncertainties for the true data to generate the uncertainties in σA_y. This dataset will be referred to as the "SYN" dataset.

In order to provide tests that simulate the problems of typical elastic scattering datasets, two additional datasets were created. The first was a dataset produced by multiplying the original SYN data by a set of random noise factors. These noise factors were distributed normally with a standard deviation of .05 and mean of 1. The estimated uncertainties were not changed after the addition of noise, reflecting the usual situation in experimental physics, where one's knowledge of uncertainties is incomplete, a lack that can influence the estimate of the best fit. This dataset will be referred to as the "NSE" dataset.

The second modified dataset was provided by an arbitrary renormalization of the whole angular distribution for each member of the NSE dataset. These renormalization factors were generated with a standard deviation of 0.05 and a mean of 1.0, one factor for each angular distribution. These renormalizations are tabulated in Table 6-5. This last dataset provides the most realistic test of the program, at least for effects resulting from dataset weakness. This dataset will be referred to as the "NRM" dataset.

6.3.1 Outline of Tests

These tests were intended originally to test the stability of the

Table 6-5

Source Potential and Best Fit Results for Synthetic Data

	Source	SYN	NSE	NRM
V_0	55.0	55.0±1.7(0.3)	54.8±0.9(1.8)	54.8±0.4(0.9)
V_t	15.0	14.9±11.3(2)	15.1±3.0(6)	15.2±3.0(7)
V_e	(-0.35)			
V_c	(1.0)			
r_0	1.25	1.25±0.05(0.01)	1.25±0.01(0.02)	1.25±0.01(0.02)
$r_{0(0)}$	(-0.32)			
a_0	0.70	0.70±0.02(0.01)	0.70±0.01(0.02)	0.70±0.01(0.02)
W_{so}	6.0	6.01±0.5(0.09)	5.93±0.5(1.)	5.98±0.3(0.7)
W_{st}	6.0	5.99±2.8(0.5)	6.43±3.0(6)	6.31±3.0(7)
W_{se}	(-0.05)			
W_{sc}	(0.0)	no Coulomb correction applied		
r_w	1.25	1.25±0.01(0.00)	1.25±0.01(0.02)	1.25±0.01(0.02)
a_w	0.70	0.70±0.04(0.01)	0.71±0.04(0.08)	0.70±0.01(0.02)
V_{so}	6.0	6.00±0.3(0.05)	5.97±0.3(0.6)	5.96±0.2(0.5)
r_{so}	1.25	1.25±0.3(0.06)	1.26±0.04(0.08)	1.27±0.04(0.09)
$r_{so(0)}$	(-0.85)			
a_{so}	0.65	0.65±0.06(0.01)	0.65±0.06(0.1)	0.64±0.05(0.1)
r_c	(1.25)			
$r_{c(0)}$	(-0.20)			
LSQ_{min}		0.03	4.2	5.1

The uncertainties are for a change in LSQ_{min} of 1.0. The quantities in parentheses are uncertainties corrected according to Eq. 6-6. See the discussion in Sect. 6.3.3 for an explanation.

The term W_{de} in the absorptive potential refers to a linear energy dependence, chosen before the current parameterization of the imaginary energy dependence had been deduced.

Dataset renormalizations for NRM

Target name	Renormalization (estimated from best fit) σ	σA_y
^{60}Ni	1.00(1.02)	1.00(0.98)
^{90}Zr	0.98(0.98)	1.07(1.05)
^{120}Sn	1.05(1.04)	0.95(0.99)
^{138}Ba	0.97(0.96)	1.00(0.98)
^{208}Pb	1.03(1.02)	1.01(1.05)

program in searching on global optical potentials. Later, the synthetic data were used to test other options in MINUIT, such as estimation of the parameter uncertainties and correlation analysis. Lastly, the data were used to test best-fit estimators.

The tests of program stability were made by simply starting a search from some set of parameter values relatively far from the initial potential, then observing the program behavior in finding the best fit to the synthetic data. These starting points were selected by three different algorithms, which were: 1) adjustment of various components (real, imaginary, spin-orbit) of the potential away from the optimum by 10% (e.g. V_0, R_0, A_0, leaving all other terms at their optimum values), 2) adjustment of all potential parameters away from the optimum by a constant fraction (e.g. 10%), and 3) adjustment of the potential parameters to exploit the known correlations in the optical potential - Vr^2, Wa_w, $V_{so}r_{so}$. The choice of these different starting points provided a means of biasing the searches that was reproducible and systematic. More exhaustive testing than this was avoided in favor of fitting real data.

6.3.2 Results of Tests

The tests were usually run using the MIGRAD algorithm of MINUIT. In general, the NRM dataset was used. Except where otherwise noted, searches were conducted to minimize the sum of the LSQ from both the $\sigma(\theta)$ and $\sigma A_y(\theta)$ data, searching on all parameters simultaneously. A sample of the starting potentials for the test searches is given in Table 6-6. The results of these tests are summarized in general terms below.

The tests showed the sensitivity of the search to the real central potential. In general, searches started with the real potential depth, radius and diffuseness parameters more than 5% higher or lower (altogether) than the source potential would not converge in a search. Often these searches would produce parameterizations which did not fit the data well; these fits were local minima in regions distant from the true potential.

Table 6-6

Starting Potentials for MINOPT Tests

True Potential

V_o	V_t	r_o	a_o	Ws_o	W_{st}	r_w	a_w	V_{so}	r_{so}	a_{so}
55.0	15.0	1.25	0.70	6.0	6.0	1.25	0.70	6.0	1.25	0.65

Seq. #	Test Starting Parameter Values										
1)	60.5	16.5	1.375	0.77	6.0	6.0	1.25	0.70	6.0	1.25	0.65
	Converges only with V_{so}, r_{so}, a_{so} fixed, using strategy (1).										
2)	49.5	13.5	1.125	0.63	6.0	6.0	1.25	0.70	6.0	1.25	0.65
	Same behavior as (1).										
3)	60.5	16.5	1.375	0.77	6.6	6.6	1.375	0.77	6.6	1.375	0.715
	Does not converge! Runs away to "non-physical" potential, using any strategy.										
4)	49.5	13.5	1.125	0.63	5.4	5.4	1.125	0.63	5.4	1.125	0.585
	Same behavior as (3).										
5)	57.7	15.7	1.310	0.74	6.6	6.6	1.375	0.77	6.6	1.375	0.715
	Converges in complex strategy (2), followed by search with strategy (1).										
6)	52.2	14.2	1.19	0.67	5.4	5.4	1.125	0.63	5.4	1.125	0.585
	Converges in similar fashion to (5).										
7)	60.5	16.5	1.19	0.77	6.6	6.6	1.375	0.63	6.6	1.125	0.715
	Converges with strategy (1) only! Better with (1) than with strategy (2) which finds less satisfactory minima.										
8)	57.7	15.7	1.31	0.74	6.6	6.6	1.375	0.77	6.6	1.25	0.715
	Converges very well in strategy (1) search. Compare with (5)!										

For other starting potentials, (real terms ≤5% different from the source potential), two types of strategies proved useful: 1) search on all parameters simultaneously, and 2) separate searches on the central potential terms and spin-orbit terms. In those cases where the search would converge successfully, strategy (1) was preferable, yielding final parameter values close to the best-fit potential in the shortest time, as well as the best uncertainty estimates. Tests for which this strategy worked were: a) the tests in group (3) on pg. 6-29, with the starting parameters adjusted according to the well-known optical model ambiguities (setting the potential depths 10% higher than the source potential), b) tests in group (1), in which the real terms of the potential were close to the true values and the other components as much as 10% higher or lower than the true values, and c) tests in all groups in which the starting potential values were all near the true potential.

In those cases where the strategy (1) failed to converge, the more complex strategy (2) generally succeeded, in which a search on the central potential parameters was performed, followed by a spin orbit search, then another search on the central potential. The convergence of this search to the best potential parameters was slower than that of strategy (1). Use of this search would usually get to a potential parameterization close enough to the best-fit potential to enable the use of strategy (1) in a second search.

The comparison of NSE and NRM searches showed little difference in the results or in the time of searches. This most likely is because the variance of the renormalization was the same as that for the noise; the normalizations were not strongly distinguishable from the noise, and did not appreciably affect the parameterization. The renormalizations and the search program estimates of them are shown in Table 6-4. Upward renormalization of all the datasets by 5% still does not affect the ultimate parameterization, although the estimated renormalizations are generally not at all correct. If the cross-section data are renormalized by 10%, the search will not converge, showing the importance of correct cross section normalization.

In general, even if the program did not signal that it had converged to a minimum, it had reached a potential close to the best-fit potential. The MIGRAD algorithm often would fail to satisfy its internal convergence criteria when started near the best fit. This appears to be a flaw in the MIGRAD algorithm, related to the way in which it selects the step size for the initial searches. This same flaw occurs in HESSE, in which a poor estimate of the covariance (e.g. from an incomplete MIGRAD search) prevented successful calculation of the covariance with HESSE. The only clear remedy was to start a search not too close to the minimum.

6.3.3 Tests on Estimation of Parameter Uncertainties

To investigate reasonable expectations for the values of the confidence limits on the parameters and to discover why the MIGRAD best-fit parameters to the synthetic data were not the same as the source potential parameterization, a search was performed on each of the datasets SYN, NSE, and NRM, starting from near the source potential. As mentioned previously, the searches could not start exactly at the source potential and reliably converge. At the end of these searches the covariance matrix was computed directly, using the HESSE command, then the MINOS confidence limits were computed for the SYN and NRM datasets. The value of UP, the 1-standard-deviation change in LSQ, was chosen to be 1.0 in all cases. The results for the HESSE estimate are shown in Table 6-5.

The resulting uncertainties are comparable for the NRM and NSE data sets, but larger for the SYN dataset, especially for the real central potential parameters, even though the fits are much better for SYN. This last result is a consequence of improperly normalized least squares, in this case where the variances of the SYN data are much too large, because of the arbitrariness of their assignment. This suggests that the uncertainties for the NSE and NRM potential searches are too small, since, by construction, the true standard deviation of the data (based on the noise) is 5%, while the standard deviations used in computing the LSQ function are about 2% for the cross section data and

about 0.01 for the Ay data. This illustrates the importance of estimating the correct variance of the data prior to estimation of the the confidence limits. The corrected uncertainties, estimated by using LSQ_{min} as in Eq. 6-6, are given in the Table 6-5, in parentheses, next to the MINUIT computed uncertainties.

The MINOS-computed uncertainties for the NRM dataset are given in Table 6-7, as well as the correlation matrix. The MINOS uncertainties are relatively symmetric, and seem to be well approximated by the covariance estimated uncertainties, as shown in Table 6-5.

6.3.4 Tests with Alternatives to Least Squares

We investigated alternatives to the least-squares fitting function because we were concerned about the effect of outlying data points on the quality of the fit. The minimum LSQ value will have significant contributions from data points which the model is not capable of describing, such as distortions in the angular distributions resulting from strong channel coupling, or simply bad data. We wished to examine fitting functions which might reduce the emphasis of these points in the least squares function.

The fitting functions tested were,

$$a) \quad \sum_{i=1}^{N} \max\left(0,\ \ln\left[\frac{(x_i - T_i(\vec{p}))^2}{\Delta x_i^2}\right]\right)$$

and,

$$b) \quad \sum_{i=1}^{N} \mathrm{ABS}\left[\frac{(x_i - T_i(\vec{p}))}{\Delta x_i}\right] \qquad 6\text{-}8$$

These functions satisfy our criterion, that the data points far from the calculation contribute less to the sum, since the functions used rise more slowly than the simple quadratic. The use of the logarithm in function (a) would ordinarily cause difficulties. Because of the logarithmic nature of the terms, a very good fit to one point can result in a large negative contribution to the function, cancelling the effects of very bad fits. This would likely force the fitting program to sacrifice the general quality of the fit for one that goes directly

Table 6-7

MINOS Uncertainties and Correlations for NRM Synthetic Dataset

The uncertainties represent a change of 1.0 in the value of the $LSQ_{min} = 5.3$.

$$V_o = 54.8^{+0.9}_{-0.9}; \quad V_t = 15.0^{+3.4}_{-3.0}; \quad r_o = 1.25^{+0.01}_{-0.01}; \quad a_o = 0.70^{+0.01}_{-0.01}$$

$$W_{so} = 5.99^{+0.5}_{-0.5}; \quad W_{st} = 6.31^{+2.8}_{-2.8}; \quad r_w = 1.25^{+0.013}_{-0.015}; \quad a_w = 0.69^{+0.04}_{-0.04}$$

$$V_{so} = 5.95^{+0.29}_{-0.27}; \quad r_{so} = 1.27^{+0.04}_{-0.04}; \quad a_{so} = 0.63^{+0.06}_{-0.05}$$

Correlation Matrix:

(Since the matrix is symmetric, it is only necessary to show the lower half.)

	V										
V	1	V_t									
V_t	0.0	1	r_o								
r_o	-0.8	-0.4	1	a_o							
a_o	0.2	0.0	-0.4	1	W_{so}						
W_{so}	-0.2	-0.1	0.3	0.1	1	W_{st}					
W_{st}	0.0	-0.2	0.1	-0.3	-0.7	1	r_w				
r_w	-0.1	-0.1	-0.1	0.4	0.4	-0.5	1	a_w			
a_w	0.3	0.3	-0.5	0.1	-0.7	0.1	-0.4	1	V_{so}		
V_{so}	0.2	0.0	-0.2	0.3	-0.3	0.1	-0.2	0.4	1	r_{so}	
r_{so}	-0.2	0.0	0.2	0.1	0.2	0.0	0.2	-0.4	-0.1	1	a_{so}
a_{so}	-0.1	0.0	0.0	0.0	-0.2	0.0	-0.1	0.3	0.3	-0.4	1

through a few points. Thus, this function was modified as shown to only include terms if the logarithm were greater than 0 (i.e. if the argument were greater than 1). The function (b) has been mentioned (Eadi71, pg. 187) as a possible fitting function, especially when the tail of the underlying distribution of the parameters is wider than the corresponding normal distribution.

These functions were tested with synthetic data, in test cases similar to those used with the standard least-squares function. In all cases tested, the convergence of the simple LSQ function was much faster than that of the test functions in Eq. 6-8. Searches using these new fitting functions tended to be relatively insensitive to the location of the source potential. This reflects the very lack of sensitivity which we sought. By constructing a function insensitive to outliers, we obtained one that was also insensitive to changes of the parameters introduced by the searching routines. The optimization routines were getting less information about the fit and so were less effective.

In view of the above results, we felt that the best modifications to the fitting function were ones that added information to the LSQ function, in particular information about the relative phase of the data and the calculation. It is this information to which the human eye is most sensitive. We have made attempts at measuring the relative phases by comparing the locations of minima and maxima in the two angular distributions (calculated and measured). The extra information was included with the LSQ function as a penalty term, added to the usual LSQ function (Jame75). This also failed to improve the convergence of the fit, in fact, hindering the rapid convergence. In this case, we believe that it was the calculation of the penalty that was at fault. Our technique proved insufficiently accurate at locating the maxima and minima in the curves, because of the relatively large angular separations of the data points for many of the datasets. The resulting searches took longer to converge than a simple LSQ-based search and resulted in inferior fits.

6.4 Search Procedure

Our procedure for establishing the global parameterization was based on examination of the dataset, the results of the testing, and the properties of MINUIT. There are two aspects to the description of our search procedure, 1) the use of MINUIT strategies and 2) the selection of data for various searches.

6.4.1 MINUIT Search Strategy

From the results of the testing, it is clear that a simple strategy in the MINUIT searches is the best. This means allowing the program to search simultaneously on as many parameters as possible in each search. For cases in which the search seems non-convergent or unstable, the number of parameters must be reduced; elimination of the spin-orbit potential parameters from the search is usually sufficient. This technique conflicts with the standard approach to optical-model fitting, one of guiding the search by slowly increasing the number of parameters searched (Rapa82). The selective searching on some parameters and not others has been shown in our testing to slow the convergence to the best fit.

The procedure in our MINOPT searches is to execute a MIGRAD search on the current parameter set, on the datasets described in the next section. This search was followed in most cases by a HESSE command to compute the covariance. This served two functions, 1) to compute more accurately the uncertainties in the parameters (in the event that MIGRAD is not able to estimate accurately the covariance), and 2) comparison of the MIGRAD covariance with the HESSE covariance served as a consistency check on the minimum and the search. If they differed greatly, then more careful attention was paid to the details of the search.

A typical search with 16 free parameters often required less than 1000 calls to FCN/OPTICS for the MIGRAD command, then about 150 calls for the HESSE algorithm. For a search on 120 datasets on the FPS-164, the time required would be approximately 3.5 hours, which is about 3×10^{10} floating point operations.

The search on a database would begin with a postulated parameterization, either derived from folding-model estimates (Sec. 2.3), or taken from a previous search on a related database. After one or two iterations (starting from different starting points), the parameters usually stabilized. When the parameterization seemed stable, the principal human search activity was adjusting the parameterization, for example, removing from the search those parameters which seemed poorly determined, or adjusting the starting point for the search.

The final step in the parameterization was the estimation of the confidence limits in MINUIT with MINOS. This technique does not always work well, since it relies heavily on the existence of a covariance to start, and because it is necessary for many searches to converge in the multi-parameter subspaces in which MINOS performs minimizations (Sect. 6.2.2). In addition, it is a very time intensive procedure, since it must perform at least 2n MIGRAD optimizations, where n is the number of parameters for which the uncertainties are requested.

6.4.2 Relative Weight and Uncertainty Normalization

The accuracy of the search and of the estimated uncertainties require that the LSQ function be normalized properly, that is, the variances used to compute the LSQ need to reflect the true variances of the data. This problem goes beyond the simple scaling of the uncertainties. In order to obtain a parameterization that represents the properties of the potential and is not strongly influenced by the differences in the assignment of the data uncertainties by different laboratories, each of the angular distributions must be normalized so that the LSQ function has the same meaning for every angular distribution. This normalization must account for errors in estimating the variance of the data and for the deficiencies of the optical model as a description of the dataset.

To address these problems, we decided to renormalize the contribution of each angular distribution to the LSQ function by dividing the LSQ value by the the minimum LSQ that can be obtained in a local (non-global) optical-model fit. This procedure approximately accounts for

both factors mentioned above, the error in the data variance and the correctness of the optical model. It is not difficult to obtain these fits, since we are not overly concerned with the particular values of such optical-model parameters. Some fits and the associated minimum LSQ values have been published in the references given for the data in Chap. 5. The best-fit LSQ values for other datasets were estimated with MINOPT. The values of the LSQ for each dataset are listed in Table 6-2; the reciprocals of those numbers are applied as weighting factors for the angular distributions in the MINOPT input file.

This procedure should not be viewed as particularly reliable. The estimated minimum least squares values were obtained in a procedure that ignored the consistency of parameters from one isotope or energy to the next, and the consistency of the predictions with our global model. The weights we calculate must be viewed only as estimates of the best LSQ value one may obtain with an optical model, accurate to one significant figure. In comparison with published results, however, they are quite close to or slightly smaller than the LSQ values published by the originators of the data.

The result of this procedure is that each dataset in the global parameterization will have the optimal value of LSQ = 1, when the global model fits as well as the local (non-global) model. In this system, all datasets should weigh equally in the final LSQ; our final parameterization and confidence limits should represent the ability of the global optical model to reproduce the local optical model fits within the uncertainties of the data.

6.4.3 Dataset Selection

An equally important part of the search procedure is the selection of the data used in the search. Our search procedure was intended to test our understanding of the function of MINUIT, while examining the scope and problems of the datasets. The pool of datasets from which we choose has been described in Chap. 5.

The datasets were selected in one of three ways: 1) large datasets at a single energy containing many targets, usually from a single lab-

oratory, 2) selected isotopes with data at many energies, including both neutron and proton scattering, and 3) large global sets of data. In the case of (1) there were, for proton scattering, the 16-MeV dataset (TUNL), the 20.4-MeV dataset (Eindhoven), the 40-MeV dataset (ORNL) and the 65-MeV dataset (RCNP); for neutron scattering there was only the 11- MeV dataset (OUAL). Searches were performed for each of these data sets independently, with the intent of determining the energy dependence of the optical parameters by comparison of the different results. These helped established likely starting values for the later global searches.

There is also some advantage to these searches, since the variances of the data are likely to be consistent within datasets from one laboratory. There is a significant disadvantage to these datasets, in that they were measured with only one projectile isospin. Thus, nuclear-structure effects in the isotopes, as well as Coulomb and A-dependent effects can mask or at least confuse determination of the isovector potential.

To study the effects of energy dependence and true isovector dependence on the global parameterization, isotopes were selected for the group (2). The best cases were Fe (21 datasets), Ni, Zr, Sn, and Pb isotopes. In these searches the isovector potential and the energy dependence were the search parameters of most interest, since for these datasets, where there is no significant A variation, the isovector nature of the potential should be clear. As mentioned in Sect. 2.4.2, this test is clouded by nuclear structure variation over the isotope chains; thus these searches acted only as a guide for the final search.

The first global dataset was formed by merging the datasets in (2). This was to create a balanced dataset, representing all energies and projectiles equally. To these were added all the TUNL proton datasets and the Osaka datasets, representing the energy extremes. This was balanced by including additional neutron scattering data. The resulting assemblage of 75 datasets was used as an intermediate dataset for establishing reasonable parameter values and testing the convergence of MINUIT. The ultimate global dataset contained all datasets available

which did not appear to have problems, as shown in Table 6-2.

6.5 Conclusion and Summary

In this chapter, the components of the global analysis have been described. These components include the parameterization, the dataset, the optical model search program and the strategy used in the search. The search program and various strategies have been tested with a limited set of synthetic data, permitting us to observe accurately the convergence properties of the search.

We conclude that this program and dataset represent a very significant improvement over previous approaches to the global parameterization of the optical model, leading not only to an optical model more representative of the non-relativistic direct-reaction regime below 65 MeV, but to a more thorough knowledge of the uncertainties and correlations in our parameterization, information largely absent from previous works of this type.

VII. Results of Analysis

7.1 Introduction

This chapter presents the potential resulting from our searches on the large elastic scattering database. The potential parameters adjusted in the final searches were those shown in the Table 6-1, although extensions to some parameterizations, such as isospin or energy dependence, were tried. The confidence limits and correlations estimated from the covariance, as well as the MINOS (Sect. 6.2) estimated uncertainties are shown. These parameters are evaluated by 1) discussing qualitatively the fits to the data shown in the figures of Chap. 4 and 5, then 2) comparing the volume integrals from the present potential with previous empirical parameterizations, with microscopically derived potentials, and with phenomenological observations from the literature.

The final discussion in this chapter is of problems with this analysis which should be resolved and of future directions in the large-scale analysis of nuclear scattering data.

7.2 Final Potential Parameterization and Uncertainty Analysis

The final parameterization was derived, following the procedures outlined in Sect. 6.4, after performing over 100 searches, involving about 10^7 separate optical model calculations. Many of the searches were tests of the sensitivity of the data to the model parameters, with the goal of eliminating parameters which were not determined by the data.

At the completion of the searches a full uncertainty analysis was performed with the MINOS option of MINUIT. The interpretation of these uncertainties presents severe problems, since it would appear that our LSQ function still does not possess the correct normalization.

7.2.1 Parameterization

The final parameterization of our semi-empirical optical potential is listed in Table 7-1 (see Table 6-1 for the parameter definitions). The parameters of the energy dependence of the absorptive potential are shown as fixed, although they were searched upon early in this search. These were fixed for the final searches, because 1) tests using the isotopes with the widest selection of incident energies for both protons and neutrons (^{54,56}Fe) showed that these parameters had large uncertainties resulting from correlations between the depths and the energy parameters, and 2) fixing the parameters at the values estimated in the Fe searches caused a very small increase in the minimum value of the least squares function value (after reoptimization of the parameters with MINUIT). The poor determination of the energy dependence of the absorptive potential is a consequence of the irregular distribution of the data in energy. Comparison of the energy dependence of the absorptive potential (Fig. 7-11) with the distribution of the data (Figs. 6-1 and 6-2) shows that the variation of W_s and W_v with energy is greatest where there is the least data.

Additional terms in the parameterization were tested and discarded as too poorly determined. We mean, by "poorly determined", that the parameter values found in searches varied significantly without sizeable changes in the LSQ value. This condition was often accompanied by slow convergence of the search. The additional terms included an isovector component for the volume absorption potential, an energy dependence for the real isovector potential, and an imaginary spin-orbit potential. The A- and E-dependence of the spin-orbit potential, predicted by folding-model calculations, proved also to be poorly determined by the data, as well as highly correlated with the other parts of the spin-orbit potential. These correlations made it difficult for the search procedure to converge.

We made some investigations of the optimal values of the "Coulomb correction" attenuation factors, α in Eq. 2.12. These factors might not be 1, as usually implied, if the interaction, e.g. absorption, were

Table 7-1

Final Parameterization of Elastic Scattering Database with Semi-Empirical Optical Potential

Minimum LSQ value: 11 Uncertainty definition: Δ(LSQ)=1.0

Parameter	Value	Uncertainty estimated by Covariance		Uncertainty estimated by MINOS
V_0	52.9 MeV	0.6	(2.3)	2.4
V_t	12.6 MeV	4.5	(5.8)	6.5
V_e	-0.30	0.03	(0.03)	0.04
r_0	1.25 fm	0.006	(0.009)	0.03
$r_{0(0)}$	-0.24 fm	0.03	(0.12)	0.23
a_0	0.69 fm	0.02	(0.04)	0.04
W_{v0}	10.1 MeV	1.5	(1.8)	2.3
W_{ve0}†	39 MeV	----		
W_{vew}†	11 MeV	----		
W_{s0}	8.96 MeV	0.5	(1.9)	1.7
W_{st}	13.6 MeV	3.3	(5.0)	5.3
W_{se0}†	38 MeV	----		
W_{sew}†	20 MeV	----		
r_w	1.32 fm	0.02	(0.02)	0.18
$r_{w(0)}$	-0.41 fm	0.08	(0.09)	0.8
a_w	0.72 fm	0.02	(0.10)	0.1
V_{so}	5.93 MeV	0.6	(0.8)	1.0
r_{so}	1.39 fm	0.2	(0.2)	>0.7
$r_{so(0)}$	-1.43 fm	0.7	(0.8)	1.6
a_{so}	0.65 fm	0.09	(0.1)	0.2
r_c	1.24 fm	----		
$r_{c(0)}$	0.12 fm	----		

† These parameters were fixed in the final searches because of low sensitivity in the search.

() These uncertainties were estimated from a subset of the global dataset. Details are given in Sect. 7.2.4.

localized in some region of r-space, e.g. the surface, and not distributed uniformly through the nucleus. The searches on the attenuation factors generally returned to the value of 1.0, with large uncertainties. They were thus fixed at the value of 1.0.

These parameters represent well the range of best-fit parameters for this dataset. Other empirical parameterizations (Becc69), when applied to the data used here gave LSQ values greater than ours by a factor of three. Fits to the data using the parameters shown in Table 7-1 are shown in the figures in Chap. 4 and 5. The solid curves are from fits with the LSQ renormalization described in Sect. 6.2; the dashed curves are from a similar fit made with unrenormalized LSQ. In each case the calculated fits have been renormalized by the optical model program to get the best fit, within the data normalization uncertainty. Visual examination of these calculations reveals relatively good fits. It must be kept in mind that we are describing the 8000 data points in the figures with a model of only 16 free parameters. The discussion which follows emphasizes the visual quality of the fits to the data, which may appear poor but still satisfy the criterion mentioned in Chap. 6, that of approximating the best local optical model fit to the particular dataset. In the next section, we discuss the variation in the normalized LSQ, which should measure the latter criterion.

For targets with $40 \leq A \leq 70$ we do not describe well the data at any energy below 65 MeV in the proton scattering. The most poorly described targets were ^{40}Ca, $^{54,56}Fe$, and the isotopes of Ni. These data were not well described even by local optical model fits, so the poor visual quality of the global fit is not surprising. In the case of neutron scattering, the lighter data are poorly described at the low energies of 10, 11, and, to a small extent, 14 MeV. These effects are similar to the effects seen in the proton scattering from the same targets, which causes a large underprediction of the backward angle cross sections by the calculations. Other empirical analyses (e.g. Becc69) tend to describe the $A<70$ data better than this analysis because they were biased by dataset selection to fit these light,

closed-shell nuclei.

For targets of A>70, the data are generally well described at all energies for both neutron and proton scattering. There are two noteworthy exceptions to this observation: ^{90}Zr(p,p) at 16 MeV and ^{92,96,98,100}Mo(n,n) at 20 MeV. The Zr scattering is underpredicted strongly compared to the fits on nearby nuclei at the same energies, although a very good local fit to these data is possible. The Mo neutron scattering is overpredicted by the calculation, again in contrast to nearby nuclei and in spite of the high quality local fits to the data. We currently have no explanation of this effect, except that these nuclei must be unusual compared to the general population of nuclei studied here.

7.2.2 Distribution of Final LSQ values

The visual quality of fit is one measure of the fits we have obtained. To see how the model has done by the standard of Chap. 6, in which the LSQ is renormalized by the value of the LSQ from the best possible local optical model fit, we show the value of the LSQ as a function of target A and incident E for proton scattering (Fig. 7-1) and neutron scattering (Fig. 7-2). The E axis extends from 0 to 70 MeV, and the A axis from 0 to 210. The intent of these figures is to provide a qualitative assessment of the LSQ function for the entire dataset, and so no vertical scale is supplied.

Examination of the figures shows many features. First, many of the problems seen in the data figures do not appear here since the difficulties exist even for the local fits, especially for the A<70 data. Next, some apparently good fits to the data have large LSQ contributions, because very good local fits are obtained, resulting in high weight for the data. The cross section data seem to be dominated by a few very large LSQ values, while the A_y and σA_y are more uniform. The general trend, at least in the proton data, is for there to be generally better fits at higher energies, with a scatter of very small LSQ's throughout.

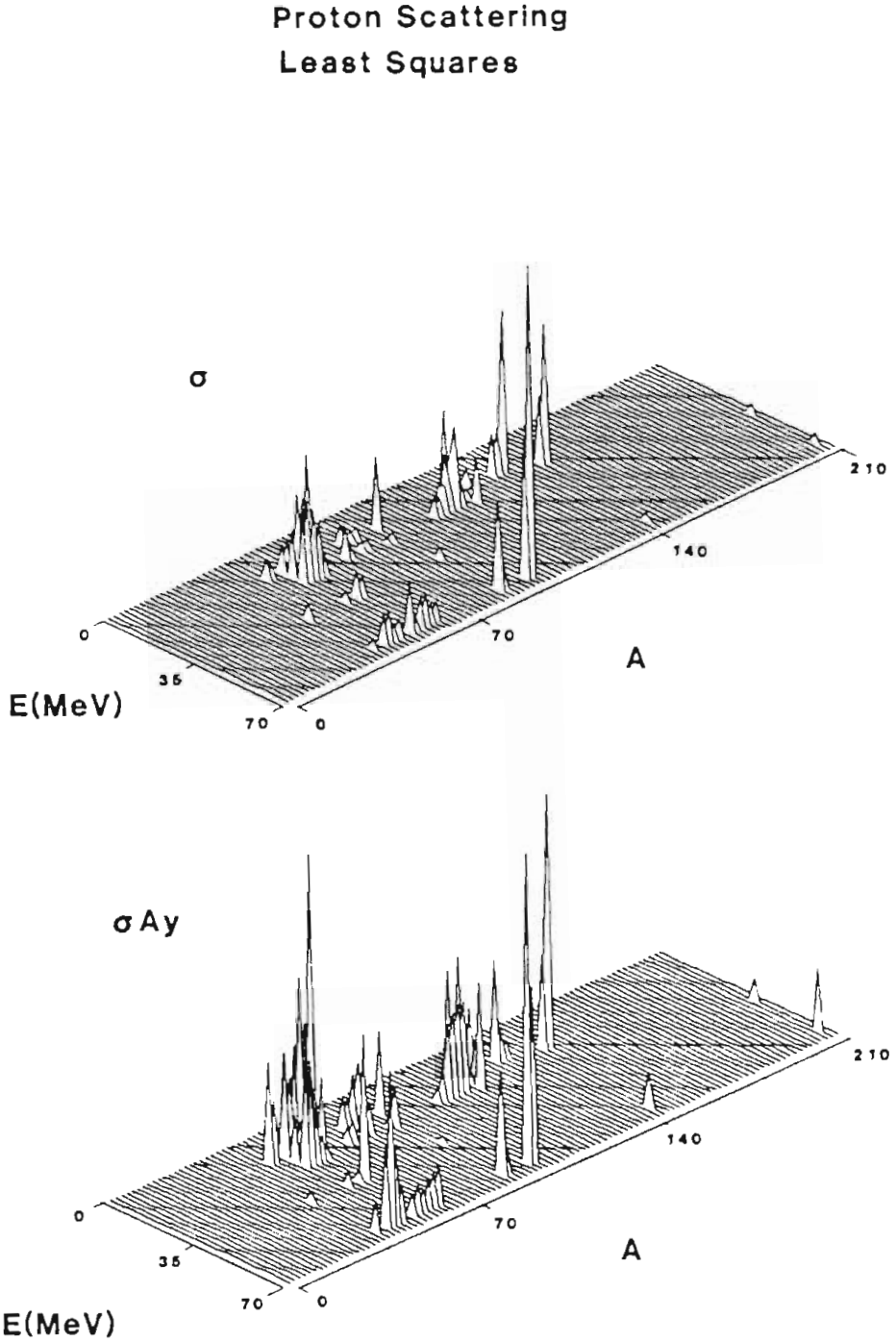

Fig. 7-1: Distribution of LSQ for the (p,p) datasets. The upper plot is the LSQ(σ), the lower is LSQ(σA_y). The range of E is from 0 to 70 MeV and the range of A is from 0 to 220. The scaling of the height is arbitrary and different in the two plots. These values are renormalized, as described in Sect. 7.2.2.

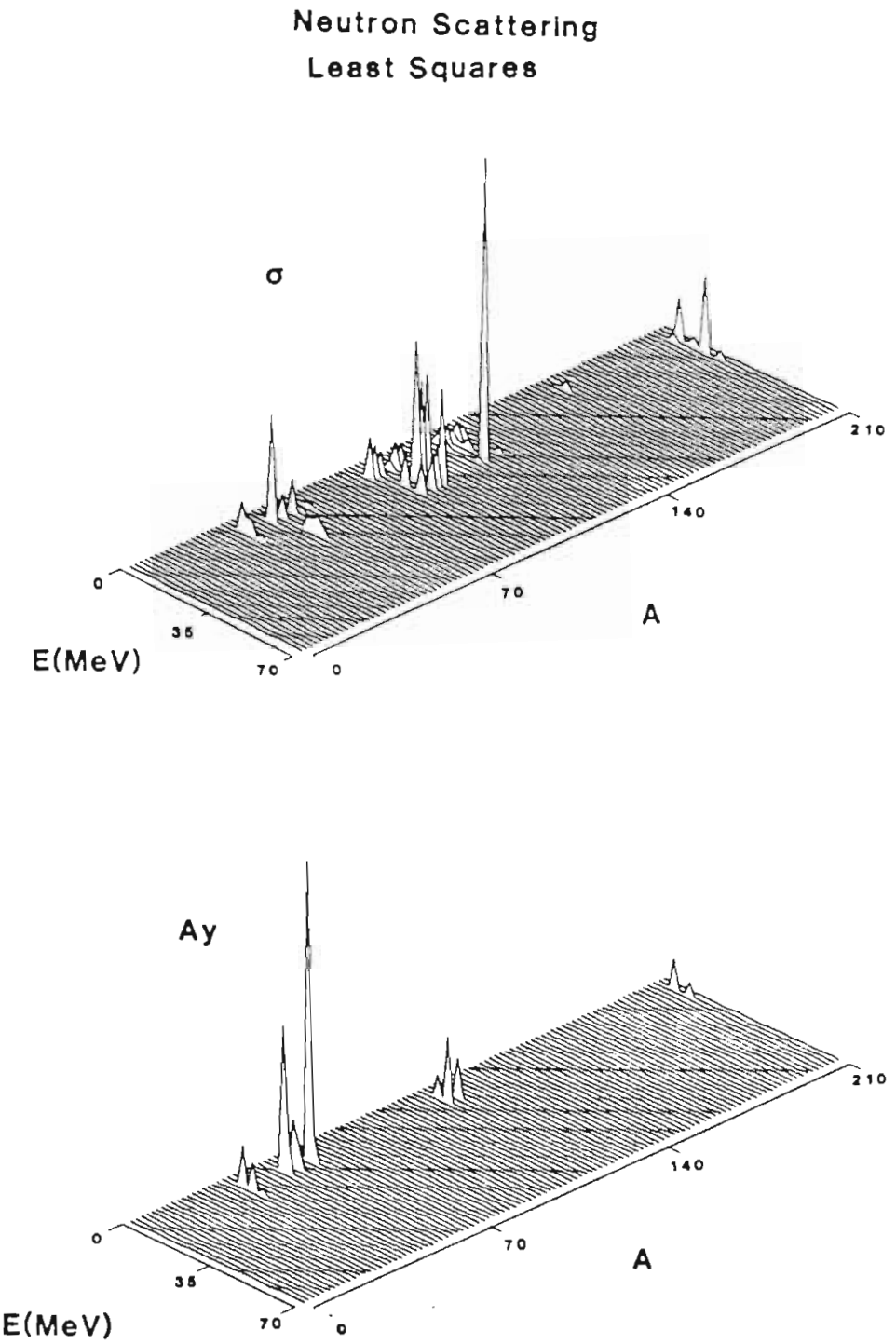

Fig. 7-2: Distribution of LSQ for (n,n) data. The upper plot is LSQ(σ) and the lower is for LSQ(A_y). The scaling is arbitrary. The values shown are renormalized as described in Sect. 7.2.2.

7.2.3 Effect of LSQ Renormalization on Final Parameters

The renormalization of the LSQ function (Sect. 6.4) was introduced because of the apparent poor distribution of the dataset LSQ's, as may be seen in Figs. 7-1 and 7-2. Our concern was for the apparent low weight which datasets from 65 MeV were having in the fit, as well as the inordinately large weight of some datasets, such as the 16-MeV Fe and Ni data, which appear to be not well described by any optical-model calculation. This new weighting was applied and used in obtaining the final fits, as shown by the solid curves in Figs. 4-1 to 5-19. To evaluate the effects of the weighting, the potential found in the weighted search was used in a search on the same data set, but with the weights for all datasets made equal. The final curves may be seen in the data figures as the dashed lines. The values of LSQ for the two parameter sets (when used in calculations on data with the same weighting) differ by less than 1%. As can be seen, the fits differ only slightly for most cases.

7.2.4 Uncertainties

Table 7-1 shows the uncertainties in the parameter values estimated from the covariance matrix (resulting from the MIGRAD search technique). These uncertainty estimates are defined as those which produce a change in the minimum value of the LSQ function (about 11) of 1. These are only valid if the function behaves parabolically in the region of the minimum. Table 7-2a shows the associated correlation matrix. There are few large correlations visible in the correlation matrix. The uncertainties are relatively large for some parts of the optical potential, most notably for the isovector terms, with 20% uncertainties, and the spin-orbit potential, with uncertainties of 10% to 50%.

The more accurate estimate of the uncertainties with MINOS is also shown in Table 7-1. These estimates have proved to be significantly larger than those from the covariance technique, apparently because of significant non-parabolic behavior of the function and because of large correlations between the parameters, especially between the various radius parameters. In particular, the real-central radius parameters

Table 7-2a

Correlation Matrix from MIGRAD Estimate of Best-Fit Parameter Values

For corresponding parameters and uncertainties, see Table 7-1. For interpretation, see Sect. 6-2 and 6-3. All terms of absolute value less than 0.2 have been omitted.

	V_o	V_t	V_e	r_o	$r_o^{(o)}$	a_o	W_{vo}	W_{so}	W_{st}	r_w	$r_w^{(o)}$	a_w	V_{so}	r_{so}	$r_{so}^{(o)}$	a_{so}
V_o	1															
V_t	-0.3	1														
V_e		-0.2	1													
r_o	-0.3		-0.3	1												
$r_o^{(o)}$	-0.4		-0.4	0.2	1											
a_o					-0.2	1										
W_{vo}		-0.2		0.3	0.4		1									
W_{so}	0.2							1								
W_{st}					0.2			0.3	1							
r_w	0.2		0.2	-0.2	-0.4		-0.2	-0.3		1						
$r_w^{(o)}$	0.2		0.3	-0.3	-0.5		-0.4	-0.3			1					
a_w						-0.7	-0.2			-0.9	0.2	1				
V_{so}			-0.2				0.3		0.2	0.3	-0.3	-0.2	1			
r_{so}	-0.4		0.4	-0.3	-0.5		-0.3	0.3		0.3	-0.5			1		
$r_{so}^{(o)}$	0.4		0.4	-0.3	0.5		0.4	0.2		-0.3	-0.4	-0.2		-0.7	1	
a_{so}										-0.2	-0.2			-0.2	0.2	1

have MINOS uncertainties which are 10 times larger than the corresponding MIGRAD uncertainties. The MINOS uncertainty suggests that our determination of the A-independent piece of the potential radius is consistent with 0. Examination of the MINOS searches shows a very strong correlation between r_0 and $r_0^{(0)}$ which is not reflected in the global search correlation matrix. It is this large negative correlation, coupled with the large uncertainty in the radius parameter r_0, which causes the large uncertainty in the parameter $r_0^{(0)}$.

In examination of an earlier difficulty with the parameterization, namely the poor quality of the fits to low-A ($\vec{p}$,p) scattering data, searches were made on a limited database of 85 datasets composed of closed-shell nuclei. This search yielded similar parameter values to those found in the global search, but made unusually large estimates of the uncertainties, based on the covariance. These were discounted until the MINOS results for the global dataset became available. The uncertainties from the "closed-shell" search are listed in Table 7-1, in parentheses, next to the uncertainties estimated in the final global search on the complete dataset. These earlier uncertainties are of the same order of magnitude as the MINOS confidence limits, with the exception of the parameter r_0. The correlation matrix produced by this search is shown in Table 7-2b, and reflects a much stronger set of correlations than found in the final global search.

From these results, it is clear that there is a problem with the uncertainty estimates in the final global search. Even though MIGRAD converges within the same criteria in both the global dataset and the restricted dataset, it does not appear to estimate the covariance in the global search correctly. Since the estimate seems more successful for a dataset only half as large, we must believe that the expansion of the dataset to include most of the available data introduces non-parabolic behavior of the LSQ function for which the covariance matrix estimate is inadequate. Because of both the accessibility of target materials and the low-energy-resolution requirements with closed-shell nuclei, the data quality is better. Also, there are data available for both proton and neutron scattering at more energies for these nuclei.

Table 7-2b

Covariance Matrix for Alternative Estimate of Covariance

For explanation of source of this matrix, see Sect. 7.2.4. See Table 7-2a for explanations of the table format.

	V_o	V_t	V_e	r_o	$r_o^{(0)}$	a_o	W_{vo}	W_{so}	W_{st}	r_w	$r_w^{(0)}$	a_w	V_{so}	r_{so}	$r_{so}^{(0)}$	a_{so}
V_o	1															
V_t	0.4	1														
V_e			1													
r_o	-0.7	-0.5	-0.2	1												
$r_o^{(0)}$	-0.9	-0.5		0.7	1											
a_o	0.6		-0.4	-0.4	-0.5	1										
W_{vo}		0.2	0.5		0.2	-0.3	1									
W_{so}	-0.4	-0.2	-0.2	0.4	0.5			1								
W_{st}	-0.2		0.2		0.2		0.2	0.5	1							
r_w		-0.2	-0.3	0.2	0.2	0.2	-0.2	0.4		1						
$r_w^{(0)}$	0.3			-0.2	-0.3		-0.2	-0.5	-0.4	-0.2	1					
a_w	0.4	0.2	0.2	-0.4	-0.5			-0.9	-0.5	-0.5	0.4	1				
V_{so}	0.3			-0.3	-0.4	0.2	-0.2	-0.2			0.2	0.3	1			
r_{so}	-0.9	-0.4		0.7	0.9	-0.4	0.2	0.6	0.3	0.2	-0.3	-0.5	-0.3	1		
$r_{so}^{(0)}$	0.9	0.4		-0.7	-0.9	0.5	-0.2	-0.5	-0.3	-0.2	0.3	0.5	0.3	-0.9	1	
a_{so}				-0.2	-0.2		-0.2	-0.2		-0.2		0.3	0.4	-0.2	0.1	1

The minimum LSQ for the fit to this sample of 85 datasets is about 1/3 smaller than that for the global sample of 143 datasets. Thus, it seems likely that this covariance problem is a function of the data quality and distribution.

In addition to making a correct estimation of the uncertainties, we must also interpret the magnitude of the uncertainties in terms of the probability that the current potential most correctly describes the data.

In order to estimate an uncertainty in the parameters, we must be able to identify the change in the LSQ function which represents a one-standard-deviation change. Our weighting procedure, described in Sect. 6.4, using the minimum LSQ value from an individual optical model fit to the data, should account for the effect of incorrect uncertainties in the data. This procedure should also account for those data which cannot be described by our assumed basis of the optical model. Even after this procedure, the minimum LSQ found was 11, far from the value we might have expected, 1. As described in Sect. 6.4, we have assumed here that our uncertainties should represent an arbitraryy 10% change in the LSQ value, that is a change of 1 in the minimum LSQ of 11. This arbitrary definition is not adequate for two reasons: (1) examination of many searches on global datasets of different combinations of data, show that the variations in the final values of the parameters is much less than those indicated by the MINOS uncertainties, and (2) the LSQ renormalization may tend to overcorrect for the effects of the model insufficiency.

The variations of the parameter values found by MINOPT in several searches (about 10) from somewhat different starting parameter sets give $\Delta(V_0)$=0.5 MeV, $\Delta(V_t)$=5 MeV, $\Delta(r_0)$=0.01 fm, $\Delta(r_0^{(0)})$=0.05 fm, all of which are much smaller than the MINOS uncertainties, yet it is this variation which we desire that the uncertainties should represent. Thus, we must suspect that choice of LSQ+ 10%(LSQ) to represent the uncertainties is too large. This would be the case if the renormalizations of the individual LSQ values were too large, as suggested in (2). At this point, the only means available to examine this question

is the use of tests, with synthetic data and small realistic datasets, to explore the effect of the LSQ renormalization on the estimate of uncertainties, and to explore the range of parameters likely to describe the data equally well.

These uncertainties also seem large because they represent the uncertainty in a parameter given that it was estimated simultaneously with the other parameters. This means that the correlations with the other parameters are included in this uncertainty. It is incorrect to say that a change in a particular parameter value by the uncertainty should give a change in the LSQ of 1. In fact, it is likely to be much larger than 1. Rather, the stated uncertainty in the parameter will give the change in LSQ of 1 only if all other parameters are adjusted to give minimum LSQ. Procedures for obtaining uncertainties in single parameters, or based only on a subset of the parameters exist and are described in (Eadi71, pg. 198).

In summary, the interpretation of our parameter uncertainties is not complete. We would hope to arrive at a suitable definition in the case of a model such as ours for data of this type. Nevertheless, with the definitions we have made, we have calculated uncertainties in the parameters in a model-independent fashion. These uncertainties are useful as relative indicators of how well the parameters are determined, and can at least tell users which parameters are most likely to change and which are least likely to change. We would also like to estimate the covariance matrix of the parameters in a model independent fashion, since we have seen strong correlations between parameters which are not indicated in the correlation matrix calculated from the parabolic approximation. MINOS does not provide any estimate of the correlations independent of the covariance matrix. The correlations are useful, even in the presence of non-linear behavior of the minimization function, for estimating uncertainties in functions of these parameters.

These optical model parameters will have many uses outside the immediate application of generating distorted waves (see, for example, Thom85); through the estimation of uncertainties including the

correlation information, each user can determine if these parameters are useful in a particular application. Until a technique can be derived for estimating correlations from the MINOS algorithm, it seems best to use the correlation matrix from the Table 7-2b, and the MINOS calculated uncertainties in Table 7-1a.

7.3 Comparison with Other Analyses

In addition to showing the calculations with the data used in the fitting, we compare this potential with results from other global parameterizations (Becc69, Rapa79b), as well as with a microscopic calculation (Jeuk77). We do not try to compare with the microscopic model of (Brie77). Their effective interaction is not available in a form usable at these energies, preventing us from making the calculations. The basis for our comparison is the volume integral per nucleon of the potentials as defined in Sect. 2.3.

The calculations were performed for several nuclei chosen 1) to span the region $40 \leq A \leq 208$ evenly, and 2) because nuclear charge densities were available (Jage74) for input into the microscopic calculations. The calculations were made using a program (McAb86) which incorporated the energy- and density-dependent potentials in the local density approximation described in (Jeuk77), including finite-range corrections with the ranges given by (Jeuk77). The nuclei were ^{40}Ca, ^{51}V, ^{55}Mn, ^{56}Fe, ^{59}Co, ^{60}Ni, ^{65}Cu, ^{68}Zn, ^{89}Y, ^{110}Cd, ^{120}Sn, ^{165}Ho, and ^{208}Pb. The matter densities used in these calculations were calculated from the parameterized charge distributions by unfolding the charge distributions of the individual protons and neutrons, then assuming that the proton and neutron distributions scale from the matter distributions as Z/A and N/A, respectively. The calculations were ultimately made using a parameterization of the charge densities as a function of A (McAb86), derived by fitting tabulated 2pF charge densities (Jage74). This was done because we found dramatic variation in the values of the volume integrals for the JLM calculations when charge densities which fit each nucleus separately were used. Because our goal is to compare global potentials, we need a calculation which averages over nuclei,

that is, one for a generic nucleus without the specific structure included in the exact densities. The parameters of the charge densities used are shown in Table 7-3.

7.3.1 Real Potential Comparison

The comparisons for the real potentials are shown in Figs. 7-3 to 7-6. The calculations for each figure were made for the incident energies of 10, 25, and 65 MeV. They are shown in two forms: 1) using the decomposition of the potential into isoscalar and isovector components, and 2) showing the proton and neutron potential volume integrals. Fig. 7-3 shows the volume integral of the real isoscalar part of the potential, as a function of A. Our isoscalar interaction agrees relatively well with the others shown, except at lower A where the earlier phenomenological potentials have relatively higher volume integrals; our energy dependence is also not as strong as any of the other potentials. The uncertainty calculated for the volume integral of the present work is about 8%; this has been calculated with the MINOS uncertainties in Table 7-1 and the covariance of Table 7-2b. Note that the "kinks" in the proton and neutron potentials (Fig. 7-5 and 7-6) arise from the not smooth variation of ϵ, the nuclear asymmetry, across the nuclei chosen.

In Fig 7-4, where the isovector volume integral is shown, the differences in the potentials are more striking. However, the uncertainty in our calculation is about 40%, being dominated by the uncertainty in the isovector depth. Even with the 40% uncertainty, it is clear that the Becc69 value for the isovector potential is much too large at most energies.

For comparison with phenomenological research, and to present the results as they are more commonly seen, Figs. 7-5 and 7-6 present the total volume integrals for (p,p) and (n,n) scattering. These were calculated for the same incident energies as the previous figures. Of course, the (p,p) scattering includes Coulomb corrections. The potential of Rapa79b is shown only for neutron scattering, since it was determined only with (n,n) scattering data. All these works agree

Table 7-3

Parameters of Nuclear Charge Radii

Nucleus	(Jage74)		Parameterized†	
	c	z	c'	z'
^{51}V	3.94	0.505	3.87	0.559
^{55}Mn	3.89	0.567	3.99	0.559
^{56}Fe	3.97	0.594	4.02	0.559
^{59}Co	4.08	0.569	4.10	0.559
^{65}Cu	4.27	0.579	4.26	0.559
^{68}Zn	4.38	0.569	4.33	0.559
^{89}Y	4.86	0.542	4.81	0.559
^{110}Cd	5.33	0.535	5.21	0.559
^{120}Sn	5.32	0.576	5.39	0.559
^{165}Ho	6.12	0.57	6.07	0.559
^{208}Pb	6.62	0.549	6.61	0.559

† The half-density radius c' is a parameterization of the local radius (Jage74), c, with the form:

$$c' = 1.238A^{1/3} - 0.721 \text{ fm.}$$

The value of z' is the arithmetic mean of the (Jage74) values of z.

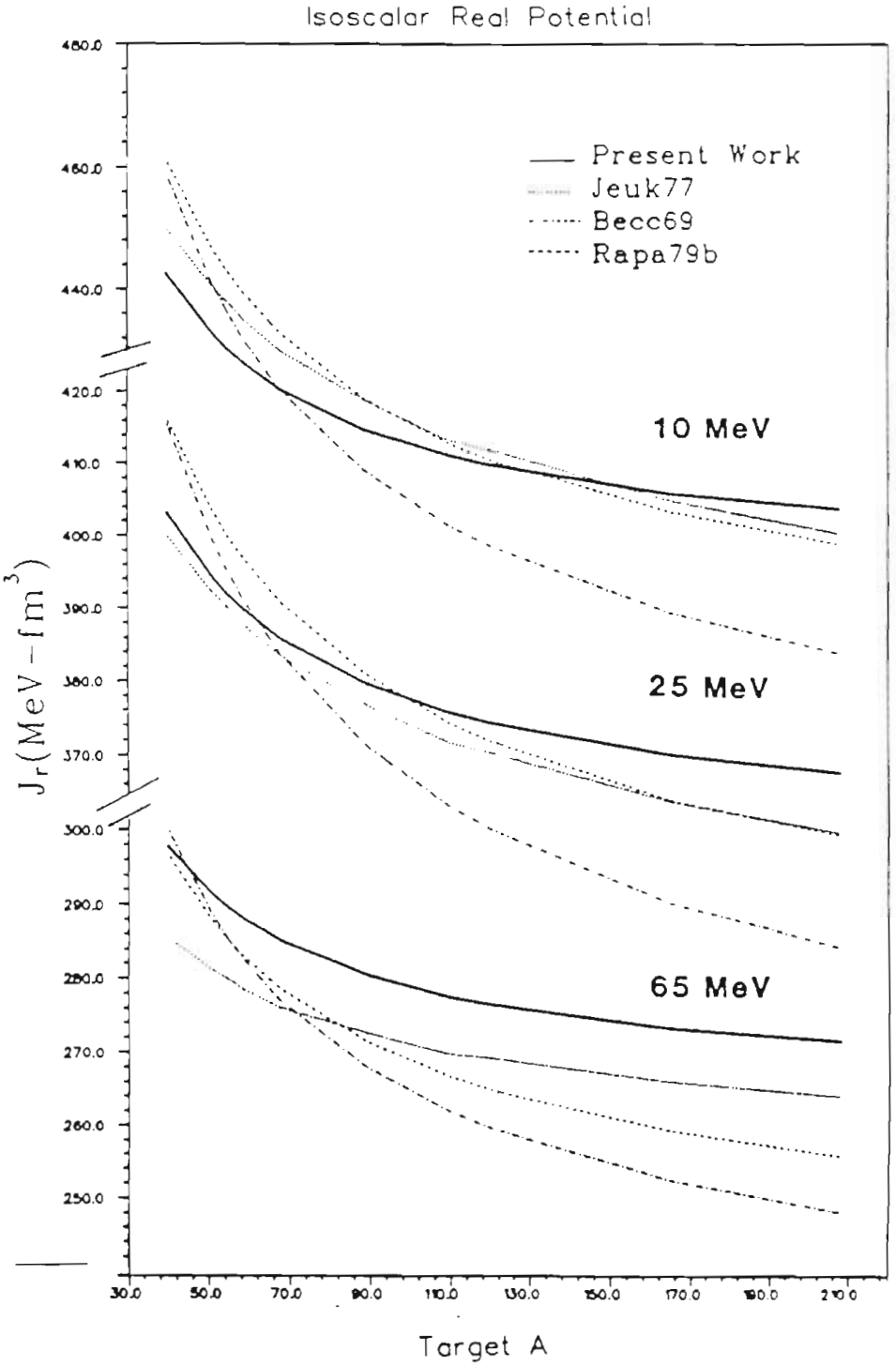

Fig. 7-3: Volume integrals of the real, isoscalar component of the optical potential. The curves are as shown and are described in Sect. 7.3.2.

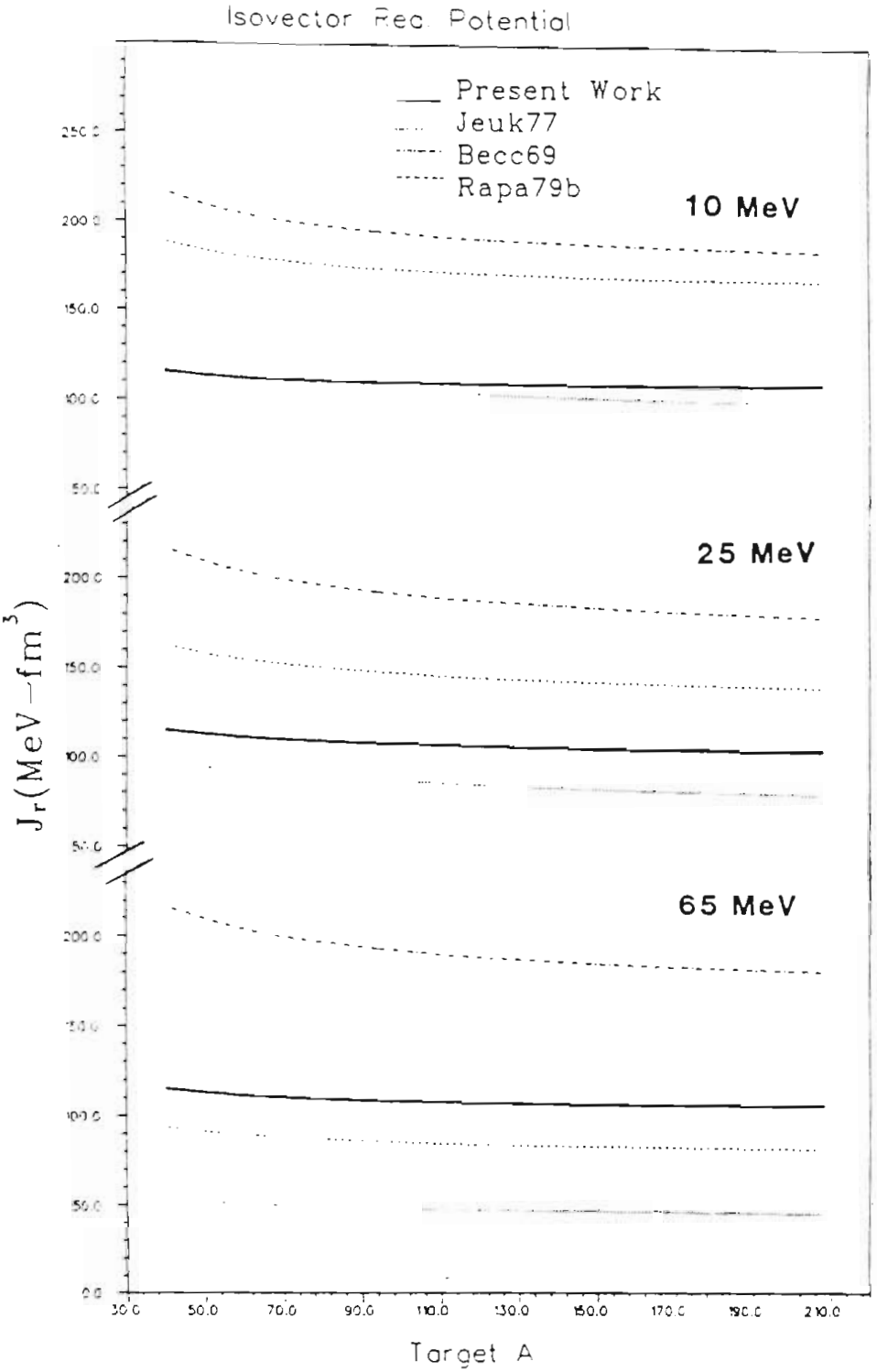

Fig. 7-4: Volume integrals of the isovector component of real potential. The curves are described in Sect. 7.3.2.

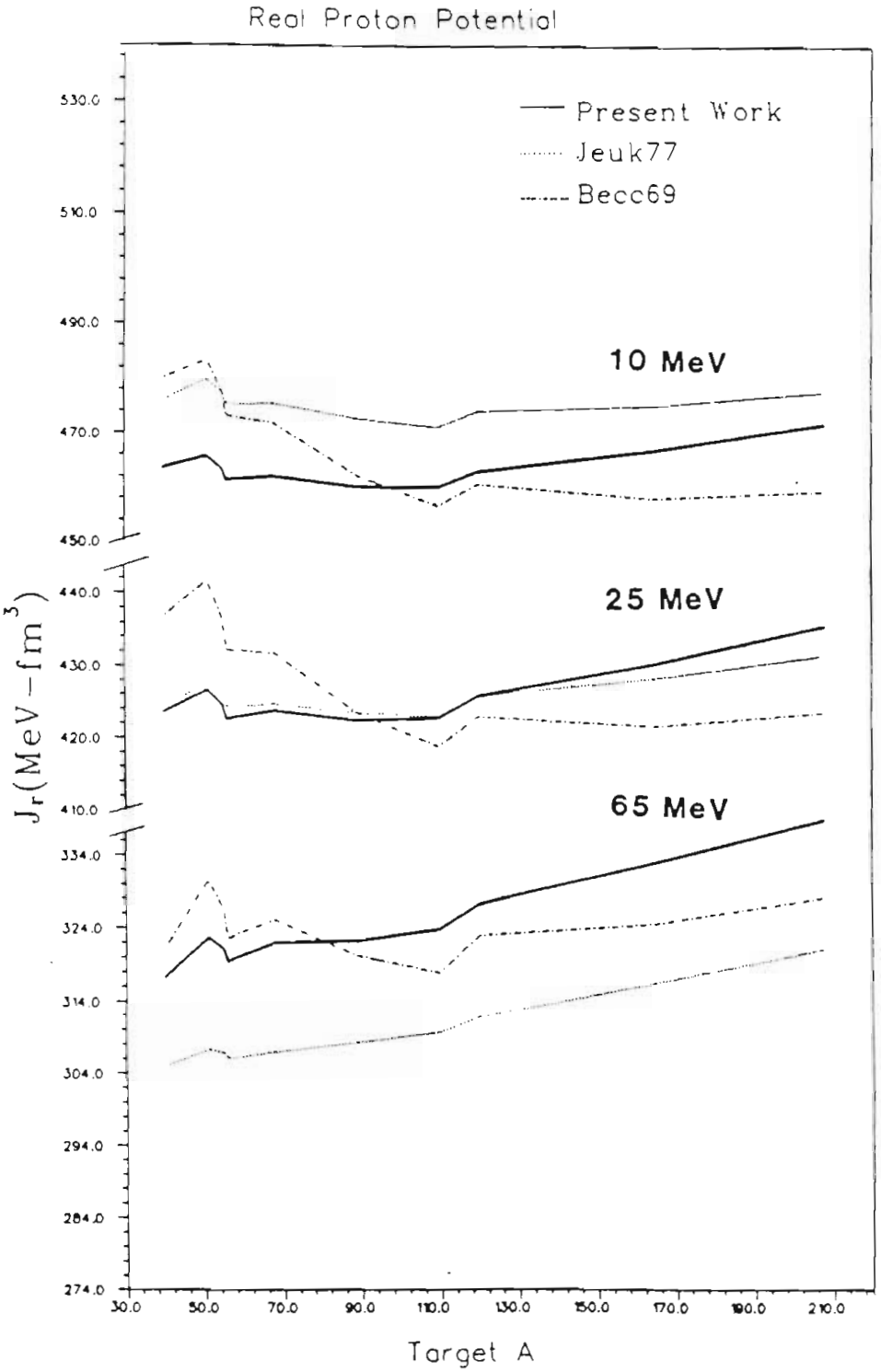

Fig. 7-5: Volume integral of the real central optical potential for proton scattering. These curves are described in Sect. 7.3.1.

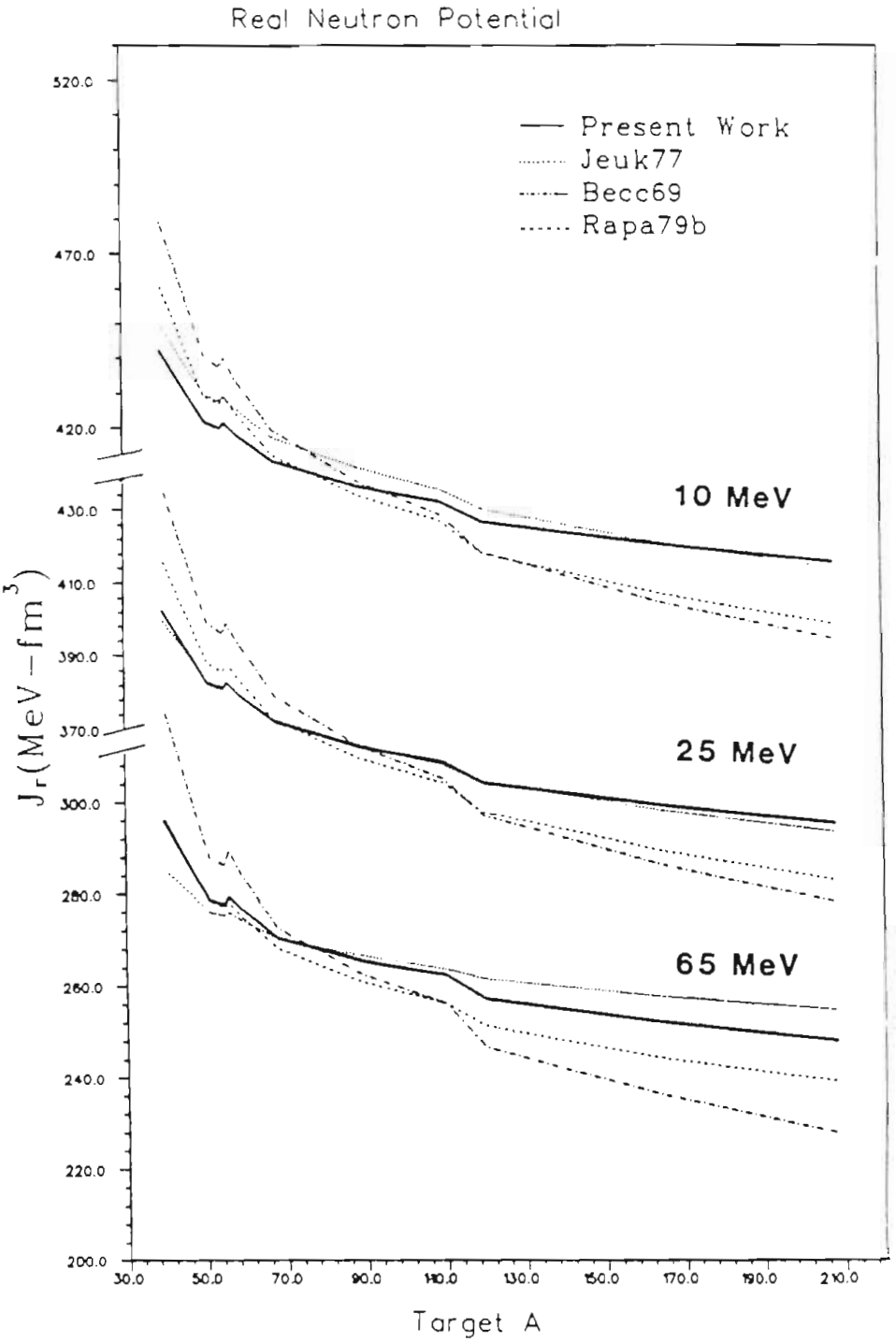

Fig. 7-6: Volume integral of the real central potential for (n,n) scattering. The curves are described in Sect. 7.3.2.

within the 8% uncertainty calculated earlier. Particularly noticeable is the close agreement between our potential and that of (Jeuk77) for all (n,n) energies and 25 MeV scattering in the (p,p). The energy 25 MeV is approximately the center of our energy range and is probably where the potential is best determined.

For a test of our consistency with analyses at higher energies, we calculated the volume integral of the real potential from the work of (Nada81) at 65 MeV where our analyses overlap. The average value for their dataset (see Sect. 2.4) is J_r/A = 314 MeV-fm^3. The average value for our potential at this energy is $J_r/A \approx 325$ MeV-fm^3, which agrees with the (Nada81) result within our uncertainty of 8%.

7.3.2 Imaginary Potential

We compare in Figs. 7-7 to 7-10 volume integrals of the imaginary potential, in a similar way to those for the real potential. The uncertainty in the isoscalar part of the interaction is about 10%, comparable to that of the real isoscalar volume integral, and about 50% for the isovector volume integrals. At most energies and A's the earlier works shown are outside the uncertainty of our potential, and at 65 MeV the difference is very significant for the (Rapa79b) potential isoscalar component. This is a consequence of the linear energy dependence they assumed for the absorptive potential, which can only be applied in a limited region of incident energy. The isovector volume integral, Fig. 7-8, is somewhat misleading for the 65 MeV comparison, since the surface absorption "cutoff" (Sect. 2.5.1) for the (Becc69) and the (Rapa79b) potentials is slightly below this energy. In these potentials, the isovector component of the absorption is only in the surface term and is zero when the surface absorption is zero. However, the isovector contribution is independent of energy up to this cutoff, and so is shown as such in this figure.

In the plots of the (p,p) and (n,n) imaginary volume integrals, one can see that the present work comes closest to being consistent with the phenomenological observation of (Agra75), J_w/A=115 MeV-fm^3 for (p,p) scattering for 10 MeV$\leq E_p \leq$200 MeV. In general, the 10% uncer-

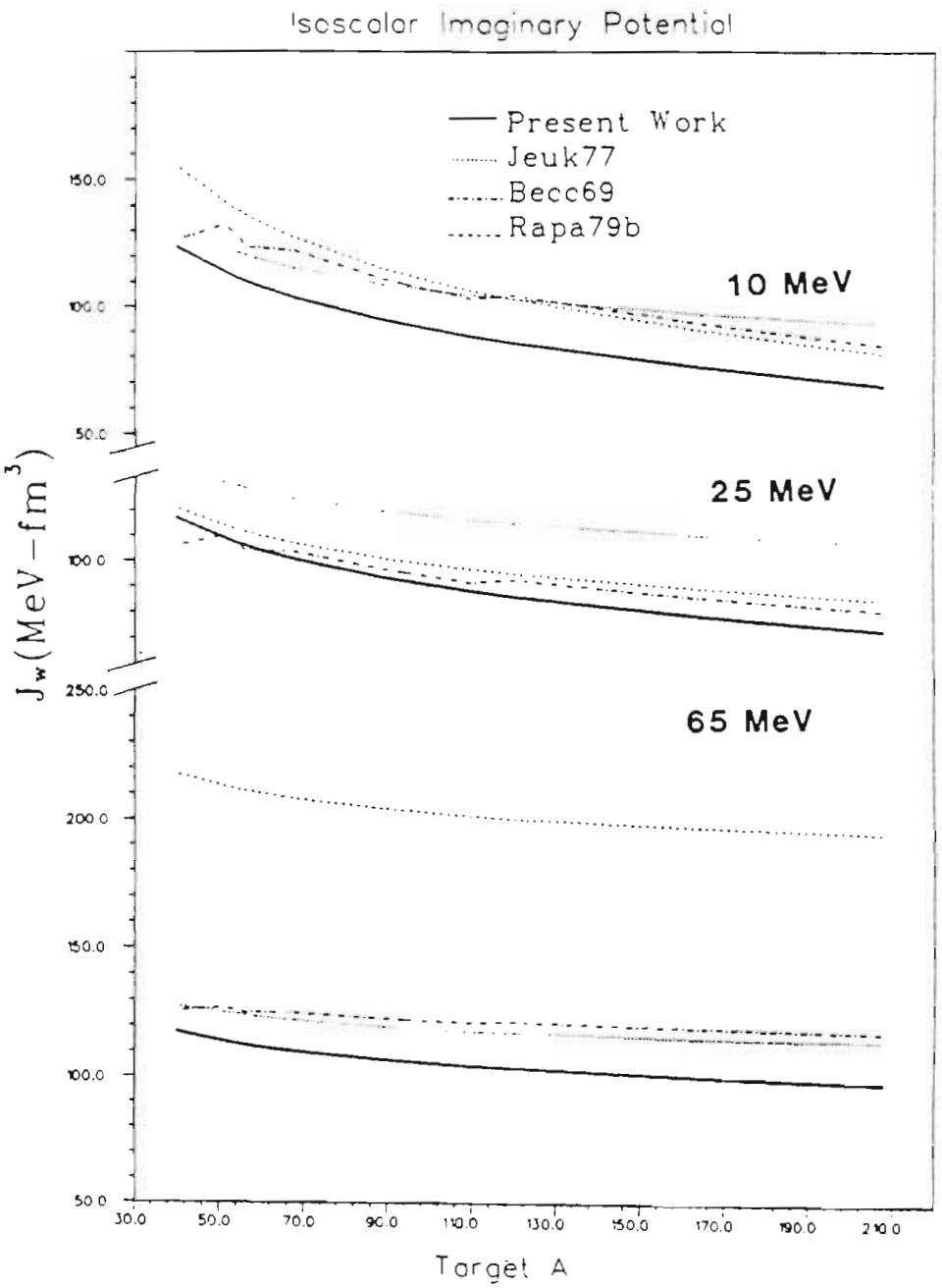

Fig. 7-7: Volume integrals of the isoscalar imaginary central potential. The curves are as shown, and are described in Sect 7.3.2.

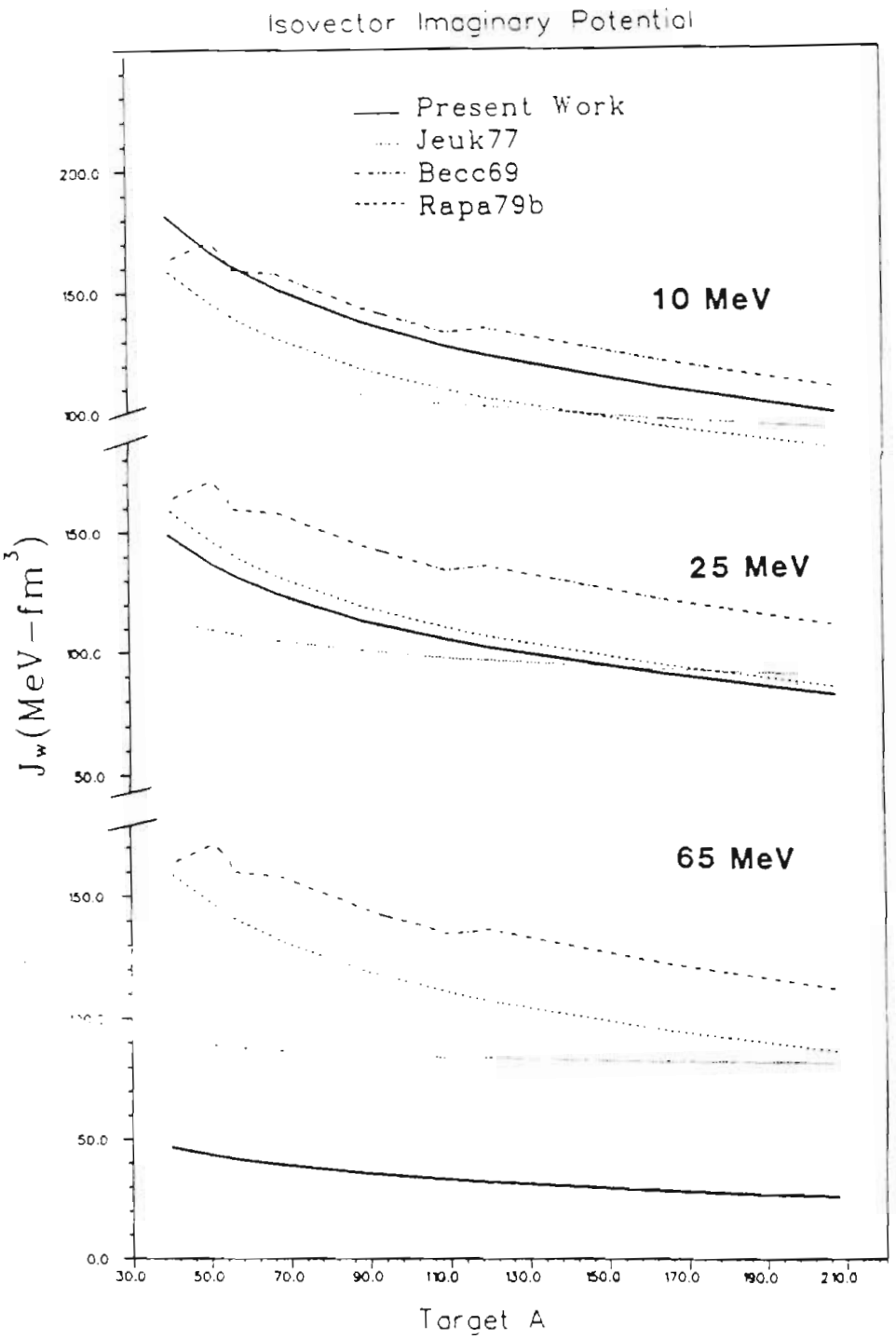

Fig. 7-8: Volume integral of the isovector imaginary central potential. The curves are as shown and are described in Sect. 7.3.3.

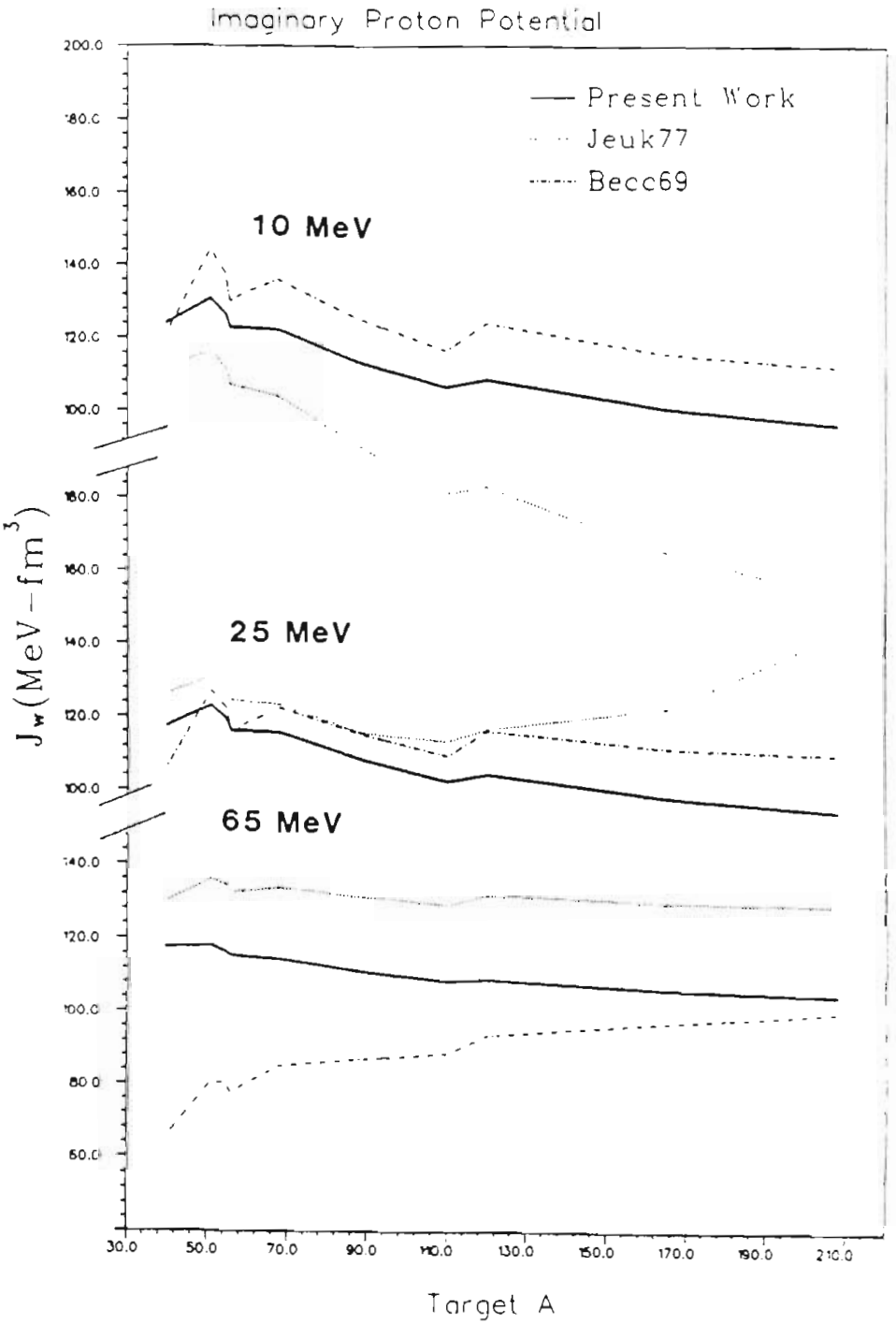

Fig. 7-9: Volume integrals for the imaginary central potential for (p,p) scattering. The curves shown are described in Sect. 7.3.3.

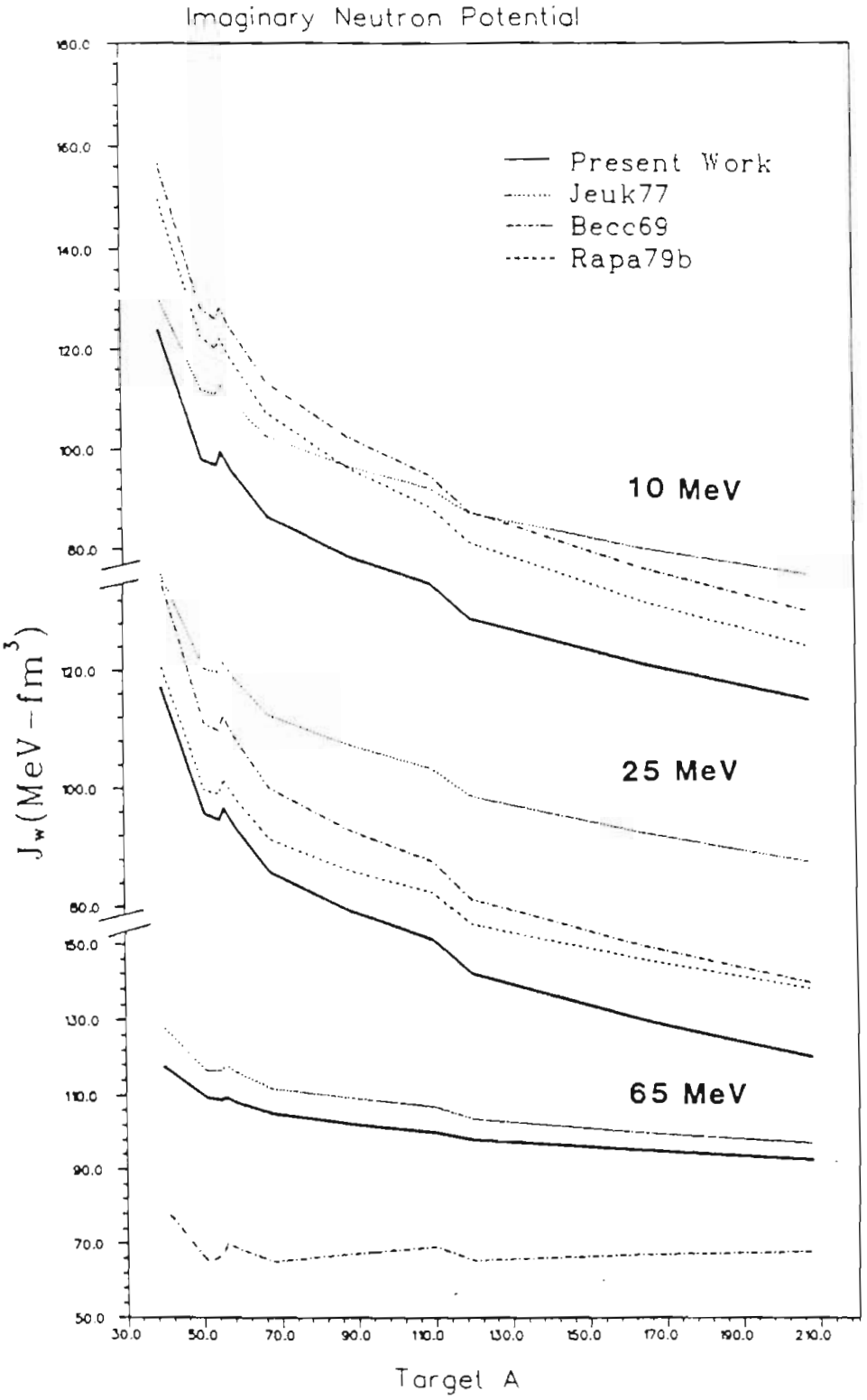

Fig. 7-10: Volume integrals for the imaginary central potential for (n,n) scattering. The curves shown are described in Sect. 7.3.3.

tainty places the volume integrals from the earlier works outside the range of consistency with our result.

In Fig. 7-11 we present the detailed energy dependence of the volume absorption for a particular nucleus, ^{110}Cd. Shown are the volume integrals for the present work, the volume integrals for (Becc69), and the phenomenology of (Agra75), as well as the decomposition of each of the empirical potentials into volume and surface components. As can be seen, over a limited energy range both empirical potentials are consistent with the (Agra75) result. Above 55 MeV, however, only the present parameterization is consistent. The microscopic potential, (Jeuk77) is not consistent at any low energy, being too small at 10 MeV, much too large at 20 to 30 MeV, and only approaching the phenomenology at 60 MeV.

A further test of our parameterization of the imaginary potential is the comparison with the (Nada81) analysis. Here they find a constant value of the volume integral of about $J_W/A=100\pm20$ MeV-fm^3, consistent with our estimate of $J_W/A\approx110$ MeV-fm^3.

7.3.3 Spin-Orbit Potential

Comparison of the spin-orbit result is straightforward, given the simplicity of the spin-orbit potential used in this work and other empirical potentials. The only microscopic calculation of the spin-orbit potential we might compare with is the work of (Brie77). Using for the comparison the integral K_R (Brie77),

$$K_R = 8\pi\, V_{so} R_{so} A^{-1/3}, \qquad 7\text{-}1$$

we see that the values for the present potential range from K_R=145 MeV-fm^3 to K_R=171 MeV-fm^3; for the Becchetti-Greenlees potential it is, K_R=157 MeV-fm^3; the result from (Brie77) is K_R=102 MeV-fm^3. The discrepancy between the empirical and microscopic results are significant. Folding-model calculations of the spin-orbit potential using other effective interactions (McAb86) are more consistent (K_R=150 MeV-fm^3) with our results. These microscopic results do agree with our result that the E- and A-dependence of the potential is small.

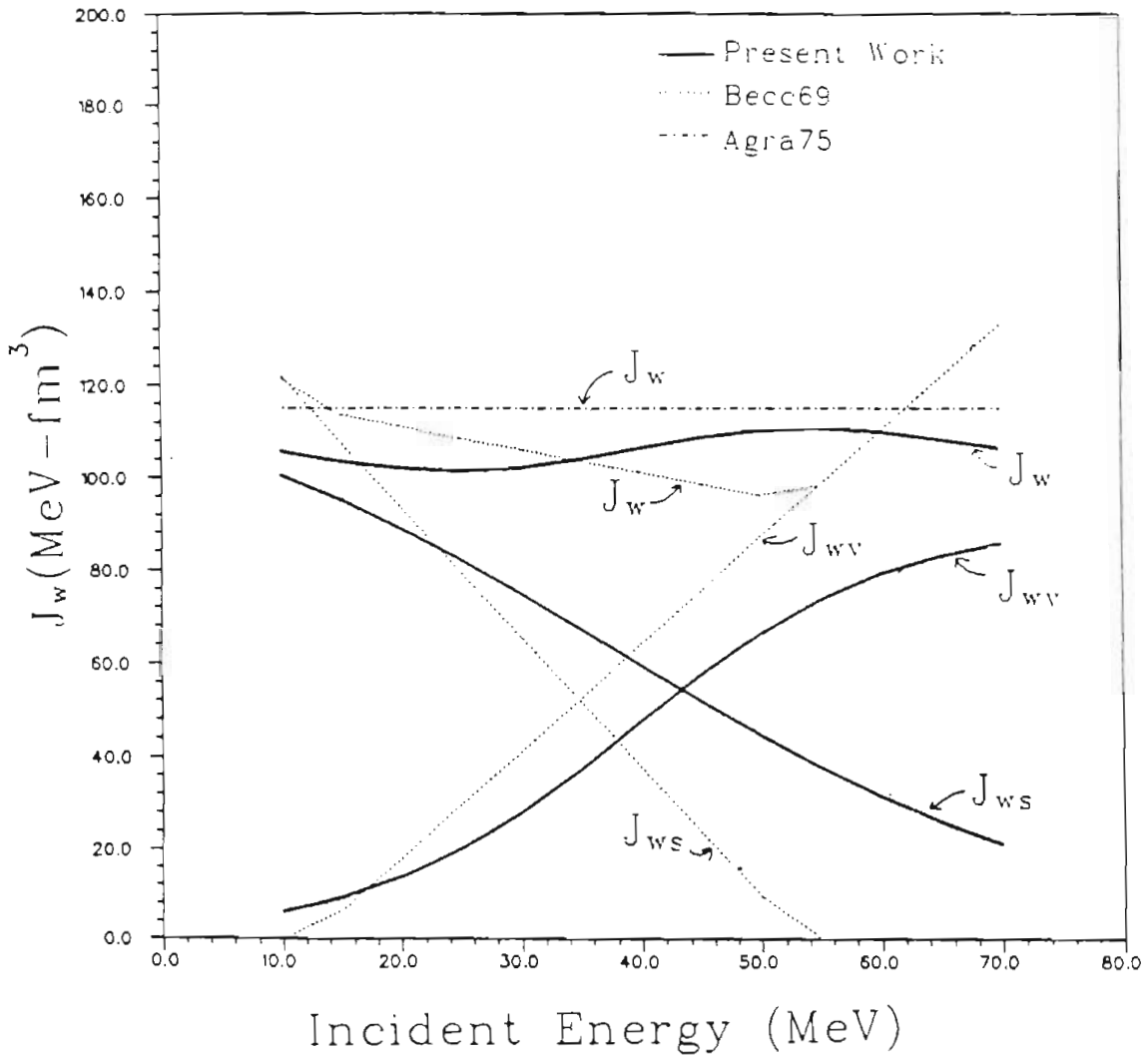

Fig. 7-11: Comparison of imaginary volume integrals for different empirical potentials and present work. The figure shows E-dependence for ^{110}Cd, comparing the different components and their sums. The solid curves are for the present work and the other curves are as shown. The dash-dot line shows the observation of (Agra75).

Our depths and geometry parameters are consistent with phenomenological observations (Coop80), which show $V_{so}=(6.0\pm0.5)-(0.023\pm0.012)E$ MeV, $r_{so}\approx1.1$ fm, and $a_{so}\approx0.62$ fm, with no A or isospin dependence.

An investigation was made of imaginary components to the spin-orbit potential (Sect. 2.2.4). This consisted of searches with and without an imaginary component of the spin-orbit potential as a variable parameter. The value found for this term was less than 1 MeV, with a MIGRAD estimated uncertainty much larger than 1 MeV. From this we concluded that this dataset is insensitive to any imaginary component of the spin-orbit potential. This is not unexpected in view of the small size (relative to the real component) of this potential as observed in $(\bar{n},n)$ scattering at low energy (Walt84).

7.4 Conclusions

This work intended to determine a semi-empirical parameterization of the nucleon-nucleus optical-model potential. This has been accomplished, but some problems remain. Nevertheless, this potential can serve as the basis for several continuing investigations, as well as the "traditional" functions of global optical potentials, as discussed in Sect. 2.1.

7.4.1 Final Potential

We have made a parameterization of the optical model by fitting a large database composed of 8000 data points in 142 datasets of 63 nuclei. This dataset is more complete than any previously used for fitting nucleon elastic scattering. These data have been fitted using a program designed expressly for global fitting of the optical potential. The process of searching on these data has involved making over 10^7 optical model calculations, which required over 100 hours on a 3-Mflop computer.

This potential describes well the large range of data given here. The real parts of this optical potential agree better with microscopic calculations of the optical model than do other empirical potentials. This potential should now replace other global optical potentials in most applications for which they have previously been used, such as the

prediction of elastic scattering, and as a source of distorted waves for other nuclear physics calculations. This potential is more suitable for comparison with microscopically derived optical potentials than previous results because (1) the database was much more extensive than in previous searches, and (2) because we have determined and included parameters which the folding model predicts as necessary.

7.4.2 Problems Remaining with this Work

The optical potential parameterization obtained is stable, by which we mean that we have found the best fit to these data and that subsequent searches will probably not find a significantly different potential which fits the data better. There are three problems with the work as it stands now: (1) the interpretation of the uncertainties, (2) the poor quality of fits to some datasets, and (3) the relative lack of data in the energy region from 30 MeV to 60 MeV.

Work must be done on making a reasonable interpretation of the uncertainties and the normalization of the LSQ function. This should proceed first through defining what we expect an uncertainty in an optical model parameter to represent. Then a procedure must be found to tell us the size of a change in LSQ that represents our definition. This may start with Monte-Carlo studies of the behavior of the fitting procedure with the optical model, to examine the factors (e.g. number of datasets, A- and E-distribution of the datasets) which contribute to variability of the final parameterization. Alternatively, if a theory of uncertainty for imprecise models of noisy data were to become available, we would have the problem solved.

The quality of the fits to some datasets may never be improved without sacrificing the global quality of the fit. Nevertheless, in conjunction with the investigations of the uncertainties, alternative parameterizations will be investigated, which may locally fit these datasets. Comparisons of the global potential with these would be useful.

7.4.3 Future Directions

There are several directions in which this research might expand. The first is to attempt to expand the database being described, to include data from other energies, and the complementary (p,n) data required for complete description of the isovector potential. The parameterization of the energy dependence of the imaginary potential and of the spin-orbit potential would be helped by the inclusion of new data in the large energy region of 30 to 60 MeV. These new measurements should include analyzing power data as well as the cross section data.

The observation of the poor fits to some datasets suggests the next possible direction for work, that of comparing parameters of detailed fits to individual nuclei with the global parameters in order to study systematics of nuclear structure. These comparisons may include simple coupled-channel calculations. The outcome of this research would be an understanding of how nuclear structure effects cause nuclei to deviate from the properties of the average nucleus. However, such calculations performed on the same scale as this research would require orders of magnitude greater computation speed than available for this work.

Finally, it should be possible to take this analysis one level deeper in the optical potential, to the parameterization of the effective interaction. This has been attempted earlier (Tarr79, Gree68); with faster computation, larger datasets, and the improved understanding of the effective nucleon-nucleon interaction available today, such a project becomes feasible. Its importance is emphasized in view of the effects of using globally parameterized densities as opposed to locally fitted densities (Jage74) in microscopic calculations (Jeuk77) of the optical potential. When the exact densities are used, the smooth behavior shown in Figs. 7-3 to 7-9 is replaced by wild fluctuations, presumably because of shell effects reflected in the exact densities. In addition, use of the exact densities removes one great uncertainty of the optical potential, that of the geometry parameters, which tend to be strongly correlated with the depth parameters. That analysis may in fact be the next generation of nuclear data fitting to follow the present semi-empirical optical-model analysis.

References

Agra75 D.C. Agrawal and P.C. Sood, Phys. Rev. C11 (1975) 1854.

Bain77 D.E. Bainum, R.W. Finlay, J. Rapaport, J.D. Carlson, and W.G. Love, Phys. Rev. C16 (1977) 1377.

Bain78 D.E. Bainum, R.W. Finlay, J. Rapaport, M.H. Hadizadeh, and J.D. Carlson, Nucl. Phys. A311 (1978) 492.

Becc69 F.D. Becchetti and G.W. Greenlees, Phys. Rev. 182 (1969) 1190.

Bert77 G. Bertsch, J. Borysowicz, H. McManus, W.G. Love, Nucl. Phys. A284 (1977) 399.

Blum66 L.N. Blumberg, E.E. Gross, A. van der Woude, A. Zucker, and R.H. Bassel, Phys. Rev. 147 (1966) 812.

Brie77 F.A. Brieva and J.R. Rook, Nucl. Phys. A291 (1977) 299; A291 (1977) 317; A297 (1977) 206; A307 (1978) 493.

Bris79 I. Brissaud, G. Berrier-Ronsin, J. Cameron, R. Frascaria, J. Kalifa, G. Bagieu, and R. de Swiniarski, Z. Phys. A293 (1979) 1.

Burk83 B.L. Burks, Ph.D. dissertation, University of North Carolina, 1983 (unpublished). Available from University Microfilms, Ann Arbor, MI.

Cleg74 T.B. Clegg, G.A. Bissinger, T.A. Trainor, Nucl. Instrum. and Methods 120 (1974) 445.

Coop80 S.G. Cooper and P.E. Hodgson, J. Phys. G6 (1980) L21.

Day67 B.D. Day, Rev. Mod. Phys. 39 (1967) 719.

DEC77 VAX-11 Architecture Handbook, Digital Equipment Corporation, (Maynard, MA, 1977).

Dela83a J.P. Delaroche, P.P. Guss, C.E. Floyd, R.L. Walter, and W. Tornow, Phys. Rev. C27 (1983) 2385.

Dela83b J.P. Delaroche, C.E. Floyd, P.P. Guss, R.C. Byrd, K. Murphy, G. Tungate, and R.L. Walter, Phys. Rev. C28 (1983) 1410.

Dela84 J.P. Delaroche, R.L. Varner, T.B. Clegg, R.E. Anderson, B.L.

Burks, E.J. Ludwig, and J.F. Wilkerson, Nucl. Phys. A414 (1984) 113.

Dice71 J.F. Dicello, G. Igo, W.T. Leland, F.G. Perey, Phys. Rev. C4 (1971) 1130.

Dodd77 D.C. Dodder, G.M. Hale, Nelson Jarmie, J.H. Jett, P.W. Keaton, Jr., R.A. Nisley, and K. Witte, Phys. Rev. C15 (1977) 518.

Eadi71 W.T. Eadie, E. Drijard, F.E. James, M. Roos, B. Sadoulet, Statistical Methods in Experimental Physics, (North Holland, Amsterdam, 1971).

East73 R.J. Eastgate, W.J. Thompson, and R.A. Hardekopf, Comp. Phys. Comm. 5 (1973) 69.

Eck77 J.S. Eck and W.J. Thompson, Am. J. Phys. 45 (1977) 161.

Elka82 S.M. El-Kadi, C.E. Nelson, F.O. Purser, R.L. Walter, A. Beyerle, C.R. Gould, and L.W. Seagondollar, Nucl. Phys. A390 (1982) 509.

Ferr77 J.C. Ferrer, J.D. Carlson, and J. Rapaport, Nucl. Phys. A275 (1977) 325.

Floy81 C.E. Floyd, dissertation, Duke University, 1981 (unpublished).

Floy83 C.E. Floyd, P.P. Guss, R.C. Byrd, K. Murphy, R.L. Walter, and J.P. Delaroche, Phys. Rev. C28 (1983) 1498.

FPS84 FPS-164 User's Handbook and Master Index, Release E (860-7481-001C), (Floating Point Systems, Portland, OR, 1984).

Fric67 M.P. Fricke, E.E. Gross, B.J. Morton, and A. Zucker, Phys. Rev. 156 (1967) 1207.

Fulm69 C.B. Fulmer, J.B. Ball, A. Scott, and M.L. Whitten, Phys. Rev. 181 (1969) 1565.

Gera84 H.V. von Geramb in Neutron-Nucleus Collisions: A Probe of Nuclear Structure, ed. J. Rapaport, R.W. Finlay, S.M. Grimes, and F.S. Dietrich, AIP Conf. Proc. 124, (1984) 14.

Goul83 C.R. Gould and N.R. Roberson, IEEE Trans. Nucl. Sci., NS-30 (1983) 3758 and references therein.

Gree68 G.W. Greenlees, G.J. Pyle and Y.C. Tang, Phys. Rev. 171 (1968) 1115.

Gree78 J.R. Green and D. Margerison, Statistical Treatment of

Experimental Data, (Elsevier, Amsterdam, 1978)

Guss82 P.P. Guss, dissertation, Duke University, 1982 (unpublished).

Guss85 P.P. Guss, R.C. Byrd, C.E. Floyd, C.R. Howell, K. Murphy, G. Tungate, R.S. Pedroni, R.L. Walter, J.P. Delaroche, and T.B. Clegg, Nucl. Phys. A438 (1985) 187.

Hall77 P.J. van Hall, J.P.M.G. Melssen, S.D. Wassenaar, O.J. Poppema, S.S. Klein, and G.J. Nijgh, Nucl. Phys. A291 (1977) 63.

Hall84 M. Haller, W. Kretschmer, R.E. Anderson, B.L. Burks, T.B. Clegg, E.J. Ludwig, R.L. Varner, J.F. Wilkerson, Nucl. Phys. A419 (1984) 45.

Hard72 R.A. Hardekopf, P.W. Lisowski, T.C. Rhea, and R.L. Walter, Nucl. Phys. A191 (1972) 468.

Hayn64 E.V. Haynsworth and K. Goldberg in Handbook of Mathematical Functions, ed. by M. Abramowitz and I.A. Stegun, (Dover, New York, 1964) pg. 803.

Hodg71 P.E. Hodgson, Nuclear Reactions and Nuclear Structure, (Clarendon Press, Oxford, 1971).

Hodg76 P.E. Hodgson, Phys. Lett. 65B (1976) 331.

Hodg84 P.E. Hodgson in Neutron-Nucleus Collisions: A Probe of Nuclear Structure, edited by J. Rapaport, R.W. Finlay, S.M. Grimes, and F.S. Dietrich, AIP Conf. Proc. 124, (1984) 1.

Hoga69 W.S. Hogan and R.G. Seyler, Phys. Rev. 177 (1969) 1706.

Hono84 G. Honore, private communication.

IBM76 Introduction to IBM Direct-Access Storage Devices and Organization Methods, (International Business Machines, Co. New York. 1976).

Ioan85 A.A. Ioannides and R.S. Mackintosh, Nucl. Phys. A438 (1985) 354.

Jaeg74 C.W. de Jaeger, H. de Vries, and C. de Vries, At. Data Nucl. Data Tables 14 (1974) 479.

Jame72 F. James, Function Minimization, in Proc. of the 1972 CERN Computing and Data Processing School, CERN 72-21 (1972).

Jame75 F. James and M. Roos, Comp. Phys. Comm. 10 (1975) 343.

Jame78 F. James, Interpretation of the Errors on Parameters as Given

by MINUIT, Supplement to CERN D-506, 1978 (unpublished).

Jeuk76 J.-P. Jeukenne, A. Lejeune, and C. Mahaux, Phys. Rep. 25C (1976) 83.

Jeuk77 J.-P. Jeukenne, A. Lejeune, and C. Mahaux, Phys. Rev. C15 (1977) 10; C16 (1977) 80.

Kail77 S. Kailas and S.K. Gupta, Phys. Lett. 71B (1977) 271.

Kail78 S. Kailas and S.K. Gupta, Phys. Rev. C17 (1978) 2236.

Kend81 J.K. Kendrick and E.J. Ludwig, Bull. Am. Phys. Soc. 26 (1981) 1234.

Kwam85 S.P. Kwam, S.T. Lam, G.C. Nielson, and H.S. Sherif, Phys. Rev. C31 (1985) 271.

Leeb79 J. Leeb and G. Eder, in Microscopic Optical Potentials, edited by H. von Geramb, (Springer Verlag, New York, 1979) pg. 181.

Mako72 W. Makofske, G.W. Greenlees, H.S. Liers, and G.J. Pyle, Phys. Rev. C5 (1972) 780.

Mari68 J.B. Marion and F.C. Young, Nuclear Reaction Analysis, (North Holland, 1968) pg. 30.

McAb86 T.L. McAbee, Ph.D. University of North Carolina, 1986 (unpublished).

Mcfa76 M.H. Mcfarlane and S.C. Pieper, PTOLEMY - A Program for Heavy-Ion Direct Reaction Calculations, ANL-76-11, Argonne National Laboratory (unpublished).

Mell83 S. Mellema, R.W. Finlay, F.S. Dietrich, F. Petrovich, Phys. Rev. C28 (1983) 2267.

Mels78 J.P.M.G. Melssen, dissertation, Technische Hogeschool Eindhoven, 1978 (unpublished).

Mels82 J.P.M.G. Melssen, P.J. van Hall, S.D. Wassenaar, O.J. Poppema, G.J. Nijgh, S.S. Klein, Nucl. Phys. A376 (1982) 183.

Melz85 R. Melzer, P. von Brentano, H. Paetz gen. Schieck, Nucl. Phys. A432 (1985) 363.

Mene71 J.J.H. Menet, E.E. Gross, J.J. Malanify, and A. Zucker, Phys. Rev. C4 (1971) 1114.

Myer73 W.D. Myers, Nucl. Phys. A204 (1973) 465.

Nada81 A.D. Nadasen, P.Schwandt, P.P. Singh, W.W. Jacobs, A.D.

Bacher, P.T. Debevec, M.D. Kaitchuk, and J.T. Meek, Phys. Rev. C23 (1981) 1023.

News74 H.W. Newson, E.G. Bilpuch, F.O. Purser, J.R. Boyce, T.B. Clegg, Nucl. Instrum. and Methods 122 (1974) 99.

Oers71 W.T.H. van Oers, Phys. Rev. C3 (1971) 1550.

Oers74 W.T.H. van Oers, Phys. Rev. C10 (1974) 307.

Ohls71 G. Ohlsen, J.L. McKibben, G.P. Lawrence, P.W. Keaton, Jr., and D.D. Armstrong, Phys. Rev. Lett. 27 (1971) 599.

Ohls73 G.G. Ohlsen and P.W. Keaton, Jr., Nucl. Instrum. and Methods 109 (1973) 41.

Orte80 Ortec Silicon Charged Particle Radiation Detectors Instruction Manual, 1980.

Oste84 F. Osterfeld and V.A. Madsen in Neutron-Nucleus Collisions: A Probe of Nuclear Structure, edited by J. Rapaport, R.W. Finlay, S.M. Grimes, and F.S. Dietrich, AIP Conf. Proc. 124, (1984) 26.

Patt76 D.M. Patterson, R.R. Doering, and A. Galonsky, Nucl. Phys. A263 (1976) 261.

Pere63 F.G. Perey, Phys. Rev. 131 (1963) 745.

Pres75 M.A. Preston and R.K. Bhaduri, Structure of the Nucleus, (Addison-Wesley, Reading, Mass., 1975)

Rapa78 J. Rapaport, T.S. Cheema, D.E. Bainum, R.W. Finlay, and J.D. Carlson, Nucl. Phys. A296 (1978) 95.

Rapa79a J. Rapaport, T.S. Cheema, D.E. Bainum, R.W. Finlay, and J.D. Carlson, Nucl. Phys. A313 (1979) 1.

Rapa79b J. Rapaport, V. Kulkarni, and R.W. Finlay, Nucl. Phys. A330 (1979) 15.

Rapa80a J. Rapaport, M. Mirzaa, H. Hadizadeh, D.E. Bainum, and R.W. Finlay, Nucl. Phys. A341 (1980) 56.

Rapa80b J. Rapaport, Phys. Lett. 92B (1980) 233.

Rapa82 J. Rapaport, Phys. Rep. 87 (1982) 25.

Saka82 H. Sakaguchi, M. Nakamura, K. Hatanaka, A. Goto, T. Noro, F. Ohtani, H. Sakamoto, H. Ogawa, and S. Kobayashi, Phys. Rev. C26 (1982) 944.

Saka83 H. Sakaguchi, Memoirs of the Faculty of Science, Kyoto University, Series A of Physics, Astrophysics, Geophysics and Chemistry, Vol. XXXVI, No. 2, Article 4, 1982.

Satc83 G.R. Satchler, Direct Nuclear Reactions, (Oxford, New York, 1983).

Schw71 P.Schwandt, T.B. Clegg, W. Haeberli, Nucl. Phys. A163 (19971) 432.

Smit82 D.L. Smith, Rev. Sci. Instrum. 54 (1983) 818.

Tarr79 A. Tarrats and J.L. Escudie, in Microscopic Optical Potentials, ed. by H.V. von Geramb, (Springer, Berlin, 1979) pg. 200.

Thom84 W.J. Thompson, Computing in Applied Science, (John Wiley and Sons, New York, 1984) pg. 152.

Thom85 W.J. Thompson, T.L. Mcabee, R.L. Varner, (to be submitted).

Tons80 S.A. Tonsfeldt, Ph.D. dissertation, University of North Carolina, 1980 (unpublished). Available from University Microfilms, Ann Arbor, MI.

TUCC84 How to Run Jobs on the FPS-164, Triangle Universities Computation Center, GIR-086-0, 1984, (unpublished).

Vaug81 D.W. Vaughn, Users Manual for the SCATDAT Data Base, 1981, (unpublished).

Varn85 R.L. Varner, UNC XSYStem Programming Guide, 1985 (unpublished).

Walt84 R.L. Walter, in Neutron-Nucleus Collisions: A Probe of Nuclear Structure, edited by J. Rapaport, R.W. Finlay, S.M. Grimes, and F.S. Dietrich, AIP Conf. Proc. 124, (1984) 53.

Wass82 S.D. Wassenaar, dissertation, Technische Hogeschool Eindhoven, 1982, (unpublished).

XSYS84 M.A. Boyd, C.R. Gould and N.R. Roberson, TUNL Xsystem Manual, 1984 (unpublished).

Yimi82 Y. Yiming, C.E. Brient, R.W. Finlay, G. Randers-Pehrson, A. Marcinkowski, R.C. Taylor, J. Rapaport, Nucl. Phys. A390 (1982) 449.

Appendix

This Appendix contains a tabulation of the angular distributions of 16 MeV $(\vec{p},p)$ scattering measured at TUNL. The procedure for the analysis of the data is described in Chapter 3 of this dissertation; the assignment of uncertainties is described in Chapter 4. For the normalization uncertainty, it is best to assume an uncertainty of 5%, for all targets but, ^{50}Ti, ^{58}Ni, ^{63,65}Cu, and ^{208}Pb. For these targets, assume a 10% normalization uncertainty.

The format of the tables is identical for each isotope. It is,

Angle, $\sigma(\theta)$, $\Delta\sigma(\theta)$, A_y, ΔA_y

All uncertainties are absolute.

TUNL Data

$^{40}Ca(p,p)$ E_p = 16 MeV

Angle(cm)	Cross Section		Analyzing Power	
25.6	561.600	8.347	-0.1171	0.0062
30.7	245.500	3.659	-0.0461	0.0064
35.8	105.000	1.540	0.1697	0.0064
40.9	65.010	0.970	0.3255	0.0069
46.0	65.460	0.956	0.0975	0.0063
51.1	76.140	1.124	-0.1819	0.0065
56.2	79.360	1.157	-0.3895	0.0062
61.3	72.890	1.082	-0.5588	0.0065
66.3	54.130	0.792	-0.6864	0.0063
71.4	37.420	0.558	-0.8087	0.0068
76.4	21.030	0.309	-0.8547	0.0064
81.4	11.410	0.177	-0.7801	0.0079
86.5	6.846	0.110	-0.4049	0.0099
91.5	7.092	0.109	-0.1203	0.0085
96.5	10.330	0.156	-0.1542	0.0078
101.4	15.170	0.228	-0.2432	0.0073
106.4	19.220	0.295	-0.2891	0.0084
111.4	21.670	0.327	-0.2995	0.0077
116.3	21.530	0.329	-0.3064	0.0082
121.3	19.500	0.296	-0.3510	0.0079
126.2	15.690	0.237	-0.4540	0.0076
131.1	11.590	0.175	-0.6177	0.0075
136.0	8.450	0.127	-0.8460	0.0070
140.9	6.834	0.103	-0.8678	0.0070
145.8	7.049	0.110	-0.4851	0.0088
150.7	8.554	0.132	0.0255	0.0087
155.6	10.540	0.157	0.4020	0.0073
160.5	12.420	0.185	0.6147	0.0069
165.4	13.500	0.201	0.6800	0.0069
170.3	13.650	0.203	0.5807	0.0069

TUNL Data

$^{48}Ti(p,p)$ E_p = 16 MeV

Angle(cm)	Cross Section		Analyzing Power	
20.4	1267.000	26.891	-0.0163	0.0099
25.5	577.600	11.730	0.0049	0.0098
30.6	278.800	5.636	0.0691	0.0099
35.7	150.200	3.032	0.1488	0.0099
40.8	93.040	1.886	0.1534	0.0101
45.9	76.590	1.544	0.0236	0.0099
50.9	63.150	1.279	-0.1479	0.0101
56.0	52.500	1.058	-0.3220	0.0099
61.1	34.550	0.706	-0.5035	0.0109
66.1	19.850	0.402	-0.7078	0.0101
71.2	9.304	0.191	-0.9241	0.0107
76.2	3.137	0.065	-0.5838	0.0110
81.2	3.110	0.066	0.8134	0.0122
86.2	5.779	0.120	0.6588	0.0115
91.2	9.087	0.185	0.2763	0.0105
96.2	10.950	0.222	-0.0208	0.0103
101.2	11.410	0.232	-0.2622	0.0103
106.2	9.769	0.198	-0.4622	0.0101
111.2	7.391	0.151	-0.6474	0.0107
116.1	5.024	0.104	-0.7803	0.0110
121.1	2.864	0.060	-0.8500	0.0115
126.0	1.351	0.029	-0.6708	0.0124
130.9	0.653	0.015	0.0121	0.0157
135.9	0.776	0.016	0.5507	0.0124
140.8	1.408	0.029	0.3456	0.0118
145.7	2.425	0.051	0.2958	0.0119
150.6	3.500	0.074	0.3520	0.0123
155.5	4.215	0.086	0.5293	0.0104
160.4	4.865	0.100	0.6488	0.0107
165.3	4.962	0.101	0.7249	0.0102
170.2	5.126	0.106	0.6286	0.0108

TUNL Data

^{50}Ti(p,p) E_p = 16 MeV

Angle(cm)	Cross Section		Analyzing Power	
25.5	637.057	13.744	0.0120	0.0083
30.6	319.104	6.849	0.0728	0.0083
35.7	174.709	3.737	0.1347	0.0082
40.8	112.565	2.417	0.1328	0.0089
45.8	82.404	1.781	0.0233	0.0082
50.9	66.022	1.445	-0.1330	0.0090
56.0	46.310	1.033	-0.2998	0.0085
61.0	31.362	0.711	-0.4673	0.0103
66.1	14.192	0.333	-0.6896	0.0096
71.1	4.269	0.116	-0.7697	0.0147
76.1	2.360	0.056	0.2196	0.0109
81.2	3.581	0.081	0.8710	0.0105
86.2	6.685	0.148	0.5072	0.0109
91.2	9.016	0.199	0.2126	0.0090
96.2	10.190	0.230	-0.0244	0.0101
101.2	9.583	0.217	-0.2415	0.0091
106.1	7.724	0.177	-0.4430	0.0094
111.1	5.302	0.126	-0.6280	0.0104
116.1	3.149	0.077	-0.7743	0.0106
121.0	1.516	0.039	-0.7081	0.0136
126.0	0.784	0.022	0.0984	0.0194
130.9	0.900	0.022	0.8293	0.0123
135.8	1.627	0.034	0.5589	0.0103
140.8	2.509	0.052	0.3250	0.0097
145.7	3.358	0.073	0.2475	0.0112
150.6	3.957	0.086	0.2869	0.0096
155.5	4.160	0.093	0.4238	0.0100
160.4	4.341	0.101	0.6185	0.0114
165.3	4.066	0.094	0.7251	0.0097
170.2	3.423	0.085	0.7183	0.0118

TUNL Data

$^{54}Fe(p,p)$ E_p = 16 MeV

Angle(cm)	Cross Section		Analyzing Power	
25.5	846.733	10.626	-0.0086	0.0067
30.5	443.877	5.617	0.0541	0.0067
35.6	264.415	3.167	0.1148	0.0065
40.7	171.294	2.070	0.1190	0.0067
45.8	124.073	1.486	0.0302	0.0065
50.8	90.357	1.106	-0.1176	0.0068
55.9	63.400	0.752	-0.3063	0.0065
60.9	36.170	0.440	-0.5066	0.0072
66.0	17.490	0.210	-0.7658	0.0068
71.0	7.177	0.095	-0.8032	0.0090
76.1	3.612	0.045	0.4346	0.0082
81.1	5.581	0.074	0.9793	0.0090
86.1	9.395	0.120	0.5839	0.0087
91.1	12.220	0.150	0.2350	0.0075
96.1	13.190	0.161	-0.0607	0.0074
101.1	12.160	0.149	-0.3374	0.0075
106.1	9.659	0.118	-0.5854	0.0073
111.0	6.655	0.084	-0.7834	0.0078
116.0	3.978	0.058	-0.8880	0.0111
120.9	2.109	0.029	-0.6481	0.0106
125.9	1.096	0.018	0.3162	0.0169
130.8	1.069	0.015	0.8857	0.0098
135.8	1.861	0.025	0.3497	0.0099
140.7	3.208	0.040	0.0049	0.0079
145.6	4.893	0.063	-0.0242	0.0090
150.5	6.264	0.079	0.1269	0.0086
155.5	7.655	0.093	0.3302	0.0073
160.4	8.235	0.100	0.5583	0.0072
165.3	8.671	0.105	0.6488	0.0071
170.2	8.529	0.104	0.6303	0.0072

TUNL Data

$^{56}Fe(p,p)$ E_p = 16 MeV

Angle(cm)	Cross Section		Analyzing Power	
20.4	2141.000	40.824	0.0170	0.0095
25.4	959.600	17.675	0.0160	0.0094
30.5	499.100	9.060	0.0649	0.0095
35.6	281.200	5.096	0.1098	0.0095
40.7	174.100	3.168	0.0959	0.0098
45.7	116.600	2.107	-0.0004	0.0095
50.8	80.890	1.476	-0.1480	0.0099
55.9	51.800	0.937	-0.3203	0.0095
60.9	28.520	0.537	-0.5106	0.0113
66.0	11.680	0.214	-0.6739	0.0099
71.0	4.104	0.082	-0.1813	0.0141
76.0	3.943	0.073	0.9492	0.0100
81.0	7.305	0.140	0.7091	0.0115
86.0	11.100	0.208	0.3580	0.0111
91.0	13.120	0.241	0.0776	0.0103
96.0	12.650	0.232	-0.1706	0.0102
101.0	10.730	0.198	-0.4012	0.0104
106.0	7.806	0.143	-0.6464	0.0101
111.0	4.914	0.093	-0.8670	0.0113
116.0	2.716	0.057	-0.9675	0.0127
120.9	1.367	0.029	-0.5325	0.0169
125.9	0.933	0.021	0.6711	0.0170
130.8	1.283	0.025	0.8497	0.0131
135.7	2.090	0.040	0.3656	0.0124
140.7	3.128	0.058	0.0118	0.0113
145.6	4.099	0.080	-0.1343	0.0133
150.5	4.568	0.091	-0.1149	0.0144
155.4	4.917	0.092	0.0540	0.0113
160.4	4.514	0.086	0.2851	0.0122
165.3	4.479	0.084	0.4975	0.0113
170.2	3.505	0.068	0.6262	0.0126

TUNL Data

$^{58}Ni(p,p)$ E_p = 16 MeV

Angle(cm)	Cross Section		Analyzing Power	
25.4	1114.512	11.098	-0.0009	0.0128
30.5	589.146	5.854	0.0548	0.0129
35.6	346.585	3.415	0.0925	0.0129
40.7	222.805	2.195	0.0665	0.0130
45.7	147.927	1.463	-0.0382	0.0129
50.8	100.012	1.000	-0.2178	0.0130
55.8	63.159	0.634	-0.4324	0.0129
60.9	33.634	0.341	-0.6640	0.0134
65.9	14.817	0.481	-0.8271	0.0134
71.0	6.232	0.204	-0.3172	0.0149
76.0	7.109	0.193	0.9587	0.0145
81.0	9.316	0.304	0.8974	0.0141
86.0	13.355	0.435	0.5165	0.0139
91.0	15.720	0.510	0.1516	0.0132
96.0	15.183	0.494	-0.1565	0.0138
101.0	12.573	0.408	-0.4507	0.0132
106.0	9.472	0.308	-0.7346	0.0134
111.0	6.268	0.204	-0.9662	0.0135
115.9	3.571	0.116	-1.0040	0.0138
120.9	2.034	0.067	-0.5412	0.0149
125.8	1.300	0.044	0.5424	0.0183
130.8	1.301	0.044	0.9630	0.0174
135.7	1.954	0.064	0.2931	0.0149
140.7	3.255	0.106	-0.1749	0.0141
145.6	5.161	0.169	-0.2673	0.0147
150.5	6.767	0.221	-0.1313	0.0142
155.4	7.945	0.258	0.0836	0.0136
160.3	8.222	0.267	0.3392	0.0136
165.3	7.749	0.252	0.5378	0.0134
170.2	6.872	0.223	0.5914	0.0135

TUNL Data

$^{60}Ni(p,p)$ E_p = 16 MeV

Angle(cm)	Cross Section		Analyzing Power	
25.4	1117.000	14.375	0.0370	0.0093
30.5	620.500	8.074	0.0646	0.0092
35.6	347.400	4.347	0.0877	0.0091
40.6	208.500	2.679	0.0487	0.0098
45.7	130.800	1.628	-0.0725	0.0092
50.8	83.140	1.075	-0.2385	0.0101
55.8	49.060	0.613	-0.4019	0.0093
60.8	25.080	0.350	-0.5534	0.0120
65.9	10.550	0.137	-0.4550	0.0102
70.9	5.571	0.082	0.5311	0.0129
75.9	7.580	0.099	0.8897	0.0097
81.0	11.990	0.162	0.5611	0.0109
86.0	15.390	0.207	0.2470	0.0110
91.0	15.820	0.203	0.0037	0.0099
96.0	13.920	0.181	-0.2405	0.0102
101.0	10.420	0.136	-0.4991	0.0103
105.9	6.820	0.089	-0.7741	0.0099
110.9	4.228	0.059	-0.9745	0.0103
115.9	2.320	0.037	-0.7100	0.0142
120.8	1.728	0.027	0.2307	0.0149
125.8	1.808	0.027	0.9287	0.0117
130.8	2.283	0.031	0.7665	0.0109
135.7	2.997	0.040	0.2675	0.0109
140.6	3.837	0.050	-0.1128	0.0102
145.6	4.626	0.064	-0.3100	0.0120
150.5	5.289	0.072	-0.2893	0.0117
155.4	5.426	0.071	-0.1269	0.0105
160.3	5.021	0.066	0.1266	0.0107
165.3	4.499	0.060	0.3756	0.0108
170.2	3.738	0.051	0.5278	0.0111

TUNL Data

$^{63}Cu(p,p)$ E_p = 16 MeV

Angle(cm)	Cross Section		Analyzing Power	
25.4	1231.854	21.825	0.0291	0.0134
30.5	641.660	11.370	0.0567	0.0135
35.5	353.020	6.255	0.0575	0.0135
40.6	193.882	3.444	0.0141	0.0136
45.7	119.191	2.115	-0.1141	0.0135
50.7	72.248	1.286	-0.2683	0.0137
55.8	38.776	0.689	-0.4128	0.0136
60.8	18.784	0.338	-0.4817	0.0142
65.8	9.062	0.163	-0.1366	0.0143
70.9	7.321	0.134	0.7388	0.0149
75.9	11.111	0.201	0.7080	0.0144
80.9	14.771	0.266	0.4164	0.0142
85.9	17.289	0.311	0.1546	0.0141
90.9	16.434	0.293	-0.0777	0.0137
95.9	12.997	0.235	-0.3196	0.0143
100.9	8.704	0.156	-0.5754	0.0139
105.9	5.185	0.094	-0.8577	0.0141
110.9	2.725	0.050	-0.9730	0.0147
115.8	1.737	0.032	-0.2552	0.0156
120.8	1.768	0.033	0.7710	0.0154
125.8	2.459	0.046	0.9120	0.0151
130.7	3.195	0.060	0.6148	0.0155
135.7	3.686	0.067	0.1655	0.0143
140.6	4.065	0.073	-0.2401	0.0143
145.5	4.396	0.082	-0.5078	0.0157
150.5	4.460	0.082	-0.5475	0.0150
155.4	4.471	0.082	-0.4015	0.0149
160.3	4.126	0.075	-0.1047	0.0147
165.2	3.523	0.064	0.2244	0.0150
170.2	2.883	0.053	0.4585	0.0148

TUNL Data

$^{65}Cu(p,p)$ E_p = 16 MeV

Angle(cm)	Cross Section		Analyzing Power	
25.4	1430.450	21.738	0.0361	0.0088
30.5	722.729	10.979	0.0501	0.0088
35.5	383.361	5.833	0.0454	0.0089
40.6	195.573	3.017	-0.0276	0.0098
45.6	113.686	1.750	-0.1650	0.0096
50.7	64.347	1.008	-0.3439	0.0107
55.7	33.693	0.523	-0.4767	0.0101
60.8	15.796	0.266	-0.3665	0.0144
65.8	9.183	0.155	0.3110	0.0146
70.8	9.643	0.164	0.8070	0.0139
75.9	13.714	0.233	0.6359	0.0147
80.9	17.747	0.286	0.2949	0.0122
85.9	18.957	0.297	0.0307	0.0107
90.9	16.875	0.261	-0.1800	0.0099
95.9	12.391	0.198	-0.4196	0.0115
100.9	7.508	0.119	-0.6943	0.0108
105.9	4.049	0.065	-0.9858	0.0108
110.8	2.099	0.036	-0.8055	0.0134
115.8	1.693	0.034	0.4379	0.0218
120.8	2.359	0.044	0.9955	0.0156
125.7	3.425	0.057	0.9055	0.0126
130.7	4.179	0.069	0.5302	0.0126
135.6	4.471	0.071	0.1094	0.0112
140.6	4.490	0.071	-0.3093	0.0110
145.5	4.313	0.076	-0.6691	0.0154
150.5	4.047	0.072	-0.7936	0.0152
155.4	3.762	0.064	-0.6714	0.0136
160.3	3.310	0.057	-0.3333	0.0150
165.2	2.535	0.044	0.1189	0.0160
170.2	1.927	0.034	0.5214	0.0163

TUNL Data

^{76}Se(p,p) E_p = 16 MeV

Angle(cm)	Cross Section		Analyzing Power	
25.3	2012.000	30.000	0.0203	0.0119
30.4	1037.000	16.000	0.0079	0.0122
35.4	517.100	7.800	-0.0050	0.0120
40.5	254.900	3.800	-0.0711	0.0133
45.5	125.100	1.900	-0.1785	0.0123
50.6	62.890	0.940	-0.2682	0.0166
55.6	34.440	0.520	-0.2239	0.0127
60.7	22.030	0.330	0.0931	0.0175
65.7	19.430	0.310	0.3698	0.0139
70.7	19.950	0.318	0.3734	0.0139
75.7	21.400	0.342	0.1769	0.0141
80.8	20.660	0.328	-0.0300	0.0138
85.8	17.110	0.269	-0.2302	0.0134
90.8	12.230	0.190	-0.4343	0.0129
95.8	7.372	0.122	-0.6032	0.0149
100.8	3.656	0.060	-0.7001	0.0145
105.7	1.769	0.031	-0.2681	0.0175
110.7	1.385	0.026	0.7830	0.0179
115.7	2.135	0.036	0.8260	0.0150
120.7	3.019	0.050	0.5318	0.0150
125.6	3.987	0.070	0.2746	0.0173
130.6	3.765	0.065	0.0393	0.0169
135.5	3.411	0.055	-0.1749	0.0153
140.5	2.830	0.048	-0.4318	0.0156
145.4	1.943	0.041	-0.7017	0.0215
150.4	1.481	0.036	-0.8188	0.0242
155.3	1.123	0.031	-0.6992	0.0215
160.3	0.976	0.022	-0.1717	0.0271
165.2	0.668	0.026	0.4617	0.0319
170.1	0.522	0.016	0.9439	0.0387

TUNL Data

$^{78}Se(p,p)$ E_p = 16 MeV

Angle(cm)	Cross Section		Analyzing Power	
25.3	2172.000	37.000	0.0183	0.0122
30.4	1108.000	19.000	0.0138	0.0124
35.4	540.000	9.200	-0.0183	0.0124
40.5	253.800	4.300	-0.0855	0.0135
45.5	120.100	2.000	-0.1980	0.0129
50.6	58.750	1.000	-0.2790	0.0144
55.6	33.980	0.580	-0.1274	0.0136
60.7	24.940	0.420	0.2072	0.0162
65.7	23.830	0.414	0.3615	0.0154
70.7	23.960	0.426	0.2951	0.0164
75.7	25.150	0.462	0.0962	0.0173
80.7	21.970	0.393	-0.0942	0.0168
85.8	17.120	0.293	-0.2778	0.0147
90.8	11.260	0.191	-0.4949	0.0141
95.8	6.253	0.116	-0.6588	0.0177
100.7	2.933	0.054	-0.6177	0.0177
105.7	1.647	0.030	0.1734	0.0183
110.7	1.847	0.033	0.8592	0.0159
115.7	2.874	0.050	0.6762	0.0151
120.7	3.820	0.065	0.3865	0.0145
125.6	4.345	0.075	0.1553	0.0148
130.6	4.146	0.071	-0.0386	0.0149
135.5	3.497	0.038	-0.2554	0.0141
140.5	2.582	0.034	-0.4743	0.0144
145.4	1.819	0.029	-0.6665	0.0207
150.4	1.262	0.023	-0.6927	0.0215
155.3	1.084	0.022	-0.2022	0.0210
160.3	1.139	0.022	0.4103	0.0199
165.2	1.181	0.022	0.8175	0.0201
170.1	1.153	0.022	0.8567	0.0189

TUNL Data

$^{80}Se(p,p)$ E_p = 16 MeV

Angle(cm)	Cross Section		Analyzing Power	
25.3	2144.000	54.000	0.0206	0.0112
30.4	1098.000	27.000	0.0124	0.0112
35.4	530.600	13.000	-0.0284	0.0112
40.5	235.300	5.900	-0.1061	0.0114
45.5	106.100	2.700	-0.2112	0.0113
50.6	51.830	1.300	-0.2385	0.0115
55.6	32.710	0.820	-0.0256	0.0113
60.6	27.170	0.680	0.2737	0.0116
65.7	28.080	0.647	0.3501	0.0114
70.7	26.400	0.611	0.2322	0.0120
75.7	27.460	0.633	0.0637	0.0115
80.7	21.360	0.495	-0.1318	0.0121
85.7	15.850	0.367	-0.3488	0.0119
90.7	9.505	0.220	-0.5595	0.0119
95.7	4.933	0.116	-0.6755	0.0131
100.7	2.396	0.056	-0.3926	0.0132
105.7	1.783	0.042	0.5119	0.0134
110.7	2.547	0.060	0.7894	0.0130
115.7	3.725	0.086	0.5052	0.0122
120.6	4.506	0.105	0.2653	0.0122
125.6	4.637	0.108	0.0626	0.0131
130.6	4.103	0.096	-0.1054	0.0133
135.5	2.991	0.075	-0.3396	0.0127
140.5	2.047	0.051	-0.5630	0.0132
145.4	1.321	0.033	-0.6701	0.0181
150.4	1.036	0.026	-0.3910	0.0211
155.3	1.140	0.028	0.3159	0.0167
160.3	1.645	0.040	0.7673	0.0152
165.2	1.834	0.046	0.8744	0.0143
170.1	2.174	0.052	0.7282	0.0142

TUNL Data

$^{82}Se(p,p)$ E_p = 16 MeV

Angle(cm)	Cross Section		Analyzing Power	
25.3	2036.000	38.462	0.0150	0.0122
30.4	1013.000	19.146	-0.0036	0.0122
35.4	464.600	8.953	-0.0314	0.0122
40.5	201.500	3.851	-0.1187	0.0123
45.5	85.490	1.622	-0.2169	0.0124
50.5	43.200	0.808	-0.2035	0.0126
55.6	29.870	0.556	0.0876	0.0125
60.6	27.730	0.519	0.3238	0.0127
65.6	29.740	0.555	0.3298	0.0125
70.7	29.390	0.547	0.2077	0.0125
75.7	25.620	0.484	0.0243	0.0131
80.7	21.450	0.402	-0.1994	0.0128
85.7	14.110	0.264	-0.4073	0.0127
90.7	7.980	0.149	-0.6295	0.0126
95.7	3.938	0.076	-0.6461	0.0136
100.7	2.214	0.042	0.0221	0.0136
105.7	2.283	0.044	0.7125	0.0131
110.7	3.224	0.061	0.6485	0.0130
115.6	4.411	0.083	0.3670	0.0127
120.6	4.736	0.089	0.1379	0.0127
125.6	4.319	0.081	-0.0496	0.0128
130.5	3.430	0.065	-0.2378	0.0131
135.5	2.303	0.043	-0.4477	0.0127
140.5	1.477	0.028	-0.6349	0.0134
145.4	0.931	0.018	-0.5310	0.0146
150.4	0.841	0.018	0.1148	0.0177
155.3	1.186	0.023	0.7306	0.0133
160.2	1.764	0.034	0.8635	0.0130
165.2	2.384	0.045	0.7655	0.0131

TUNL Data

$^{90}Zr(p,p)$ E_p = 16 MeV

Angle(cm)	Cross Section		Analyzing Power	
25.3	3170.000	26.978	0.0094	0.0089
30.3	1613.000	12.882	-0.0223	0.0089
35.4	792.100	6.209	-0.0745	0.0089
40.4	340.000	2.711	-0.1567	0.0094
45.5	131.000	1.021	-0.2409	0.0090
50.5	53.980	0.462	-0.1870	0.0104
55.5	39.870	0.313	0.1992	0.0091
60.6	45.800	0.400	0.3671	0.0109
65.6	52.390	0.411	0.2736	0.0090
70.6	52.230	0.428	0.1431	0.0091
75.6	44.550	0.350	-0.0450	0.0090
80.6	33.060	0.270	-0.2527	0.0094
85.7	20.500	0.171	-0.5053	0.0098
90.7	10.470	0.087	-0.7484	0.0099
95.7	4.842	0.043	-0.7411	0.0106
100.6	3.199	0.030	0.2320	0.0114
105.6	4.056	0.035	0.7908	0.0102
110.6	6.052	0.060	0.6010	0.0117
115.6	7.925	0.075	0.3016	0.0114
120.6	8.325	0.078	0.0684	0.0113
125.5	7.485	0.065	-0.1391	0.0104
130.5	6.016	0.054	-0.3291	0.0107
135.5	4.086	0.035	-0.5257	0.0101
140.4	2.472	0.023	-0.7036	0.0106
145.4	1.462	0.017	-0.6038	0.0140
150.3	1.235	0.016	0.1675	0.0159
155.3	1.683	0.016	0.8111	0.0112
160.2	2.558	0.024	0.8922	0.0105
165.2	3.507	0.032	0.7702	0.0102
170.1	4.383	0.041	0.5588	0.0103

TUNL Data

$^{116}Sn(p,p)$ E_p = 16 MeV

Angle(cm)	Cross Section		Analyzing Power	
25.2	5186.000	77.314	-0.0004	0.0069
30.3	2444.000	36.458	-0.0164	0.0070
35.3	1022.000	15.249	-0.0605	0.0070
40.3	409.500	6.143	-0.0727	0.0072
45.4	191.800	2.868	-0.0142	0.0070
50.4	143.200	2.156	0.1040	0.0074
55.4	136.300	2.037	0.1339	0.0070
60.4	124.400	1.876	0.0874	0.0074
65.5	100.600	1.506	-0.0001	0.0071
70.5	68.430	1.041	-0.1087	0.0078
75.5	40.310	0.605	-0.2369	0.0072
80.5	20.580	0.328	-0.3259	0.0093
85.5	11.010	0.173	-0.1924	0.0088
90.5	8.871	0.144	0.2620	0.0099
95.5	10.930	0.168	0.3993	0.0079
100.5	13.450	0.212	0.2932	0.0090
105.5	14.310	0.217	0.1305	0.0075
110.5	13.250	0.210	-0.0489	0.0093
115.5	10.720	0.172	-0.2240	0.0097
120.4	7.526	0.124	-0.3815	0.0104
125.4	4.642	0.076	-0.4600	0.0098
130.4	2.830	0.048	-0.3733	0.0116
135.4	1.979	0.034	-0.0270	0.0118
140.3	1.877	0.032	0.3365	0.0111
145.3	2.316	0.046	0.3701	0.0159
150.3	2.934	0.052	0.2690	0.0129
155.2	3.752	0.062	0.1560	0.0110
160.2	4.503	0.072	0.0981	0.0095
165.1	5.160	0.084	0.0639	0.0102
170.1	5.979	0.100	0.0793	0.0111

TUNL Data

^{120}Sn(p,p) E_p = 16 MeV

Angle(cm)	Cross Section		Analyzing Power	
25.2	5078.000	44.765	-0.0026	0.0048
30.2	2252.000	19.894	-0.0262	0.0049
35.3	919.500	8.128	-0.0551	0.0049
40.3	365.700	3.291	-0.0587	0.0053
45.3	196.500	1.746	0.0257	0.0050
50.4	158.200	1.431	0.1051	0.0054
55.4	149.600	1.328	0.1037	0.0050
60.4	125.200	1.140	0.0525	0.0055
65.4	93.500	0.836	-0.0296	0.0051
70.5	57.870	0.547	-0.1320	0.0062
75.5	31.520	0.285	-0.2526	0.0053
80.5	15.900	0.175	-0.2543	0.0087
85.5	10.340	0.106	0.0174	0.0076
90.5	10.570	0.112	0.3211	0.0080
95.5	12.720	0.120	0.3185	0.0061
100.5	14.440	0.147	0.1954	0.0074
105.5	13.990	0.129	0.0498	0.0057
110.5	11.970	0.126	-0.1040	0.0081
115.4	8.982	0.099	-0.2497	0.0088
120.4	5.984	0.072	-0.3728	0.0100
125.4	3.744	0.043	-0.3496	0.0094
130.4	2.577	0.032	-0.0959	0.0113
135.3	2.274	0.025	0.2160	0.0090
140.3	2.499	0.027	0.3113	0.0086
145.3	2.939	0.036	0.2219	0.0107
150.2	3.283	0.040	0.0769	0.0104
155.2	3.442	0.036	-0.0467	0.0082
160.2	3.459	0.037	-0.1240	0.0082
165.1	3.395	0.042	-0.1385	0.0107
170.1	3.290	0.041	-0.0999	0.0112

TUNL Data

$^{124}Sn(p,p)$ E_p = 16 MeV

Angle(cm)	Cross Section		Analyzing Power	
25.2	4951.000	58.580	-0.0178	0.0047
30.2	1946.000	23.123	-0.0328	0.0049
35.3	815.200	9.678	-0.0546	0.0048
40.3	318.900	3.918	-0.0406	0.0062
45.3	199.400	2.372	0.0414	0.0049
50.4	161.300	1.985	0.0981	0.0062
55.4	153.100	1.818	0.0801	0.0048
60.4	114.600	1.434	0.0354	0.0068
65.4	82.350	0.982	-0.0465	0.0050
70.4	47.420	0.584	-0.1585	0.0061
75.5	24.300	0.293	-0.2358	0.0054
80.5	13.360	0.181	-0.1557	0.0088
85.5	10.640	0.144	0.1729	0.0089
90.5	12.350	0.159	0.2970	0.0072
95.5	14.080	0.177	0.2426	0.0066
100.5	14.610	0.185	0.1235	0.0070
105.5	12.970	0.159	-0.0129	0.0060
110.4	10.170	0.134	-0.1592	0.0079
115.4	6.980	0.096	-0.2783	0.0091
120.4	4.572	0.067	-0.3185	0.0105
125.4	3.171	0.044	-0.1704	0.0097
130.4	2.773	0.040	0.1539	0.0101
135.3	3.013	0.040	0.2926	0.0083
140.3	3.279	0.042	0.2364	0.0075
145.3	3.510	0.054	0.0921	0.0122
150.2	3.458	0.048	-0.0444	0.0095
155.2	3.108	0.044	-0.1950	0.0098
160.2	2.692	0.036	-0.2892	0.0081
165.1	2.206	0.033	-0.3461	0.0112
170.1	1.847	0.030	-0.2619	0.0128

TUNL Data

^{134}Ba(p,p) E_p = 16 MeV

Angle(cm)	Cross Section		Analyzing Power	
25.2	7010.055	81.747	0.0106	0.0071
30.2	3008.501	35.571	-0.0028	0.0072
35.3	1244.104	13.663	-0.0280	0.0071
40.3	524.941	6.075	-0.0072	0.0083
45.3	303.512	3.367	0.0496	0.0074
50.3	246.632	2.898	0.0849	0.0085
55.4	211.732	2.347	0.0665	0.0073
60.4	166.408	1.988	0.0131	0.0091
65.4	110.919	1.230	-0.0641	0.0076
70.4	62.085	0.719	-0.1567	0.0088
75.4	32.163	0.362	-0.2053	0.0081
80.4	18.475	0.245	-0.0855	0.0122
85.4	15.826	0.205	0.1850	0.0115
90.4	18.113	0.226	0.2379	0.0102
95.4	19.982	0.238	0.1719	0.0092
100.4	19.373	0.238	0.0532	0.0100
105.4	16.117	0.185	-0.0625	0.0084
110.4	12.052	0.148	-0.1836	0.0102
115.4	8.061	0.105	-0.2617	0.0118
120.4	5.371	0.074	-0.2154	0.0132
125.4	4.104	0.055	-0.0251	0.0123
130.3	4.009	0.054	0.1655	0.0121
135.3	4.347	0.055	0.2248	0.0106
140.3	4.789	0.060	0.1781	0.0100
145.3	4.794	0.070	0.0735	0.0141
150.2	4.506	0.065	-0.0366	0.0136
155.2	3.890	0.052	-0.1682	0.0121
160.1	3.099	0.042	-0.2542	0.0123
165.1	2.418	0.036	-0.3090	0.0143
170.1	1.853	0.029	-0.2789	0.0158

TUNL Data

$^{136}Ba(p,p)$ E_p = 16 MeV

Angle(cm)	Cross Section		Analyzing Power	
25.2	6640.119	114.378	-0.0010	0.0050
30.2	2727.999	47.229	-0.0208	0.0051
35.2	1112.976	18.996	-0.0327	0.0051
40.3	467.947	8.110	-0.0099	0.0061
45.3	288.716	4.949	0.0593	0.0053
50.3	239.093	4.162	0.0891	0.0062
55.4	208.141	3.561	0.0517	0.0052
60.4	158.410	2.773	-0.0032	0.0068
65.4	101.620	1.741	-0.0782	0.0056
70.4	58.722	1.031	-0.1523	0.0074
75.4	28.657	0.497	-0.1902	0.0067
80.4	17.416	0.332	-0.0050	0.0116
85.4	16.450	0.317	0.2186	0.0117
90.4	19.559	0.354	0.2332	0.0087
95.4	21.229	0.382	0.1591	0.0084
100.4	20.229	0.365	0.0567	0.0086
105.4	16.250	0.285	-0.0732	0.0074
110.4	11.967	0.216	-0.2007	0.0091
115.4	7.514	0.146	-0.2703	0.0124
120.4	5.149	0.101	-0.2136	0.0127
125.4	4.167	0.081	0.0381	0.0126
130.3	4.513	0.085	0.2238	0.0105
135.3	5.077	0.092	0.2359	0.0087
140.3	5.626	0.100	0.1502	0.0077
145.2	5.661	0.107	0.0394	0.0109
150.2	5.031	0.093	-0.0734	0.0102
155.2	4.168	0.076	-0.1784	0.0097
160.1	3.159	0.058	-0.2748	0.0095
165.1	2.262	0.044	-0.3275	0.0124
170.1	1.571	0.031	-0.3198	0.0133

TUNL Data

^{138}Ba(p,p) E_p = 16 MeV

Angle(cm)	Cross Section		Analyzing Power	
25.2	6849.000	59.906	-0.0052	0.0052
30.2	2842.000	24.610	-0.0213	0.0052
35.2	1124.000	9.350	-0.0275	0.0052
40.3	490.200	4.158	0.0129	0.0058
45.3	316.900	2.584	0.0748	0.0053
50.3	271.100	2.297	0.0800	0.0058
55.3	228.200	1.854	0.0453	0.0052
60.4	167.200	1.450	-0.0183	0.0063
65.4	103.100	0.846	-0.0947	0.0054
70.4	53.260	0.483	-0.1800	0.0074
75.4	26.070	0.223	-0.1669	0.0064
80.4	17.710	0.190	0.0870	0.0107
85.4	18.940	0.200	0.2756	0.0103
90.4	22.270	0.209	0.2427	0.0079
95.4	23.590	0.219	0.1389	0.0078
100.4	20.940	0.199	0.0251	0.0081
105.4	16.090	0.158	-0.1048	0.0088
110.4	10.860	0.110	-0.2345	0.0095
115.4	6.855	0.085	-0.2855	0.0135
120.4	4.766	0.058	-0.1411	0.0134
125.3	4.509	0.053	0.1220	0.0126
130.3	5.216	0.054	0.2655	0.0100
135.3	5.971	0.058	0.2447	0.0087
140.3	6.613	0.060	0.1249	0.0073
145.2	6.409	0.070	0.0196	0.0112
150.2	5.593	0.057	-0.0865	0.0095
155.2	4.360	0.045	-0.2100	0.0102
160.1	3.185	0.032	-0.2859	0.0092
165.1	2.150	0.027	-0.3568	0.0137
170.1	1.453	0.019	-0.3415	0.0134

TUNL Data

$^{208}Pb(p,p)$ E_p = 16 MeV

Angle(cm)	Cross Section		Analyzing Power	
25.1	17830.000	266.980	-0.0023	0.0046
30.1	7845.000	115.752	0.0032	0.0045
35.2	3984.000	58.714	0.0205	0.0046
40.2	2362.000	34.642	0.0225	0.0045
45.2	1553.000	22.792	0.0052	0.0045
50.2	994.600	14.579	-0.0262	0.0046
55.2	590.200	8.657	-0.0588	0.0046
60.2	329.900	4.846	-0.0649	0.0048
65.3	193.800	2.850	-0.0163	0.0049
70.3	140.300	2.080	0.0640	0.0053
75.3	123.100	1.813	0.0863	0.0050
80.3	110.800	1.668	0.0505	0.0065
85.3	91.810	1.391	-0.0125	0.0069
90.3	69.390	1.039	-0.0796	0.0062
95.3	47.040	0.712	-0.1276	0.0069
100.3	30.560	0.471	-0.1367	0.0079
105.3	21.110	0.324	-0.0846	0.0075
110.3	19.100	0.314	0.0145	0.0104
115.3	17.780	0.298	0.0612	0.0113
120.2	18.580	0.304	0.0741	0.0104
125.2	17.000	0.269	0.0552	0.0089
130.2	16.810	0.263	0.0176	0.0084
135.2	13.970	0.217	0.0169	0.0080
140.2	11.570	0.179	0.0602	0.0080
145.2	9.299	0.166	0.0564	0.0139
150.1	7.454	0.132	0.1652	0.0137
155.1	6.085	0.105	0.1867	0.0125
160.1	5.276	0.089	0.2119	0.0120
165.1	4.830	0.087	0.2145	0.0139
170.0	4.483	0.078	0.1685	0.0132

TUNL Data

$^{209}Bi(p,p)$ E_p = 16 MeV

Angle(cm)	Cross Section		Analyzing Power	
25.1	17330.000	113.990	-0.0021	0.0052
30.1	7684.000	50.774	0.0038	0.0052
35.2	3869.000	23.958	0.0132	0.0052
40.2	2320.000	14.589	0.0243	0.0054
45.2	1535.000	9.411	0.0049	0.0052
50.2	994.300	6.223	-0.0272	0.0054
55.2	597.700	3.662	-0.0549	0.0053
60.2	338.700	2.197	-0.0687	0.0060
65.3	198.200	1.248	-0.0148	0.0057
70.3	143.700	0.963	0.0556	0.0058
75.3	123.900	0.795	0.0838	0.0057
80.3	110.100	0.723	0.0457	0.0060
85.3	92.620	0.666	-0.0115	0.0068
90.3	70.730	0.454	-0.0688	0.0059
95.3	48.200	0.338	-0.1358	0.0068
100.3	31.970	0.219	-0.1322	0.0067
105.3	22.020	0.157	-0.0788	0.0071
110.3	18.160	0.172	0.0065	0.0107
115.3	17.390	0.155	0.0811	0.0099
120.2	17.490	0.166	0.0721	0.0108
125.2	17.520	0.134	0.0627	0.0080
130.2	16.170	0.132	0.0222	0.0088
135.2	13.910	0.102	0.0281	0.0075
140.2	11.590	0.090	0.0505	0.0082
145.2	9.048	0.094	0.0680	0.0121
150.1	7.562	0.083	0.1281	0.0129
155.1	6.156	0.058	0.1660	0.0108
160.1	5.273	0.052	0.1884	0.0115
165.1	4.722	0.049	0.2032	0.0121
170.0	4.479	0.047	0.1442	0.0124

TUNL Data

$^{238}U(p,p)$ E_p = 16 MeV

Angle(cm)	Cross Section		Analyzing Power	
25.1	19630.000	336.493	-0.0030	0.0085
30.1	9190.000	158.662	-0.0064	0.0089
35.1	5003.000	83.442	0.0104	0.0084
40.2	2899.000	50.324	0.0087	0.0100
45.2	1846.000	30.773	0.0145	0.0085
50.2	1161.000	20.181	-0.0084	0.0105
55.2	736.400	12.280	-0.0096	0.0085
60.2	455.800	8.386	-0.0103	0.0132
65.2	307.800	5.160	0.0025	0.0088
70.2	231.100	3.930	0.0307	0.0096
75.2	175.700	2.953	0.0293	0.0090
80.2	142.700	2.451	0.0212	0.0101
85.2	113.100	1.946	-0.0069	0.0101
90.2	85.200	1.457	-0.0161	0.0099
95.2	65.860	1.129	-0.0181	0.0100
100.2	50.200	0.876	-0.0283	0.0109
105.2	39.360	0.675	0.0063	0.0100
110.2	31.320	0.576	0.0050	0.0131
115.2	27.300	0.504	0.0183	0.0132
120.2	23.260	0.437	0.0348	0.0140
125.2	20.640	0.370	0.0086	0.0119
130.2	18.100	0.327	0.0171	0.0124
135.2	16.200	0.286	0.0130	0.0112
140.2	14.340	0.255	0.0095	0.0115
145.1	13.200	0.256	0.0371	0.0151
150.1	12.170	0.239	0.0650	0.0156
155.1	11.190	0.206	0.0568	0.0129
160.1	10.650	0.197	0.0690	0.0131
165.1	10.030	0.187	0.0486	0.0135
170.0	9.574	0.179	0.0509	0.0137